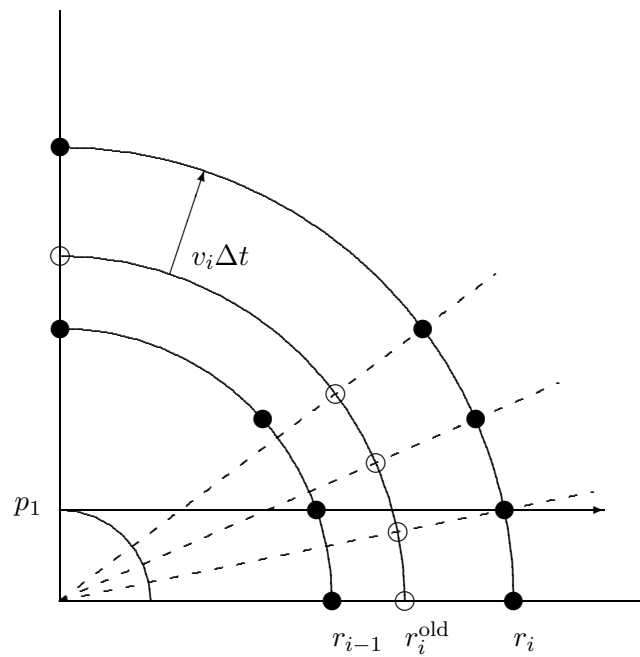


Max-Planck-Institut für Astrophysik

Radiation Hydrodynamics with Neutrinos: Stellar Core Collapse and the Explosion Mechanism of Type II Supernovae

Markus Rampp



Max-Planck-Institut für Astrophysik

Radiation Hydrodynamics with Neutrinos: Stellar Core Collapse and the Explosion Mechanism of Type II Supernovae

Markus Rampp

Vollständiger Abdruck der von der Fakultät für Physik
der Technischen Universität München zur Erlangung des akademischen Grades eines
Doktors der Naturwissenschaften
genehmigten Dissertation.

Vorsitzender: Univ.-Prof. Dr. F. von Feilitzsch

Prüfer der Dissertation:

1. Hon.-Prof. Dr. W. Hillebrandt
2. Univ.-Prof. Dr. M. Lindner

Die Dissertation wurde am 30.05.2000 bei der Technischen Universität München eingereicht und durch die Fakultät für Physik am 13.07.2000 angenommen.

Contents

1	Introduction	1
1.1	Stellar core-collapse and supernova explosions	2
1.1.1	The current paradigm	2
1.1.2	The role of neutrino transport	5
1.2	Aims of this thesis	8
2	The Equations of Radiation Hydrodynamics	11
2.1	Radiative transfer	11
2.1.1	Basic definitions and equations	11
2.1.2	Radiative transfer in moving media	17
2.1.3	Comoving frame radiative transfer equations	18
2.1.4	Characteristics and formal solution	21
2.1.5	Specifics of neutrino transport	22
2.2	Hydrodynamics	23
2.2.1	Basic considerations	23
2.2.2	Multicomponent flows	24
2.3	Radiation hydrodynamics	25
2.3.1	Coupling hydrodynamics to radiative transfer	25
2.3.2	Conservation properties	27
3	Numerical Radiation Hydrodynamics	31
3.1	Hydrodynamics and equation of state	31
3.1.1	The PROMETHEUS code	31
3.1.2	Equation of state	32
3.2	Radiative transfer	35
3.2.1	Variable Eddington factor method	35
3.2.2	Multi-group formulation of the moment equations	37
3.2.3	Formal solution of the Boltzmann equation	43
3.3	Details of coupling radiative transfer and hydrodynamics	48
3.3.1	Schedule of updates	48
3.3.2	Conservative mapping algorithm	49
3.4	Approximate multi-dimensional neutrino transport	50

4	Radiative Transfer Problems	53
4.1	Radiative transfer on a static background	53
4.1.1	Propagation of a light pulse	53
4.1.2	Homogeneous sphere	56
4.1.3	Static scattering atmospheres	59
4.1.4	Radiative transfer in general relativity	62
4.2	Radiative transfer in stationary background media	65
4.2.1	Differentially expanding gray scattering atmospheres	65
4.2.2	Differentially expanding nongray isothermal atmospheres	67
4.2.3	Frame dependence	70
4.3	Concluding remarks	72
5	Stellar Core Collapse and the Supernova Explosion Mechanism	75
5.1	Stellar core-collapse	75
5.1.1	Physics of stellar core-collapse	76
5.1.2	Investigated models	79
5.2	Post-bounce evolution of a $15 M_{\odot}$ progenitor star	92
5.2.1	Preliminaries	93
5.2.2	Numerical model	93
5.2.3	Results	95
5.2.4	Discussion	111
6	Summary and Conclusions	113
Appendix		
A	Neutrino Opacities	117
A.1	Basic considerations	117
A.1.1	Detailed balance	118
A.1.2	Neutrino absorption and emission	119
A.1.3	Scattering	119
A.1.4	Numerical implementation	123
A.2	Explicit expressions for various interaction processes	123
A.2.1	Neutrino absorption and emission by free nucleons	123
A.2.2	Neutrino absorption and emission by heavy nuclei	124
A.2.3	Neutrino-nucleon scattering	125
A.2.4	Coherent scattering of neutrinos off heavy nuclei	126
A.2.5	Inelastic scattering of neutrinos off charged leptons	129
Bibliography		133
Acknowledgements		141
Curriculum Vitae		143

Chapter 1

Introduction

Roughly every second, somewhere in the visible universe a gigantic explosion terminates the existence of a star that has before been living quietly for millions of years. A dramatic increase in the brightness of the dying star makes a “new” star appear in the sky, where in most cases no astrophysical object has been observed before. Adequately named *supernovae*, these spectacular explosions reach peak brightnesses that rival and in some cases even outshine the entire galaxy hosting the explosion, until they fade again within a few months. The brightest of these events can nowadays be traced to the outskirts of the universe. Once or twice a century, a supernova happens to explode in our own galaxy, and even more rarely, an unobscured view of such nearby events is granted to human observers. During the past millennium, a few of these “galactic” supernovae could be witnessed by the naked eye, at least in one case even during daylight. With the advent of modern astronomy, supernovae were routinely observed and became classified as major differences in their appearance were discovered. Two large classes of supernovae were identified according to the presence (the so-called Type II supernovae) or absence (Type I supernovae) of hydrogen lines in the optical spectra. Meanwhile further sub-classification — the relevant notation appends letters to the two basic types (Type Ia, Ib, etc.) — has become necessary.

But which kind of physical mechanism makes supernovae explode? What are the progenitors of supernovae and what is the source of these enormous amounts of energy? How is the explosion finally triggered? These basic questions have challenged scientists for many decades and it is fair to say that our present day understanding of the physics of supernovae is far from being complete.

As it turns out, observations of the electromagnetic radiation — until recently the only way to receive information about remote astronomical objects — are unfortunately of no immediate help for getting clues about the explosion mechanism of supernovae. Observational facts are merely consistent with a sudden release of the right amounts of energy deep inside some progenitor star, a site which is obscured from our view by thick layers of hot, opaque stellar material. The optical spectrum of a supernova, on the contrary, is formed in the very outer layers of the exploding star: If the star has lost its hydrogen envelope prior to the explosion, a Type I supernova is observed, if not, the supernova gets classified as Type II.

On the theoretical side, two basic scenarios have been worked out in the past. Supernovae of Type Ia, the optically brightest of all supernovae, are thought to be caused by a thermonuclear explosion of a white dwarf that is completely disrupted in this event. We will not consider them in this work. Here we are concerned with supernovae of Type II (and of Type Ib/c), which, according to present knowledge, are powered by the huge reservoir of gravitational binding energy that is released, when the core of a massive star collapses to form a compact object (i. e. a neutron star

or a black hole). For convenience, the common name “core-collapse supernovae” is often used for supernovae of Type II and of Type Ib/c.

In view of the core-collapse model, the stunning optical display of an exploding supernova becomes considerably leveled out. Even with our modern telescope-aided eyes we are able to witness only a minor side show of a virtually much more spectacular event: The overwhelming fraction (about 99% of a few times 10^{53} erg, or 10^{12} times the energy our present-day sun radiates within a year) of the energy released during a supernova explosion is neither contained in electromagnetic radiation nor in the kinetic energy of the explosion debris, but is carried by neutrinos of all flavours. This necessarily leads to the suspicion that, though being weakly interacting particles (the characteristic cross section of weak interactions is $\sigma_0 \simeq 10^{-44}$ cm²), neutrinos might play a crucial role for the explosion.

When on February 23rd 1987, Sanduleak –69 202, a blue supergiant star residing in our close-by satellite galaxy, the Large Magellanic Cloud, exploded to become the famous Supernova SN 1987A, about two dozens of these weakly interacting particles could be caught in the underground water tanks of the Irvine-Michigan-Brookhaven (IMB) and the Kamiokande II facilities as well as in the Baksan Scintillator Telescope (BST). With the lucky event of Supernova SN 1987A (it was the closest visible supernova since Kepler’s of 1604) and the capture of a few of its neutrinos, it was for the first time possible to “look” deep inside a core-collapse supernova, down to its very centre, where the explosion is triggered. The analysis of the neutrinos from SN 1987A confirmed the basic theoretical picture of the events in the interior of a typical core collapse supernova, yet the signal was obviously much too weak, to allow for more advanced diagnostics concerning the explosion mechanism.

1.1 Stellar core-collapse and supernova explosions

1.1.1 The current paradigm

Already in 1934, only two years after Chadwick had discovered the neutron, Baade & Zwicky (1934) “*with all reserve [...] advance[d] the view that supernovae represent the transitions from ordinary stars to neutron stars, which in their final stages consist of extremely closely packed neutrons*”. Although much observational and theoretical progress has been made since then, and many physical principles and important details that are crucial for the supernova mechanism to work have been identified, the basic picture of the early 1930’s — somewhat amazingly — still holds nowadays. In the following, we shall briefly outline (a more elaborate discussion on certain aspects will be given later on) the modern “standard picture” of the explosion mechanism of a core-collapse supernova that has emerged during the last few decades (for a comprehensive review see e. g. Bethe 1990).

Prompt vs. delayed explosions

Massive stars ($M \gtrsim 8 M_\odot$) quietly go through all the successive stages of nuclear burning and finally breed in their interior a central core that consists of the most tightly bound elements of the iron group (mainly ^{56}Fe and ^{56}Ni). Under the conditions met in this so-called iron core the pressure balancing the core’s own gravitational force is provided by a degenerate gas of relativistic electrons. Such a configuration is known to become unstable when its mass comes close to the Chandrasekhar mass, which amounts to roughly $1.4 M_\odot$. The iron core inside a massive star inevitably approaches its Chandrasekhar limit, since in a shell immediately surrounding the core, silicon burning is active

and continuously adds its ashes — made of iron group nuclei — to the mass of the iron core. Eventually, endothermic photodisintegration of heavy nuclei and progressive electron captures onto free protons and heavy nuclei weaken the vital pressure support and trigger a dynamical collapse of the iron core. In the absence of burnable fuel, the core proceeds to collapse under the pull of its own gravitational field — unnoticed by the rest of the hosting star — on a free fall time scale, which is of the order of 0.1 s. Only when nuclear densities are reached in the central parts of the iron core ($\rho_c \simeq 3 \times 10^{14} \text{ g cm}^{-3}$), repulsive nuclear forces are able to account for a sudden and dramatic rise of the incompressibility of the matter, which, within fractions of a millisecond halts the collapse of the innermost part of the core (comprising roughly half of the mass of the entire iron core). Until then, only fractions of a second have passed since the onset of the final instability.

Due to its inertia, the inner core overshoots its new equilibrium and rebounds (“bounces”) into the outer core, which is still collapsing with velocities exceeding a tenth of the speed of light. At the surface of the rebounding inner core, a strong hydrodynamic shock wave forms, finally detaches and starts propagating outwards through the outer core. The hydrodynamic shock is the fundamental physical mechanism that turns the implosion into an outwardly directed explosion: Kinetic energy of the infalling material being decelerated in passing the shock wave is converted into internal energy which by virtue of the resulting pressure increase supports the outward motion of the shock wave. Originally it was thought that the shock wave is able to reach and expel the outer envelope of the star. This was motivated by the fact that the energy, the shock wave is given at birth was found to be several times the observed kinetic explosion energies ($\simeq 10^{51} \text{ erg}$). However, on its passage through the outer parts of the iron core, the shock suffers from severe energy losses, e. g. due to the energy that is spent for the dissociation of the infalling iron material into nucleons and by a prompt burst of neutrinos. After having propagated only a few hundred kilometers, the shock comes to halt typically still well inside the iron core of the star (e. g. Mayle 1985; Hillebrandt 1987; Mayle, Wilson, & Schramm 1987; Bruenn 1989a,b; Myra & Bludman 1989). Only for very special combinations of physical parameters (like the stellar model of the progenitor or the incompressibility of nuclear matter) accounting for an extraordinarily small outer core to be passaged by the shock and large initial shock energies, this so-called “prompt explosion” scenario might work. In particular, no prompt explosions have been found to occur in stars more massive than $10 M_{\odot}$.

An alternative scenario has been worked out, in which neutrinos manage to revive the stalled hydrodynamic shock (Wilson 1985; Bethe & Wilson 1985). It relies on the following basic findings: Only in the very beginning of the collapse, neutrinos produced by electron captures are able to leave the iron core unhindered. With the collapse proceeding to higher densities ($\rho \simeq 10^{12} \text{ g cm}^{-3}$), neutrinos become “trapped” by the infalling matter, i. e. due to the high opacities the time scale for neutrinos to diffuse outwards becomes larger than the collapse time scale of the core. As a consequence, only a modest fraction of neutrinos is lost from the collapsing core (e. g. Sato 1975; Mazurek 1976). Thus, instead of being radiated immediately by neutrinos, most of the gravitational binding energy released during collapse gets stored as internal energy (mainly in the form of electron degeneracy energy) in the dense inner core. This energy is eventually released in neutrinos (being the most weakly interacting particles present) but on a much longer time scale: After the core bounce, it takes neutrinos hundreds of milliseconds to diffuse through the newly formed protoneutron star towards its “surface”. Only there matter becomes sufficiently transparent to neutrinos to enable them to almost stream off freely. One may therefore consider the hot and dense protoneutron star as a powerful neutrino source which shines for seconds and radiates away the gravitational binding energy that was converted into internal energy during

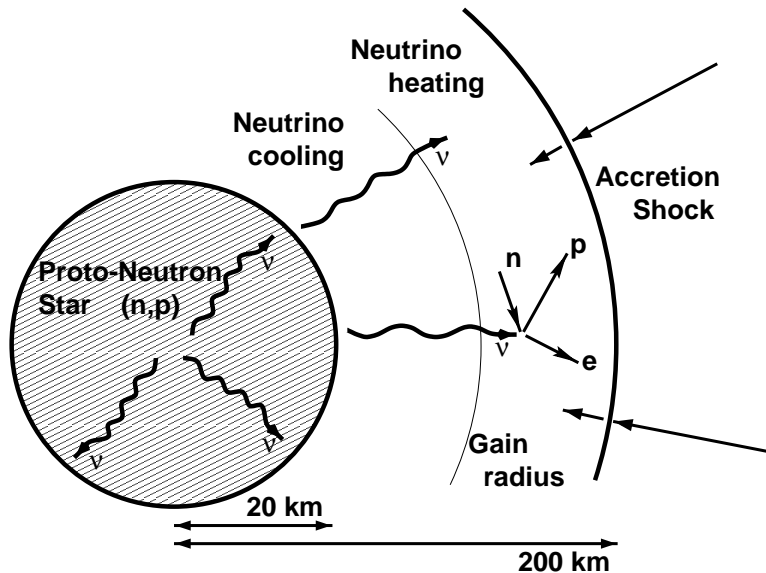


Figure 1.1: Schematic view of the central regions of the collapsed core of a massive star about 100 ms after core bounce, when the hydrodynamic shock wave has stalled some hundred kilometers from the centre. Through the standing shock wave infalling matter gets accreted (straight arrows) onto the protoneutron star. Deep inside, neutrinos slowly diffuse (indicated by wrinkled arrows) towards the surface of the protoneutron star. From there they can almost stream off freely, cooling this region. Below the shock, a small fraction of the emitted neutrinos is reabsorbed by free nucleons. The neutrino-heated matter provides additional pressure support for the shock. If the heating is sufficiently strong, the shock wave gets revived, propagates through the entire star and finally expels the outer layers of the star in a supernova explosion.

collapse. The situation that arises about 100 ms after shock formation is sketched in Fig. 1.1: Immediately underneath the standing shock wave (“accretion shock”) that has stalled at a radius of a few hundred kilometers, a region of dilute stellar material can build up, where the physical conditions favor a net deposition of neutrino energy (see e. g. Bethe & Wilson 1985; Bethe 1990; Bruenn 1993). With only a small fraction ($\simeq 1\%$) of the huge reservoir of gravitational binding energy ($\simeq 10^{53}$ erg) radiated by the protoneutron star being reabsorbed in this region, the standing shock can be revived to cause a healthy supernova explosion. The time scale for this to happen is of the order of several hundred milliseconds, which motivated the name “delayed” explosion as compared to the “prompt” explosions happening on the hydrodynamical time scale, which is about two orders of magnitude smaller.

Current problems of supernova research

The pioneering calculations of Wilson (1985) and Bethe & Wilson (1985) have been superseded by quite a number of progressively refined investigations, which shed some doubt on the early numerical results. Although the existence of a neutrino heating region was confirmed to be a generic feature (e. g. Bruenn 1993), the viability of the delayed explosion mechanism could not be demonstrated convincingly yet because Bruenn and others (e.g. Hillebrandt 1987) did not get explosions in their models. However, during the last few years it has been pointed out that supernova models have to be extended beyond the physics considered so far in a number of respects.

One sort of problems is concerned with convective phenomena inside (Keil, Janka, & Müller 1996; Keil 1997) or near the “surface” (Mezzacappa, Calder, Bruenn, Blondin, Guidry, Strayer, & Umar 1998a) of the newly formed protoneutron star as well as in the region below the shock (Herant, Benz, & Colgate 1992; Herant, Benz, Hix, Fryer, & Colgate 1994; Burrows, Hayes, & Fryxell

1995; Janka & Müller 1996; Müller & Janka 1997; Mezzacappa, Calder, Bruenn, Blondin, Guidry, Strayer, & Umar 1998b; Kifonidis, Plewa, Janka, & Müller 2000) as observed in multi-dimensional hydrodynamical simulations. The significance of convection for the explosion mechanism derives from the facts that in addition to the neutrino diffusion, convective mass motions provide another means of transporting energy from the depths of the protoneutron star to its surface where it is carried away by neutrinos a fraction of which is reabsorbed farther out, as well as from above the gain radius (see Fig. 1.1), where the neutrino heating rates peak, to the shock, where the increase of the pressure supports the shock’s outward motion. In effect, the shock revival is facilitated by convection. Strong supporting evidence for convective phenomena derives also from observations of supernova SN 1987A, which, in many respects can only be explained if extensive mixing processes were in effect deeply inside the star already during the first few hundred milliseconds of the explosion (see Müller 1998, and references cited therein).

Much activity is currently also devoted to the study of the complicated microphysics of the hot and dense nuclear matter in the newly formed neutron star (Schinder 1990; Raffelt & Seckel 1995; Raffelt, Seckel, & Sigl 1996; Janka, Keil, Raffelt, & Seckel 1996; Reddy, Prakash, & Lattimer 1998; Burrows & Sawyer 1998, 1999; Yamada 2000; Yamada & Toki 2000). At densities exceeding $\rho \gtrsim 10^{14} \text{ g cm}^{-3}$, spatial and temporal correlations between nucleons as well as effects due to the recoil of the nucleons have been shown to become important for calculating neutrino cross sections. It is also being emphasized that the cross sections have to be derived consistently from the underlying nuclear equation of state. A number of these investigations indicate, that the “standard” approximations (Tubbs & Schramm 1975; Schinder & Shapiro 1982; Bruenn 1985) used so far in supernova models might have considerably *overestimated* the neutrino opacities at the relevant densities. Reduced opacities would enable neutrinos to diffuse more quickly through the protoneutron star, and thus enhanced luminosities and heating rates are expected.

1.1.2 The role of neutrino transport

This thesis is concerned with a third sort of problems, namely the details of the transport of energy, momentum and lepton number by neutrinos, which plays a particularly important role for all stages of a core-collapse supernova: During collapse, the exact amount of lepton number and energy loss prior to neutrino trapping has been shown to critically determine the location inside the core where the bounce shock forms and thus the energy it is initially given. Because the shock loses several times 10^{51} erg — which is most of its initial energy — for disintegrating a few tenths of a solar mass of iron-group material on its passage through the outer iron core, only a relatively small shift ($\simeq 10\%$ of the core mass) of the shock formation position can have dramatic consequences for the success or failure of the explosion.

Soon after its formation, the hydrodynamic shock reaches regions which are sufficiently transparent to release a short but intense burst of neutrinos produced in the shock heated matter. During this outburst, the shock loses another 10^{51} erg of energy, which, again, is a substantial fraction of its initial energy and therefore has to be calculated accurately.

Finally and probably most importantly, the amount of energy which is absorbed in the heating region and thus the success of the shock revival mechanism is sensitively determined by the local neutrino distribution. Since the neutrino absorption cross sections strongly depend on the neutrino energy — typically the cross sections are proportional to the *square* of the energy — the heating rates are not only determined by the total neutrino luminosity of the protoneutron star but also by the spectral distribution of the neutrinos: The same luminosity but radiated with a harder

spectrum leads to considerably increased heating rates. In addition, also the angular distribution of the neutrinos enters the heating rate: For a given protoneutron star luminosity, the number (and total energy) of neutrinos that can be absorbed in the heating region is larger if the degree of isotropy of the local neutrino distribution is higher.

In view of the above considerations an accurate calculation of the neutrino transport dynamically coupled to the equations governing the evolution of the stellar matter clearly seems to be required. This, however, comprises a complicated problem that can only be tackled numerically. It has so far not been treated in a satisfactory manner.

Overview of methods

In previous work, neutrino transport has been computed with a number of numerical methods employing increasingly sophisticated approximations. The main differences are connected with the handling of the angular and spectral dependence of the neutrino phase-space distribution.

Among the first methods were simple *leakage schemes*, where neutrinos merely act as local sinks of energy (and possibly momentum and lepton number). According to local neutrino emission rates, energy is simply removed from the star. No radiative transport is calculated.

Quite a variety of *diffusion methods* have been put forward during the past decades. They all rely on the assumption that neutrinos interact sufficiently frequently with the ambient matter by scatterings and absorptions so that the mean free path gets substantially smaller than the typical length scales of the system (in analogy to electromagnetic radiation the system is said to be “optically thick” to neutrinos in this case). Under these circumstances, the local distribution of neutrinos in phase space can be assumed to be only weakly anisotropic and a simple diffusion equation can be used for describing the energy transport. When the condition of optical thickness is not fulfilled, diffusion schemes are known to give superluminal speeds for the transport of energy. This can be avoided by a so called *flux limiting* procedure, which employs a simple interpolation for the energy flux between optically thick regions, where the diffusion approximation holds, and optically thin regions, where neutrinos stream freely with the speed of light¹. Whereas the two mentioned physical limits are attained correctly, the interpolation is purely arbitrary in the intermediate regime. Various diffusion methods mainly differ in the way the energy dependence of the neutrino transport is handled. The so-called *multi(energy)-group flux-limited diffusion* schemes (MGFLD for short; see Bruenn 1985) have to be considered as the most sophisticated approach of this category, since they compute the energy dependent transport (in diffusion approximation) by considering a number of neutrino energies separately.

In order to take into account also the angular dependence of the neutrino distribution function properly, and thereby avoiding the introduction of ad hoc prescriptions like flux-limiting, the Boltzmann transport equation itself has to be solved. The so-called *discrete angles* method (S_N -method) employs a direct discretization of the Boltzmann equation (e. g. Carlson 1967; Yueh & Buchler 1977; Mezzacappa & Bruenn 1993a; Yamada, Janka, & Suzuki 1999; Mezzacappa & Messer 1999). While the angular and spectral properties of the radiation field can in principle be accounted for “exactly”, practical calculations are limited by computer resources and suffer from unsatisfactory angular resolution.

These problems are avoided in *variable Eddington factor* methods (Freeman et al. 1968), which are based on the solution of angular moments of the Boltzmann equation. The two moment equations of lowest order describe the transport of radiation energy and momentum, respectively.

¹We assume the neutrinos to have a vanishing rest mass.

The moment equations constitute a hierarchical set of partial differential equations and thus must be supplemented by a closure relation — the variable Eddington factor —, similar to the equation of state closing the equations of hydrodynamics. The quality of approximation for the Boltzmann equation is determined by the particular choice for the variable Eddington factor. In principle, excellent accuracy in describing the angular variation of the radiation field can be achieved.

Monte Carlo methods (see e. g. Janka 1991b, and references cited therein) are also able to provide accurate solutions of the Boltzmann equation. By following the trajectories of individual sample particles, the neutrino distribution function is constructed by a statistical approach without direct use of a numerical grid, rather than being solved for as it is done within the methods based on the discretized transport equations. In many respects Monte Carlo methods are easier to handle and to generalize than other techniques. On the other hand, in order to guarantee the desired statistical accuracy, a sufficiently large number of particles have to be followed by the calculation. This number usually makes Monte Carlo methods too expensive for computing the neutrino transport in combination with hydrodynamical supernova simulations.

Consequences for supernova modeling

The majority of the more advanced *core-collapse* calculations have employed the multi-group flux-limited diffusion approximation (MGFLD) of neutrino transport. Throughout the inner parts of the iron core, the neutrino opacities are large enough to guarantee that a diffusion equation yields a good approximation to the transport equations, and hence MGFLD can be expected to give reasonable results. In the outer regions, however, where the flux limiter is in effect in order to prohibit superluminal transport, the results obtained with MGFLD are much more questionable, but are regarded as less significant for the dynamics of core-collapse and the details of shock formation. Both hypotheses were in principle confirmed by the comparative studies of Mezzacappa & Bruenn (1993b,c). Employing a discrete angles (S_N) method, they obtained reference solutions for the transport that could be used to validate core-collapse simulations employing the MGFLD approximation. While rather good agreement between results obtained with both methods was found throughout the inner core — in particular for the important physical quantities determining the shock formation point — considerable deviations appeared in the outer regions of the iron core. As far as neutrino transport is concerned, the models of Mezzacappa & Bruenn (1993b,c) have so far been the most elaborate — and presumably computationally the most expensive — core-collapse simulations. However, with the S_N -method only a rather poor angular resolution of the neutrino distribution can be afforded with the computational resources available at present and in the near future. This might affect the quality of the results (cf. Yamada et al. 1999), especially when these simulations are eventually extended into the post-bounce phase.

The so far most sophisticated published neutrino-radiation hydrodynamical simulations that were also extended into the *post-bounce* phase have relied on the MGFLD approximation (Bruenn 1993; Bruenn, Mezzacappa, & Dineva 1995). However, the heating region that has developed below the stalled shock about 0.1 s after core bounce, where the exact number and energy of neutrinos critically determines the amount of heating, coincides with the domain where MGFLD fails to provide a reasonable approximation to neutrino transport: Neutrinos run out of equilibrium with the stellar medium further inside, below the “surface” of the protoneutron star and reach the free-streaming limit only considerably far above the heating region. In between, called the “semi-transparent” (or “transition”) region, the MGFLD approximation relies on an ad hoc interpolation between the diffusion and the free-streaming regime and therefore fails to reliably calculate the

spectrum and the degree of anisotropy of the neutrinos (Janka 1991b, 1992; Messer, Mezzacappa, Bruenn, & Guidry 1998; Mezzacappa & Messer 1999; Yamada et al. 1999). Moreover, Messer et al. (1998) and Mezzacappa & Messer (1999) conclude that the heating rates are actually considerably *underestimated* as an artifact of the particular flux limiting method used in the models of Bruenn (1993) and Bruenn et al. (1995), which all failed to explode. All these findings are, however, drawn from stationary neutrino transport calculations which were performed only for a few static snapshots of the temporal evolution of a supernova core, and thus no definite conclusions concerning the dynamics can be drawn.

1.2 Aims of this thesis

The considerations of the previous sections immediately demonstrate that it is necessary to overcome the severe technical limitations concerning the neutrino transport, which are still inherent to all contemporary supernova models. In the light of the known deficiencies, which even the most sophisticated spherically symmetric models suffer from, conclusions drawn from the consideration of “additional” physics like convective phenomena or improved microphysics in detailed numerical models appear to be at least premature, unless the neutrino transport can be handled with adequate accuracy. Hence, progress in the numerical modeling and physical understanding of core-collapse supernovae is considered to be closely connected to achievements in the treatment of the neutrino transport.

This was the motivation to develop a new numerical tool which is capable of calculating accurate neutrino transport and for the first time allows one to *reliably* study the physics of core-collapse supernovae by neutrino-radiation hydrodynamical simulations. Especially the possibility for generalizing a method to multi-dimensional applications is an important aspect to be considered in the development. The finding that existing schemes like the S_N -method might not fulfil this requirement served as another strong motivation to develop a new method.

As we have indicated previously, a transport scheme should be able to handle the full phase-space dependence of the neutrino distribution function accurately and thus has to be based on the Boltzmann transport equation. In particular, also the angular distribution of the neutrinos must be described properly. With the resulting increased dimensionality of the problem, computational efficiency becomes a major issue: Even the idealized case of a spherically symmetric supernova entails the solution of a (numerically stiff) three-dimensional, time-dependent (the distribution function depends on time and radial position in the star as well as on the energy and the direction of propagation of the neutrinos) transport problem coupled to the hydrodynamics, which challenges even modern supercomputers. We chose a variable Eddington factor method since by focussing on the radiation moment equations the dimensionality of the problem is reduced by one. The remaining dependence of the distribution function on the angle of neutrino propagation relative to the radial direction can be handled very accurately and efficiently by exploiting the specific symmetries of the problem. Moreover, we have been able to generalize the method for application to multi-dimensional problems. We shall argue that for studying convective phenomena in core-collapse supernovae, the proposed scheme can be expected to give a reasonable approximation to genuinely multi-dimensional neutrino-radiation hydrodynamics (which appears to be out of reach currently). At the same time, compared to one-dimensional calculations the computational load increases only relatively mildly with the number of spatial zones used to resolve the second (and third) dimension of the star, as opposed to similar approaches based, e. g., on the S_N -method.

In the course of this work we apply the new method in simulations of spherically symmetric core-collapse which has so far not been studied extensively to the level of accuracy of the Boltzmann equation. The interesting post-bounce phase is studied in the specific case of a progenitor star of $M = 15 M_{\odot}$. We present a simulation of a core-collapse supernova that follows the evolution covering the collapse, bounce and shock propagation phase for almost 600 ms, in total. For the first time, an accurate treatment of the neutrino transport was used throughout the entire evolution which allows one to discuss the viability of the delayed explosion mechanism without the imponderabilities of an insufficient treatment of the neutrino transport. In this thesis we have restricted ourselves to spherically symmetric problems with “standard microphysics” since even in this case the demands on the computational resources are enormous. In future applications, improved microphysics and multi-dimensional convection effects shall be investigated.

This thesis is subdivided into the following parts: The equations of radiation hydrodynamics to be solved and their numerical implementation are introduced in Chapters 2 and 3, respectively. Results for a number of idealized test problems are then presented in Chapter 4. Subsequently, in Chapter 5, the new scheme is applied to “realistic” neutrino-radiation hydrodynamical supernova simulations (the treatment of the relevant neutrino opacities is detailed in Appendix A). A summary of the thesis will be given in Chapter 6, together with concluding remarks and an outlook on future work.

Chapter 2

The Equations of Radiation Hydrodynamics

The equations of radiation hydrodynamics to be introduced in the course of this chapter describe the coupled evolution of physical systems that contain “radiation” and a “fluid”. The distinction between both components is not given a priori but depends on the physical conditions of the system under consideration. In our specific application to core-collapse supernovae, for example, we shall see in Chap. 5 that the stellar “fluid” can be assumed to contain nucleons and nuclei, charged leptons and photons (!), whereas the neutrinos have to be treated separately as “radiation”.

In the most general case one has to consider statistical ensembles of particles of different kinds in phase-space. Each of the ensembles may be described physically by its own particle distribution function. What we will call the “fluid” is the subsystem of particles that admits a hydrodynamical description, which, e. g. requires that the mean free path between interactions of those particles is very small compared to the scales of macroscopic variations in the system. Hence mean quantities like the local density of mass, defined as statistical averages on a macroscopic scale, can be used to describe the “hydrodynamic state” of the fluid, whose evolution is governed by the equations of hydrodynamics. But generally not all kinds of particles fulfil these requirements. If the mean free path between interactions becomes comparable to, or even larger than the dimensions of the system, the hydrodynamic approximation obviously breaks down and the particles have to be treated as “radiation”: Retaining the full dependence on all phase-space coordinates, the physical state of the radiation field is given in terms of a distribution function, which evolves in time according to the equation of radiative transfer.

In the following, we first introduce the equation of radiative transfer and then briefly discuss the equations of hydrodynamics and their coupling to radiative transfer.

2.1 Radiative transfer

2.1.1 Basic definitions and equations

Boltzmann equation

The physical state of a statistical ensemble of particles with given statistics (e. g. Bosons, Fermions) described by the particle distribution function $f(t, \mathbf{r}, \mathbf{p})$ in phase space where $g/h^3 \cdot f(t, \mathbf{r}, \mathbf{p}) d^3\mathbf{r} d^3\mathbf{p}$ is the number of particles occupying the phase-space volume $d^3\mathbf{r} d^3\mathbf{p}$ at (\mathbf{r}, \mathbf{p}) (g denotes the

statistical weight of the particles; e. g. $g = 1$ for Dirac neutrinos, $g = 2$ for photons; $h = 2\pi\hbar$ is Planck's constant). The temporal evolution of the distribution function is governed by the Boltzmann equation

$$\frac{\partial}{\partial t}f + \frac{d\mathbf{r}}{dt} \nabla_{\mathbf{r}}f + \frac{d\mathbf{p}}{dt} \nabla_{\mathbf{p}}f = \left(\frac{df}{dt}\right)^{\text{coll.}}. \quad (2.1)$$

Particles with vanishing rest mass, usually referred to as “radiation” in the classical sense, move along straight rays with the speed of light, and hence $d\mathbf{r}/dt = \mathbf{n}c \equiv \mathbf{p}/|\mathbf{p}|c$. If, in addition, no external forces are present ($\dot{\mathbf{p}} \equiv 0$), equ. (2.1) becomes the familiar Boltzmann equation of radiative transfer:

$$\frac{1}{c} \frac{\partial}{\partial t}f + \mathbf{n} \nabla_{\mathbf{r}}f = B. \quad (2.2)$$

The Boltzmann equation (2.2) is a hyperbolic partial differential equation. Specifically, for a given source term B , equ. (2.2) is a linear advection equation with characteristic speed c : Along a line element of length $\Delta s = \mathbf{n} \Delta \mathbf{r}$ and within the time interval $\Delta t = \Delta s/c$, the change of the distribution function of particles entering at one end (s, t) and emerging at the other end ($s + \Delta s, t + \Delta t$) results from interactions (absorptions, emissions and scatterings) of the particles with an ambient medium as given by the “collision term” B . Introducing the “emissivity” $\tilde{\eta}$ and the opacity χ (which is the inverse of the mean free path), the collision term can be written as (scattering processes can be treated as absorptions with subsequent emissions)

$$B := \frac{1}{c} \left(\frac{df}{dt}\right)^{\text{coll.}} \equiv \tilde{\eta} - \chi f. \quad (2.3)$$

Specific intensity and its angular moments

Introducing the monochromatic specific intensity

$$\mathcal{I} := \left(\frac{\epsilon}{hc}\right)^3 c \cdot f, \quad (2.4)$$

and the emissivity

$$\eta := \left(\frac{\epsilon}{hc}\right)^3 c \cdot \tilde{\eta}, \quad (2.5)$$

the Boltzmann equation (2.2) reads

$$\frac{1}{c} \frac{\partial}{\partial t} \mathcal{I} + \mathbf{n} \nabla_{\mathbf{r}} \mathcal{I} = S \equiv \eta - \chi \mathcal{I}, \quad (2.6)$$

where ϵ is the energy of the radiation. Rewriting the momentum-space part of a phase-space volume element as ($d\Omega$ denotes the solid angle element)

$$d^3\mathbf{p} = \epsilon^2/c^3 d\epsilon d\Omega, \quad (2.7)$$

the quantities $\mathcal{I}(t, \mathbf{r}, \epsilon, \mathbf{n}) d\Omega d\epsilon \mathbf{n} \mathbf{r}/|\mathbf{r}| dA dt$ and $\epsilon^{-1} \mathcal{I}(t, \mathbf{r}, \epsilon, \mathbf{n}) d\Omega d\epsilon \mathbf{n} \mathbf{r}/|\mathbf{r}| dA dt$ can be interpreted as the amount of energy and particle number, respectively, which, during the time dt is carried by radiation within the frequency interval $h^{-1}[\epsilon, \epsilon + d\epsilon]$ through the surface element dA

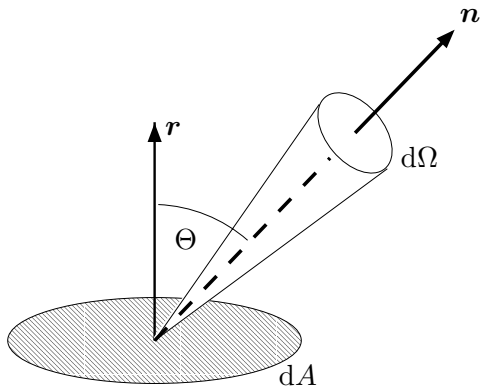


Figure 2.1: Illustration of the geometric quantities used for the definition of the specific intensity \mathcal{I} : dA is the area of a surface element with an outwardly directed normal $\mathbf{r}/|\mathbf{r}|$. The coordinate Θ measures the angle between \mathbf{r} and the direction \mathbf{n} of a beam of radiation which is propagating into the solid angle $d\Omega$.

(with the outwardly directed normal $\mathbf{r}/|\mathbf{r}|$) into the solid angle $d\Omega$ about the direction \mathbf{n} (see Fig. 2.1). The source term $S := (\epsilon/hc)^3 c \cdot B \equiv \eta - \chi \mathcal{I}$ is interpreted as the amount of radiation energy in a unit frequency interval contained within the unit solid angle around the direction \mathbf{n} that is exchanged with a material element of unit volume per unit time interval.

Angular moments of the monochromatic specific intensity are defined as the following integrals over all angular directions

$$J(t, \mathbf{r}, \epsilon) := \frac{1}{4\pi} \int d\Omega \mathcal{I}(t, \mathbf{r}, \epsilon, \mathbf{n}) = \frac{c}{4\pi} E(t, \mathbf{r}, \epsilon), \quad (2.8)$$

$$H_i(t, \mathbf{r}, \epsilon) := \frac{1}{4\pi} \int d\Omega n_i \mathcal{I}(t, \mathbf{r}, \epsilon, \mathbf{n}) = \frac{1}{4\pi} F_i(t, \mathbf{r}, \epsilon), \quad (2.9)$$

$$K_{ij}(t, \mathbf{r}, \epsilon) := \frac{1}{4\pi} \int d\Omega n_i n_j \mathcal{I}(t, \mathbf{r}, \epsilon, \mathbf{n}) = \frac{c}{4\pi} P_{ij}(t, \mathbf{r}, \epsilon), \quad (2.10)$$

⋮

where E denotes the (monochromatic) radiation energy-density, \mathbf{F} the density of the (monochromatic) energy flux (the momentum density is given by $1/c^2 \mathbf{F}$), and P_{ij} are the components of the stress tensor \mathbf{P} . Moments of higher order do not admit an immediate physical interpretation.

Moment equations

Forming angular moments of the Boltzmann equation (2.6) one obtains the hierarchical set of monochromatic moment equations:

$$\frac{1}{c} \frac{\partial}{\partial t} J + \nabla \cdot \mathbf{H} = S^{(0)} \quad (0^{\text{th}}\text{-order moment equation}), \quad (2.11)$$

$$\frac{1}{c} \frac{\partial}{\partial t} \mathbf{H} + \nabla \cdot \mathbf{K} = \mathbf{S}^{(1)} \quad (1^{\text{st}}\text{-order moment equation}), \quad (2.12)$$

⋮

with the corresponding source terms being defined as

$$\begin{aligned} S^{(0)}(t, \mathbf{r}, \epsilon) &:= \frac{1}{4\pi} \int d\Omega S(t, \mathbf{r}, \epsilon, \mathbf{n}), \\ S^{(1)}(t, \mathbf{r}, \epsilon) &:= \frac{1}{4\pi} \int d\Omega \mathbf{n} S(t, \mathbf{r}, \epsilon, \mathbf{n}). \\ &\vdots \end{aligned} \tag{2.13}$$

As a result of the angular integrations, the system of moment equations is of reduced dimensionality compared to the original radiative transfer equation. Based on this simplification and the fact that the (lowest order) equations admit a very straightforward physical interpretation (namely as transport equations for radiation energy and momentum), the moment equations are of prime importance for radiative transfer theory and its applications.

For practical calculations, the infinite system (2.11, 2.12, ...) has to be truncated at some finite level n_{\max} and an appropriate closure relation has to be provided, which allows one to eliminate one of the $n_{\max} + 1$ radiation moments (usually the moment of order $n_{\max} + 1$ is reexpressed in terms of the moments of order $\leq n_{\max}$). In general, this again requires the solution of the Boltzmann equation of radiative transfer, and one is tempted to suspect that employing the system of moment equations does not provide much of a gain compared to solving the original Boltzmann equation. However, for reasons that will become evident in the next chapter, this is not the case, and focussing on the moment equations has indeed proven to be extremely useful, in particular when it comes to numerical applications.

Spherical symmetry

In order to further reduce the dimensionality of the radiative transfer problem, we will henceforth assume that the *spatial* variation of all quantities can be described by only one coordinate. In this case, it can be shown that in addition to this spatial coordinate r , the time t and the frequency $h^{-1}\epsilon$, the specific intensity depends only on one angular coordinate Θ . In spherical coordinates, Θ is measured as the angle between the radial direction \mathbf{r} (with $r := |\mathbf{r}|$) and the direction of propagation \mathbf{n} of the radiation (see Fig. 2.1):

$$\mu := \cos \Theta := \frac{\mathbf{r} \cdot \mathbf{n}}{r}. \tag{2.14}$$

Spherical symmetry furthermore implies that the energy flux points into the radial direction

$$\mathbf{F} = 4\pi \frac{\mathbf{r}}{r} H, \tag{2.15}$$

and that the only relevant quantity of the stress tensor is the 33-component, which is identified with the scalar “radiation pressure”

$$P = \frac{4\pi}{c} K_{33} \equiv \frac{4\pi}{c} K. \tag{2.16}$$

The scalar components of the monochromatic moments are defined as

$$\{J, H, K, L, \dots\} = \frac{1}{2} \int_{-1}^{+1} \mathcal{I} d\mu \mu^{\{0,1,2,3,\dots\}}. \tag{2.17}$$

Introducing the normalized moments of order k , ($k \in \mathbb{N}_0$)

$$m^{(k)} := \frac{\frac{1}{2} \int_{-1}^{+1} d\mu \mathcal{I} \mu^k}{\frac{1}{2} \int_{-1}^{+1} d\mu \mathcal{I}}, \quad (2.18)$$

the following relations can easily be verified, given the non-negativity of the specific intensity:

$$|m^{(k)}| \leq 1, \quad (2.19)$$

$$0 \leq m^{(2k+2)} \leq m^{(2k)}, \quad (2.20)$$

$$|m^{(2k+1)}| \leq m^{(2k)}. \quad (2.21)$$

Analogous expressions hold for the moments also in the more general case, when no special symmetry is assumed to be present. In particular, we note the important inequalities

$$\begin{aligned} |\mathbf{F}| &\leq cE, \\ P_{ij} &\leq E, \end{aligned} \quad (2.22)$$

which state that the velocity of the energy flux is bounded by the speed of light and that the radiation pressure does not exceed the energy density.

Finally, in spherical symmetry the Boltzmann equation (2.6) for the specific intensity and its first two moment equations read

$$\frac{1}{c} \frac{\partial}{\partial t} \mathcal{I} + \mu \frac{\partial}{\partial r} \mathcal{I} + \frac{1 - \mu^2}{r} \frac{\partial}{\partial \mu} \mathcal{I} = S, \quad (2.23)$$

with $\mathcal{I} = \mathcal{I}(t, r, \epsilon, \mu)$ and $S = S(t, r, \epsilon, \mu)$, and

$$\frac{1}{c} \frac{\partial}{\partial t} J + \frac{1}{r^2} \frac{\partial}{\partial r} (r^2 H) = S^{(0)}, \quad (2.24)$$

$$\frac{1}{c} \frac{\partial}{\partial t} H + \frac{1}{r^2} \frac{\partial}{\partial r} (r^2 K) + \frac{K - J}{r} = S^{(1)}, \quad (2.25)$$

with $J = J(t, r, \epsilon)$, $H = H(t, r, \epsilon)$, $K = K(t, r, \epsilon)$, and

$$S^{(k)}(t, r, \epsilon) := \frac{1}{2} \int_{-1}^{+1} d\mu \mu^k S(t, r, \epsilon, \mu). \quad (2.26)$$

Limiting cases of the Boltzmann equation

Two well known limiting cases of the Boltzmann equation are obtained in vacuum and in the regime where the rate of interactions of radiation with the medium is sufficiently large so that the mean free path of radiation is very small.

Diffusion approximation: If the mean free path of radiation is small compared to the scales of spatial variations of the specific intensity (i. e. the medium is “optically thick”), the radiation field can be assumed to be only weakly anisotropic. In this case the radiative transfer equation simplifies considerably (the following description is based on Shapiro & Teukolsky 1983, Appendix I).

For the ease of explanation we specify a particular form of the emissivity and the opacity. If the interaction of radiation and matter proceeds via isotropic emission and absorption, and isoenergetic scattering with a differential cross section which is proportional to the cosine of the scattering angle, the emissivity and the opacity can be written as¹ (the dependence of the quantities on the coordinates t and ϵ is suppressed)

$$\eta(r, \mu) = \kappa_a \mathcal{I}^{\text{eq}}(r) + \kappa_s^{(0)}(r) J(r) + \kappa_s^{(1)}(r) \mu H(r), \quad (2.27)$$

and

$$\chi(r, \mu) = \kappa_a(r) + \kappa_s^{(0)}(r), \quad (2.28)$$

where \mathcal{I}^{eq} is the specific intensity of radiation, which is in local thermodynamical equilibrium with the matter (cf. Appendix A.1.2). In the quasisteady limit the first moment equation (equ. 2.25) in spherical coordinates (assuming spherical symmetry) reads²

$$\frac{\partial}{\partial r} K + \frac{3K - J}{r} = -\chi^{\text{tr}} H, \quad (2.29)$$

where the transport opacity (i. e. the inverse mean free path for momentum exchange of radiation with the matter)

$$\chi^{\text{tr}} = \kappa_a + \kappa_s^{(0)} - \frac{\kappa_s^{(1)}}{3} \quad (2.30)$$

has been introduced. For weakly anisotropic radiation one finds $K = 1/3 \cdot J$ to first order and therefore

$$H = -\frac{1}{3\chi^{\text{tr}}} \frac{\partial J}{\partial r}. \quad (2.31)$$

When equ. (2.31) is inserted into the zeroth moment equation (equ. 2.24) the diffusion equation

$$\frac{1}{c} \frac{\partial}{\partial t} J - \frac{1}{r^2} \frac{\partial}{\partial r} \left(r^2 \frac{1}{3\chi^{\text{tr}}} \frac{\partial J}{\partial r} \right) = S^{(0)} \quad (2.32)$$

is obtained. If the radiation field is stationary (i. e. $\partial_t J \equiv 0$), eqns. (2.31, 2.32) imply the important relation

$$\frac{\partial}{\partial r} (r^2 H) = 0, \quad (2.33)$$

which states that the (monochromatic) luminosity $L := (4\pi r)^2 H$ is conserved if radiation and matter are in local thermodynamical equilibrium ($S^{(0)} \equiv 0$ in this case; cf. Appendix A.1.1).

¹For all radiation-matter (or neutrino-matter) interaction processes considered in the course of this work the opacity and emissivity can be written in the form of eqns. (2.27, 2.28), with the exception of inelastic neutrino-electron scattering (cf. Appendix A.2.5), whose contribution to the transport opacity can be written in a similar way (see Cernohorsky 1994)

²The term $c^{-1} \partial_t H$ can be estimated to be smaller than $\chi^{\text{tr}} H$ by the ratio of the mean free path of the radiation and the typical scales of spatial variations of the radiation field (e. g. Mihalas & Mihalas 1984). By definition of the diffusion regime this ratio is small compared to unity. Yet, H does not necessarily have to be assumed to be time-independent provided that changes of the background medium (and hence χ^{tr}) and J occur on sufficiently long time scales.

Wave limit: In vacuum ($\eta \equiv \chi \equiv 0$; the medium is “optically thin”) the transport equation (in spherical symmetry and employing spherical coordinates) admits the particular solution of a monochromatic spherical wave. For the angular moments of this solution one finds $J \equiv H \equiv K \equiv \dots$, and therefore the first two moment equations (eqns. 2.24, 2.25) lead to the familiar wave equation in spherical coordinates

$$\frac{1}{c^2} \frac{\partial^2}{\partial t^2} J - \frac{1}{r^2} \frac{\partial^2}{\partial r^2} (r^2 J) = 0. \quad (2.34)$$

2.1.2 Radiative transfer in moving media

It has proven particularly useful in (numerical) radiation hydrodynamics to measure the *physical* properties of the radiation field like specific intensity \mathcal{I} , frequency $h^{-1}\epsilon$, angle of propagation μ , source terms S , etc. with respect to a frame which is locally comoving with the fluid. Since by definition of this so-called “comoving frame” (also “Lagrangian frame” or “local proper frame”), matter is instantaneously at rest everywhere, common microscopic derivations for describing the interaction between matter and radiation (i. e. opacities and emissivities) apply in this frame and generally also yield the most simple expressions³. Though in principle appropriate transformation laws may be used (and have been used) to obtain opacities and emissivities in any other than the comoving frame the physical content of the resulting expressions is often obscured by this procedure and the actual computations pose severe numerical difficulties (see e. g. Mihalas & Mihalas 1984, §99).

Usage of the comoving frame, however, comes not without cost: Thus far we have tacitly assumed that the equations of radiative transfer are set up in an inertial frame of reference. Since a set of frames each moving with a velocity that is in general not constant in space and time is *not* inertial, one cannot expect equ. (2.2) to apply also in the comoving frame. For example, the equality $\dot{\mathbf{p}} \equiv 0$ which enters the inertial frame radiative transfer equation (2.2) is explicitly violated in non-inertial frames by definition. Therefore, when written down in the comoving frame, one has to expect additional terms to appear in the Boltzmann equation. The resulting equations and a sketch of their derivation will be presented in the subsequent sections.

At this point it is important to note that the *frame of reference*, where *physical quantities* are measured, has to be carefully distinguished from the employed *coordinates* which are used to simply *label events* in spacetime. Although a specific choice of coordinates always provides also a “natural” way to define a corresponding frame (the so-called “induced basis” or “holonomic frame” whose basis vectors are tangents to the coordinate lines), one is not necessarily bound to this correspondence (one might, for example, employ spherical coordinates for the three-dimensional Euclidean space, yet use Cartesian components to describe vectors). If one, e. g., chooses Lagrangian coordinates to label events in the spacetime manifold⁴, the corresponding induced basis is the “comoving frame” as defined previously. However, one is in principle free to use Eulerian coordinates instead to label events, yet keep the comoving frame to measure physical quantities. The linear map which transforms between the induced basis (“Eulerian frame”) and the comoving frame can be deduced from the transformation of the corresponding coordinates.

³e. g. the emissivity $\eta(t, r, \epsilon, \mu)$ of thermal radiation is isotropic only in the local rest frame of the medium: $\eta = \eta(t, r, \epsilon)$

⁴In the specific context of radiative transfer, the situation is slightly more complicated when concepts from differential geometry are invoked since the distribution function is not defined simply on the spacetime manifold itself but on six-dimensional phase space described as the tangent bundle over the manifold (see the Appendix of Lindquist 1966, for a more formal discussion).

2.1.3 Comoving frame radiative transfer equations

Based on the treatise of Mihalas & Mihalas (1984, see also Mihalas 1998), we give a brief summary of the two “classical” lines of derivation of the comoving frame radiative transfer equations. As usual, we restrict ourselves to the case of a spherically symmetric medium.

Note that whereas all physical quantities have been tacitly assumed to be measured in the Eulerian frame up to here, they are always assumed to be measured in the comoving frame from now on without altering the notation. When referring to quantities that are defined in frames of reference other than the comoving frame hints will be given at the appropriate position.

Special relativistic derivation

Mihalas (1980) has given a derivation that works within the framework of *special relativity*. One starts from the inertial frame equation of transfer in Eulerian coordinates (cf. equ. 2.23), utilizes the Lorentz invariance of the quantities \mathcal{I}/ϵ^3 and S/ϵ^2 , and invokes appropriate transformation rules to rewrite all quantities in the comoving frame, which is related to the inertial frame by local Lorentz transformations.

Frequencies and angles in the comoving frame are, for example, obtained by applying a standard Lorentz transformation to the radiation four-momentum $\epsilon/c(1, \mathbf{n})^T$ in the inertial frame. The tedious part of the derivation comprises the rewriting of all partial derivatives with respect to space-time coordinates that are taken at *fixed inertial frame* energy and angle of propagation (equ. 2.23) in terms of derivatives with *fixed comoving frame* energy and angle of propagation. In applying the appropriate chain rules, partial derivatives with respect to energy and angle of propagation enter the equation, which have not been present in the inertial frame equation (equ. 2.23). These terms account e. g. for the effects of redshift (or blueshift) and angular aberration of radiation traveling between frames that are in relative motion with respect to each other.

The resulting special relativistic comoving frame transfer equation for the specific intensity together with the moment equations of zeroth and first order are denoted in Mihalas (1980, eqns. 2.12, 2.14, 2.15). Here, we write down only the corresponding equations after they have been reduced to order $\mathcal{O}(\beta)$, where $\beta := v/c$ denotes the ratio of the fluid velocity and the speed of light:

$$\begin{aligned}
& \left(\frac{1}{c} \frac{\partial}{\partial t} + \beta \frac{\partial}{\partial r} \right) \mathcal{I} + \mu \frac{\partial}{\partial r} \mathcal{I} + \frac{1 - \mu^2}{r} \frac{\partial}{\partial \mu} \mathcal{I} \\
& + \frac{\partial}{\partial \mu} \left\{ (1 - \mu^2) \left[\mu \left(\frac{\beta}{r} - \frac{\partial \beta}{\partial r} \right) - \frac{1}{c} \frac{\partial \beta}{\partial t} \right] \mathcal{I} \right\} \\
& - \frac{\partial}{\partial \epsilon} \left\{ \epsilon \left[(1 - \mu^2) \frac{\beta}{r} + \mu^2 \frac{\partial \beta}{\partial r} + \mu \frac{1}{c} \frac{\partial \beta}{\partial t} \right] \mathcal{I} \right\} \\
& + \left[(3 - \mu^2) \frac{\beta}{r} + (1 + \mu^2) \frac{\partial \beta}{\partial r} + \mu \frac{2}{c} \frac{\partial \beta}{\partial t} \right] \mathcal{I} = S, \tag{2.35}
\end{aligned}$$

$$\begin{aligned}
& \left(\frac{1}{c} \frac{\partial}{\partial t} + \beta \frac{\partial}{\partial r} \right) J + \frac{1}{r^2} \frac{\partial}{\partial r} (r^2 H) \\
& - \frac{\partial}{\partial \epsilon} \left\{ \epsilon \left(\frac{\beta}{r} (J - K) + \frac{\partial \beta}{\partial r} K + \frac{1}{c} \frac{\partial \beta}{\partial t} H \right) \right\} \\
& + \frac{\beta}{r} (3J - K) + \frac{\partial \beta}{\partial r} (J + K) + \frac{2}{c} \frac{\partial \beta}{\partial t} H = S^{(0)}, \tag{2.36}
\end{aligned}$$

$$\begin{aligned}
& \left(\frac{1}{c} \frac{\partial}{\partial t} + \beta \frac{\partial}{\partial r} \right) H + \frac{1}{r^2} \frac{\partial}{\partial r} (r^2 K) + \frac{K - J}{r} \\
& - \frac{\partial}{\partial \epsilon} \left\{ \epsilon \left(\frac{\beta}{r} (H - L) + \frac{\partial \beta}{\partial r} L + \frac{1}{c} \frac{\partial \beta}{\partial t} K \right) \right\} \\
& + 2 \left(\frac{\partial \beta}{\partial r} + \frac{\beta}{r} \right) H + \frac{1}{c} \frac{\partial \beta}{\partial t} (J + K) = S^{(1)}. \tag{2.37}
\end{aligned}$$

Here and in the following we frequently suppress functional dependences like $\mathcal{I} \equiv \mathcal{I}(t, r, \epsilon, \mu)$, $S \equiv S(t, r, \epsilon, \mu)$, $J \equiv J(t, r, \epsilon)$, $S^{(0)} \equiv S^{(0)}(t, r, \epsilon)$, $\beta \equiv \beta(t, r)$, ... in our notation. Note that in (eqns. 2.35–2.37) all physical quantities, in particular also the collision integrals and their angular moments are assumed to be measured in the comoving frame but the choice of coordinates (r, t) is Eulerian. With the simple replacement $\partial/\partial t + v\partial/\partial r \rightarrow D/Dt$, Lagrangian coordinates can be used.

For future reference we also write down the transformations (correct to order $\mathcal{O}(\beta)$) which allow to relate the *frequency-integrated* moments in the comoving (“Lagrangian”) and in the inertial (“Eulerian”) frame of reference (indicated by the “Eul”-superscript).

$$\begin{aligned}
J^{\text{Eul}} &= J + 2\beta H, \\
H^{\text{Eul}} &= H + \beta(J + K), \\
K^{\text{Eul}} &= K + 2\beta H. \tag{2.38}
\end{aligned}$$

The transformation (2.38) can easily be deduced from a Lorentz-transformation of the radiation stress-energy tensor (e. g. Mihalas & Mihalas 1984). In principle also relations for *monochromatic* moments can be derived by transforming the specific intensity \mathcal{I} , the angle cosine μ and the energy ϵ , which, however, leads to much more complicated expressions.

General relativistic derivation

For completeness, we briefly outline another conceptually different approach to the derivation of the comoving frame transport equation that has earlier been adopted by Castor (1972). It allows us to introduce the equations of *general relativistic* radiative transfer.

Lindquist (1966) has derived a covariant transfer equation and has specialized it for particles of zero rest mass interacting with a spherically symmetric medium supplemented with the comoving frame metric (r is a Lagrangian coordinate)

$$ds^2 = -e^{2\Phi(t,r)} c^2 dt^2 + e^{2\Lambda(t,r)} dr^2 + R(t,r)^2 d\Omega^2 \tag{2.39}$$

The “Lindquist-equation” and its moment equations of zeroth and first order — noted here for future reference — read⁵:

$$\begin{aligned}
& \frac{1}{c} \frac{\partial}{\partial t} \mathcal{I} + e^\Phi \Gamma \left[\mu \frac{\partial}{\partial R} \mathcal{I} + \frac{1 - \mu^2}{R} \frac{\partial}{\partial \mu} \mathcal{I} \right] \\
& + \frac{\partial}{\partial \mu} \left\{ (1 - \mu^2) \left[\mu \left(\frac{U}{R} - \frac{1}{c} \frac{\partial \Lambda}{\partial t} \right) - \Gamma \frac{\partial e^\Phi}{\partial R} \right] \mathcal{I} \right\} \\
& - \frac{\partial}{\partial \epsilon} \left\{ \epsilon \left[(1 - \mu^2) \frac{U}{R} + \mu^2 \frac{1}{c} \frac{\partial \Lambda}{\partial t} + \Gamma \mu \frac{\partial e^\Phi}{\partial R} \right] \mathcal{I} \right\} \\
& + \left[(3 - \mu^2) \frac{U}{R} + (1 + \mu^2) \frac{1}{c} \frac{\partial \Lambda}{\partial t} + 2\mu \Gamma \frac{\partial e^\Phi}{\partial R} \right] \mathcal{I} = e^\Phi S, \tag{2.40}
\end{aligned}$$

$$\begin{aligned}
& \frac{1}{c} \frac{\partial}{\partial t} J + \frac{\Gamma}{R^2} \frac{\partial}{\partial R} (R^2 H e^\Phi) \\
& - \frac{\partial}{\partial \epsilon} \left\{ \epsilon \left[\frac{U}{R} (J - K) + \frac{1}{c} \frac{\partial \Lambda}{\partial t} K + \Gamma \frac{\partial e^\Phi}{\partial R} H \right] \right\} \\
& + \frac{U}{R} (3J - K) + \frac{1}{c} \frac{\partial \Lambda}{\partial t} (J + K) + \Gamma \frac{\partial e^\Phi}{\partial R} H = e^\Phi S^{(0)}, \tag{2.41}
\end{aligned}$$

$$\begin{aligned}
& \frac{1}{c} \frac{\partial}{\partial t} H + \frac{\Gamma}{R^2} \frac{\partial}{\partial R} (R^2 K e^\Phi) + e^\Phi \Gamma \frac{K - J}{R} \\
& - \frac{\partial}{\partial \epsilon} \left\{ \epsilon \left[\frac{U}{R} (H - L) + \frac{1}{c} \frac{\partial \Lambda}{\partial t} L + \Gamma \frac{\partial e^\Phi}{\partial R} K \right] \right\} \\
& + \Gamma \frac{\partial e^\Phi}{\partial R} J + 2 \left(\frac{U}{R} + \frac{1}{c} \frac{\partial \Lambda}{\partial t} \right) H = e^\Phi S^{(1)}, \tag{2.42}
\end{aligned}$$

with

$$U := \frac{1}{c} \frac{\partial R}{\partial t}. \tag{2.43}$$

Note that in (eqns. 2.40–2.42), the time derivative $\partial/\partial t$ has to be taken at fixed *Lagrangian coordinate* r .

In general, the metric functions $\Phi(t, r)$, $\Lambda(t, r)$, $R(t, r)$, and $\Gamma(t, r) := e^{-\Lambda} \partial_r R$ have to be computed numerically from the Einstein field equations. When working to order $\mathcal{O}(v/c)$ and in a flat spacetime, it is however possible to express these functions analytically in terms of only the velocity field and its first time-derivative (“fluid acceleration”) by relating the metric in the inertial frame and the “Lindquist-metric” (equ. 2.39) adopted for the comoving-frame with local Lorentz transformations. The result is a special relativistic, comoving frame transfer equation correct to order $\mathcal{O}(v/c)$, which is equivalent to equ. (2.35). Details of the derivation can be found in Castor (1972).

The two “classical” approaches outlined above are both specific in their choice of *coordinates*: Whereas the derivation of the special relativistic equations (Mihalas 1980) employs Eulerian spherical coordinates from the beginning, the general relativistic approach due to Castor (1972) is bound

⁵In writing equations (2.40–2.42) in a “conservative” form, we have tacitly assumed the backreaction of the radiation field on the metric functions to be negligible.

to the usage of Lagrangian coordinates. Only in the nonrelativistic $\mathcal{O}(v/c)$ -limit one can safely employ other coordinates (e. g. by making the replacement $\partial/\partial t + v\partial/\partial r \rightarrow D/Dt$), yet keep the physical quantities being defined in the comoving frame.

For this reason it is not possible to derive a special relativistic transfer equation by simply taking the “flat space limit” (i. e. $e^{\Phi} \rightarrow 1, \Gamma \rightarrow 1, R \rightarrow r$) of the Lindquist equation (2.40)⁶. The reason for this is simple: The Lorentz metric in comoving coordinates is in general not diagonal and hence cannot be reexpressed in terms of the Lindquist metric (equ. 2.39), if the comoving and Eulerian coordinates are related by an arbitrary velocity field (in the $\mathcal{O}(v/c)$ -limit, the non-diagonal terms in the Lorentz metric in comoving coordinates vanish). Although we will not deal with highly relativistic flows in this work, it is worthwhile to note that the stated principle lack of generality was overcome by Riffert (1986), who has derived a comoving frame transfer equation, which is based on the covariant transport equation of Lindquist (1966), but can be specialized to an *arbitrary* choice of coordinates.

2.1.4 Characteristics and formal solution

Powerful (numerical) solution strategies for the Boltzmann equation are based on its so-called “formal solution”. We consider the Boltzmann equation in Cartesian coordinates for a static background medium at first. If the emissivity and opacity are known functions of t , \mathbf{r} , ϵ and \mathbf{n} , the radiative transfer equation (2.2) is a first order linear partial differential equation which can be solved by the method of characteristics. The characteristic equations of equ. (2.2) read (see, e. g. Körner 1992)

$$\frac{dt}{d\alpha} = c^{-1}, \quad (2.44)$$

$$\frac{d\mathbf{r}}{d\alpha} = \mathbf{n}, \quad (2.45)$$

$$\frac{d\mathcal{I}}{d\alpha} = \eta - \chi\mathcal{I}. \quad (2.46)$$

The first two equations define the characteristic curves of the Boltzmann equation (2.2), which are obviously straight (light-) rays in spacetime. The partial differential equation (2.2) simplifies to the ordinary differential equation (2.46), which can be readily integrated to give

$$\mathcal{I}(t, \mathbf{r}; \epsilon, \mathbf{n}) = \int ds \eta(t - s/c, \mathbf{r} - \mathbf{n}s; \epsilon, \mathbf{n}) \cdot e^{-\tau(t - s/c, \mathbf{r} - \mathbf{n}s; \epsilon, \mathbf{n})}, \quad (2.47)$$

where we have introduced the optical depth

$$\tau(t - s/c, \mathbf{r} - \mathbf{n}s; \epsilon, \mathbf{n}) = \int_0^s ds' \chi(t - s'/c, \mathbf{r} - \mathbf{n}s'; \epsilon, \mathbf{n}). \quad (2.48)$$

In order to match initial and boundary conditions imposed on \mathcal{I} at $t = 0$ and at the boundary surface, respectively, the integration in equ. (2.47) is restricted to $s \in [0, \min(ct, |\mathbf{r} - \mathbf{r}_b|)]$ where \mathbf{r}_b denotes the point of intersection of the ray $\mathbf{r} - \mathbf{n}s$ with the boundary surface. See Mihalas & Mihalas (1984, §79) for details.

Equation (2.47) admits a straightforward physical interpretation: At a given point (t, \mathbf{r}) in spacetime the specific intensity of radiation with a given frequency $h^{-1}\epsilon$ and direction of propagation

⁶Instead, the *static* limit (equ. 2.23) is recovered by such a procedure.

\mathbf{n} is determined by the sum of all radiation quanta of the same frequency which have been emitted along the ray $\mathbf{r} - \mathbf{n}s$ into the direction \mathbf{n} at retarded times $t - s/c$, exponentially attenuated by the optical depth τ the radiation has encountered during the travel. Equation (2.47) is called a “formal solution”⁷ of the Boltzmann equation, since in general the emissivity η and the opacity χ are not known as a function of the spacetime coordinates, but depend on the desired solution itself (e. g. the contribution of isotropic, elastic scattering to the emissivity reads $\eta = \kappa_s/(4\pi) \int d\Omega \mathcal{I}$). Nevertheless, the existence of a formal solution allows to construct efficient numerical schemes for solving the Boltzmann equation like the variable Eddington factor method which will be introduced in the next chapter.

Though in principle, the method of characteristics can also be applied to the Boltzmann equation expressed in other coordinates and/or frames of reference, the equations defining the characteristics tend to become more complicated and in general cannot be solved analytically. Thus, general quadrature solutions like equ. (2.47) were known only for a few specific cases (e.g. for the Boltzmann equation in spherical coordinates assuming a spherically symmetric, static background medium, see Yorke 1980; Körner 1992). Only recently it was realized (Baschek, Efimov, Von Waldenfels, & Wehrse 1997) that a general quadrature solution for the Boltzmann equation in any coordinate system and also in the local rest frame of relativistically moving observers can easily be given without referring to the explicit form of the Boltzmann equation in these coordinates. Instead of trying to solve the characteristic equations of the Boltzmann equation expressed in the specific coordinates under consideration, the Cartesian coordinates which appear in the known quadrature solution equ. (2.47) are simply rewritten in terms of the new coordinates. Of course, Lorentz-invariant quantities like \mathcal{I}/ϵ^3 , η/ϵ^2 , and $\chi\epsilon$ have to be used in the case of relativistically moving observers. See Baschek et al. (1997) for details and some instructive examples.

2.1.5 Specifics of neutrino transport

Up to now we have not specified the physical properties of the particular radiation quanta under consideration. Results have been mainly drawn from the extensive literature about radiative transfer with photons and use has sometimes implicitly been made of the special physical properties of photons being bosons with vanishing rest mass. We now briefly discuss the applicability of the results stated so far to the special case of neutrino transport in core-collapse supernovae (see Schinder & Shapiro 1986, for a concise summary).

Throughout this work, we make the standard assumption that neutrinos are *massless Fermions* within the standard model of electroweak interaction theory, which gives rise to a number of differences between photon- and neutrino transport:

Neutrinos come as particles and antiparticles in three different flavours each of which is capable of carrying energy, momentum and the corresponding lepton number. Obviously a transport equation like equ. (2.2) has to be solved for each neutrino species in principle and it has to be ensured that in a numerical scheme the individual lepton numbers, i. e. the number of charged leptons plus the number of the corresponding neutrinos, is conserved individually for each of the three lepton flavours. In the light of the overwhelming evidence for a *finite rest mass* of neutrinos that has been accumulated over the past few years, an additional remark is in order: According

⁷In the following we will use the term “formal solution” in the more general sense of a solution of the Boltzmann equation, which assumes that the emissivity and the opacity are known functions of the momentum-space coordinates. This “formal solution” does not necessarily have to be obtained by solving eqns. (2.44–2.48).

to experimental and theoretical upper limits (see e. g. Mohapatra & Pal 1991; Raffelt 1996) the neutrino rest masses are still tiny (e. g. $m_{\nu_e} \lesssim 10$ eV) compared to the scale of neutrino energies that is relevant in core-collapse supernovae ($\langle \epsilon_{\nu_e} \rangle \simeq 10$ MeV). Hence, the neutrino rest mass is obviously irrelevant for the dynamics and thus for our purposes the left hand side of the Boltzmann equation (equ. 2.2) is well suited for describing the evolution of the neutrino distribution function. Neutrino oscillations in a supernova core are also unimportant if the mass differences and mixing angles are such that solar and atmospheric neutrino anomalies are explained (Hannestad, Janka, Sigl, & Raffelt 2000).

As far as the interaction of radiation with matter is concerned, we have not been specific yet. Neutrino opacities and emissivities will be discussed in detail in Appendix A. Here it suffices to note that for Fermi-Dirac particles like neutrinos “stimulated absorption” (or “blocking”) is the analogue of what is known as “stimulated emission” of Bosonic radiation.

2.2 Hydrodynamics

Usually, the equations of hydrodynamics for an ideal fluid are derived as conservation laws for mass (particle number⁸), momentum and energy (see e. g. Landau & Lifschitz 1991). In the present context it is instructive to briefly recall the basic assumptions and fundamental steps of the derivation of the equations of hydrodynamics from statistical mechanics (see e. g. Mihalas & Mihalas 1984, §30) and compare to the case of radiative transfer.

2.2.1 Basic considerations

As opposed to “radiation” the mean free paths between interactions of particles in a “gas” or a “fluid” are by definition much smaller than the length scales of interest of the system under consideration. It is therefore possible to introduce the concept of a “fluid element”, which is still much smaller in linear extent than the size of the system, yet it contains a number of particles that is sufficiently large to introduce mean quantities on a macroscopic scale like a mean mass density, mean momentum density, mean internal energy density etc. These mean quantities are treated as continuous functions of the space coordinates, without referring explicitly to the physical state of individual particles which constitute the fluid elements.

Mathematically, the properties of a fluid element are described by moments of a particle distribution function over momentum space. For example the mass density ρ and the momentum density $\rho \mathbf{v}$ are given by $\rho(t, \mathbf{r}) = \int m f(t, \mathbf{r}, \mathbf{p}) d^3 \mathbf{p}$, and $\rho \mathbf{v}(t, \mathbf{r}) = \int m \mathbf{u} f(t, \mathbf{r}, \mathbf{p}) d^3 \mathbf{p}$, respectively, with m being the mass of an individual particle and $m \mathbf{u}$ its momentum. In order to obtain dynamical equations for the evolution of the mean quantities, one constructs moments of the Boltzmann equation over momentum space, which leads to the hierarchical set of Maxwell-Boltzmann transport equations. The familiar equations of hydrodynamics are recovered, when this system is truncated on the level of the second moment. The Maxwell-Boltzmann transport equation for the moment of zeroth order leads to the equation of continuity, first order gives the Euler equation and second order the energy equation.

⁸If nuclear reactions are present, baryon number (n_B denotes the baryon number density) rather than rest mass (ρ_0 is the rest mass density) is to be employed as the conserved quantity. With “mass (density)” we mean the number density of baryons times the atomic mass unit $m_u = 1.66 \times 10^{-24}$ g in the following ($\rho := n_B m_u$). m_u is not to be confused with the mean baryonic mass \bar{m}_B defined by $\rho_0 \equiv n_B \bar{m}_B$. The latter relation is exact, but \bar{m}_B depends on the composition (cf. Müller 1998, Chap. 4.3).

For an ideal fluid characterized by the mass density ρ , the Cartesian components of the velocity vector $(v_1, v_2, v_3)^T$, the internal energy density ρe and the gas pressure p , the equations of hydrodynamics in Cartesian coordinates finally read (sum over i implied):

$$\partial_t \rho + \partial_i(\rho v_i) = 0, \quad (2.49)$$

$$\partial_t(\rho v_k) + \partial_i(\rho v_i v_k + \delta_{ik} p) + \rho \partial_k \Phi = Q_{Mk}, \quad (2.50)$$

$$\partial_t(\rho e + \frac{1}{2} \rho v^2) + \partial_i(\{\rho e + \frac{1}{2} \rho v^2 + p\} v_i) + \rho v_i \partial_i \Phi = Q_E + v_i Q_{Mi}, \quad (2.51)$$

where Φ denotes an external potential (e. g. the gravitational potential of the fluid) and Q_{Mk} and Q_E are additional source terms that cannot be written in general as gradients of a potential (e. g. the momentum and energy exchange of the fluid with a radiation field). δ_{ik} is the Kronecker symbol.

Comparison to radiative transfer

Similar to the moment equations of radiative transfer, a closure relation (“equation of state”) has to be provided for the equations of hydrodynamics in order to express the stress tensor (which, for inviscid fluids is given by the isotropic pressure p) in terms of the moments ρ and ρe .

Since by definition of the hydrodynamic approximation the mean free paths of individual fluid particles are very small compared to the characteristic length scales of the flow and nuclear reactions proceed sufficiently rapidly so that the hydrodynamic variables change adiabatically on the reaction time scale, the fluid, as opposed to radiation, can be assumed to be in local thermodynamical equilibrium. Hence the particle distribution function of the fluid particles is isotropic and its functional dependence on the energy of the particles is known (e. g. for non-interacting particles the equilibrium distribution is given by a Fermi-Dirac or a Bose-Einstein distribution depending on the statistics the fluid particles obey). Thus the moments p , ρ and ρe can readily be calculated as a function of the local values of the parameters of the equilibrium distribution (i. e. the temperature T and the chemical potential μ) which gives the desired closure relation. Different from radiative transfer it is therefore not necessary to explicitly solve for the distribution function in order to construct closure relations.

As a side remark we note that it was attempted to construct equation of state-like closure relations also for the moment equations of radiative transfer involving only local values of the lowest order moments (typically ≤ 2) of the distribution function. A classical example is the “Eddington approximation” $K = 1/3 J$ which assumes the distribution function to be isotropic. The latter is true if the mean free path for radiation is very short compared to the typical length scales of the system. However, the assumptions taken for constructing closure relations that are solely based on the local radiation moments usually impose additional constraints on the most general solution of the transfer equation (cf. Körner 1992; Körner & Janka 1992; Smit, Cernohorsky, & Dullemond 1997). Hence, solutions obtained with these so-called “moment closure” methods have to be tested against the general transport solution (see e.g Smit, van den Horn, & Bludman 2000).

2.2.2 Multicomponent flows

Advection of mass fractions

In general a fluid does not consist of only a single species of particles but will be a mixture of various chemical components, each of which contributes individually e. g. to the gas pressure. In such cases

where the thermodynamic variables depend on the composition, which in turn changes with time due to nuclear reactions and — unless the coordinate system is chosen to be comoving with the fluid — due to the advection of the particles with the fluid flow (diffusive processes are neglected here), the individual species have to be treated separately in the equations of hydrodynamics: Each of the N_s (nuclear) species is characterized by a partial mass density $\rho_j = \rho X_j$, $j \in \{1, \dots, N_s\}$ for which an advection equation similar to the equation of continuity holds (sum over i implied):

$$\partial_t(\rho X_j) + \partial_i(\rho X_j v_i) = Q_{Nj}. \quad (2.52)$$

X_j is called the “mass fraction”⁹ of the j -th species, with $\sum_{j=1}^{N_s} X_j = 1$. The source term Q_{Nj} accounts for local changes in the chemical composition (e. g. due to nuclear reactions).

Nuclear statistical equilibrium

If the fluid is locally in nuclear statistical equilibrium (NSE; i. e. nuclear reactions proceed sufficiently rapidly so that reactive equilibrium is established instantaneously compared to hydrodynamical time scales), the number of independent quantities required to define the hydrodynamic state reduces substantially. For an electrically neutral fluid in NSE, all local thermodynamic variables can be computed from only three independent quantities, e. g., the mass density, the net electron fraction Y_e (i. e. the number density of electrons minus positrons divided by the number density of baryons) and temperature (see e. g. Shapiro & Teukolsky 1983, Sect. 2.1). Instead of solving the system (2.52), it suffices in this case to supplement the equations of hydrodynamics (2.49–2.51) by a single advection equation for the electron-fraction (sum over i implied):

$$\partial_t(\rho Y_e) + \partial_i(\rho Y_e v_i) = Q_N. \quad (2.53)$$

The NSE composition $\{X_j\}_{j=1\dots N_s}$, which, for example is required to calculate interaction rates for neutrinos, can be computed from the Saha equations (see e. g. Shapiro & Teukolsky 1983).

2.3 Radiation hydrodynamics

2.3.1 Coupling hydrodynamics to radiative transfer

From a naive point of view the coupling of the equations of hydrodynamics to the radiative transfer equations appears to be a straightforward exercise: The source terms appearing on the rhs. of the monochromatic moment equations (2.36, 2.37) were defined as the rate of net-energy and net-momentum exchange (per unit frequency interval and unit volume) between the fluid and the radiation field. By conservation of total energy (i. e. energy of the fluid plus radiation) and momentum (i. e. momentum of the fluid plus radiation), the fluid’s energy density and momentum density has to change by exactly the opposite amount of changes for the radiation. Summing over all frequencies the source terms are therefore¹⁰

$$Q_E = -4\pi \int_0^\infty d\epsilon S^{(0)}(\epsilon) \quad , \quad Q_{M_i} = -\frac{4\pi}{c} \int_0^\infty d\epsilon S_i^{(1)}(\epsilon). \quad (2.54)$$

⁹According to our convention (see the footnote on page 23) the “mass fraction” is defined as $X_j = m_u A_j n_j / \rho_j = A_j n_j / n_B$, where n_j is the number density of the nuclear species j with atomic number A_j .

¹⁰In order to sort out the proportionality factors, recall that the radiation energy density is $4\pi/c \int_0^\infty d\epsilon J$ and the momentum density is $4\pi/c^2 \int_0^\infty d\epsilon H$.

For neutrino transport, there is an additional conserved quantity, namely the total (electron¹¹) lepton number (i. e., there is a continuity equation for the number density of electrons minus positrons in the fluid $n_e = m_u^{-1} \rho Y_e$ plus the number density of electron neutrinos minus electron antineutrinos $4\pi/c \int_0^\infty d\epsilon \epsilon^{-1} J$). Thus, the net source term (electron neutrinos minus antineutrinos) that enters the continuity equation for the net electron number (electrons minus positrons; equ. 2.53) must read:

$$Q_N = -4\pi m_u \int_0^\infty d\epsilon \epsilon^{-1} S^{(0)}(\epsilon). \quad (2.55)$$

While the arguments stated above obviously hold as they stand in the absence of fluid velocities, it is not so clear in which frame of reference the source terms have to be evaluated, if the radiating fluid is moving. In this case it has proven to be essential to perform a rigorous analysis within the framework of relativity, starting from the covariant conservation laws for the fluid stress-energy tensor in the presence of a radiation four-force (see e. g. Castor 1972). Only then, the reduction to a particular order of approximation in (v/c) may be safely carried out.

To order $\mathcal{O}(v/c)$, and in a comoving frame of reference (not to be confused with the employed coordinates, which are chosen to be Eulerian spherical coordinates here; cf. Sect 2.1.2) the momentum, energy and electron fraction equations adopt their familiar Newtonian form (cf. eqns. 2.50, 2.51; adding v times equ. (2.56) and equ. (2.57), equation (2.51) can be recovered.)

$$\frac{\partial}{\partial t}(\rho v) + \frac{1}{r^2} \frac{\partial}{\partial r}(r^2 \rho v v) + \frac{\partial}{\partial r} p = Q_M, \quad (2.56)$$

$$\frac{\partial}{\partial t}(\rho e) + \frac{1}{r^2} \frac{\partial}{\partial r}(r^2(\rho e + p) v) = Q_E, \quad (2.57)$$

$$\frac{\partial}{\partial t}(\rho Y_e) + \frac{1}{r^2} \frac{\partial}{\partial r}(r^2 \rho Y_e v) = Q_N, \quad (2.58)$$

where we have assumed spherical symmetry to apply and have omitted terms that are due to the gravitational potential for simplicity. As an essential result of the relativistic analysis the radiation source terms Q_E , Q_M and Q_N as defined in eqns. (2.54, 2.55) have to be necessarily evaluated in the *comoving frame*, which in particular requires that the radiation field quantities entering¹² $S^{(0)}$ and $S^{(1)}$ are calculated in, or transformed to the comoving frame (see Castor 1972).

While there is obviously no difference to order $\mathcal{O}(v/c)$ between the inertial and the comoving frame equations of hydrodynamics, the analysis of Castor (1972) shows that the frame dependent terms manifest themselves already at this order of approximation in the equations of radiative transfer and in particular in the source terms entering the equations of hydrodynamics. Moreover, as we shall see in the next section, even if the velocities are very small compared to the speed of light, a careful distinction between different frames of reference is essential in order to obtain an accurate and physically consistent description of the coupled system of fluid and radiation.

¹¹Here it is assumed for simplicity that muon and tau lepton numbers vanish.

¹²In purely absorbing media, characterized by the absorption opacity κ_a , the energy exchange is for example given by $Q_E = -4\pi \int_0^\infty d\epsilon \kappa_a (b - J)$ where $b := (\epsilon/hc)^3 c \cdot f^{\text{eq}}$ is the isotropic intensity of radiation which is in local thermodynamical equilibrium with the medium. The corresponding momentum exchange reads $Q_M = 4\pi/c \int_0^\infty d\epsilon \kappa_a H$.

2.3.2 Conservation properties

Energy conservation

By spectral integration of the monochromatic radiation moment equations (2.36, 2.37) the following equations for the total radiation energy density $E := 4\pi/c \int_0^\infty d\epsilon J(\epsilon)$

$$\frac{\partial}{\partial t} E + \frac{1}{r^2} \frac{\partial}{\partial r} (r^2(F + vE)) + \frac{v}{r}(E - P) + \frac{\partial v}{\partial r} P = -Q_E \quad (2.59)$$

(“*first law of thermodynamics for the radiation field*”), and for the total radiation flux density $F := 4\pi \int_0^\infty d\epsilon H(\epsilon)$

$$(v \frac{\partial}{\partial t} + v^2 \frac{\partial}{\partial r}) F + v \frac{1}{r^2} \frac{\partial}{\partial r} (r^2 P) + \frac{v}{r}(P - E) + 2v \left(\frac{\partial v}{\partial r} + \frac{v}{r} \right) F = -v Q_M \quad (2.60)$$

are obtained, where the latter equation has been multiplied by the velocity. Neglecting radiation terms that are of order $\mathcal{O}(v^2/c^2)$ ¹³ and adding both equations (2.59) and (2.60) to the total energy equation for the fluid ($v \cdot (2.56) + (2.57)$; “*first law of thermodynamics for the fluid*”)

$$\frac{\partial}{\partial t} (\rho e + \frac{1}{2} \rho v^2) + \frac{1}{r^2} \frac{\partial}{\partial r} \left(r^2 (\rho e + p + \frac{1}{2} \rho v^2) v \right) = Q_E + v Q_M, \quad (2.61)$$

we obtain a conservation law for the total energy density (i. e. the energy density of the fluid plus radiation)

$$\frac{\partial}{\partial t} (\rho e + \frac{1}{2} \rho v^2 + E^{\text{Eul}}) + \frac{1}{r^2} \frac{\partial}{\partial r} \left(r^2 \{ (\rho e + p + \frac{1}{2} \rho v^2) v + F^{\text{Eul}} \} \right) = 0. \quad (2.62)$$

We have introduced the *Eulerian frame* energy flux density $F^{\text{Eul}} = F + v(E + P)$ (cf. equ. 2.38) and have used $\partial_t E^{\text{Eul}} = \partial_t E + \mathcal{O}(v^2/c^2)$. Again, source terms that are due to the gravitational potential, nuclear energy generation, etc. have been omitted for simplicity. Equation (2.62) is sometimes referred to as the “*first law of thermodynamics for the radiating fluid*” (e. g. Mihalas 1998).

Particle number conservation

Similarly, by spectral integration of ϵ^{-1} times the monochromatic radiation moment equation (2.36) we obtain a conservation law for the number density $\mathcal{N} := 4\pi/c \int_0^\infty d\epsilon \mathcal{J}(\epsilon)$ (with $\mathcal{J} := J/\epsilon$) of particles ($\mathcal{F} := 4\pi \int_0^\infty d\epsilon \mathcal{H}$, with $\mathcal{H} := H/\epsilon$ denotes the number flux density)

$$\frac{\partial}{\partial t} \mathcal{N} + \frac{1}{r^2} \frac{\partial}{\partial r} (r^2 (\mathcal{F} + v\mathcal{N})) = -Q_N, \quad (2.63)$$

which, by adding to equ. (2.53) leads to a conservation law for the total electron lepton number

$$\frac{\partial}{\partial t} (n_e + \mathcal{N}^{\text{Eul}}) + \frac{1}{r^2} \frac{\partial}{\partial r} \left(r^2 \{ n_e v + \mathcal{F}^{\text{Eul}} \} \right) = 0. \quad (2.64)$$

To order $\mathcal{O}(v/c)$, the *Eulerian frame* number flux density is given by $\mathcal{F}^{\text{Eul}} = \mathcal{F} + v\mathcal{N}$ (to be deduced likewise equ. 2.38).

¹³Note that $c^{-1}|F| \leq E$.

Importance of $\mathcal{O}(v/c)$ -terms

In obtaining the energy conservation laws we have distinguished between the inertial and the co-moving frame radiation quantities and have made use of appropriate transformations between those frames of reference. If one fails to make this distinction — e. g. by ignoring all velocity dependent terms in the equations of radiative transfer (in effect one erroneously makes the identifications $F \equiv F^{\text{Eul}}$, $E \equiv E^{\text{Eul}}$, etc.) — the different forms of energy conservation (i. e. eqns. 2.61 and 2.62) are obviously no longer consistent with each other (unless *static* situations, i. e. $v \equiv 0$ also in the equations of hydrodynamics, are considered).

Moreover, Castor (1972, see also Mihalas & Mihalas 1984, §96 or Stone, Mihalas, & Norman 1992 for a comprehensive analysis) has shown, that choosing any one of the mutually inconsistent energy equations (equ. 2.61 or equ. 2.62) can give rise to serious errors in the energy balance in either the optically thick or the optically thin regime, if the radiation field is intense. By dimensional arguments it can be demonstrated that whereas one of the limiting cases can always be reproduced correctly without taking into account the velocity dependent terms in the radiative transfer equation, the solution in the other regime can actually get *dominated* by the velocity dependent terms of order $\mathcal{O}(v/c)$. For example, if one decides to use equ. (2.61), a sufficiently accurate treatment of the optically thin regions is achieved¹⁴, but in the diffusive regime the velocity dependent terms not properly accounted for can be larger than the net absorption-emission term, which is clearly unacceptable (Castor 1972). If, instead, equ. (2.62) is employed, the difficulty is reversed and errors arise in regions which are almost transparent to radiation. For both cases the size of errors that result, e. g. in the determination of the temperature of the fluid, can be estimated to be of the order of P/p , the ratio of the radiation pressure to the gas pressure (Castor 1972). For the radiation momentum equation, the situation is less critical (e. g. Mihalas & Mihalas 1984; Dorfi 1998), since the velocity dependent terms enter the total energy balance only at order $\mathcal{O}(v^2/c^2)$.

To summarize, if a radiating fluid flow spans both the optically thick and the optically thin regime, certain velocity dependent terms of $\mathcal{O}(v/c)$ are essential to keep in the radiative transfer equations, even if $v \ll c$. Otherwise, besides logical inconsistencies, errors, e. g. in the determination of the temperature of the fluid can arise, which do *not* vanish with order $\mathcal{O}(v/c)$ of the velocity but with P/p , the ratio of the radiation pressure to the gas pressure. This can be unacceptable if P/p is not small.

Gravity and total energy conservation

The Newtonian potential of a fluid is governed by Poisson's equation

$$\nabla^2 \Phi = 4\pi G \rho, \quad (2.65)$$

with the well known solution

$$\Phi(t, r) = -G \int d^3 r' \frac{\rho(t, r')}{|\mathbf{r}' - \mathbf{r}|}. \quad (2.66)$$

Integrating the total energy equation (equ. 2.51) over the computational domain and neglecting boundary terms, we are able to verify the conservation of total energy in the form

$$\partial_t (E_{\text{int}}^{\text{tot}} + E_{\text{kin}}^{\text{tot}} + E_{\text{rad}}^{\text{tot}} + E_{\text{pot}}^{\text{tot}}) = 0, \quad (2.67)$$

¹⁴The neglect of the internal energy of the radiation and the work done by radiation pressure in equ. (2.61) is not serious in this case, since by definition of the optically thin regime, radiation is only weakly coupled to the fluid.

with the internal energy $E_{\text{int}}^{\text{tot}} := \int d^3\mathbf{r}' \rho e$, the kinetic energy $E_{\text{kin}}^{\text{tot}} := 1/2 \int d^3\mathbf{r}' \rho v^2$, the radiation energy in the Eulerian frame $E_{\text{rad}}^{\text{tot}} := \int d^3\mathbf{r}' E^{\text{Eul}}$ and the gravitational potential energy $E_{\text{pot}}^{\text{tot}} := 1/2 \int d^3\mathbf{r}' \rho \Phi$. Note that in deriving equ. (2.67) one explicitly refers to the specific definition of the potential (equ. 2.66)¹⁵.

¹⁵Straightforward manipulations lead to the equation $\partial_t(E_{\text{int}}^{\text{tot}} + E_{\text{kin}}^{\text{tot}} + E_{\text{rad}}^{\text{tot}} + E_{\text{pot}}^{\text{tot}}) = 1/2 \int d^3\mathbf{r} (\rho \partial_t \Phi - \Phi \partial_t \rho)$. The rhs. vanishes with Φ according to equ. (2.66).

Chapter 3

Numerical Radiation Hydrodynamics

This chapter deals with the numerical implementation of the equations of radiation hydrodynamics introduced in Chapter 2. We proceed within the general framework of an operator splitting approach (see e. g. LeVeque 1998, for a mathematical analysis), which allows us to largely decouple the algorithms for solving the equations of radiation hydrodynamics into a hydrodynamics part and a radiative transfer part. Note that also numerical methods for a combined treatment of radiation hydrodynamics problems have been developed (e. g. Dai & Woodward 1998, 2000; Lowrie, Morel, & Hittinger 1999; Dorfi 1999). These methods, however, solve less ambitious problems (i. e., assuming the radiative transport to be either purely diffusive or solely by free streaming, and/or prescribing the frequency dependence of the radiation by some “gray” approximation, etc.) compared to those considered in this work.

First, in Section 3.1, a few remarks are made on our methods for solving the equations of hydrodynamics and on the equation of state we used. Then, in Section 3.2, our newly developed scheme for treating the neutrino transport is described in detail. Subsequently, in Section 3.3, some important aspects of the coupling of the hydrodynamics code to the method for neutrino transport are discussed. In Section 3.4 a generalization of the method that allows to compute neutrino transport in multi-dimensional supernova simulations is sketched.

3.1 Hydrodynamics and equation of state

3.1.1 The PROMETHEUS code

For the integration of the equations of hydrodynamics we utilize the Newtonian finite-volume hydrodynamics code PROMETHEUS¹ developed by Bruce Fryxell and Ewald Müller (Fryxell, Müller, & Arnett 1989). PROMETHEUS is a direct Eulerian, time-explicit implementation of the Piecewise Parabolic Method (PPM) of Colella & Woodward (1984). The method falls into the class of the so-called (high-order²) Godunov methods. There is an extensive literature about Godunov schemes in general, PPM and a number of its implementations in particular, as well as a large number of applications to various physical and astrophysical problems. For an introduction to the basic concepts of Godunov methods and for further references, see e. g. LeVeque (1998); Müller (1998). An interesting historical perspective was recently given by the inventor of these schemes (Godunov

¹**P**ROgram for **M**ulti-dimensional **E**ulerian **T**hermonuclear **H**ydrodynamics with **E**xplicit **U**pwind **S**econd-Order **D**ifferencing

²PPM achieves second-order accuracy in space and time for the homogeneous equations of hydrodynamics.

1999). Of the numerous advantages Godunov schemes have over more conventional finite difference methods for tackling partial differential equations we mention only a few important ones: Godunov schemes exactly reproduce the nature of the equations of hydrodynamics being conservation laws for mass, momentum and energy. By employing Riemann-solvers, the nonlinearity in the equations is explicitly taken into account. Thus, such kind of schemes are particularly well suited to follow discontinuities in the fluid flow like shocks or composition interfaces. Multidimensional problems are another area of application, where high-order Godunov schemes are superior to most of the other competing numerical methods as far as computational efficiency and numerical accuracy is concerned (cf. Carpenter, Droegemeier, Woodward, & Hane 1989, for some illustrative examples).

The variant of PROMETHEUS used in our radiation hydrodynamics code was kindly provided to us by Keil (1997). The code allows us to include general relativistic corrections to the Newtonian gravitational potential. In addition, we have augmented the program by a simplified version of the “Consistent Multifluid Advection”-method (CMA) proposed by Plewa & Müller (1999).

3.1.2 Equation of state

The equation of state (EoS for short) due to Lattimer & Swesty (1991) is a mean-field EoS for describing hot and dense nuclear matter. It is based on the finite temperature compressible liquid-drop model of Lattimer, Pethick, Ravenhall, & Lamb (1985). Matter is described as a mixture of electrons, positrons, photons, free neutrons and protons, alpha-particles and a single “representative” species of heavy nuclei. The different forms of matter are assumed to be in equilibrium with respect to strong and electromagnetic interactions. Leptons and photons are described as ideal relativistic Fermi and Bose gases, respectively. The seven nuclear parameters that enter the equation of state (cf. Lattimer & Swesty 1991, Sect. 2.2) are the saturation density of symmetric nuclear matter ($n_s = 0.155 \text{ fm}^{-3}$), the binding energy of saturated, symmetric nuclear matter ($B = 16 \text{ MeV}$), the incompressibility modulus of bulk nuclear matter ($K_s = 180 \text{ MeV}$), the symmetry energy parameter of bulk nuclear matter ($S_V = 29.3 \text{ MeV}$), the nucleon effective mass for saturated, symmetric matter ($m^*/m = 1$), the surface tension of symmetric nuclear matter ($\sigma_s = 1.15 \text{ MeV fm}^{-3}$), and the surface symmetry energy parameter ($S_s = 45.8 \text{ MeV}$).

Since the Lattimer & Swesty-EoS assumes matter to be in nuclear statistical equilibrium (NSE) it is applicable only for sufficiently high temperatures and densities. A more general equation of state, which consistently extends to lower temperatures and densities being not available, we have supplemented the Lattimer & Swesty-EoS with an equation of state for an ideal baryon gas and an ideal gas of electrons, positrons and photons provided by Janka (1999). The latter includes Coulomb lattice corrections for the pressure, energy density, entropy, and adiabatic index.

In general, the NSE regime is bounded from below by a complicated hyperplane in (ρ, T, Y_e) -space. For our purposes we have found it sufficient to put the transition between the two regimes (and thus equations of state) at a fixed value of the density ρ : If the density of a fluid element fulfils the condition $\rho > \rho_0 = 6 \times 10^7 \text{ g cm}^{-3}$, the temperature in a supernova simulation always happens to be large enough ($T \gtrsim 0.5 \text{ MeV}$) to guarantee NSE to be valid, and hence, the Lattimer-Swesty EoS can be used under these circumstances. If the density drops below the value ρ_0 , the non-NSE equation of state is invoked. Since both equations of state employ similar physical approximations for densities within the range $10^7\text{--}10^8 \text{ g cm}^{-3}$, the transition between both equations of state occurring across the (T, Y_e) -plane at $\rho_0 = 6 \times 10^7 \text{ g cm}^{-3}$ is sufficiently smooth, as far as e. g. the pressure, internal energy density and chemical potentials as a function of density are concerned.

Freeze-out of the chemical composition

With the chemical composition, however, a delicate technical complication arises: The equation of state of Lattimer & Swesty (1991) describes the composition of the matter by a mixture of nucleons, α -particles and a heavy nucleus with (non-integer!) mass and charge numbers (A, Z) , which is considered to be representative of a mixture of nuclear species that coexist at given (ρ, T, Y_e) . Assuming NSE conditions, the corresponding number densities of the nuclear constituents and the mass- and charge-number of the representative heavy nucleus are given as a function of the local values of the density, temperature and electron fraction. Now imagine some fluid element, which e. g. expands and cools adiabatically. Due to the decreasing density and temperature, nuclear reactions proceed less and less frequently within this fluid element, until at some point they cease on the dynamical or other relevant time scales and no more changes in the chemical composition occur. The composition is said to have "frozen out". In our approximation, this is assumed to happen instantaneously, when the density drops below the value $\rho_0 = 6 \times 10^7 \text{ g cm}^{-3}$. In a hydrodynamics scheme one would simply like to fix the values $n_n(\rho_0), \dots, n_{(A(\rho_0), Z(\rho_0))}(\rho_0), A(\rho_0), Z(\rho_0)$ of the corresponding quantities at freeze-out, until that particular fluid element possibly reenters the NSE regime at some later time. Such a procedure can be implemented straightforwardly only into a *Lagrangian* hydrodynamics scheme where one may simply "label" a fluid element with the values (A, Z) describing the properties of its current representative heavy nucleus.

When, on the contrary, Eulerian (or any other than Lagrangian) coordinates are used, the situation gets more complicated: The chemical composition as measured at a fixed position in space changes not only due to nuclear reactions but also due to advection of particles with the fluid flow. Thus, an additional partial differential equation must be solved for each individual nuclear species (cf. equ. 2.52), which in turn requires introducing a set of species $\{(A_k, Z_k)\}_{k=1, \dots, N_s}$ to be *predefined* at the beginning of the calculation. In order to be able to account for all different mixtures of nuclear species one should include neutrons ($k = 1$), protons ($k = 2$), α -particles ($k = 3$) and a number of suitably selected heavy nuclei ($k = 4, \dots, N_s$).

Now let us consider a grid cell in which the density drops below ρ_0 . In analogy to the Lagrangian case we would then like to fix the composition of the *fluid element* (and not of the grid cell!) which is associated with that grid cell at this instant of time. In order to do so, we have to first describe the freeze-out composition $n_n(\rho_0), \dots, n_{(A(\rho_0), Z(\rho_0))}(\rho_0)$ by the predefined set of species $\{(A_k, Z_k)\}_{k=1, \dots, N_s}$ which are subsequently advected across the computational domain by the homogeneous advection equations (2.52). This appears to be a trivial task, as far as neutrons, protons and α -particles are concerned. For the representative heavy nucleus, however, the exact value $(A(\rho_0), Z(\rho_0))$ is very likely not present within the set $\{(A_k, Z_k)\}_{k=4, \dots, N_s}$. If we were simply selecting the pair (A_j, Z_j) which is, by some measure closest to $(A(\rho_0), Z(\rho_0))$, charge neutrality and baryon number conservation would obviously be violated, unless by chance $(A(\rho_0), Z(\rho_0)) = (A_j, Z_j)$ for some j .

In order to avoid this problem, we employ the following alternative procedure, which is applied at every timestep to every³ grid cell of the computational domain, where NSE holds: We first associate the representative heavy nucleus (A, Z) as computed in NSE, with the particular species

³Note, however that the single purpose of this global mapping procedure is to allow us describing the potential freeze-out of the NSE composition. If NSE conditions hold, the "mapped composition" $n_n, n_p, n_\alpha, n_{(A_4, Z_4)}, \dots, n_{(A_{N_s}, Z_{N_s})}$ neither enters the equation of state nor is it used to calculate neutrino opacities.

$(A_j, Z_j) \in \{(A_k, Z_k)\}_{k=4\dots N_s}$ that simultaneously fulfils the conditions

$$\begin{aligned} A_j - Z_j &\geq A - Z, \\ Z_j &\leq Z, \\ |A_j - A| &\leq |A_k - A| \quad \forall k \in \{4, \dots, N_s\}. \end{aligned} \quad (3.1)$$

For given values of n_n , n_α (taken identical to their values in NSE) and Y_e , the quantities n_p and $n_{(A_j, Z_j)}$ can be calculated by invoking charge neutrality and baryon number conservation. It can be shown that the first two conditions in equ. (3.1) guarantee that $n_p \geq 0$ and $n_{(A_j, Z_j)} \geq 0$ hold. The third condition in equ. (3.1) ensures that the closest (by baryon number) nucleus (A_j, Z_j) in the set $\{(A_k, Z_k)\}_{k=4, \dots, N_s}$ gets selected. In order to uniquely determine (A_j, Z_j) , no isobars must be present in the set $\{(A_k, Z_k)\}_{k=4, \dots, N_s}$.

Thermodynamic consistency of the numerical use of the EoS ?

Both the Lattimer & Swesty-EoS and the non-baryonic part of the low-density equation of state are stored in tabular form for our calculations. Intermediate values are obtained by trilinear interpolation in $\log \rho$, $\log T$, Y_e and bilinear interpolation in $\log(\rho Y_e)$, $\log T$, respectively.

It was claimed by Swesty (1996) that a more sophisticated interpolation scheme might be necessary to guarantee ‘‘thermodynamic consistency’’ of the interpolated quantities taken from a tabular EoS, unless the grid spacing of the table is sufficiently fine. In particular, Swesty (1996) suspects the appearance of ‘‘unphysical entropy production or loss in otherwise adiabatic flows’’, which, if present, would seriously affect the results of core-collapse simulations.

In order to exclude this possibility for our tabular equation of state, we have performed the following simple test calculation (cf. Swesty 1996, §4): In the absence of heat production or loss, the first law of thermodynamics reads

$$de + p d\left(\frac{1}{n}\right) = 0, \quad (3.2)$$

where e denotes the internal energy per nucleon, n the number density of nucleons and p the pressure of the fluid. According to equ. (3.2), the entropy per nucleon s does not change under adiabatic compression or expansion of a particular fluid element (since the left hand side of equ. 3.2 equals Tds in this case).

The adiabatic compression of a single fluid parcel with some initial entropy per baryon s_0 is simulated by solving a time-implicit discretized version of equ. (3.2)

$$e^{n+1} - e^n + p^{n+1} \left(\frac{1}{n^{n+1}} - \frac{1}{n^n} \right) = 0, \quad (3.3)$$

coupled to the equation of state which relates the pressure and the energy per baryon to the temperature (the electron fraction Y_e is kept fixed throughout the calculation):

$$p^{n+1} = p^{n+1}(n^{n+1}, T^{n+1}, Y_e), \quad e^{n+1} = e^{n+1}(n^{n+1}, T^{n+1}, Y_e). \quad (3.4)$$

We prescribe the relative compression ratio as 1% per timestep, (i. e. $n^{n+1} = 1.01n^n$), and evolve the coupled system of equations (3.3, and 3.4) in time. By monitoring the time evolution of the entropy per baryon $s^{n+1} = s^{n+1}(n^{n+1}, T^{n+1}, Y_e)$, we can check the compatibility of the use of an interpolated EoS-table with equ. (3.2).

The described test calculation was performed for several combinations of values for Y_e and s_0 that are typically encountered in core-collapse simulations. After approximately 1000 timesteps or a total compression ratio of 10^4 we find the deviations from adiabaticity to be negligible ($\max_n |s^n - s_0|/s_0 < 10^{-3}$). In fact, the adiabaticity of the evolution was much more seriously affected, when the accuracy of the numerical integration of equ. (3.2) was degraded (e. g. by allowing for relative compression ratios significantly larger than 1%). We conclude that our tabulations of both equations of state are sufficiently finely spaced to guarantee thermodynamic consistency in the desired sense, without employing more sophisticated (and computationally more expensive) interpolation procedures. The Lattimer & Swesty-EoS has 180 and 120 logarithmically spaced entries for $5 \times 10^7 \text{ g cm}^{-3} \leq \rho \leq 3 \times 10^{15} \text{ g cm}^{-3}$ and $0.1 \text{ MeV} \leq T \leq 80 \text{ MeV}$, respectively and 50 equally spaced entries for $0.001 \leq Y_e \leq 0.6$. The lepton and photon EoS table due to Janka (1999) has 441 entries for $10^{-10} \text{ g cm}^{-3} \leq \rho Y_e \leq 10^{12} \text{ g cm}^{-3}$ and 141 entries for $8.6 \times 10^{-6} \text{ MeV} \leq T \leq 86 \text{ MeV}$.

3.2 Radiative transfer

In this section we first briefly outline some of the general properties of the variable Eddington factor method that is used to solve the neutrino transport. Because the particular advantages of this approach might not be obvious, we try to elaborate a little on its motivation. Subsequently, the finite difference equations constituting the algorithm are presented in detail.

3.2.1 Variable Eddington factor method

In the presence of scattering, the collision integral appearing on the rhs. of the Boltzmann equation contains also angular moments of the specific intensity (cf. eqns. A.1, A.23), which makes the Boltzmann equation an *integro-partial differential equation*. For various reasons, this type of equation is in general much more complicated to solve than an “ordinary” partial differential equation. Here we will only point out the fundamental *technical* difficulties encountered in the numerical solution of the Boltzmann equation as an integro-partial differential equation that are related to this specific property. As the most simple example let us consider one-dimensional radiative transfer in a static, spherically symmetric background medium, which interacts with radiation solely via isotropic, elastic scattering. The transfer equation in this case reads (cf. eqns. A.1, A.33):

$$\frac{1}{c} \frac{\partial}{\partial t} \mathcal{I} + \mu \frac{\partial}{\partial r} \mathcal{I} + \frac{1 - \mu^2}{r} \frac{\partial}{\partial \mu} \mathcal{I} = \kappa_s \cdot (J - \mathcal{I}). \quad (3.5)$$

In a straightforward finite-difference representation (used e. g. by the S_N -method) of equ. (3.5), the integral

$$J := \frac{1}{2} \int_{-1}^{+1} d\mu \mathcal{I} \approx \sum_{k=1}^K w_k \mathcal{I}_k, \quad (3.6)$$

appearing on the right hand side of equ. (3.5) is approximated by an appropriate numerical quadrature formula which is characterized by the set of weights $\{w_k\}_{k=1,\dots,K}$ and the set of discrete angles $\{\mu_k\}_{k=1,\dots,K}$, where the distribution function is defined. Contrary to the finite difference approximation of the *gradient* $\partial/\partial\mu$, which typically couples a particular grid point of the $\{\mu_k\}$ -mesh to only a *few neighbouring points* (typically two), the quadrature formula approximating the *integral* $\int_{-1}^{+1} d\mu$ introduces a simultaneous coupling of *all* K angular grid-points in the set $\{\mu_k\}_{k=1,\dots,K}$.

When equ. (3.5) is solved by an implicit method, which, as we shall see below turns out to be necessary in radiative transfer calculations, this requires the inversion of large (blocked) matrices that would be simple band-matrices in the absence of the integral term. For this reason, even on current supercomputers only a relatively small number of angular grid-points (typically $K \lesssim 10$) can be afforded to cover the angular range $-1 \leq \mu \leq 1$ (see e. g. Mezzacappa & Bruenn 1993b,c; Mezzacappa & Messer 1999). Especially far from a central source, where the radiation is strongly peaked⁴ about the forward direction $\mu = 1$, this is apparently insufficient to resolve the radiation field properly (cf. Yamada et al. 1999).

Two alternative methods that circumvent the direct discretization of the integral terms by an iterative procedure have been routinely employed in radiative transfer calculations: In the most simple approach, called "Lambda iteration", the radiation moments entering the rhs. of the Boltzmann equation are assumed to be known at first.

Starting from an initial guess for the radiation intensity, moments are calculated (using equ. 3.6) and equ. (3.5) can be solved as an "ordinary" partial differential equation. This results in an improved estimate for the radiation field which in turn is used to recalculate moments and the rhs. of equ. (3.5), and so on. This procedure is iterated to convergence. However, it can be demonstrated by physical arguments (see e. g. Mihalas & Mihalas 1984, §83) that the rate of convergence is very slow, if scattering dominates the collision integral of the Boltzmann equation. Under such conditions hundreds of iteration steps can be necessary in order to achieve convergence. This prohibitively large number can be substantially reduced by applying the so-called "Accelerated Lambda Iteration" technique (ALI), but depending on the problem and the specifics of the employed method, still several tens of iteration steps have to be performed. Since in supernova cores the neutrino opacity for muon and tau neutrinos is dominated by scattering, "Lambda iteration" of the Boltzmann equation appears not a method of first choice for neutrino transport.

The second class of iterative methods that are known (Mihalas & Mihalas 1984, §83) not to suffer from the aforementioned problems employ an iteration between the radiation moment equations of zeroth and first order, and some (a priori unspecified) procedure to calculate the "variable Eddington factor" that is required to close the system of moment equations. If the variable Eddington factor is computed from a formal solution of the Boltzmann equation (i. e. emissivities and opacities are assumed to be known; cf. Sect. 2.1.4), the converged solution of the coupled equations is equivalent to a direct solution of the Boltzmann-equation itself. The iteration starts with a formal solution of the Boltzmann equation where an estimate of the moments of the radiation intensity (taken e. g. from the solution of the previous timestep) is used in the source terms (i. e. in the rhs. of equ. 3.5). From this formal solution, the Eddington factor can be computed, which allows one to solve the system of moment equations, which in turn provides an improved estimate for the moments of the radiation intensity that enter the rhs. of the Boltzmann equation. Typically, only a few iteration steps are required to achieve convergence in the numerical sense. The advantage of this method derives mainly⁵ from two, mutually interconnected facts: Firstly, by focussing on the solution of the *moment equations*, the dimensionality of the problem is reduced. This also appears to be the more natural approach, since it is in general only the *moments* of the radiation field that enter the equations of radiation hydrodynamics. Secondly, very efficient methods for

⁴ $\mathcal{I}(d, \mu) = 0$ for $-1 \leq \mu < \sqrt{1 - R^2/d^2}$. R is the radius of the central source and d its distance to the observer (cf. Sect. 4.1.2).

⁵In addition, in the course of implementing and testing the entire numerical scheme one can make use of the advantage that major parts of the algorithm can be *logically decoupled* from each other.

computing a *formal* solution of the Boltzmann equation have been developed in the past. Even an appropriately approximated Boltzmann equation is in most cases sufficient to compute closure relations (Eddington factors) that still guarantee excellent accuracy of the solution of the moment equations (see e. g. the discussion in Mihalas 1998, §98). In addition, when the formal solution is computed on a so called “tangent ray grid” (see below), even strongly forwardly peaked radiation fields can be resolved remarkably well. The use of a tangent ray grid also reduces the dimensionality of the Boltzmann problem in spherical coordinates.

In the following sections we describe the algorithms we have implemented in order to solve the system of moment equations and the Boltzmann equation iteratively by a variable Eddington factor method. Many of the ideas have been borrowed from the fundamental treatise of Mihalas & Mihalas (1984). We have also profited considerably from a radiative transfer code for static background media developed by Körner (1992). Burrows, Young, Pinto, Eastman, & Thompson (2000) have recently proposed a method which seems to employ concepts similar to those adopted by our algorithm. In order to shorten the notation, we describe only the version of the algorithm with Newtonian gravity. The implementation of the general relativistic variant of the algorithm has been done along exactly the same lines and a detailed description would merely require the introduction of a wealth of decorations with terms containing “ e^ϕ ” and “ Γ ”. We describe two versions of the program. One employs a numerical grid that is fixed in space (Eulerian grid), the other uses *coordinates* that follow the fluid flow (Lagrangian grid). Note that in both cases physical quantities are measured in the comoving (Lagrangian) *frame of reference*.

3.2.2 Multi-group formulation of the moment equations

Model equations

We start from the monochromatic moment equations (eqns. 2.36 and 2.37) coupled to the equation for the specific internal energy (i. e. internal energy per unit mass) and electron fraction of the stellar medium whose updates due to neutrino source terms are done in an operator-split step. As pointed out by Castor (1972) and Mihalas & Mihalas (1984), it is essential to retain all $\mathcal{O}(\beta)$ terms in the radiation energy equation (equ. 2.36) whereas the velocity-dependent terms may be dropped in the momentum equation (equ. 2.37). See Sect. (2.3.2) for details. With these additional approximations our model equations read in the comoving frame of reference:

$$\begin{aligned} \frac{1}{c} \frac{D}{Dt} J_\nu &+ \frac{1}{r^2} \frac{\partial}{\partial r} (r^2 H_\nu) \\ &- \frac{\partial}{\partial \epsilon} \left\{ \epsilon \left(\frac{\beta}{r} (1 - f_{K\nu}) + \frac{\partial \beta}{\partial r} f_{K\nu} + \frac{1}{c} \frac{\partial \beta}{\partial t} f_{H\nu} \right) J_\nu \right\} \\ &+ \frac{\beta}{r} (3 - f_{K\nu}) J_\nu + \frac{\partial \beta}{\partial r} (1 + f_{K\nu}) J_\nu + \frac{2}{c} \frac{\partial \beta}{\partial t} f_{H\nu} J_\nu = S_{E\nu}^{(0)}, \quad \nu \in \{\nu_e, \bar{\nu}_e, \dots\}, \end{aligned} \quad (3.7)$$

$$\frac{1}{c} \frac{D}{Dt} H_\nu + \frac{1}{r^2} \frac{\partial}{\partial r} (r^2 f_{K\nu} J_\nu) + \frac{f_{K\nu} - 1}{r} J_\nu = S_{E\nu}^{(1)}, \quad \nu \in \{\nu_e, \bar{\nu}_e, \dots\}, \quad (3.8)$$

$$\frac{\delta}{\delta t} e = -\frac{4\pi}{\rho} \int d\epsilon \sum_{\nu \in \{\nu_e, \bar{\nu}_e, \dots\}} S_{E\nu}^{(0)}(\epsilon), \quad (3.9)$$

$$\frac{\delta}{\delta t} Y_e = -\frac{4\pi m_u}{\rho} \int d\epsilon \left(S_{N\nu_e}^{(0)}(\epsilon) - S_{N\bar{\nu}_e}^{(0)}(\epsilon) \right). \quad (3.10)$$

where we have suppressed the functional dependences $J_\nu = J_\nu(t, r, \epsilon)$, $H_\nu = H_\nu(t, r, \epsilon)$, $f_{K_\nu} = f_{K_\nu}(t, r, \epsilon)$, \dots , $\beta = \beta(t, r)$. $S_{E_\nu}^{(0)}(t, r, \epsilon)$, and $S_{E_\nu}^{(1)}(t, r, \epsilon)$ describe the exchange of energy and momentum with the stellar medium (cf. eqns. 2.54, 2.56, 2.57). Note that our definition of the ν -subscript (“neutrino type”) is different from the literature about photon transport, where the ν -subscript (“frequency”) usually is used to label monochromatic quantities. The derivative $\delta/\delta t$ in (eqns. 3.9, 3.10) indicates that the change of the specific internal energy and the electron fraction of the medium due to neutrinos is calculated in an operator-split way⁶. $D_t = \partial_t + v\partial_r$ denotes the Lagrangian derivative.

Note that by virtue of introducing the “Eddington factors” (see sect. 3.2.3 for their actual computation)

$$f_{H_\nu}(t, r, \epsilon) = \frac{H_\nu}{J_\nu}, \quad f_{K_\nu}(t, r, \epsilon) = \frac{K_\nu}{J_\nu} \quad (3.11)$$

the system of moment equations has been closed.

In order to construct a conservative numerical scheme for the system of moment equations, we have to integrate equations (3.7 and 3.8) over a zone of the numerical (r, ϵ) -mesh.

Spatial discretization

After the moment equations (3.7 and 3.8) have been integrated over a zone ΔV of the radial mesh one wants to write evolution equations for the zone-integrated quantities $\int_{\Delta V} J_\nu dV$ and $\int_{\Delta V} H_\nu dV$. However, for a moving spatial grid one has to take into account that the volume ΔV of a grid cell is time-dependent and therefore the operators D_t and $\int_{\Delta V} dV$ cannot simply be interchanged. In the special case of a Lagrangian grid (i. e. the velocity of the numerical grid is set equal to the fluid velocity) the “moving grid transport theorem” reads (see e. g. Müller 1991)

$$D_t \int_{\Delta V} (\xi dV) = \int_{\Delta V} (\partial_t \xi) dV + \int_{\Delta V} \text{div}(\xi \mathbf{v}) dV, \quad (3.12)$$

with $\xi \equiv \xi(r, t)$. Using the definition of the Lagrangian derivative $D_t = \partial_t + \mathbf{v} \text{grad}$ we obtain from equ. (3.12):

$$\int_{\Delta V} (D_t \xi) dV = D_t \int_{\Delta V} \xi dV - \int_{\Delta V} (\xi \text{div} \mathbf{v}) dV. \quad (3.13)$$

Equation (3.13) finally allows one to rewrite the the zone-integrated moment equations as evolution equations for the zone-integrated moments. With a Eulerian grid we simply write the Lagrangian derivative in eqns. (3.7 and 3.8) as $D_t = \partial_t + \mathbf{v} \text{grad}$ and may then safely interchange the operators ∂_t and $\int_{\Delta V} dV$:

$$\int_{\Delta V} (D_t \xi) dV = \partial_t \int_{\Delta V} (\xi dV) - \int_{\Delta V} (\xi \text{div} \mathbf{v}) dV + \int_{\Delta V} \text{div}(\xi \mathbf{v}) dV. \quad (3.14)$$

Again, equation (3.14) allows to rewrite the the zone-integrated moment equations as evolution equations for the zone-integrated moments, but now on a Eulerian grid.

⁶For example, the full problem $\partial_t(\rho Y_e) + 1/r^2 \partial_r (r^2 \rho Y_e v) = Q_N$ (equ. 2.58) is split into the equations $\partial_t(\rho Y_e) + 1/r^2 \partial_r (r^2 \rho Y_e v) = 0$ and $\delta_t Y_e = Q_N/\rho$, which are solved in two subsequent and independent steps.

In order to apply Gauss' theorem we make the approximation

$$\int_{\Delta V} \xi \operatorname{div} \mathbf{v} \, dV \approx \bar{\xi} \int_{\Delta V} \operatorname{div} \mathbf{v} \, dV = \bar{\xi} \oint_{d(\Delta V)} \mathbf{v} \, d\mathbf{A}, \quad (3.15)$$

where $\bar{\xi}$ is some suitably chosen zone average value of ξ .

The computational domain $r_{\min} \leq r \leq r_{\max}$ is covered by $N_r + 1$ radial zones. As the zone centre $r_{i+1/2}$ we define the volume-weighted mean of the zone interfaces r_i and r_{i+1} :

$$r_{i+1/2} := \left(\frac{1}{2} \cdot (r_i^3 + r_{i+1}^3) \right)^{1/3}, \quad i = 0, \dots, N_r. \quad (3.16)$$

The volume of a cell is given by

$$\Delta V_{i+1/2} := \frac{4\pi}{3} (r_{i+1}^3 - r_i^3). \quad (3.17)$$

“Density-like” quantities like $J_{i+1/2}$, $K_{i+1/2}$, $f_{K_{i+1/2}}$ are defined on zone centres, whereas the “flux-like” quantity H_i is defined on the interfaces of radial zones. “Miscentred” quantities like e. g. J_i or $H_{i+1/2}$ are in general calculated from the nearest values ($J_{i-1/2}$ and $J_{i+1/2}$, or H_i and H_{i+1} , respectively) by linear interpolation.

Spectral discretization

The spectral range $0 \leq \epsilon \leq \epsilon_{\max}$ is covered by a discrete energy grid consisting of N_ϵ energy “bins”, where the centres of these energy bins are given in terms of the interface values as

$$\epsilon_{j+1/2} := \frac{1}{2} \cdot (\epsilon_j + \epsilon_{j+1}), \quad j = 0, \dots, N_\epsilon - 1. \quad (3.18)$$

The width of an energy bin is given by

$$\Delta \epsilon_{j+1/2} := \epsilon_{j+1} - \epsilon_j. \quad (3.19)$$

The radiation moments are defined as average values within energy bins:

$$X_{j+1/2} := \frac{1}{\Delta \epsilon_{j+1/2}} \cdot \int_{\epsilon_j}^{\epsilon_{j+1}} d\epsilon X(\epsilon). \quad (3.20)$$

Here and in the following the symbol X stands for one of the moments J or H (and also $\mathcal{J} := J/\epsilon$ or $\mathcal{H} := H/\epsilon$).

Time differencing

If one were to solve the radiation moment equations (3.7, 3.8) numerically by a time-explicit method, the CFL⁷ stability criterion (see e. g. LeVeque 1992) would impose limits on the numerical timestep, which are set by the characteristic speed of spatial advection c and by the advection velocity in

⁷named after Courant, Friedrichs and Lewy.

energy space $\simeq \epsilon v/r$ (for a von Neumann stability analysis of the wave equation see e. g. Press, Teukolsky, Vetterling, & Flannery 1992, Chap. 19):

$$\Delta t \leq \min\left\{\frac{\Delta r}{c}, \frac{\Delta \epsilon}{c \epsilon \beta/r}\right\}, \quad (3.21)$$

where Δr and $\Delta \epsilon$ are the zone widths of the radial and the energy grid, respectively. Assuming typical values for the model dependent quantities $\Delta \epsilon/\epsilon \simeq 0.1$ and $\beta \lesssim 0.1$ one finds for equ. (3.21) that the timestep limit set by the spatial advection is more restrictive by a factor of the grid resolution $\Delta r/r$. In any case the maximum size of the timestep allowed by equ. (3.21) is much smaller (roughly by the ratio of the sound speed and the speed of light) than the limit set by hydrodynamics. Moreover, the source terms introduce a characteristic time scale of

$$\Delta t = \frac{1}{c\chi} = \frac{\Delta r}{c\Delta\tau}, \quad (3.22)$$

which would pose an upper limit on the numerical timestep which, e. g. in the opaque interior of a protoneutron star, where the optical depth $\Delta\tau$ of individual grid cells cannot be avoided to be large in practical calculations can be smaller than the minimum of equ. (3.21) by orders of magnitude. The source terms are said to be “stiff” for this reason.

The above considerations suggest that in order to avoid the restrictive CFL condition and to efficiently cover the different time scales of the problem, a time-implicit finite differencing must be employed for the transport equations (3.7, 3.8). It is also very important that the source terms $S_E^{(0)}$ and $S_N^{(0)}$ are coupled implicitly to the equations (3.9, 3.10) which describe the exchange of internal energy and electron fraction with the stellar medium.

Finite-differenced moment equations

Applying the aforementioned procedures (see eqns. 3.14, 3.15, 3.20) to the moment equations (3.7, 3.8), we obtain for each neutrino species $\nu \in \{\nu_e, \bar{\nu}_e, \nu_\mu, \dots\}$ the finite differenced moment equations. On a Eulerian grid they read:

$$\begin{aligned} & \frac{J_{i+1/2,j+1/2,\nu}^{n+1} - J_{i+1/2,j+1/2,\nu}^n}{ct^{n+1} - ct^n} + \frac{4\pi}{\Delta V_{i+1/2}} (r_{i+1}^2 H_{i+1,j+1/2,\nu}^{n+1} - r_i^2 H_{i,j+1/2,\nu}^{n+1}) \\ & + \frac{4\pi}{\Delta V_{i+1/2}} (r_{i+1}^2 \beta_{i+1} J_{u(i+1),j+1/2,\nu}^{n+1/2} - r_i^2 \beta_i J_{u(i),j+1/2,\nu}^{n+1/2}) \\ & - \frac{1}{\Delta \epsilon_{j+1/2}} \left\{ \epsilon_{j+1} w_{i+1/2,j+1,\nu} J_{i+1/2,j+1,\nu}^{n+1} - \epsilon_j w_{i+1/2,j,\nu} J_{i+1/2,j,\nu}^{n+1} \right\} \\ & + \left[\frac{\beta}{r} \right]_{i+1/2} (1 - f_K)_{i+1/2,j+1/2,\nu} J_{i+1/2,j+1/2,\nu}^{n+1} \\ & + \left[\frac{\partial \beta}{\partial r} \right]_{i+1/2} f_K_{i+1/2,j+1/2,\nu} J_{i+1/2,j+1/2,\nu}^{n+1} \\ & + \frac{1}{c} \left[\frac{\partial \beta}{\partial t} \right]_{i+1/2} f_H_{i+1/2,j+1/2,\nu} J_{i+1/2,j+1/2,\nu}^{n+1} = S_E^{(0)n+1}{}_{i+1/2,j+1/2,\nu}, \end{aligned} \quad (3.23)$$

$$\begin{aligned}
& \frac{H_{i,j+1/2,\nu}^{n+1} - H_{i,j+1/2,\nu}^n}{ct^{n+1} - ct^n} + \frac{4\pi}{\Delta V_i} (r_{i+1/2}^2 (f_K J)_{i+1/2,j+1/2,\nu}^{n+1} - r_{i-1/2}^2 (f_K J)_{i-1/2,j+1/2,\nu}^{n+1}) \\
& + \frac{4\pi}{\Delta V_i} (r_{i+1/2}^2 \beta_{i+1/2} H_{u(i+1/2),j+1/2,\nu}^{n+1/2} - r_{i-1/2}^2 \beta_{i-1/2} H_{u(i-1/2),j+1/2,\nu}^{n+1/2}) \\
& - \frac{4\pi}{\Delta V_i} H_{i,j+1/2,\nu}^{n+1} (r_{i+1/2}^2 \beta_{i+1/2} - r_{i-1/2}^2 \beta_{i-1/2}) \\
& + \frac{4\pi}{\Delta V_i} J_{i,j+1/2,\nu}^{n+1} (f_K - 1)_{i,j+1/2,\nu} \cdot 0.5 (r_{i+1/2}^2 - r_{i-1/2}^2) = S_E^{(1)n+1}{}_{i,j+1/2,\nu}.
\end{aligned} \tag{3.24}$$

Since the radiation moments are defined on a staggered mesh, the finite-difference equations are second-order accurate in space. The differencing is fully implicit in time (“backward Euler”) and hence first-order accuracy in time is achieved. As an exception the advection terms⁸ appearing in the second line of equ. (3.23) and equ. (3.24) are treated with higher accuracy in time:

$$X^{n+1/2} := (1 - \zeta)X^n + \zeta X^{n+1}. \tag{3.25}$$

For stability reasons, the interpolation parameter $\zeta = 0.51$ was chosen slightly larger than 0.5, which makes the treatment “almost” second-order accurate in time (see e. g. Dorfi 1998). Different from the general treatment of “miscentred” quantities the interface values J_i and $H_{i+1/2}$ needed in the advection terms were replaced by the *upwind* values $J_{u(i)}$ and $H_{u(i+1/2)}$ where the corresponding indices are defined by

$$u(i) := \begin{cases} i - 1/2 & \text{for } \beta_i > 0 \\ i + 1/2 & \text{else.} \end{cases} \tag{3.26}$$

The “flux” in energy space across the boundaries between energy zones appearing in the third line of equ. (3.23) is given in terms of the advection velocity

$$w_{i+1/2,j,\nu} := \left[\frac{\beta}{r} \right]_{i+1/2} (1 - f_K)_{i+1/2,j,\nu} + \left[\frac{\partial \beta}{\partial r} \right]_{i+1/2} f_{K i+1/2,j,\nu} + \frac{1}{c} \left[\frac{\partial \beta}{\partial t} \right]_{i+1/2} f_{H i+1/2,j,\nu}, \tag{3.27}$$

and the interface value $J_{i,j,\nu}$ which is defined as the *geometrical* mean of $J_{i,j-1/2,\nu}$ and $J_{i,j+1/2,\nu}$.

Boundary conditions

For the solution of the moment equations (3.7, 3.8), boundary conditions have to be specified at $r = r_{\min}$, $r = r_{\max}$, $\epsilon = 0$ and $\epsilon = \epsilon_{\max}$. For the radial domain the boundary conditions are iteratively obtained from the solution of the Boltzmann equation (see below for the boundary conditions employed there), which has the advantage that in the moment equations no assumptions have to be made about the angular distribution of the specific intensity at the boundaries. Specifically, at the outer boundary the flux factor $f_{H\nu}(t, r = r_{\max}, \epsilon)$ and at the inner boundary the first moment $H(t, r = r_{\min}, \epsilon)$ — both obtained from the solution of the Boltzmann equation in the current iteration step — are used to eliminate $H_{0,j+1/2,\nu}^{n+1}$ and $J_{N_r+1/2,j+1/2,\nu}^{n+1}$ from eqns. (3.23) and (3.24), respectively.

At $\epsilon = 0$ the flux in energy space vanishes and hence we simply set $\epsilon_0 w_{i+1/2,0,\nu} J_{i+1/2,0,\nu}^{n+1} = 0$ in equ. (3.23). At the upper boundary of the spectrum the flux in energy space $\epsilon_{N_\epsilon} w_{i+1/2,N_\epsilon,\nu} J_{i+1/2,N_\epsilon,\nu}^{n+1}$ is obtained by a geometrical extrapolation of the moments $J_{i+1/2,N_\epsilon-2,\nu}$ and $J_{i+1/2,N_\epsilon-1,\nu}$ and by a linear extrapolation of the advection velocity using $w_{i+1/2,N_\epsilon-2,\nu}$ and $w_{i+1/2,N_\epsilon-1,\nu}$.

⁸When a Lagrangian grid with $r^{n+1} = r^n + (t^{n+1} - t^n)c\beta^n$ is used, the advection terms vanish identically.

Finite differenced source term

The finite differenced versions of the operator-splitted source terms for the energy and lepton number equations of the medium (eqns. 3.9, 3.10) read:

$$\frac{e_{i+1/2}^{n+1} - e_{i+1/2}^n}{t^{n+1} - t^n} = -\frac{4\pi}{\rho_{i+1/2}} \sum_{j=0}^{N_\epsilon-1} \sum_{\nu \in \{\nu_e, \bar{\nu}_e, \dots\}} S_E^{(0)n+1}{}_{i+1/2, j+1/2, \nu}, \quad (3.28)$$

$$\frac{Y_{e_{i+1/2}}^{n+1} - Y_{e_{i+1/2}}^n}{t^{n+1} - t^n} = -\frac{4\pi m_u}{\rho_{i+1/2}} \sum_{j=0}^{N_\epsilon-1} \left(S_N^{(0)n+1}{}_{i+1/2, j+1/2, \nu_e} - S_N^{(0)n+1}{}_{i+1/2, j+1/2, \bar{\nu}_e} \right). \quad (3.29)$$

Lepton number conservation

The derivative with respect to the radiation energy $\partial/\partial\epsilon$ which appears in the finite differenced (monochromatic) neutrino energy equation (equ. 3.23) has been written in a conservative form. When a summation over all energy bins is performed in equ. (3.23), the terms containing fluxes across the boundaries of the energy bins telescope and an appropriate finite differenced version of the total (i. e. spectrally integrated) neutrino energy equation is recovered exactly (cf. equ. 2.59). This essential property does however not hold automatically also for the neutrino number density $\mathcal{N} := 4\pi/c \int_0^\infty d\epsilon \mathcal{J}(\epsilon) \equiv 4\pi/c \int_0^\infty d\epsilon J(\epsilon)/\epsilon$, when the naive definition $\mathcal{J}_{i+1/2, j+1/2, \nu} := J_{i+1/2, j+1/2, \nu}/\epsilon_{j+1/2}$ is adopted. By inserting the latter definition into equ. (3.23) and summing over all energy bins, it can easily be verified that the corresponding fluxes across the boundaries of energy bins do not cancel and hence the algorithm would not guarantee the conservation of the total lepton number (cf. eqns. 2.63, 2.64).

In order to avoid this problem, we first write down the moment equations for the specific "number-intensity" \mathcal{I}/ϵ and recast them into a conservative form, which results in a system similar to equations (3.23) and (3.24). Introducing $\mathcal{J}_{i+1/2, j+1/2, \nu}$ (and $\mathcal{H}_{i+1/2, j+1/2, \nu}$) as new *independent* variables for the (monochromatic) neutrino number density (and number flux density), this system can be easily discretized conservatively. It is solved together with equations (3.23, 3.24, 3.28, 3.29). Note that treating the monochromatic energy density and the monochromatic number density as independent variables does not violate the constraint $\mathcal{J}(\epsilon) \equiv J(\epsilon)/\epsilon$, since the quantities $J_{i+1/2, j+1/2, \nu}$ and $\mathcal{J}_{i+1/2, j+1/2, \nu}$ are to be interpreted as *average values* within the energy bin $[\epsilon_j, \epsilon_{j+1}]$, rather than functions to be evaluated at $\epsilon_{j+1/2}$ (cf. equ. 3.20).

Numerical solution

For given Eddington factors $f_{K_{i+1/2, j+1/2, \nu}}$ and $f_{H_{i, j+1/2, \nu}}$ and flow field $\beta_{i+1/2}$, the nonlinear system of equations (eqns. 3.23, 3.24, their counterparts for the radiation number moments, and eqns. 3.28, 3.29) is solved numerically by Newton-Raphson iteration (e.g Press et al. 1992). This requires the inversion of the block-pentadiagonal system⁹

$$\sum_{\nu' \in \{\nu_e, \bar{\nu}_e, \dots\}} \sum_{j'=0}^{N_\epsilon-1} \left(A_{i, jj'\nu\nu'}^{(0)} \delta X_{i-1, j'\nu'} + A_{i, jj'\nu\nu'}^{(1)} \delta X_{i-1/2, j'\nu'} \right. \\ \left. + A_{i, jj'\nu\nu'}^{(2)} \delta X_{i, j'\nu'} + A_{i, jj'\nu\nu'}^{(3)} \delta X_{i+1/2, j'\nu'} + A_{i, jj'\nu\nu'}^{(4)} \delta X_{i+3/2, j'\nu'} \right) = R_{i, j, \nu}, \quad (3.30)$$

⁹If a Lagrangian grid is used, the system reduces to a block-tridiagonal form because $A^{(0)} = A^{(4)} \equiv 0$.

with

$$\begin{aligned} i &= 0, 1/2, 1, \dots, N_r - 1/2, N_r, \\ j &= 0, \dots, N_\epsilon - 1, \\ \nu &\in \{\nu_e, \bar{\nu}_e, \dots\}, \end{aligned}$$

where δX is the vector of Newton corrections, and $A_i^{(a)}$ are the non-zero $(2N_\epsilon N_\nu + 2) \times (2N_\epsilon N_\nu + 2)$ sub-matrices of the Jacobian. All partial derivatives with respect to the radiation moments can be calculated analytically, whereas the derivatives with respect to electron fraction and specific internal energy have to be computed numerically by finite differences.

3.2.3 Formal solution of the Boltzmann equation

In order to provide the closure relations (the “variable Eddington factor”) for the truncated system of moment equations, we compute a formal solution of the Boltzmann equation, i. e. we assume that the emissivity η and the opacity χ entering the rhs. of equ. (2.23) are known functions of the coordinates t , r , ϵ and μ (in practice, a guess is given by the solution of the moment equations in every iteration step).

Model equations

Following Mihalas & Mihalas (1984) we start with the modified Boltzmann equation on a Lagrangian coordinate grid

$$\frac{1}{c} \frac{D}{Dt} \mathcal{I} + \mu \frac{\partial}{\partial r} \mathcal{I} + \frac{1 - \mu^2}{r} \frac{\partial}{\partial \mu} \mathcal{I} + \left[(3 - \mu^2) \frac{\beta}{r} + (1 + \mu^2) \frac{\partial \beta}{\partial r} + \mu \frac{2}{c} \frac{\partial \beta}{\partial t} \right] \mathcal{I} = S_E, \quad (3.31)$$

where, compared to the original $\mathcal{O}(\beta)$ -Boltzmann equation (2.35), some of the velocity dependent terms have been omitted. Equation (3.31) neglects the impact of relativistic Doppler shift and aberration on the spectral distribution of the specific intensity. All the omitted terms are however of order $\mathcal{O}(\beta)$ or higher order in β . For computing only *normalised* moments to be used as a closure relation for the moment equations this appears to be a reasonable approximation. In Chapter 4 we shall give empirical support for this statement.

The model equation (3.31) has the following properties:

- When equ. (3.31) is integrated over angle, the $\mathcal{O}(\beta)$ -moment equations can be recovered.
- Hence, the velocity dependent rate of work done by the radiation pressure is correctly accounted for.
- The characteristic curves of equ. (3.31) are straight rays, which allows to employ efficient algorithms for the numerical solution as known from radiative transfer on static media.

In summary, the model equation (3.31) seems to provide a reasonable approximation for computing the closure relations, it is consistent with the moment equations and it can be solved efficiently on a tangent ray grid: Making the change of variables (cf. Yorke 1980; Mihalas & Mihalas 1984; Körner 1992; Baschek et al. 1997)

$$(r, \mu) \mapsto (s := \mu r, p := r \sqrt{1 - \mu^2}), \quad \mu \geq 0, \quad (3.32)$$

and introducing the symmetric and antisymmetric averages of the specific intensity

$$j(t, s, p) := \frac{1}{2}(\mathcal{I}(\mu) + \mathcal{I}(-\mu)), \quad \mu \geq 0, \quad (3.33)$$

$$h(t, s, p) := \frac{1}{2}(\mathcal{I}(\mu) - \mathcal{I}(-\mu)), \quad \mu \geq 0, \quad (3.34)$$

and the source terms

$$s_E(t, s, p) := \frac{1}{2}(S_E(\mu) + S_E(-\mu)), \quad \mu \geq 0, \quad (3.35)$$

$$u_E(t, s, p) := \frac{1}{2}(S_E(\mu) - S_E(-\mu)), \quad \mu \geq 0, \quad (3.36)$$

equ. (3.31) can be split into the two equations

$$\frac{1}{c} \frac{D}{Dt} j + \frac{\partial}{\partial s} h + \left(3 \frac{\beta}{r} + \frac{\partial \beta}{\partial r} \right) j + \mu^2 \left(\frac{\partial \beta}{\partial r} - \frac{\beta}{r} \right) j + \mu \frac{2}{c} \frac{\partial \beta}{\partial t} h = s_E, \quad (3.37)$$

$$\frac{1}{c} \frac{D}{Dt} h + \frac{\partial}{\partial s} j = u_E. \quad (3.38)$$

When the integrations $\int_0^1 d\mu$ and $\int_0^1 d\mu \mu$ are performed for equ. (3.37) and equ. (3.38), respectively, the moment equations (3.7, 3.8) are recovered exactly. Note that in order to preserve this property for eqns. (3.37 and 3.8) the velocity dependent terms were neglected in deriving equ. (3.38) from equ. (3.31) (cf. Mihalas & Mihalas 1984, §98).

Upon introducing the new variables (equ. 3.32), the *dimensionality* of the original model equation was reduced by one in the sense that the two-dimensional partial differential equation (PDE) (equ. 3.31) was transformed to a set of one-dimensional PDEs (eqns. 3.37, 3.38), which depend on the second coordinate only in a parametric way¹⁰. This property greatly simplifies the numerical solution of the system.

Finite-difference equations

The equations (3.37, 3.38) are discretized on a so-called “tangent ray grid” (for an illustration, see Fig. 3.1), whose geometry is an immediate consequence of the transformation of variables given by equ. (3.32). A “tangent ray” k is defined by its “impact parameter” $p_k = r_k$ at $\mu = 0$. The coordinate s serves to measure the pathlength along the ray. On each tangent ray k , a staggered numerical mesh is introduced for the coordinate s . The zone boundaries (centres) of this mesh are given by the ray’s intersections with the zone boundaries (centres) of the radial grid (cf. Fig. 3.1). With the “flux-like” variable h being defined on the zone boundaries s_{i_k} and the “density-like” variable j being defined on the zone centres $s_{i+1/2,k}$, the finite-differenced equations (3.37, 3.38)

¹⁰By this means we recover the genuinely “one-dimensional” character of the PDE (equ. 2.2), in which the angle of propagation is only a parameter (cf. Baschek et al. 1997).

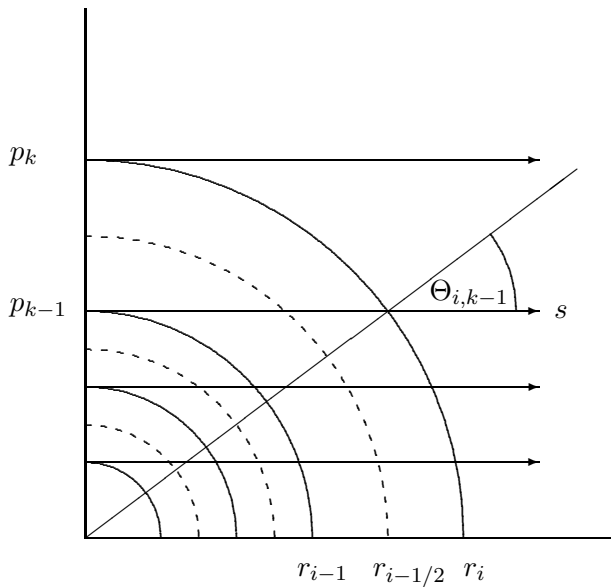


Figure 3.1: Basic geometry of the tangent ray grid. Each intersection of a radial shell r_i (solid circles) with a tangent ray defined by its “impact parameter” p_k (straight lines) defines an angular grid point $\mu_{ik} = \cos(\Theta_{ik}) = \sqrt{1 - p_k^2/r_i^2}$. These points also mark the zone boundaries of a finite-difference grid for the s -coordinate which is set up along each ray. The centres of this mesh are located at the intersections of the tangent rays with the centres of the radial grid (dashed circles). Spherical symmetry implies that for each radial shell i the set of angular grid points μ_{ik} describes the angular distribution of the specific intensity at the radial position r_i . The grid automatically accounts for an increased angular resolution at large radii and small angles.

finally can be written in the form ($k = K_0, \dots, N_r$; $i_k = k, \dots, N_r$)¹¹

$$\frac{j_{i_k+1/2,k}^{n+1} - \tilde{j}_{i_k+1/2,k}^n}{ct^{n+1} - ct^n} + \frac{h_{i_k+1,k}^{n+1} - h_{i_k,k}^{n+1}}{s_{i_k+1,k}^{n+1} - s_{i_k,k}^{n+1}} + A_{i_k+1/2,k}^{n+1} j_{i_k+1/2,k}^{n+1} + B_{i_k+1/2,k}^{n+1} h_{i_k+1/2,k}^{n+1} = 0, \quad (3.39)$$

$$\frac{h_{i_k,k}^{n+1} - \tilde{h}_{i_k,k}^n}{ct^{n+1} - ct^n} + \frac{j_{i_k+1/2,k}^{n+1} - j_{i_k-1/2,k}^{n+1}}{s_{i_k+1/2,k}^{n+1} - s_{i_k-1/2,k}^{n+1}} + A_{i_k,k}^{n+1} j_{i_k,k}^{n+1} + B_{i_k,k}^{n+1} h_{i_k,k}^{n+1} = 0, \quad (3.40)$$

where the coefficients A and B are combinations of the velocity and angle-dependent terms and the source terms appearing in eqns. (3.37, 3.38). The definition of \tilde{j} and \tilde{h} will be given later, for the moment one may ignore the tilde symbol.

Boundary conditions

For the solution of the model Boltzmann equation (3.31), boundary conditions have to be provided, which specify the radiation intensities $\mathcal{I}^+(t, r_{\min}, \mu) := \mathcal{I}(t, r_{\min}, \mu \geq 0)$ and $\mathcal{I}^-(t, r_{\max}, -\mu) := \mathcal{I}(t, r_{\max}, \mu \leq 0)$ at the inner ($r = r_{\min}$) and at the outer boundary ($r = r_{\max}$), respectively. By virtue of the definitions (3.33, 3.34) the boundary conditions imply a relation between j and h at the inner and at the outer boundary.

On the tangent ray grid boundary conditions must be specified for each ray k at $s_{k,k}$ and at $s_{N_r,k}$. At the inner boundary ($i_k = 0$; $k = K_0, \dots, 0$ and $s_{-1/2,k}^{n+1} := s_{0,k}^{n+1}$ in equ. 3.40) we set

$$j_{-1/2,k}^{n+1} := \mathcal{I}_{0,k}^+ - h_{0,k}^{n+1}, \quad (3.41)$$

¹¹If an inner boundary condition at some finite radius $r_{\min} > 0$ is used, a number of “core rays” $k = K_0, K_0 + 1, \dots, -1$ ($-K_0 \in \mathbb{N}$) which penetrate the innermost radial shell ($p_k \leq r_{\min}$) can be defined in order to describe the angular distribution of the radiation at the inner boundary. For details see e. g. Yorke (1980); Körner (1992); Dorfi (1998).

with $\mathcal{I}_{0,k}^+ := \mathcal{I}(t, r_{\min}, \mu_{0,k})$. For the remaining rays ($k = 1, \dots, N_r$), equ. (3.34) implies

$$h_{k,k}^{n+1} = 0, \quad (3.42)$$

since $\mu_{k,k} = 0$. At the outer boundary (setting $i_k = N_r$; $k = K_0, \dots, N_r$ and $s_{N_r+1/2,k}^{n+1} := s_{N_r,k}^{n+1}$ in equ. 3.40) we have

$$j_{N_r+1/2,k}^{n+1} := \mathcal{I}_{N_r,k}^- + h_{N_r,k}^{n+1}, \quad (3.43)$$

with $\mathcal{I}_{N_r,k}^- := \mathcal{I}(t, r = r_{\max}, -\mu_{N_r,k})$.

In the course of this work we use the specific inner boundary conditions $\mathcal{I}^+(t, r_{\min}, \mu) = \mathcal{I}_0 + \mu \mathcal{I}_1$, which is valid at large optical depth (the parameter \mathcal{I}_1 can e. g. be determined by an equilibrium diffusion approximation) or $\mathcal{I}^+(t, 0, +1) = \mathcal{I}^-(t, 0, -1)$, which, if $r_{\min} = 0$ is required by spherical symmetry. In all simulations we have assumed that no radiation is entering the computational domain through the outer boundary, which means that $\mathcal{I}^-(t, r_{\max}, -\mu) = 0$.

Numerical solution

By virtue of the approximations leading to the model Boltzmann equation (3.31) and upon introducing a tangent ray grid, the system (3.39, 3.40) together with the boundary conditions (3.41–3.43) can be solved *independently* for each impact parameter p_k , and — because pair processes are neglected — each type of neutrino (for simplicity we have dropped the index ν in our notation), and — because Doppler shift is neglected — each neutrino energy ϵ_j (index j also suppressed).

For the same reasons as given in Sect. 3.2.2 we have employed fully implicit (“backward Euler”) time differencing, which, according to eqns. (3.39, 3.40) requires the *separate* solution of $N_k \times N_\epsilon \times N_\nu$ ($N_k := N_r - K_0 + 1 \geq N_r$ is the number of tangent rays) tridiagonal linear systems of dimension $\leq N_r$. On vector machines, this can be done very efficiently by employing a vectorization over the index k (Fischer 1998). The other indices labeling the type of neutrino and the neutrino energy in principle would also allow for vectorization (or parallel computation).

Once the numerical solution for j and h has been obtained, the monochromatic moments and thus the Eddington factors $f_H = H/J$ and $f_K = K/J$ can be computed using the numerical quadrature formulae

$$\begin{aligned} J(r_i) &= \int_0^1 d\mu j(r_i, \mu) \approx \sum_{k=K_0}^i j_{ik} a_{ik}, \\ H(r_i) &= \int_0^1 d\mu \mu h(r_i, \mu) \approx \sum_{k=K_0}^i h_{ik} b_{ik}, \\ K(r_i) &= \int_0^1 d\mu \mu^2 j(r_i, \mu) \approx \sum_{k=K_0}^i j_{ik} c_{ik}. \end{aligned} \quad (3.44)$$

Explicit expressions for the quadrature weights a_{ik} , b_{ik} and c_{ik} can be found in Yorke (1980).

Unless the velocity field vanishes identically (in this case $\tilde{j} \equiv j$ and $\tilde{h} \equiv h$ in eqns. 3.39 and 3.40, respectively), an additional complication arises, since the partial derivative D/Dt has to be performed not only at fixed Lagrangian coordinate (the index i in our case) but also for a fixed

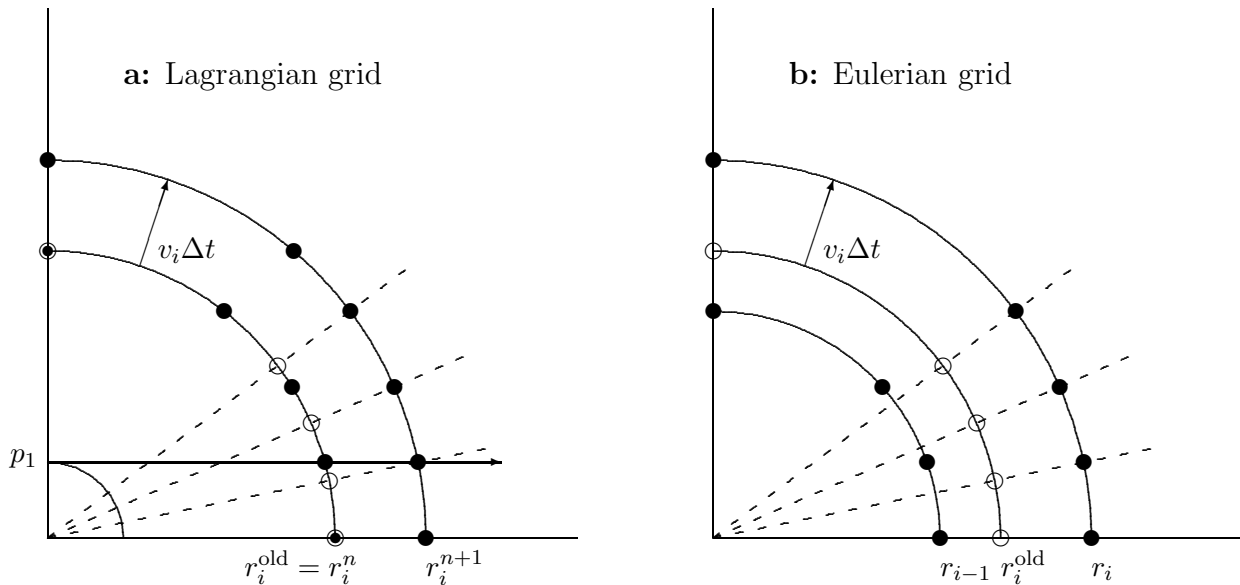


Figure 3.2: A moving tangent ray grid at the old (t^n) and new ($t^{n+1} = t^n + \Delta t$) time level (filled circles; note that for simplicity we have drawn a special case in panel **a** assuming $v_{i'} = 0$, which for $i' < i$ implies $p_{i'} = \text{const.}$). The filled circles mark the positions where the quantities j and h are known from the solution of the previous timestep. For $v \neq 0$ these positions do not coincide with the locations $(r_i^{\text{old}}, \mu_{ik}^{n+1})$, where initial values of the radiation field are required for computing the current timestep (open circles). The latter positions are subject to the requirement that the D/Dt operator has to be evaluated at fixed Lagrangian *and* angular coordinate (Lines of constant angle cosines $\mu = \text{const.}$ are drawn as dashed lines.). Thus, in the case of a Lagrangian grid (panel **a**) an interpolation in the angular coordinate is required, whereas for a Eulerian grid (panel **b**) also an interpolation in radius has to be performed. See the text for further details.

value of the angle cosine μ . The angular grid $\{\mu_{ik}^n\}$ which is attached to the radius r_i^n , however, moves as the radial position r_i^n changes with time. As a consequence, the values of h at the old time level used e. g. in equ. (3.40) are¹² $\tilde{h}_{ik}^n := h(t^n, r_i^n, \mu_{ik}^{n+1})$ and not $h_{ik}^n := h(t^n, r_i^n, \mu_{ik}^n)$, the solution computed in the previous timestep (cf. Mihalas & Mihalas 1984, §98). At the beginning of the timestep we therefore have to interpolate the radiation field for each fixed radial index i from the $\{\mu_{ik}^n\}$ -grid onto the $\{\mu_{ik}^{n+1}\}$ -grid (cf. Fig. 3.2a).

If a Eulerian grid is used for the radial discretization, the situation is slightly more complex: The (model) Boltzmann equation (3.31) in Eulerian coordinates *cannot* be decoupled into a set of one-dimensional PDEs by employing the transformation (equ. 3.32). On the tangent ray grid the $v\partial_r$ -term which originates from making the replacement $D_t = \partial_t + v\partial_r$ in equ. (3.31) would couple grid points of different tangent rays. Therefore we would like to solve the Boltzmann equation in its Lagrangian form as given by equ. (3.31), yet we do not want advance the numerical coordinate grid with the fluid flow. This can be accomplished in two similar ways. One might perform a numerical timestep on a Lagrangian grid as described previously and afterwards, by interpolation “re-map” the solution back onto the Eulerian grid which remains fixed in space throughout the calculation. Alternatively one can, at the beginning of the timestep, “pre-map” the specific intensity onto a Lagrangian grid, which is chosen such that it coincides with the Eulerian grid after the timestep has been completed and no more interpolation is necessary at the end of the timestep. We have

¹²Analogous expressions hold for \tilde{j} .

implemented the latter of the two variants, since the corresponding algorithm is more similar to the one used in the (genuinely) Lagrangian grid version of our program (Fig. 3.2a). Accordingly, at the beginning of each timestep we calculate for each radial coordinate r_i of the Eulerian grid the radius of the corresponding Lagrangian shell at the old time level, which is given by $r_i^{\text{old}} := r_i - v_i \Delta t$, first. The values \tilde{h}^n which are required on the resulting $\{\mu_{ik}^{\text{old}}\}$ -mesh are obtained from h^n by a bilinear interpolation using the four nearest neighbours of the $\{\mu_{ik}\}$ -mesh (cf. Fig. 3.2b).

3.3 Details of coupling radiative transfer and hydrodynamics

3.3.1 Schedule of updates

As we have briefly mentioned previously, the complete update of the hydrodynamic and radiation variables is decoupled into a number of subsequent independent steps (“operator splitting”): Starting from the hydrodynamic state $(\rho^n, e^n, Y_e^n, v^n)$ at the old time level t^n , the time-explicit PPM-algorithm first computes a solution of the equations of hydrodynamics without any source terms. From the updated density, the gravitational potential can be calculated by equ. (2.66) and finally the gravitational source terms are applied to the total energy equation and the momentum equation (cf. eqns. 2.50, 2.51). This completes the “hydrodynamic” sub-step whose size Δt_{Hyd} is determined by the CFL-condition (see e. g. LeVeque 1992). Performing in total N_{Hyd}^n hydrodynamic sub-steps, where $N_{\text{Hyd}}^n \in \mathbb{N}$ is computed as the largest integer that fulfils the condition¹³

$$\sum_{i_n=1}^{N_{\text{Hyd}}^n} \Delta t_{\text{Hyd}}^{i_n} \leq \Delta t_{\text{RT}}^{\text{max}}, \quad (3.45)$$

where $\Delta t_{\text{RT}}^{\text{max}}$ is the maximum allowed size for the radiative transfer timestep, the hydrodynamic state is updated from time level t^n to the new time level t^{n+1} given by

$$t^{n+1} = t^n + \Delta t^n = t^n + \sum_{i_n=1}^{N_{\text{Hyd}}^n} \Delta t_{\text{Hyd}}^{i_n}. \quad (3.46)$$

The partially updated (due to hydrodynamical advection and gravitation) state $(\rho^{n+1}, e^*, Y_e^*, v^{**})$ is then mapped onto the radiative transfer grid (see equ. 3.48 for a definition of v^{**}). During the implicit transport timestep of size Δt^n , the radiative transfer equations coupled to the operator-splitting electron fraction and internal energy equations (eqns. 3.7 – 3.10) are solved, which enables the calculation of the energy and lepton number source terms $(e^{n+1} - e^*)/\Delta t^n$ and $(Y_e^{n+1} - Y_e^*)/\Delta t^n$ which are defined on the grid where the transport is solved. Note that since the transport grid in general does not coincide with the hydrodynamics grid, the fully updated specific internal energy e^{n+1} and electron fraction Y_e^{n+1} cannot readily be used to describe the new hydrodynamic state. Instead of simply interpolating the quantities e^{n+1} and Y_e^{n+1} back onto the hydrodynamics grid, we first map the source terms by a conservative procedure (see below). Only then the updates for

¹³Usually the timestep of the implicit transport scheme is larger than the hydrodynamic timestep, since for an implicit method the timestep is limited by accuracy rather than stability considerations: Typically, we allow for relative changes of 10% for the monochromatic radiation moments. In addition we limit the number N_{Hyd}^n by the requirement that during the timestep Δt^n the relative changes of the density, temperature, internal energy density and electron fraction must not exceed values of 2%, 10%, 5% and 5%, respectively.

the electron number density and the total energy density is performed on the hydrodynamics grid according to

$$\begin{aligned} (\rho e + \frac{1}{2}\rho v^2)^{n+1} &= \rho^{n+1}(e + \frac{1}{2}\rho v^2)^* + (Q_E + vQ_M)^{n+1} \cdot \Delta t^n, \\ (\rho Y_e)^{n+1} &= \rho^{n+1}Y_e^* + Q_N^{n+1} \cdot \Delta t^n. \end{aligned} \quad (3.47)$$

For updating the medium's momentum density (the velocity, say, since the mass density is not changed in the transport step) due to the momentum exchange with the neutrinos we employ the following predictor-corrector method (see e. g. Press et al. 1992): At the beginning of the transport timestep, an estimate of the velocity at the intermediate time $t^n + 0.5\Delta t^n$ is computed using the corresponding source term from the previous timestep:

$$\rho^{n+1}v^{**} = \rho^{n+1}v^* + Q_M^n \cdot 0.5\Delta t^n. \quad (3.48)$$

The velocity $v^{**} \equiv \beta \cdot c$ enters the transport equations. After the transport timestep has been completed, the new source term is used to correct the estimate v^{**} according to:

$$\rho^{n+1}v^{n+1} = \rho^{n+1}v^{**} + (Q_M^{n+1} - 0.5 \cdot Q_M^n) \cdot \Delta t^n. \quad (3.49)$$

3.3.2 Conservative mapping algorithm

The numerical algorithms for the *independent* numerical solution of the equations of hydrodynamics and the neutrino transport equations are formulated in a conservative way. This, however, is not sufficient to guarantee the conservation of total energy (i. e. internal, kinetic and gravitational potential energies of the fluid plus the total neutrino energy), momentum and lepton number (i. e. the number of electron neutrinos and electrons minus the number of positrons and electron antineutrinos), if both systems are discretized on different numerical grids. In this case we additionally have to make sure that the radiation source terms that enter both systems with opposite signs cancel exactly after spatial integration over the grids has been performed. This property should hold also “locally”, i. e. the numerical integrals over any subvolume of the computational domain that is covered by the two different grids should also cancel. In the following we describe the algorithm that fulfils both requirements by construction. It is used to map the source terms as defined on the transport grid (unprimed symbols in the following) into the corresponding quantities $-(Q_E + vQ_M)$, $-Q_M$, and $-Q_N$, which are defined on the grid where the equations of hydrodynamics are solved (primed symbols). Although it is not explicitly demanded by conservation arguments we use the same procedure also in the other direction for mapping the hydrodynamic variables onto the transport grid.

In describing the mapping procedure we refer to a “density” ρ (which, in practice stands for the source terms $S_N^{(0)}$, $S_E^{(0)} + \beta S_E^{(1)}$, and $S_E^{(1)}$, and also for the electron number density $m_u^{-1}\rho Y_e$, the fluid energy density ρe and momentum density ρv_i , the source terms $(e^{n+1} - e^*)/\Delta t^n$, $(Y_e^{n+1} - Y_e^*)/\Delta t^n$, etc.) of a quantity $m = \int \rho dV$ (called “mass” here), which has to be conserved by the mapping.

Case A $\{\Delta V'\} \subset \{\Delta V\}$: We first consider the special case of a cell $\{\Delta V'\}$ which is a subset of the cell $\{\Delta V\}$: In order to assign a suitable average value $\rho' := \Delta m'/\Delta V'$ to the former, we have to calculate the integral

$$\Delta m' := \int_{\Delta V'} \rho dV', \quad (3.50)$$

which requires the prescription of the functional form of the density ρ within the original zone $\{\Delta V\}$. One possibility would be to use one of the reconstruction algorithms used in (high-order) Godunov schemes like e. g. PPM (see Dai & Woodward 1996, for an approach of this kind). Yet we take a simpler approach and use the linear function

$$\rho(r) = \rho_{i+1/2}^c + \delta\rho_{i+1/2} \cdot (r - r_{i+1/2}), \quad r_i \leq r \leq r_{i+1}, \quad (3.51)$$

with the two parameters $\rho_{i+1/2}^c$ and $\delta\rho_{i+1/2}$. The parameter $\delta\rho_{i+1/2}$ is computed as a “monotonized slope”, which is basically given by the harmonic mean of the left and right-handed difference approximation to the local gradient using the three adjacent original data $\{\rho_{i-1/2}, \rho_{i+1/2}, \rho_{i+3/2}\}$ (for details see e. g. Ruffert 1992, and references cited therein). Unless cartesian coordinates are used, the zone centre value $\rho_{i+1/2}^c := \rho(r_{i+1/2})$ is in general not identical with the (known) average value $\rho_{i+1/2}$. In spherical coordinates, for example, $\rho_{i+1/2}^c$ has to be computed using the definition of the average value $\rho_{i+1/2}$:

$$\rho_{i+1/2} \Delta V_{i+1/2} = 4\pi \int_{r_i}^{r_{i+1}} (\rho_{i+1/2}^c + \delta\rho_{i+1/2} \cdot (r - r_{i+1/2})) r^2 dr. \quad (3.52)$$

The slope $\delta\rho_{i+1/2}$ has been calculated previously. Once the two parameters $\rho_{i+1/2}^c$ and $\delta\rho_{i+1/2}$ have been determined, the conservatively “interpolated” value ρ' can be computed by evaluating the integral (3.50) over the cell $\{\Delta V'\}$.

Case B $\{\Delta V\} \subset \{\Delta V'\}$: If, on the other hand, the cell $\{\Delta V\}$ is completely overlapped by $\{\Delta V'\}$, the contribution of the cell $\{\Delta V\}$ to the total mass contained within $\{\Delta V'\}$ is simply given by $\rho\Delta V$.

General Case: By dividing $\{\Delta V'\}$ into suitable subvolumes, the general case of an arbitrary relative orientation of both grids can always be reduced to combinations of the two special situations (Case A and Case B) described above. The conservatively “interpolated” value ρ' is then obtained by adding up the contributions of the individual subvolumes of $\{\Delta V'\}$ to the total *mass* $\Delta m'$ contained within $\{\Delta V'\}$ and by dividing by the total volume $\Delta V'$.

3.4 Approximate multi-dimensional neutrino transport

In the introduction we have pointed out the significance of convective phenomena for the explosion mechanism of core-collapse supernovae. Here we describe a generalization of the variable Eddington factor method to develop an approximation of multi-dimensional neutrino transport, which can be considered to be adequate for studying the effects of neutrinos in multi-dimensional hydrodynamical simulations.

Basic considerations

Due to the high dimensionality of the transport problem (in general the specific intensity depends on three spatial coordinates, two angles of propagation¹⁴, the energy of the neutrinos and time),

¹⁴One can easily convince oneself that two angles are required even if the spatial variations are restricted to only two dimensions.

simulating genuinely three-dimensional, time-dependent neutrino transport appears to be not feasible at present. Therefore one has to think about reasonable approximations.

Approximate treatment of neutrino transport in multi-dimensional hydrodynamic supernova simulations can make use of the assumption that no global deviations from spherical symmetry are present in regions of the star where neutrinos are tightly coupled to the stellar medium (which obviously excludes the treatment of rotationally deformed stars). From multi-dimensional hydrodynamical simulations of convective processes in the supernova core we know that

- (1) inside the opaque protoneutron star deviations of the thermodynamical quantities from spherical symmetry due to convection are only of the order of a few percent (Keil 1997). Moreover, the time scale of the local fluctuations is short compared to the neutrino diffusion time scale. Hence, on the neutrino diffusion time scale no persistent local gradients in lateral and azimuthal directions are present in the stellar medium, which allows one to disregard the neutrino transport into these directions as a first approximation which is at least correct in the temporal average.
- (2) between the neutrinospheres and the stalled hydrodynamic shock convective overturn occurs and thus deviations from spherical symmetry are present on larger angular scales (Herant et al. 1992, 1994; Burrows et al. 1995; Janka & Müller 1996; Müller & Janka 1997; Mezzacappa et al. 1998b; Kifonidis et al. 2000), but the neutrinos are only marginally coupled to the stellar medium in these regions, and transport in the lateral directions does therefore not play a role here.

As a first — but, as we shall see, unacceptable — approximation one might consider to apply a given one-dimensional transport scheme to compute the transport on a spherically symmetric “image” of the star, which is obtained at each timestep by averaging the multi-dimensional hydrodynamical stellar model over angles. One would then use the transport result to calculate the local exchange of energy and lepton number with the stellar medium at each position in the star. However, in order to reproduce local thermodynamical equilibrium (i. e. heating balances cooling) inside the opaque protoneutron star where the neutrino emission and absorption rates are extremely large, the specific intensity must be able to adjust to the local conditions with high accuracy, which is obviously not the case in the simple angle-averaged treatment. Even worse, the conservation of total energy (i. e. the energy of the stellar fluid plus neutrinos) and lepton number cannot be fulfilled because the treatment of the source terms in the multi-dimensional hydrodynamical equations and in the neutrino transport equations is not symmetric. We conclude that even if the deviations from spherical symmetry are small one must treat the coupling between neutrinos and stellar fluid “locally”, which means that the dependence of the neutrino energy and momentum density on the position in the star must be taken into account.

Strategy

A better approach for an approximate multi-dimensional neutrino transport is the following: Under the circumstances spelled out at the beginning of this section the specific intensity $\mathcal{I}(t, r, \vartheta, \phi; \epsilon, \mathbf{n})$ can be assumed to depend only weakly on longitude ϕ and latitude ϑ of the background medium. Hence, like in the spherically symmetric case, the dependence of the specific intensity on the direction of propagation \mathbf{n} can be described by only one angle $\mu := \mathbf{n} \cdot \mathbf{r}/|\mathbf{r}|$. The flux is thus approximated as $\mathbf{F} = 4\pi\mathbf{r}/|\mathbf{r}| \cdot H(t, r, \vartheta, \phi; \epsilon)$ and the scalar $P = 4\pi/c \cdot K(t, r, \vartheta, \phi; \epsilon)$ suffices to define the radiation stress tensor.

In the moment equations (eqns. 2.11, 2.12), gradients in the ϑ - and the ϕ -direction, which describe the transport of energy and neutrino number into these lateral and azimuthal directions, are neglected, yet the parametric dependence of the (scalar) moments on the coordinates ϑ and ϕ is retained and the radial transport is computed using the moment equations independently in each angular zone of the stellar model. Since for each latitude ϑ and longitude ϕ the moment equations (eqns. 3.7, 3.8) are solved in this case together with the operator-splitted electron fraction and internal energy equations (eqns. 3.9, 3.10), radiative equilibrium can be attained correctly and conservation of energy can be fulfilled. In order to obtain closure relations for the moment equations the variable Eddington factor method as described for a spherically symmetric background medium (see the previous sections) is applied to an angularly averaged “image” of the star (i. e. $\xi(t, r) := (4\pi)^{-1} \int_{-1}^{+1} d \cos \vartheta \int_0^{2\pi} d\phi \xi(t, r, \vartheta, \phi)$, with $\xi \in \{\rho, T, Y_e, \beta, \dots\}$). Note that the variable Eddington factor as a normalised moment of the neutrino distribution should not show significant variation with the angular coordinates of the star. Notice also that in contrast to the strictly one-dimensional transport rejected in the discussion above, the treatment suggested now solves the neutrino energy and moment equations for the radial transport in each angular zone of the star, and only for closing these sets of moment equations a single universal variable Eddington factor is used.

Computational efficiency

Let $\Delta t_{1D}^{\text{CPU}}$ be the computation time required for calculating a timestep of the full one-dimensional transport problem and let $n^{\text{It}} \in \mathbb{N}$ be the number of steps that are necessary for the iteration between the moment equations and the Boltzmann equation to converge. If $n_{\vartheta, \phi} := n_{\vartheta} \cdot n_{\phi}$ is the total number of angular zones that resolve the background star the computation time for calculating one timestep of the multi-dimensional problem with our method is

$$\Delta t^{\text{CPU}} = \Delta t_{1D}^{\text{CPU}} + \frac{n_{\vartheta, \phi}}{n^{\text{It}}} \cdot \Delta t_{1D}^{\text{CPU}} = \left(1 + \frac{n_{\vartheta, \phi}}{n^{\text{It}}}\right) \cdot \Delta t_{1D}^{\text{CPU}}. \quad (3.53)$$

Note that the iteration procedure ($n^{\text{It}} > 1$) has to be performed only once, namely on the angularly averaged “image” of the background medium. With typical values¹⁵ of $n^{\text{It}} = 3 \dots 10$ and large values of $n_{\vartheta, \phi} (\simeq 100)$ the computational effort for solving the multi-dimensional problem goes like

$$\Delta t^{\text{CPU}} \approx (0.1 \dots 0.3) n_{\vartheta, \phi} \cdot \Delta t_{1D}^{\text{CPU}}, \quad (3.54)$$

to be compared with $\Delta t^{\text{CPU}} = n_{\vartheta, \phi} \cdot \Delta t_{1D}^{\text{CPU}}$, which would result for a straightforward application of the one-dimensional method to a number of $n_{\vartheta, \phi}$ angular zones.

¹⁵When comparing with the numbers $n^{\text{It}} = 2 \dots 5$ that shall be quoted in Sect. 4.3 one has to take into account that in the test problems considered there no variations of the background medium are present.

Chapter 4

Radiative Transfer Problems

In a few cases, where a particularly simple radial dependence of the emissivity and the opacity is adopted, stationary solutions of the Boltzmann equation of radiative transfer could be calculated analytically or were computed semi-analytically or numerically to high accuracy. These problems provide ideal test cases for our new numerical implementation of the equations of radiative transfer introduced in the previous chapter. We impose suitably chosen initial and boundary conditions and solve the time-dependent radiative transfer equations numerically, until a stationary state is reached. The stationary state radiation field can then be compared to reference solutions. Besides evaluating the accuracy and efficiency of the method, some clues can be obtained about the degree of its robustness, e. g. by varying the initial conditions or the boundary conditions. In addition, some of the test problems can serve to illustrate important physical aspects of radiative transfer.

Section 4.1 deals with radiative transfer problems using *static* background models, i. e. solutions of the Boltzmann equation in the form of equ. (2.23) are examined. Potential differences between numerical results and the reference solutions must necessarily be attributed to deficiencies in the numerics, caused e. g. by truncation errors. In Section 4.2, we calculate radiative transfer in the co-moving frame to order $\mathcal{O}(v/c)$ in moving (yet stationary) atmospheres. The $\mathcal{O}(v/c)$ -approximation is tested by comparing to solutions of the fully relativistic transfer equation. We also compare results from a comoving frame simulation with those obtained in a Eulerian frame of reference. The problems discussed in this chapter do neither refer to specific properties of neutrinos nor will the equations of radiation hydrodynamics, i. e. the coupling of the radiative transfer equation to the equations of hydrodynamics, be tested. Both aspects are addressed in Chapter 5.

4.1 Radiative transfer on a static background

We first consider the simplest class of radiative transfer problems, namely those where the “background medium” is assumed to be static, i. e. the radial profiles of the emissivity and opacity do not change with time and the velocity and acceleration vanish everywhere and at all times. As usual, the background medium is assumed to be spherically symmetric.

4.1.1 Propagation of a light pulse

Here, we compare two different algorithms for computing the formal solution of the time-dependent Boltzmann equation concerning their ability to correctly propagate a pulse of radiation across some radial distance. One method is based on a finite differenced Boltzmann equation (Mihalas

& Klein 1982). It is used to calculate the variable Eddington factor in our transport code (see Sect. 3.2.3). The other method makes use of the general quadrature solution along characteristics of the Boltzmann equation (Yorke 1980; Körner 1992; Baschek et al. 1997). For convenience, we set $c \equiv 1$ in this section.

Model

As a physical model we may envisage a central point source emitting radiation into a spherical, static and homogeneous atmosphere bounded by two spheres of radius r_0 and $R > r_0$. The only interaction of radiation with the atmosphere is due to absorption ($S = -\kappa_a \mathcal{I}$). The central source is active during the time interval $-r_0 \leq t < \infty$. Initially ($t = 0$), there is no radiation inside the atmosphere.

By symmetry, the specific intensity vanishes for all but the radial direction of propagation. It is therefore sufficient to follow the propagation of the light pulse along a single radial (characteristic) ray. The dependence of the specific intensity on the angle can thus conveniently be suppressed in the notation, writing

$$\begin{aligned}\mathcal{I}^+(t, s) &:= \delta(\mu - 1) \cdot \mathcal{I}(t, s, \mu), \\ \mathcal{I}^-(t, s) &:= \delta(\mu + 1) \cdot \mathcal{I}(t, s, \mu),\end{aligned}\tag{4.1}$$

with $s := r - r_0$. The equations to be solved are (cf. equ. 2.23)

$$\partial_t \mathcal{I}^+(t, s) + \partial_s \mathcal{I}^+(t, s) = -\kappa_a \mathcal{I}^+(t, s),\tag{4.2}$$

$$\partial_t \mathcal{I}^-(t, s) - \partial_s \mathcal{I}^-(t, s) = -\kappa_a \mathcal{I}^-(t, s),\tag{4.3}$$

subject to the boundary conditions $\mathcal{I}^+(t, 0) = \mathcal{I}_0$ (for $t \geq 0$) and $\mathcal{I}^-(t, s_{\max}) = 0$, and the initial condition $\mathcal{I}^\pm(0, s) = 0$ (for $0 < s < s_{\max} := R - r_0$). The analytical (weak) solution can easily be verified to read:

$$\mathcal{I}^-(t, s) \equiv 0, \text{ and } \mathcal{I}^+(t, s) = \begin{cases} \mathcal{I}_0 \cdot \exp(-\kappa_a s) & \text{for } s \leq t, \\ 0 & \text{else.} \end{cases}\tag{4.4}$$

Results

Employing the Boltzmann solver based on the finite difference method (Mihalas & Klein 1982, see Chap. 3 for our implementation), we have computed two models with atmospheres spanning the range $0 < s \leq 200$. The equidistant radial grid was given a resolution of $\Delta s = 1$. Model ‘‘VAC’’ assumes a vacuum atmosphere ($\kappa_a \equiv 0$), whereas the absorbing atmosphere of model ‘‘ABS’’ is characterized by $\kappa_a \equiv 0.01$, resulting in a total optical depth of $\tau = 2$. Figure 4.1 shows our results for \mathcal{I}^+ at the time $t = 100$, together with the analytical solution (equ. 4.4). We define the position of the numerically broadened light front as the radius, where the mean of the true pre and postfront value of the intensity is reached. In all cases one recognizes that the mean *propagation speed* is correctly reproduced, with some tiny decrease of accuracy visible for very large timesteps. The *shape* of the light front, however, deviates from the true solution. One observes an artificial precursor together with a reduced intensity behind the front, both effects resulting in a spatial broadening of the front. A clear trend towards larger diffusive broadening with increasing timesteps can be seen from Fig. 4.1 and Table 4.1. This phenomenon was also observed by Mihalas & Klein (1982), who

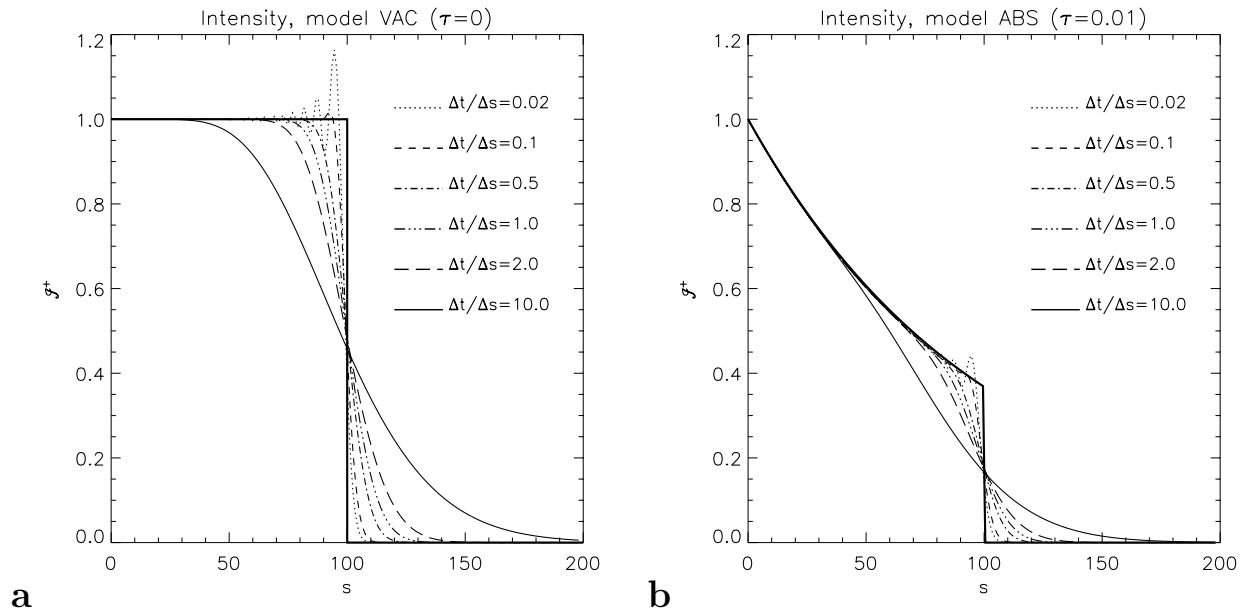


Figure 4.1: Outwardly directed specific intensity \mathcal{I}^+ computed by our Boltzmann solver as a function of position s at time $t = 100$ for different values of the timestep (thin lines) together with the analytical solution (bold line). Panel **a** shows model “VAC” with no absorption, panel **b** shows the absorbing case model “ABS”.

reported very similar results from their test problems. For timesteps Δt significantly smaller than the radial zone width, a case not discussed by Mihalas & Klein (1982), we observe some spurious postfront oscillations (see also Mihalas & Weaver 1982, §5). Their maximum amplitude, however, does not grow with time which is in agreement with a local von Neumann stability analysis for the fully implicit implementation of the equations (see e. g. Mihalas & Klein 1982). However, it might be necessary to introduce some artificial diffusivity (see e. g. Blinnikov, Eastman, Bartunov, Popolitov, & Woosley 1998, Appendix A) in order to damp the oscillations, if present in practical applications (the remedy suggested by Mihalas & Weaver (1982) was not helpful in the test cases considered here).

Following Yorke (1980), we define the width δs of the front by the number of grid points (or the radial distance) for which \mathcal{I}^+ lies between 0.1 and 0.9 times its true postfront value. Table 4.1 summarizes our results for the width of the front and compares them to simulations done with an implementation of the method of characteristics (Yorke 1980; Körner 1992). The latter method has the advantage to exactly reproduce the analytical solution without any smearing of the front, if the light front is advanced by exactly one grid cell per timestep. Though the ability to reproduce the exact solution appears to be a very appealing property of the method of characteristics, the necessary condition $\Delta t = \Delta x$ can hardly ever be accomplished in realistic simulations. The simple reason is that in typical astrophysical simulations the radial resolution can be varying over several orders of magnitude, whereas in most of the numerical schemes a global value for the timestep has to be prescribed. Moreover, when doing radiation hydrodynamical simulations one is usually interested in resolving time scales different from those given by the speed of propagation of light fronts and typical zone widths. Accordingly, timesteps which can be very different from the optimum for light front propagation are used in real applications. Our finite difference method thus seems to

$\Delta t/\Delta s$	#	model VAC		model ABS	
		δs (FD)	δs (CH)	δs (FD)	δs (CH)
0.02	5000	6	25	6	26
0.1	1000	8	–	8	–
0.5	200	18	16	16	20
1.0	100	26	1	22	1
2.0	50	37	26	29	26
10.0	10	80	–	55	–

Table 4.1: Width of the light front δs (see the text for a definition) as a function of the timestep Δt (or the number of timesteps # required for the light front to reach $s = 100$) computed with two different numerical methods: Our code employs the finite difference method (“FD”) as proposed by Mihalas & Klein (1982). It is compared with a method of characteristics (“CH”; Yorke 1980). Numbers obtained with the latter method are taken directly from Yorke (1980, Tables 1,2). They were, in addition, confirmed by an implementation of this numerical scheme by Körner (1992).

be preferable to the methods of characteristics as far as the resolution of the pulse is concerned (cf. Table 4.1).

4.1.2 Homogeneous sphere

The “homogeneous sphere” is a test problem frequently employed for radiative transfer calculations (e. g. Bruenn 1985; Schinder & Bludman 1989; Smit et al. 1997). Physically, one can think of a static, homogeneous and isothermal sphere of radius R radiating into vacuum. Inside the sphere, the only interaction of radiation with the background medium is isotropic absorption and thermal emission of radiation. Despite its simplification, the model covers some important numerical as well as physical issues that are typically met in practical applications: Probably any finite difference method is challenged by the discontinuity at the surface of the sphere. Moreover, for an optically thick sphere, the sudden transition from radiation diffusion inside the sphere to free streaming into the ambient vacuum — a similar but less extreme situation arises in the neutrino heating region of a core-collapse supernova — is a major source of error in many of the approximate radiative transfer methods like e. g. flux-limited diffusion.

Model

The model is defined by setting $S = \kappa_a(b - \mathcal{I})$ with $b = \text{const.}$, $\kappa_a = \text{const.}$ for $0 \leq r \leq R$, and $\kappa_a = b \equiv 0$ for $r > R$. The boundary conditions are:

$$\begin{aligned} \mathcal{I}(r = 0, \mu = 1) &= \mathcal{I}(r = 0, \mu = -1), && \text{“symmetry”} \\ \mathcal{I}(r = R_{\text{max}}, \mu) &= 0, && -1 \leq \mu \leq 0, \quad \text{“no incoming radiation”} \end{aligned} \quad (4.5)$$

Since for this choice of parameters, the right hand side of the Boltzmann equation contains no terms that depend explicitly on the angular moments of the radiation field, the solution of equ. (2.23) can be obtained by computing a formal solution. The result for the stationary state is (see e. g. Smit et al. 1997)

$$\mathcal{I}(r, \mu) = b(1 - e^{-\kappa_a s(r, \mu)}) \quad (4.6)$$

with the abbreviations

$$s(r, \mu) := \begin{cases} r\mu + Rg(r, \mu) & \text{if } r < R, \quad -1 \leq \mu \leq +1, \\ 2Rg(r, \mu) & \text{if } r \geq R, \quad \sqrt{1 - (\frac{R}{r})^2} \leq \mu \leq +1, \\ 0 & \text{else,} \end{cases} \quad (4.7)$$

$$\text{where } g(r, \mu) := \sqrt{1 - (\frac{r}{R})^2(1 - \mu^2)}. \quad (4.8)$$

The solution (4.6–4.8) depends on only three physical parameters, namely the radial position relative to the radius of the sphere, r/R , its total optical depth $\tau = \kappa_a R$, and the equilibrium intensity b . The latter merely acts as a scale factor for the solution.

Results

The radial grid consists of 213 radial zones covering the range between $r = 0$ and $r = R_{\max} \approx 12R$. Approximately 200 zones were distributed logarithmically between $r \approx 0.0006R_{\max}$ and $r = R_{\max}$, about two thirds of which were spent to resolve the sphere. Initially we set $\mathcal{I} \approx 0$ everywhere and evolve the radiation field until a stationary state is reached.

In Fig. 4.2 we display the stationary state solutions for two models, one with $\tau = b = 4$ (Fig. 4.2a,c,e) and another with $\tau = b = 26$ (Fig. 4.2b,d,f), representative of a sphere with low and high opacity, respectively. In general, the results of our numerical solution agree very well with the true solution. The Eddington factor K/J (as obtained from the solution of the Boltzmann equation) and the flux factor H/J (as obtained from the solution of the moment equations) both show remarkable agreement with the analytical solution. Inside the opaque sphere the flux factor follows the analytical solution over many orders of magnitude (Fig. 4.2e,f). In both models, the transition to free streaming is reproduced very accurately (Fig. 4.2c–f). The latter property is usually only poorly reproduced by flux-limited diffusion methods (see e. g. Bruenn 1985; Smit et al. 1997). Also the forward peaking of the radiation field far from the surface of the sphere (cf. eqns. 4.6–4.8) is accounted for excellently by our method: At $r = R_{\max}$, the tangent ray geometry of our grid yields approx. 150 angular grid points to resolve the radiation field from the central source which appears at an angular size of only $\Theta \approx 5^\circ$ ($\cos \Theta \approx 0.996$). These numbers have to be compared with calculations employing the discrete angles (S_N) method: In dynamical neutrino transport calculations, typically only 10 angular grid points can be afforded at most to cover the range $0 \leq \cos \Theta \leq 1$.

Although we have used a geometrical radial zoning for our tangent ray grid, we do not find any systematic effects caused by a “bias” in angular binning as claimed by Burrows et al. (2000). Far from a central source, they claim Eddington factors and flux factors that asymptote to between 0.96 and 0.98 instead of 1.0 in this case. For example we find values of $K/J = 0.996602$ and $H/J = 0.999361$ for the Eddington factor and the flux factor at $r = R_{\max}$ (in the model with $\tau = 4$), to be compared with $K/J = 0.996636$ and $H/J = 0.998626$ obtained from the analytical solution (eqns. 4.6–4.8).

For the mean intensity J we observe a systematic trend towards larger deviations from the true solution for spheres with larger total optical depth τ . In our “low opacity” case ($\tau = 4$, see Fig. 4.2a), there is hardly any difference visible whereas in the “high opacity” case ($\tau = 26$, see Fig. 4.2b) the numerical solution slightly overestimates the true solution in a small region beneath

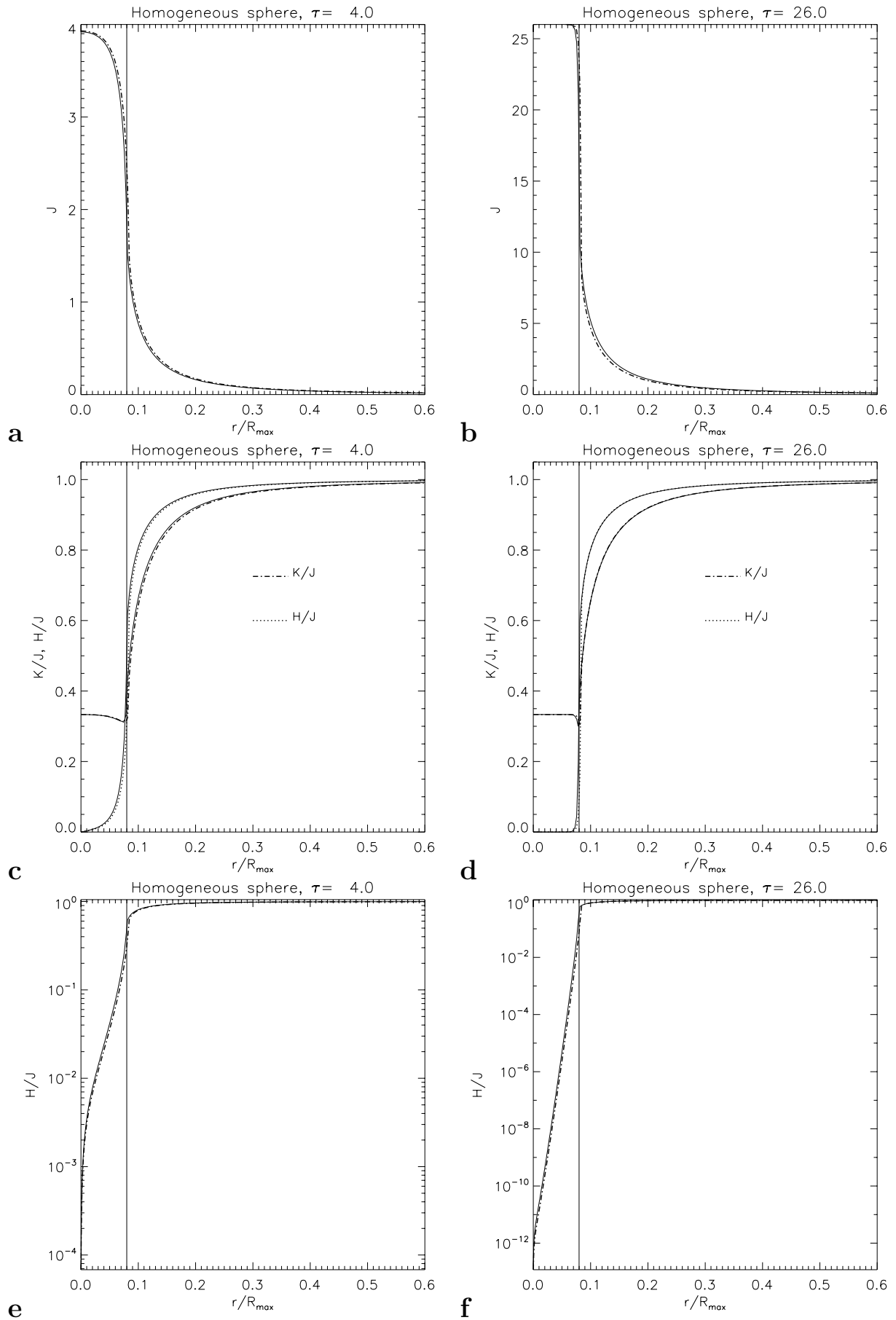


Figure 4.2: Numerical (bold dotted and dash-dotted lines) and analytic (thin solid lines) stationary state solutions vs. radius (normalized to the radius R_{\max} of the outer boundary) of homogeneous sphere problem with “low” ($\tau = 4$, left column, panels **a**, **c**, **e**) and “high” opacity ($\tau = 26$, right column, panels **b**, **d**, **f**). Panels **a** and **b** show the zeroth moment of the specific intensity. In panels **c** and **d** the Eddington factor K/J (dotted) and the flux factor H/J (dash-dotted) are displayed. The latter quantity is shown in panels **e** and **f** on a logarithmic scale. The thin vertical line marks the surface R of the homogeneous sphere.

the surface of the sphere and underestimates it in the ambient vacuum region. The effect is more pronounced for even larger values of the optical depth.

The reason for this is the opacity jump bounding the radiating sphere from the vacuum, which, provided the opacity inside is large, accounts for an almost sudden transition from the opaque interior of the sphere to transparency outside when the surface of the sphere is approached. This transition to transparency, described by the decrease in the optical depth (here: $\tau(r) = \kappa_a (R - r)$, if $r < R$; $\tau(r) = 0$, elsewhere) from $\tau \gtrsim 1$ to $\tau = 0$ occurs in a boundary layer which is located beneath the surface of the sphere. In our “high opacity” case, this layer is geometrically much more thin compared to the “low opacity” case and thus the resulting larger radial gradients of the radiation field are numerically less well resolved (we use the same radial grid in both cases). In fact, in the “low opacity” case a number radial zones each of which is optically thin ($\Delta\tau \approx 0.15$) are able to properly resolve the transition from $\tau \gtrsim 1$ to $\tau = 0$, whereas in the “high opacity” case this occurs within a single zone of the numerical grid ($\Delta\tau \approx 2.3$) and hence cannot be modeled correctly. This explains the better quality of the numerical results for the less opaque spheres. The problem is suspected to be common to all finite difference methods. It might be partly overcome by using a higher spatial resolution in the vicinity of large opacity or emissivity jumps and/or higher-order difference schemes.

Since due to the absence of scattering, the solution of the homogeneous sphere problem is already given by the formal solution of the Boltzmann equation, the model allows us to test the algorithm for solving the Boltzmann equation independently from the numerical solution of the moment equations. Because no information from the solution of the moment equations is required for solving the Boltzmann equation, no iteration between both parts is necessary. For the stationary state solution we find that the moments obtained by numerical integration of the intensities as computed by the Boltzmann solver are consistent with the moments directly computed by the moment equations to within an accuracy of less than a percent.

4.1.3 Static scattering atmospheres

Hummer & Rybicki (1971) have published stationary state solutions for the spherical analogue of the classical Milne problem. The model comprises a static, spherically symmetric, pure scattering atmosphere of some radius R_{\max} , with a central point source that is emitting radiation with a constant luminosity L_0 . Due to the presence of scattering, the problem defies solution by simply computing the formal solution of the Boltzmann equation.

Model

The opacity of the atmosphere is assumed to be solely due to isotropic scattering with a simple power-law dependence on radius¹:

$$\chi(t, r) \equiv \kappa_s(r) = r^{-n}, \quad 0 < r \leq R_{\max}, \quad (n > 1). \quad (4.9)$$

The emissivity vanishes within the atmosphere ($\eta \equiv 0$) and no radiation is entering from outside ($\mathcal{I}(t, R_{\max}, \mu) = 0$, for $-1 \leq \mu < 0$).

For a number of atmospheres defined by various combinations of the parameters $n \in \{1.5, 2, 3\}$, $R_{\max} = 0.1 \dots 100$ and $L_0 = (4\pi)^2$, Hummer & Rybicki (1971) have computed numerically the

¹By a redefinition of the unit of length we have set the scale factor $\alpha > 0$ which is present in the original form $\kappa_s(r, t) = \alpha r^{-n}$ to unity (cf. Hummer & Rybicki 1971, Equ. 1.1).

zeroth moment J and the Eddington factor K/J of the stationary state solution as a function of radius. They claim values of less than a percent for the accuracy of these results. The stationary state solution for the first moment H as a function of radius can easily be obtained analytically from the zeroth order moment equation (2.24):

$$H(r) = \frac{L_0}{(4\pi)^2} \frac{1}{r^2}. \quad (4.10)$$

This means that the luminosity is conserved ($L(r) := 4\pi r^2 \cdot 4\pi H(r) = L_0$). Hummer & Rybicki (1971) also give useful asymptotic expressions applicable to regions of very low and very high optical depth, respectively.

Results

The idealized concept of a central point source with given luminosity L_0 is in practice modeled by imposing a suitable inner boundary condition at some finite radius R_{\min} which bounds the atmosphere from below. Since all atmospheres with a scattering opacity according to Equ. (4.9) become optically thick at sufficiently small radius, it is reasonable to employ a diffusion ansatz for the radiation field at the inner boundary:

$$\mathcal{I}(t, R_{\min}, \mu) = \mathcal{I}_0 + \mu \mathcal{I}_1. \quad (4.11)$$

In our program, only the quantity

$$h(t, R_{\min}, \mu) := \frac{1}{2} (\mathcal{I}(t, R_{\min}, \mu) - \mathcal{I}(t, R_{\min}, -\mu)) = \mu \mathcal{I}_1 \quad (4.12)$$

needs to be specified. Using equ. (4.10), and $H = \int_0^1 d\mu \mu h$ (cf. equ. 3.44) the parameter \mathcal{I}_1 is easily verified to be $\mathcal{I}_1 = 3H(R_{\min}) = 3L_0/(4\pi R_{\min})^2$.

We have computed stationary state solutions for the two sets of parameter combinations

- $n = 1.5$, $R_{\min} = 0.001$, $R_{\max} \in \{0.1, 1, 10, 100\}$, and
- $n = 2$, $R_{\min} = 0.01$, $R_{\max} \in \{0.1, 1, 10, 20\}$.

The total optical depth reached at $r = R_{\min}$ is larger than 55 for all of the models of the former class ($n = 1.5$) and larger than 90 for all of the models with $n = 2$. Hence, the inner boundary is placed at a radius which is sufficiently small to justify the usage of the boundary condition (4.11).

In the ($n = 1.5$)-models the standard radial grid consisted of 200 logarithmically distributed zones with some extra resolution near the surface of the atmosphere, whereas we have used 250 equidistant radial zones for the ($n = 2$)-models. Additional tests with 500 radial grid points have been performed for some selected models. No significant changes in the results were observed. Figures 4.3a–c show a number of examples of our tests together with the results of Hummer & Rybicki (1971). The agreement is excellent. In all models we are able to recover the analytical solution given by equ. (4.10) to within a relative accuracy of at least 10^{-4} throughout the entire atmosphere.

In order to test the sensitivity of the results to the particular choice (equ. 4.11) adopted for the angular dependence of the specific intensity at the inner boundary, we have calculated a model assuming the “wrong” inner boundary condition

$$\mathcal{I}(t, R_{\min}, \mu) = \delta(\mu - 1) \cdot \mathcal{I}_{\text{in}} \quad (4.13)$$

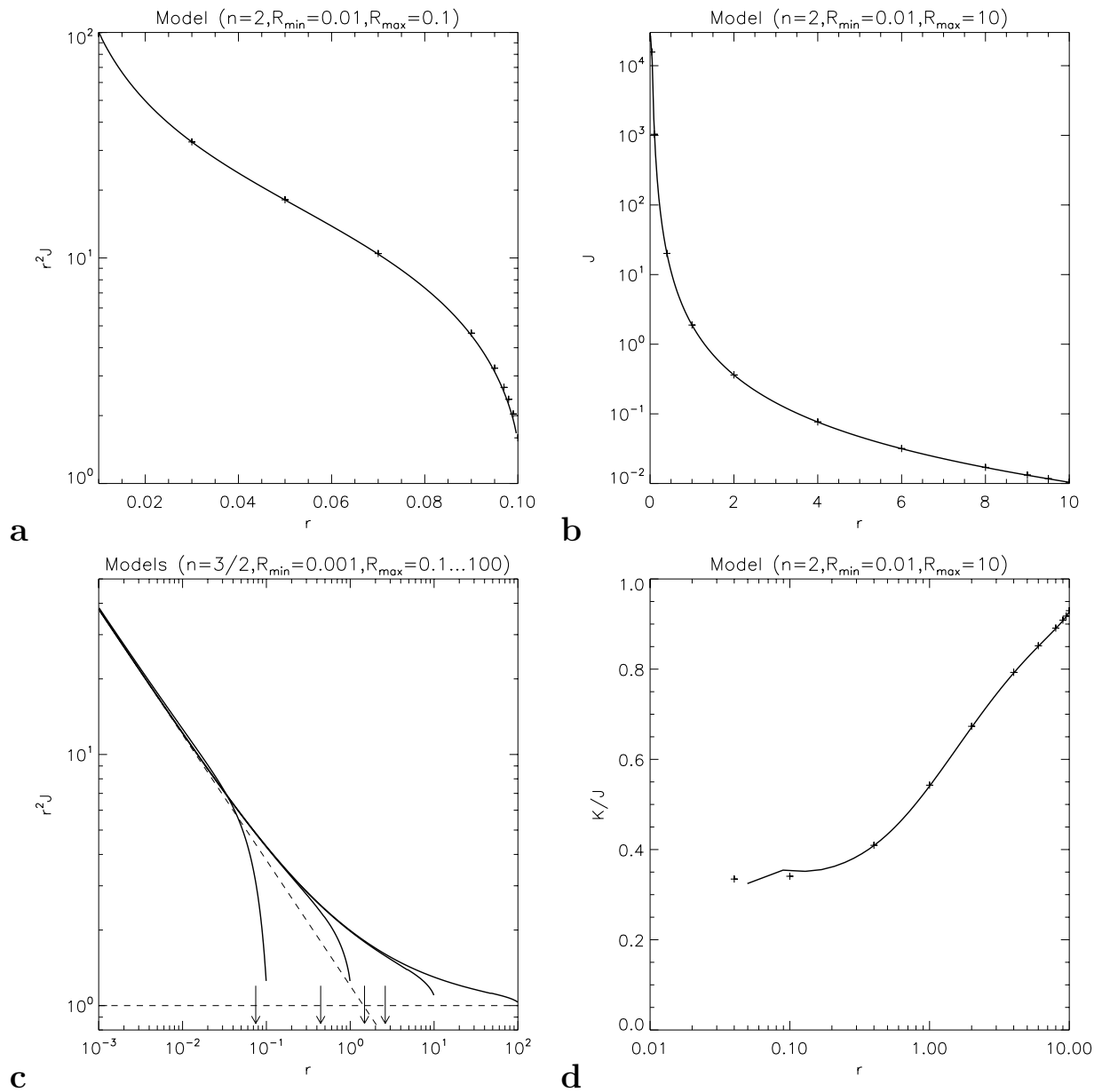


Figure 4.3: Stationary state solutions for selected radiation quantities as a function of radius obtained with our radiative transfer code (solid lines) compared to the reference solutions (crosses) and asymptotic solutions (dashed lines) of Hummer & Rybicki (1971). Panel **a**: mean intensity J (times r^2) for the combination of model parameters $(n = 2, R_{\min} = 0.01, R_{\max} = 0.1)$; Panel **b**: mean intensity J for $(n = 2, R_{\min} = 0.01, R_{\max} = 10)$; Panel **c**: $r^2 J$ for models with $(n = 3/2, R_{\min} = 0.001, R_{\max} \in \{0.1, 1, 10, 100\})$. The small arrows indicate the radial position, where $\tau = 1$ is reached in each atmosphere; Panel **d**: Eddington factor K/J for the model with the “wrong” inner boundary condition and the model parameters $(n = 2, R_{\min} = 0.01, R_{\max} = 10)$.

instead. The parameter \mathcal{I}_{in} is chosen such that $L(R_{\min}) = L_0$. This inner boundary condition would model a centrally “hollowed” atmosphere, which is irradiated from below by the central point source. Figure 4.3d shows the stationary state Eddington factor as a function of radius for

this model. The numerical solution notably deviates from the reference solution only within a few of the innermost radial zones. Note that already at the centre of the innermost zone of our numerical grid (at $r = 0.05$) the Eddington factor has dropped from the boundary value 1.0 to a value which is accurate to within less than 10 percent. It is the large opacity at small radii that immediately forces any radiation field entering from below to adopt an almost isotropic angular pattern which is consistent with the “true” inner boundary condition (equ. 4.11).

4.1.4 Radiative transfer in general relativity

Schinder & Bludman (1989) treated the previously discussed radiative transfer problems of the homogeneous sphere (Sect. 4.1.2) and the static scattering atmospheres (Sect. 4.1.3) in the presence of strong gravitational fields. They numerically computed stationary state solutions for the general relativistic equations of radiative transfer for a static background medium and compared the results to the weak field limit. On a static background ($\partial_t R = \partial_t \Lambda \equiv 0$), the general relativistic moment equations (2.41, 2.42) simplify to

$$\begin{aligned} \frac{1}{c} \frac{\partial}{\partial t} J + \frac{\Gamma}{R^2} \frac{\partial}{\partial R} (R^2 H e^\Phi) - \epsilon \Gamma \frac{\partial e^\Phi}{\partial R} \cdot \frac{\partial H}{\partial \epsilon} &= e^\Phi S^{(0)}, \\ \frac{1}{c} \frac{\partial}{\partial t} H + \frac{\Gamma}{R^2} \frac{\partial}{\partial R} (R^2 K e^\Phi) - \epsilon \Gamma \frac{\partial e^\Phi}{\partial R} \cdot \frac{\partial K}{\partial \epsilon} \\ + e^\Phi \Gamma \frac{K - J}{R} + \Gamma \frac{\partial e^\Phi}{\partial R} (J - K) &= -e^\Phi S^{(1)}. \end{aligned} \quad (4.14)$$

Following Schinder & Bludman (1989), we apply the following change of coordinates

$$(R, \epsilon) \mapsto (R, \epsilon_\infty := e^\Phi \epsilon), \quad (4.15)$$

which induces the transformation

$$\begin{aligned} \left. \frac{\partial}{\partial R} \right|_\epsilon &= \left. \frac{\partial}{\partial R} \right|_{\epsilon_\infty} + \epsilon \partial_R e^\Phi \cdot \left. \frac{\partial}{\partial \epsilon_\infty} \right|_R, \\ \left. \frac{\partial}{\partial \epsilon} \right|_R &= e^\Phi \cdot \left. \frac{\partial}{\partial \epsilon_\infty} \right|_R \end{aligned} \quad (4.16)$$

for the partial derivatives. The advantage of introducing the new coordinates is that the moment equations (4.14) simplify considerably since they decouple in energy space²:

$$\frac{1}{c} \partial_t J + \frac{\Gamma}{R^2} \frac{\partial}{\partial R} (R^2 H e^\Phi) = e^\Phi S^{(0)} \quad (4.17)$$

$$\frac{1}{c} \partial_t H + \frac{\Gamma}{R^2} \frac{\partial}{\partial R} (R^2 K e^\Phi) + e^\Phi \Gamma \frac{K - J}{R} + \Gamma \frac{\partial e^\Phi}{\partial R} (J - K) = -e^\Phi S^{(1)} \quad (4.18)$$

Hence, all radiation quantities depend only *parametrically* on ϵ_∞ .

²Even more importantly, the Boltzmann equation itself simplifies in the sense that it allows for constructing a tangent ray scheme which is of the same dimensionality as in the absence of general relativistic effects (cf. Schinder & Bludman 1989, §II b). Since the method used by Schinder & Bludman (1989) can only be applied in the special case of a *static background*, we have not attempted to implement a fully general relativistic tangent ray scheme based on the coordinate change (equ. 4.15).

Model

Here, we are mainly interested in the question what effect the physical approximations that necessarily enter our tangent ray scheme for computing the Eddington factor have on the stationary state solution of the general relativistic moment equations (which, in the static case can obviously be solved by our method without any additional approximations to the general form of these equations). Different from the general relativistic homogeneous sphere, Schinder & Bludman (1989) find for the scattering atmospheres significant deviations of the general relativistic Eddington factor from its values in the weak-field case. The scattering atmosphere thus appears to be an ideal test case for our purposes.

Following Schinder & Bludman (1989), we employ the parameters $R_{\max} = 10$ and $n = 2$. The variation of the metric functions e^Φ and Γ as a function of radius is depicted in Fig. 4.4a. All other model parameters like boundary conditions and initial conditions, etc. are the same as in the “weak-field”-case (see Sect. 4.1.3). As we have already mentioned, we have made no attempt to adjust our tangent ray scheme for calculating the Eddington factor to the properties of the present problem, i. e. as usual the characteristics are assumed to be straight rays. Gravitational redshift and ray bending are not included in this part of the algorithm. The only general relativistic effects that are accounted for in the formal solution of the Boltzmann equation are the contraction of rods and the gravitational time dilation.

Results

The stationary state Eddington factor as computed by our program is displayed as a function of radius in Fig. 4.4c. Comparing our result to the corresponding “weak-field” case ($e^\Phi = \Gamma \equiv 1$) we find differences of the order of only a few percent (the “weak-field” case is not plotted in Fig. 4.4c !), which indicates that the contraction of rods and time dilation, which are the only general relativistic effects implemented in our tangent ray scheme, are of minor importance for the Eddington factor. Most of the differences relative to the relativistically correct results (diamonds in Fig. 4.4c), must therefore be attributed to general relativistic ray bending and, less important, gravitational redshift, which are not correctly accounted for in our calculations. The deviation of the characteristic curves from straight rays is indeed significant, as can be seen from Schinder & Bludman (1989, Fig. 9).

The analytical stationary-state solution for the radiation flux density, which is easily verified³ to read $R^2 e^\Phi H(R, \epsilon_\infty) = C(\epsilon_\infty)$, (with $C(\epsilon_\infty) \in \mathbb{R}$), is reproduced to within an accuracy of 10^{-7} . This, of course, was to be expected for the scattering atmosphere, since in the stationary state, the solution $H(r)$ is solely determined by the zeroth moment equation (4.17), with no reference to the (incorrect) Eddington factor.

More remarkably, the quality of our solution for the mean intensity $J(r)$, whose governing equation in the stationary state (equ. 4.18) is directly influenced by the Eddington factor, appears to be rather good. As can be seen from Fig. 4.4b, the trends set by general relativity are reproduced correctly throughout the entire atmosphere. The quantitative agreement appears to be quite satisfactory as well. In judging the accuracy of our results one has to keep in mind that the model computed here is a rather extreme case in two respects: Firstly, the deviations of the metric functions e^Φ and Γ from unity (see Fig. 4.4a) are much larger than those encountered in supernova

³Note that the more familiar result $R^2 e^{2\Phi} H(R) = \text{const.}$ only holds for the total (i. e. energy integrated) “flux density” $H(R) := \int H(R, \epsilon) d\epsilon = e^{-\Phi} \int H(R, \epsilon_\infty) d\epsilon_\infty$.

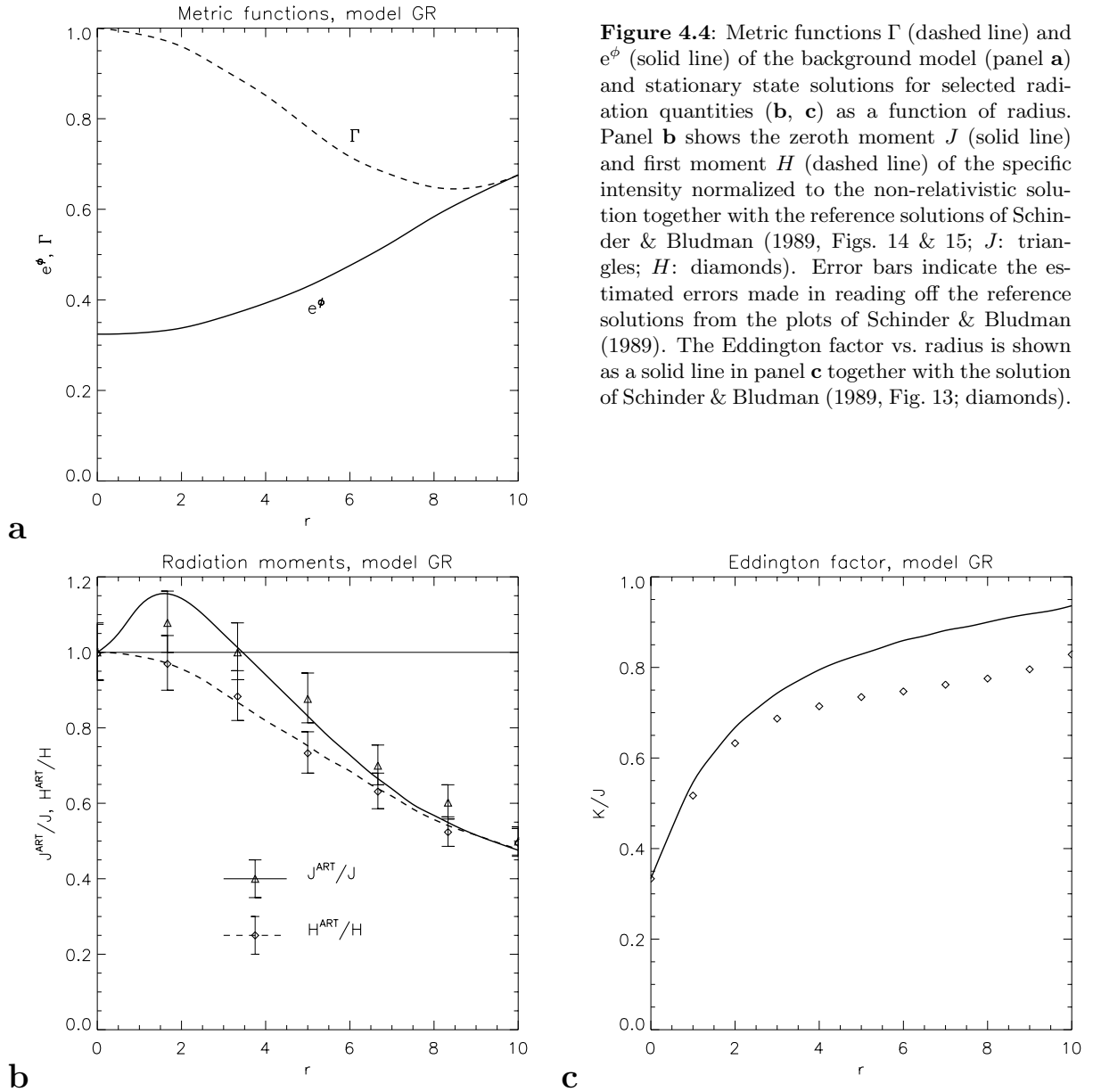


Figure 4.4: Metric functions Γ (dashed line) and e^ϕ (solid line) of the background model (panel **a**) and stationary state solutions for selected radiation quantities (**b**, **c**) as a function of radius. Panel **b** shows the zeroth moment J (solid line) and first moment H (dashed line) of the specific intensity normalized to the non-relativistic solution together with the reference solutions of Schinder & Bludman (1989, Figs. 14 & 15; J : triangles; H : diamonds). Error bars indicate the estimated errors made in reading off the reference solutions from the plots of Schinder & Bludman (1989). The Eddington factor vs. radius is shown as a solid line in panel **c** together with the solution of Schinder & Bludman (1989, Fig. 13; diamonds).

simulations. Typically, the maximum deviation from unity amounts to only 0.2 for both e^ϕ and Γ . Secondly, as stated in the beginning, the effect of a non-flat spacetime on the radiation field was observed by Schinder & Bludman (1989) to be much larger for the purely scattering model discussed here than in the purely absorbing case. In real applications we expect to meet situations that are somewhere inbetween these two extremes.

4.2 Radiative transfer in stationary background media

In this section we consider radiative transfer problems in moving, yet stationary background media, which means that in addition to time-independent radial profiles of the opacity and emissivity, a time-independent velocity field as a function of radius is prescribed. Stationary-state solutions for the radiation field are expected to exist in such cases and have been computed to high accuracy for some test problems including differentially moving relativistic atmospheres. By comparison with relativistic calculations, we are not only able to test our implementation of the velocity dependent terms but also judge the quality of the employed $\mathcal{O}(v/c)$ -approximation of special relativistic effects in the equations of radiative transfer. Upon introducing a non-vanishing velocity field a particular frame has to be specified, where physical quantities are measured. In all cases considered in this work, the latter is chosen to be the Lagrangian or comoving *frame of reference*. This has to be distinguished from the (numerical) *coordinate grid* that is used to simply label the events in spacetime (cf. Sect. 2.1.2). Although the transformation between different coordinate grids is trivial from an analytic point of view (e. g. the simple replacement $\partial/\partial t + v\partial/\partial r \rightarrow D/Dt$ transforms from Eulerian to Lagrangian coordinates), the numerical treatment can be involved (cf. our algorithm for computing a formal solution of the radiative transfer equation in Eulerian coordinates, Sect. 3.2.3). Therefore we present test results obtained with two different versions of our radiative-transfer code, one which uses Lagrangian coordinates and another which employs a Eulerian coordinate grid.

4.2.1 Differentially expanding gray scattering atmospheres

Mihalas (1980) has published stationary-state solutions for the same type of purely scattering atmospheres as introduced in the previous sections. In addition to the static case, a number of model atmospheres expanding differentially with relativistic velocities were considered.

Model

According to the functional form of the dependence of the expansion velocity ($v \equiv c\beta$) on radius

$$\beta(r) = \beta_{\max} \left(\frac{r - r_{\min}}{r_{\max} - r_{\min}} \right)^m, \quad \text{with } m \in \{1, 2\}, \quad (4.19)$$

two classes of atmospheres are studied as test problems. The case $m = 1$ is referred to as the “linear velocity law”, the case $m = 2$ is called “quadratic velocity law”. Different models are labeled by the parameter $0 \leq \beta_{\max} < 1$, which is the maximum expansion velocity in units of c reached at the surface of the atmosphere ($r = r_{\max}$).

The scattering opacity of the expanding atmospheres is the same as for the static scattering atmospheres discussed previously in Section 4.1.3 except for the unit of length, which, for the ease of comparison, is here chosen identical to the work of Mihalas (1980). The latter investigation employs

$$\chi(t, r, \epsilon) \equiv \kappa_s(r) = \alpha r^{-2}, \quad r_{\min} \leq r \leq r_{\max} \quad (4.20)$$

and uses the parameters $r_{\min} = 1$, $r_{\max} = 11$ and $\alpha = 10.989$, which correspond to the atmosphere with $r_{\max} = 1$ in the units of Hummer & Rybicki (1971) who use $\alpha = 1$. According to equ. (4.20), an optical depth of unity is reached at a radius of $r \approx 5.5$. Since the opacity does not depend on the frequency of the radiation, the atmospheres are referred to as “gray”. In this case, the $\partial/\partial\epsilon$ -terms appearing in the comoving-frame Boltzmann equation vanish.

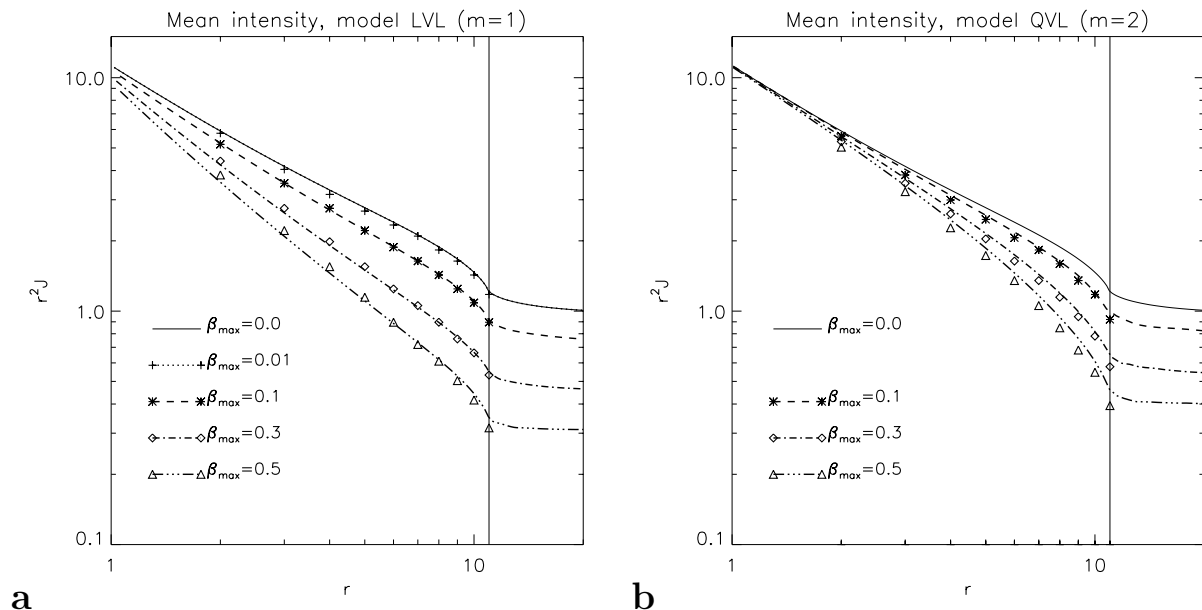


Figure 4.5: Stationary-state angular mean J (times r^2) of the specific intensity as measured in the comoving frame of reference as a function of radius for the gray scattering atmospheres expanding according to the linear (model “LVL”; panel **a**) and the quadratic (model “QVL”; panel **b**) velocity law (solid lines). The thin vertical line marks the upper boundary of the atmospheres. Different line styles of the curves correspond to the parameter β_{\max} which gives the maximum expansion velocity in units of c reached at the surface ($r = 11$) of a model atmosphere. The thin solid curve corresponds to the static case. Reference solutions (symbols) are taken from Mihalas (1980, Fig. 2).

Results

For our simulations we use a numerical grid with 200 radial points, which were initially distributed logarithmically between r_{\min} and r_{\max} . Following Mihalas (1980) as closely as possible we impose the boundary conditions

$$\begin{aligned} \mathcal{I}(t, r_{\min}, \mu) &= 11 + 3\mu, & 0 \leq \mu \leq 1 \\ \mathcal{I}(t, R(t), \mu) &= 0, & -1 \leq \mu \leq 0, \quad R(t) = r_{\max} + \beta_{\max} ct \end{aligned} \quad (4.21)$$

to mimic radiation from a central point source with a luminosity $L_0 = (4\pi)^2$ irradiating the atmosphere. No radiation is entering at $r = r_{\max}$ from outside. As an initial condition ($t = 0$) we used the stationary state solution of the corresponding static atmosphere (see Sect. 4.1.3). The examples presented here were obtained using a Lagrangian coordinate grid⁴. Our calculations were terminated when the radiation field (as measured in the comoving frame of reference) showed no more substantial temporal variations at any given radial position. We refer to our results as “stationary-state solutions” in this sense. We have also tested the Eulerian grid version of the code with a less extensive set of models. The results are practically identical.

We compare our stationary-state solutions with results obtained by Mihalas (1980). In the latter investigation a numerical method for solving the stationary radiative transfer equation that is accurate to all orders in v/c was used. We therefore do not only test the correct numerical

⁴Grid points leaving the atmosphere at r_{\max} into “vacuum” were given the velocity $\beta = \beta_{\max}$ and the opacity $\chi = 0$.

implementation of the $\mathcal{O}(v/c)$ equations (2.35, 2.36, 2.37), but we can also get a handle on the quality of the $\mathcal{O}(v/c)$ -approximation to the special relativistic transfer equation.

We first briefly state some of the general features of the solutions as discussed in detail by Mihalas (1980): At any given radius, the value of J , which is proportional to the radiation energy density measured by a comoving observer, decreases with increasing expansion velocity (cf. Fig. 4.5). This is understood physically in terms of the effects of the redshift and a smaller rate of arrival (relativistic time dilation) of photons emitted by a rapidly receding source. This trend is more pronounced for the linear velocity law, since, for the same surface velocity β_{\max} it accounts for larger velocities deeper inside the atmosphere as compared to the quadratic velocity law. Thus, the aforementioned effects begin to occur deeper inside and therefore manifest themselves more strongly throughout the entire atmosphere. For the same value of β_{\max} , the curves for the linear velocity law thus eventually fall below the solutions obtained with the quadratic velocity law as one moves towards the outer boundary of the model envelope.

As can be seen from Fig. 4.5, all general trends stated above are reproduced correctly by our implementation of the $\mathcal{O}(v/c)$ equations. The accuracy to which the fully relativistic solutions are recovered even for $\beta_{\max} = 0.5$ is remarkable.

4.2.2 Differentially expanding nongray isothermal atmospheres

Mihalas (1980) has computed stationary state solutions also for relativistically expanding *nongray* atmospheres, i. e. the opacity (and emissivity) depend explicitly on the radiation frequency and the full frequency dependence of the comoving frame Boltzmann equation has to be retained. The atmospheres were assumed to be stationary, isothermal and emit a purely thermal continuum of radiation, i. e. no radial or temporal variations of the source function are present and the opacity is solely due to absorption and emission.

Model

Introducing the dimensionless frequency $\xi = \epsilon/T$ (the temperature T is measured in units of the Boltzmann constant k_B , the emissivity reads

$$\eta(\xi) = \kappa_a(\xi) b(\xi) = \kappa_a(\xi) \frac{\xi^3}{\exp(\xi) - 1}. \quad (4.22)$$

The absorption opacity $\chi = \kappa_a$ was given a step-like functional dependence on frequency, characterized by the frequency ξ_0 where the step is located and some characteristic width Δ which accounts for a continuous variation of κ_a across the step:

$$\chi(r, \xi) \equiv \kappa_a(r, \xi) = \begin{cases} \chi_1(r) \exp[-(\xi - \xi_0)^2/\Delta^2] + \chi_2(r) (1 - \exp[-(\xi - \xi_0)^2/\Delta^2]), & \text{for } \xi \leq \xi_0, \\ \chi_1(r), & \text{for } \xi > \xi_0, \end{cases} \quad (4.23)$$

with

$$\chi_1(r) := \frac{10\alpha}{r^2} \quad \text{and} \quad \chi_2(r) := \frac{\alpha}{r^2}, \quad \alpha := 10.9989. \quad (4.24)$$

Thus, the optical depth at a given radius is about 10 times smaller for “low-frequency” radiation ($\xi < \xi_0$) as compared to radiation with “high” frequency ($\xi > \xi_0$). Following Mihalas (1980), we consider the two examples:

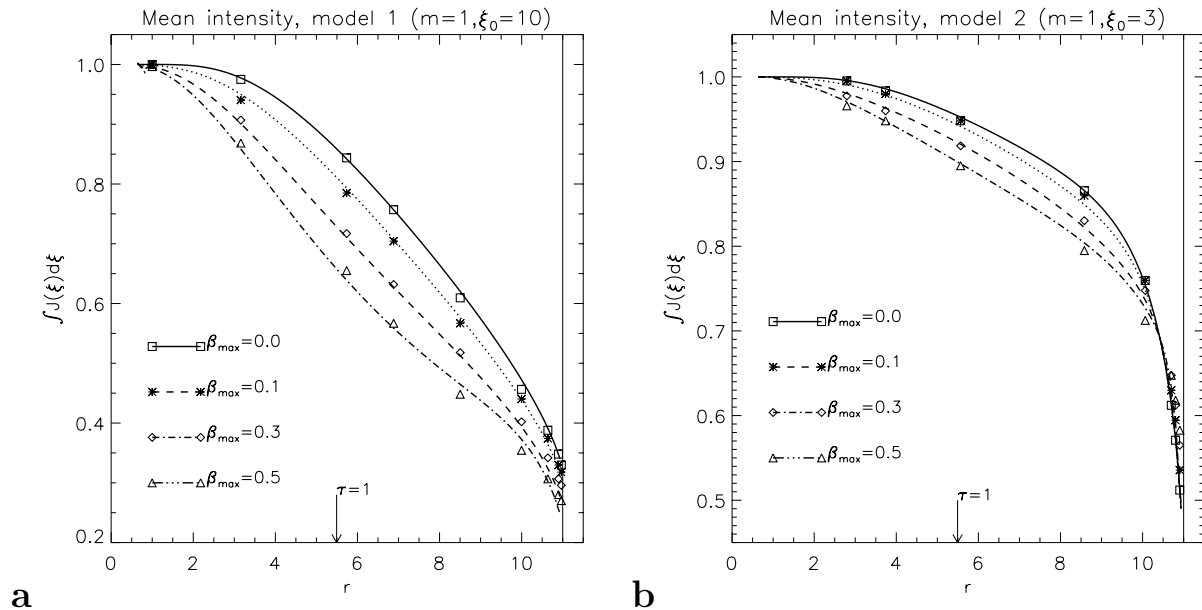


Figure 4.6: Frequency integrated angular mean of the comoving frame intensity ($\int_0^\infty d\xi J(\xi)$) as a function of radius for our $\mathcal{O}(v/c)$ stationary state solutions (lines). The thin vertical line marks the upper boundary of the atmospheres. Short arrows point to the position where an optical depth (which is calculated for $\xi < \xi_0$) of unity is reached. Reference solutions (symbols) obtained with a fully relativistic code have been taken from Mihalas (1980, Figs. 3 and 5), where the read-off error is approximately given by the size of the symbols. The maximum velocity β_{\max} of each atmosphere is indicated by different line styles and symbols, respectively. In panel **a** results for model (1) with the opacity step located at $\xi_0 = 10$ ($\Delta = 0.25$) are depicted. Panel **b** shows results for model (2) with $\xi_0 = 3$ ($\Delta = 0.2$).

(1) $\xi_0 = 10$, $\Delta = 0.25$,

(2) $\xi_0 = 3$, $\Delta = 0.2$.

In the former case the frequency ξ_0 , where the opacity jump is located, is considerably larger than the frequency of the maximum of the Planck function ($\xi_{\max} = 2.82$), whereas it is very close to the maximum in the latter case.

The radial extent of the atmospheres was chosen to be $0 \leq r \leq 11$ in both cases. For all models the “linear velocity law” ($m = 1$, cf. equ. 4.19) for prescribing the expansion velocity as a function of radius was used. The results presented below were obtained using a Eulerian coordinate grid. Very similar results hold for the version which employs a Lagrangian grid.

Results

We have used 200 logarithmically distributed radial zones for the radial range $1 \leq r \leq 11$, supplemented by a few additional zones⁵ which were distributed between $0 \leq r < 1$. Boundary conditions were chosen as usual: Spherical symmetry at the origin of coordinates requires

⁵These zones were not present in the calculations of Mihalas (1980). However, due to a sufficiently high optical depth at $r \lesssim 1$ for all frequencies, the additional “boundary zones” (we set their velocity to zero) do not influence the radiation field at $r > 1$.

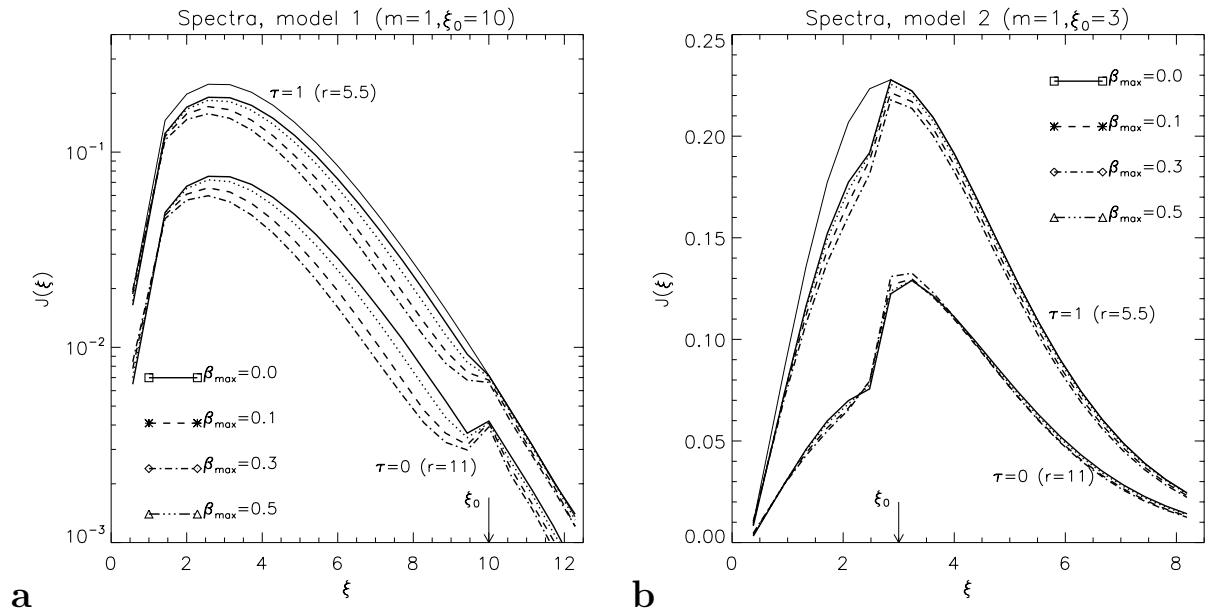


Figure 4.7: Spectral distribution of the angular mean J of the comoving frame intensity for our stationary state solutions of the $\mathcal{O}(v/c)$ radiative transfer equation (bold lines). Spectra are displayed for the radial positions corresponding to an optical depth (which is calculated for $\xi < \xi_0$) of unity and for the surface of the atmosphere. For comparison, the equilibrium intensity (Planck function) at an optical depth of unity is plotted as a thin line. The maximum velocity (β_{\max}) of each expanding atmosphere is indicated by different line styles. Panel **a** shows results for model (1), where the opacity step (short arrow in the plots) is located at $\xi_0 = 10$ ($\Delta = 0.25$). Panel **b** shows model (2) with $\xi_0 = 3$ ($\Delta = 0.2$). Our results may be compared to Mihalas (1980, Figs. 4 and 6).

$\mathcal{I}(t, r = 0, \mu = 1) = \mathcal{I}(t, r = 0, \mu = -1)$, and demanding that no radiation is entering through the surface of the envelopes translates to the condition $\mathcal{I}(t, r = 11, \mu \leq 0) = 0$.

The energy grid consisted of 21 bins (very similar results have been obtained using 8 and 12 bins, instead) of equal width covering the range $0 \leq \xi \leq 12$ for model (1) and $0 \leq \xi \leq 8$ for model (2), respectively.

Details about the stationary-state solutions and their physical interpretation can be found in Mihalas (1980, §IV). We again briefly summarize some of the main results (cf. Mihalas 1980, Figs. 3–6). For model (1), profiles of the total (i.e. spectrally integrated) mean intensity depend on the surface expansion velocities in a way that is very similar to the gray case discussed in the previous section, whereas model (2) shows a significantly different behaviour in this respect. This can be understood by noting that for model (1) the opacity as a function of frequency is constant throughout the major part of the emission spectrum and hence the envelope can be regarded as effectively gray. The monotonic decrease of the integrated mean intensity with increasing velocity (cf. Mihalas 1980, Fig. 3) can therefore be explained by the same arguments that were given for the gray case before. Inspection of the spectral distribution of the mean intensity confirms this interpretation (Mihalas 1980, Fig. 4).

For model (2) on the other hand, the opacity jump is located close to the spectral maximum of the Planck function and therefore effects due to the spectral variation of the opacity have to be included in the analysis. Nevertheless, since the inner parts of the envelope are opaque for photons of all frequencies, one observes the same trends for the mean intensity as a function of

expansion velocity there as noted for the effectively gray model (1). Approaching the surface, the envelope becomes optically thin first to the “low frequency” part of the spectrum, i. e. radiation with frequency $\xi < \xi_0$. Radiation in this part of the spectrum consequently decouples from local conditions at greater distance from the surface and therefore gets radially more diluted than does high-frequency radiation. Since in model (2), the “low frequency”-part ($\xi < \xi_0$) of the emission spectrum (cf. equ. 4.22), contains significantly less contribution to the total intensity as compared to model (1), the frequency integrated mean intensity at the surface is larger in model (2) than it is in model (1). When expansion is allowed radiation of any given frequency received by the observer at the surface had a higher frequency in the local rest frame of the medium further inside. Thus on its way towards the surface a larger fraction of the radiation remains within the spectral range exposed to high opacity, as compared to the static case. In effect, the opacity step has been redshifted. Therefore the coupling of the radiation to the background medium is more efficient for larger expansion velocities and, as a consequence, the mean intensity at the surface is enhanced (cf. Mihalas 1980, Figs. 5, 6). In both expanding models one notices that the influence of the sharp opacity jump on the spectra becomes superposed by redshift effects.

In our test calculations we are able to reproduce all qualitative trends found by Mihalas (1980). The quantitative agreement for the zeroth angular moment J of the specific intensity is within the order of a few percent (see Fig. 4.6), even for the case of $\beta_{\max} = 0.5$. This, as previously stated, does not only prove the accuracy of our numerical implementation, but even more importantly also justifies the physical approximations inherent to the underlying finite difference equations. Note that in applications of our code to supernova calculations, one expects velocities that are not in excess of $v \approx 0.2c$.

A rigorous comparison of the spectral distribution of the angular mean J of the intensity as calculated by our radiative transfer code (cf. Fig. 4.7) with the results of Mihalas (1980) is difficult, since he shows only results for the static case and the rather extreme case $\beta_{\max} = 0.8$. The latter atmosphere obviously cannot be modeled reasonably with our $\mathcal{O}(\beta)$ -code. Nevertheless, by inspection of Figs. 3 and 4 of Mihalas (1980) one can infer that a continuous and monotonic trend with increasing expansion velocity exists which maps the ($\beta_{\max} = 0$)-spectrum into the ($\beta_{\max} = 0.8$)-spectrum. Under this assumption we can claim that the shapes of our spectra as displayed in Fig. 4.7a show the correct dependence on the expansion velocity. The assumption of a monotonic trend is somewhat more questionable for model (2) (cf. Mihalas 1980, Figs. 5, 6), but it appears to be present at least within the range $0 \leq \beta_{\max} \lesssim 0.3$. This trend is seen for our spectra (cf. Fig. 4.7b).

4.2.3 Frame dependence

Problem

We have formulated and discretized the equations of radiative transfer in the comoving frame of reference, mainly for the reason that the interaction of radiation with matter is treated most easily in this local rest frame of the material. When transformed e. g. to the Eulerian frame, the interaction terms appearing on the right hand side of the transfer equation can get painfully complicated when both frames are connected by a non-uniform velocity field. However, the Eulerian frame is an inertial frame of reference and thus the left hand side of the transfer equation attains its most simple form, since the velocity field does not appear. For this reason, the comoving frame approach may be criticized, since in the absence of interaction between radiation and matter, the dependence of the solution on the velocity field might be “misleading, since it is solely a result of

choosing a moving reference frame” (Lowrie et al. 1999).

From a physical point of view we do not consider these points to be in favour of any of the approaches, since all physical quantities, once *calculated correctly*, can be transformed between different frames by application of appropriate Lorentz transformations. Yet we have to demonstrate that our particular numerical implementation of the comoving frame equations indeed shows the correct transformation properties (to order $\mathcal{O}(v/c)$). Potential sources for unphysical artifacts caused by the choice of a moving reference frame might be the omission of $\mathcal{O}(v/c)$ -terms in the model Boltzmann equation (3.31) as well as errors due to the discretization of the equations.

Results

We show results taken from a neutrino transport calculation using a thermally and hydrodynamically frozen post-bounce model of the supernova calculation by Bruenn (1993). The background model is characterized as some hot and dense inner core at rest with a radius of $r \approx 110$ km, where the neutrinos are tightly coupled to the medium and thus are distributed according to local thermodynamical conditions. This inner core is surrounded by a differentially contracting outer atmosphere, which is nearly transparent to the radiation. Velocities in the outer atmosphere range from $v(r = 140\text{km}) \approx -0.12c$ to $v(r = 250\text{km}) \approx -0.08c$.

Figure 4.8 shows the components E and F of the stress-energy tensor (scaled by $r^2 c$). Due to the large inwardly directed velocities in the outer atmosphere, the radiation emanating from the inner source is received blueshifted by the observers which are locally comoving with the atmospheric flow-field (see the bold lines in Fig. 4.8). When the stress-energy tensor is transformed to the Eulerian frame, this effect obviously disappears (thin lines in Fig. 4.8). Comparing this to the stress-energy tensor that has been obtained by solving the transport equations in the Eulerian frame directly (dashed lines in Fig. 4.8), good agreement is found both for the energy and the flux density in the moving atmosphere, which demonstrates that no unphysical frame dependence is present.

Figure 4.8 contains an interesting side-result: In our Eulerian frame (“reference”)-calculation, we have simply ignored all velocity-dependent terms and have in effect solved the radiative transfer equation for static media (cf. equ. 2.23). By ignoring the velocity dependent transformation of the source terms one however does in general *not* solve a truly Eulerian (nor a Lagrangian) transfer equation⁶, even if the velocities are very small compared to the speed of light (cf. Mihalas & Mihalas 1984). This is illustrated by Fig. 4.8b, where in the inner core of the star ($r \lesssim 100$ km) one notices significant deviations of the flux obtained from the incorrect transport equation for static media from the true Eulerian flux F^{Eul} (which according to equ. (2.38) is the sum of the diffusive flux F and the advected flux $v(E + P)$), although matter is nearly at rest, there. This is due to the fact that at great optical depth, where $E \gg F/c$ and $P \gg F/c$, the advected flux $v(E + P)$ is of considerable magnitude compared to F , even if $v \ll c$. One also notices from Figure 4.8 that in the opaque interior, the true *comoving frame* flux (and radiation energy density) are well reproduced by ignoring all velocity dependent terms in the radiation moment equations. If, and only if the radiation flux and energy density obtained from such a static transfer calculation are interpreted as comoving frame quantities they may be used together with a total energy equation in the form of equ. (2.62) in the optically thick regime (cf. Sect. 2.3.2). Also in the transparent regime, the true

⁶This does not affect the arguments given above, since in the outer parts of the core, where we have assumed our “reference” calculation to be truly Eulerian, the opacities and emissivities are extremely small and therefore their transformation can be safely neglected.

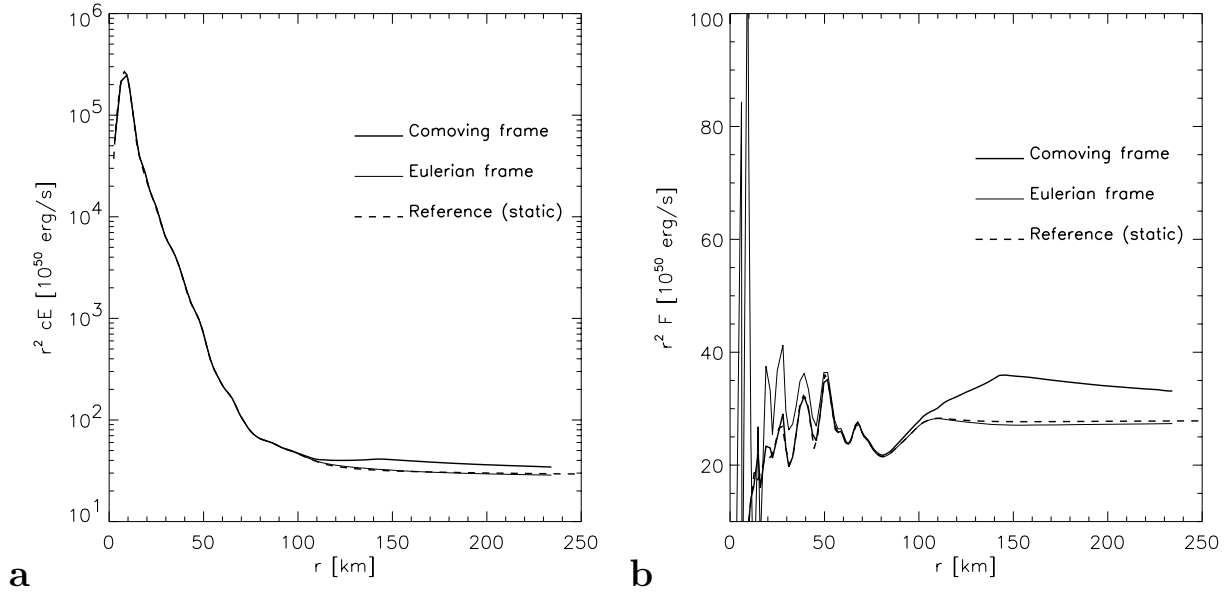


Figure 4.8: Comparison of the stationary state solutions of the comoving frame transfer equations (bold lines) after being transformed to the Eulerian frame (thin lines) with a reference calculation performed in the Eulerian frame from the beginning (dashed lines). Panel **a** shows the total energy density of neutrinos (times $r^2 c$), panel **b** displays the total energy flux density (times r^2).

comoving frame flux would be obtained by a static calculation if the velocities were small compared to c . However, according to the analysis given in Sect. 2.3.2, using equ. (2.62) in the optically thin regime would give incorrect results, provided the radiation pressure was a substantial fraction of the gas pressure. This once more underlines the necessity to carefully distinguish between different frames of reference in radiative transfer calculations.

4.3 Concluding remarks

In this chapter we have discussed applications of our newly developed radiative transfer code to a number of idealized test problems. The first class of problems encompassing a variety of static model atmospheres served to demonstrate that the angular part of the phase-space dependence of the distribution function can be handled with excellent accuracy by the variable Eddington factor method. Also the remaining phase-space coordinate, namely radiation frequency, is accounted for appropriately as was demonstrated by a second class of tests involving (mildly relativistically) moving, yet stationary model atmospheres. Two kinds of approximations that enter our equations could be justified empirically: First we employ an $\mathcal{O}(v/c)$ -approximation to the special relativistic, comoving frame radiative transfer equation. For our purposes this approximation has proven to give accurate and physically consistent results. Second, omitting some of the velocity dependent terms for determining the Eddington factor turned out not to be harmful to the overall accuracy with which the system of radiation moment equations is solved.

At the same time, the method works very efficiently. Only a few iterations (typically 1–5) between the formal solution of the Boltzmann equation and the system of moment equations,

which is of reduced dimensionality compared to the Boltzmann equation, are necessary to achieve convergence. Computing the formal solution in order to obtain an accurate Eddington factor requires only about 10%–20% of the total computer time.

Chapter 5

Stellar Core Collapse and the Supernova Explosion Mechanism

In the following we employ our newly developed neutrino-radiation hydrodynamics method to study the gravitational collapse of stellar iron cores and address the neutrino-mediated “delayed” explosion mechanism of Type II supernovae. We focus on the particular role of neutrino transport, which is known to be of crucial importance, especially for the delayed mechanism, but has not been treated in a satisfactory manner yet. Although known to be important for the explosion, we will not consider multi-dimensional processes such as convection. All models presented in this chapter will assume the star to be spherically symmetric. We do also not take into account modifications of the “standard” microphysics (i. e. the thermodynamic equation of state and neutrino opacities) used here and in other work (e. g. Bruenn 1985; Mezzacappa & Bruenn 1993b,c; Bruenn 1993; Bruenn et al. 1995; Bruenn & Mezzacappa 1997). Currently, modifications of the neutrino opacities are discussed to become important for stellar matter at nuclear densities (see e. g. Janka 2000, for a recent review and pointers to the literature). The inclusion of these new aspects in the microphysics and also the consideration of multi-dimensional effects in our simulations will be subject of a future step.

The particular purpose of the neutrino-radiation hydrodynamical supernova simulations to be presented here is twofold. First, it remains to be demonstrated that also in *dynamical* situations involving the complicated (though “standard”) microphysics of neutrino-matter interactions, our method is able to solve the equations of radiation hydrodynamics with sufficient numerical accuracy. The collapse phase of a Type II supernova is a good test problem for this purpose, since it is a theoretically well studied phenomenon. Only one group (Mezzacappa & Bruenn 1993b,c) has so far published dynamical core-collapse simulations employing the Boltzmann equation (solved by an S_N -method) for the neutrino transport. Our calculations, presented in Chap. 5.1 may serve as an independent verification of these studies. Second, by extending our simulations into the post-bounce phase (Chap. 5.2), we are able to address the study of an accurate neutrino transport for the delayed explosion mechanism (Rampp & Janka 2000).

5.1 Stellar core-collapse

We have already outlined the basic features of the core-collapse scenario in the introduction (Chap. 1). Here, we elaborate more on processes that have been shown to be decisive for the

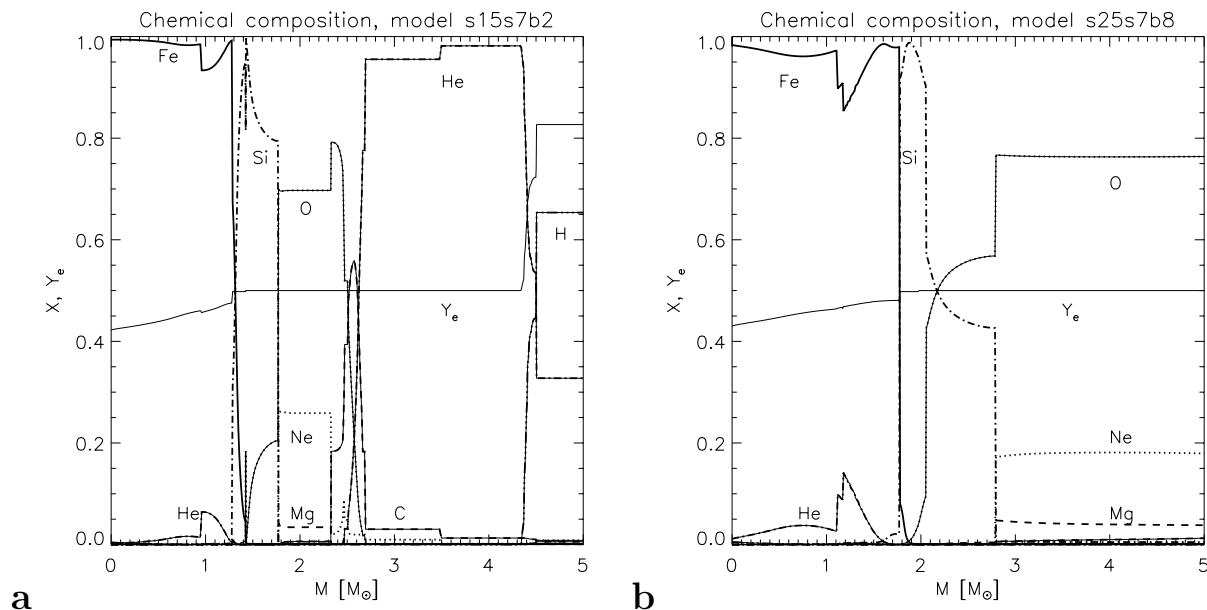


Figure 5.1: Chemical composition of two different stellar models for supernova progenitor stars. Panel **a** shows the mass-fractions X of different elements and the electron fraction Y_e for the innermost $5 M_\odot$ of the stellar model “s15s7b2” with a total main-sequence mass of $15 M_\odot$. It is representative of stars with relatively small iron cores which are considered in this work. For comparison panel **b** shows the same quantities for the $25 M_\odot$ model “s25s7b8” which has a substantially larger iron core. The data for both stellar models were kindly provided by Woosley (1999) and Heger (2000).

post-bounce evolution of the core as well as for the delayed supernova explosion mechanism. This is preceded by a brief summary of the fundamental physical picture as suggested by contemporary core-collapse models. The following discussion is largely based on the works of Shapiro & Teukolsky (1983); Bruenn (1985); Müller (1990); Mönchmeyer (1993); Suzuki (1994).

5.1.1 Physics of stellar core-collapse

Basic assumptions and approximations

We know from the theory of stellar evolution that in the deep interiors of massive stars ($M \gtrsim 8 M_\odot$) nuclear burning can proceed under hydrostatic conditions up to silicon burning, leaving a central core mainly made of iron group nuclei. Lighter elements like silicon, oxygen, neon and magnesium, helium and hydrogen dominate the composition in distinct layers which surround the iron core in an “onion-shell like” structure (see e. g. the textbooks of Clayton 1983; Kippenhahn & Weigert 1990). As an example for the progenitor’s structure, Fig. 5.1 shows the chemical composition of two different stellar models, one of a $15 M_\odot$ star which is representative of a star with a small iron core, as compared to a $25 M_\odot$ star having a larger iron core. For our exploratory simulations, we will focus on the former class of progenitor models, since a small iron core is thought to be most favorable for obtaining a successful supernova explosion.

Central densities and temperatures in the iron core are typically $\rho_c \approx 10^{10} \text{ g cm}^{-3}$ and $T_c \approx 10^{10} \text{ K}$, respectively. The electron fraction (i. e. the number of electrons per baryon) amounts to $Y_e \approx 0.43$. The central entropy per baryon is of the order of $s \approx 1k_B$. Under such conditions,

reactions mediated by strong and electromagnetic interactions proceed sufficiently rapid to establish equilibrium on the hydrodynamical time scale of the core ($t_{\text{Hyd}} \simeq 100$ ms), which implies that nuclear statistical equilibrium (NSE) holds (cf. Sect. 2.2.2).

On hydrodynamical time scales diffusive energy transport by photons and heat conduction by electrons can be neglected due to the extremely short mean free paths of these particles. Also the viscosity of the core matter is unimportant (Flowers & Itoh 1976). Hence, the core matter including photons may be well approximated as an ideal fluid whose evolution is governed by the equations of hydrodynamics (2.49–2.51). In the course of this work we adopt an additional simplifying assumption, namely we assume that the star is spherically symmetric. We will also not take into account general relativistic corrections to the Newtonian equations of hydrodynamics.

Weak interactions and neutrino transport

For densities $\rho \lesssim 10^{12}$ g cm $^{-3}$, the mean free paths of neutrinos are comparable to the radius of the iron core ($R \approx 1000$ km). Hence, weak interactions cannot be assumed to be in equilibrium and transport processes by neutrinos must be taken into account explicitly by solving the equations of neutrino transport (cf. Chap. 2).

Under the conditions met in the iron core, only electron neutrinos are present in appreciable number for the following reasons: For $\rho Y_e \gtrsim 0.43 \times 10^{11}$ g cm $^{-3}$, one estimates a chemical potential of at least $\mu_{e^-} \gtrsim 20$ MeV for the degenerate (and relativistic) electron gas. With $\mu_{e^+} = -\mu_{e^-}$ (because of the reaction $e^+ + e^- \rightleftharpoons \gamma + \gamma$) and $T \simeq 1$ MeV one finds the number density of positrons to be negligibly small, and thus electron antineutrino production via positron capture by neutrons or electron-positron pair annihilation is not effective. The production of other neutrino flavours (e. g. via the process $e^- \rightleftharpoons \mu^- + \nu_e + \bar{\nu}_\mu$) is suppressed as a consequence of the large rest masses of the corresponding charged leptons (e. g. $m_\mu \approx 200m_e$) and the fact that the chemical potential of the degenerate electron Fermi-distribution remains too small during collapse to account for a significant population of states exceeding the muon rest energy. The electron neutrinos are mainly produced by electron captures onto free protons and on protons bound in heavy nuclei. Over a wide range of energies, the neutrino opacity is dominated by the coherent scattering of neutrinos off heavy nuclei (cf. Fig. 5.2), followed by neutrino-electron scattering. Only during the early phases of the collapse, the mean free paths of neutrinos are large compared to the radius of the iron core and neutrinos produced by weak interactions are able to escape from the core. When densities of the order of $\rho \simeq 10^{12}$ g cm $^{-3}$ are reached, the diffusion time scale of neutrinos exceeds the hydrodynamical time scale of the core, and neutrinos become “trapped” by the infalling matter. Eventually, with the establishment of β -equilibrium (at $\rho \gtrsim 3 \times 10^{12}$ g cm $^{-3}$), also the weak interactions come into equilibrium. As we shall see shortly, the onset of neutrino-trapping has important consequences for the equation of state and hence for the overall collapse dynamics.

Gravitational instability, equation of state and collapse dynamics

The central iron core of an evolved massive star is mainly supported by the degeneracy pressure of a relativistic gas of electrons which implies that the density and the pressure are related by $p \propto \rho^\gamma$ with an adiabatic exponent of $\gamma = 4/3$. The mass of the iron core is close to the so-called “Chandrasekhar mass” (cf. Shapiro & Teukolsky 1983, Chap. 18)

$$M_{\text{Ch}} \approx 5.83 \cdot Y_e^2 \cdot M_\odot, \quad (5.1)$$

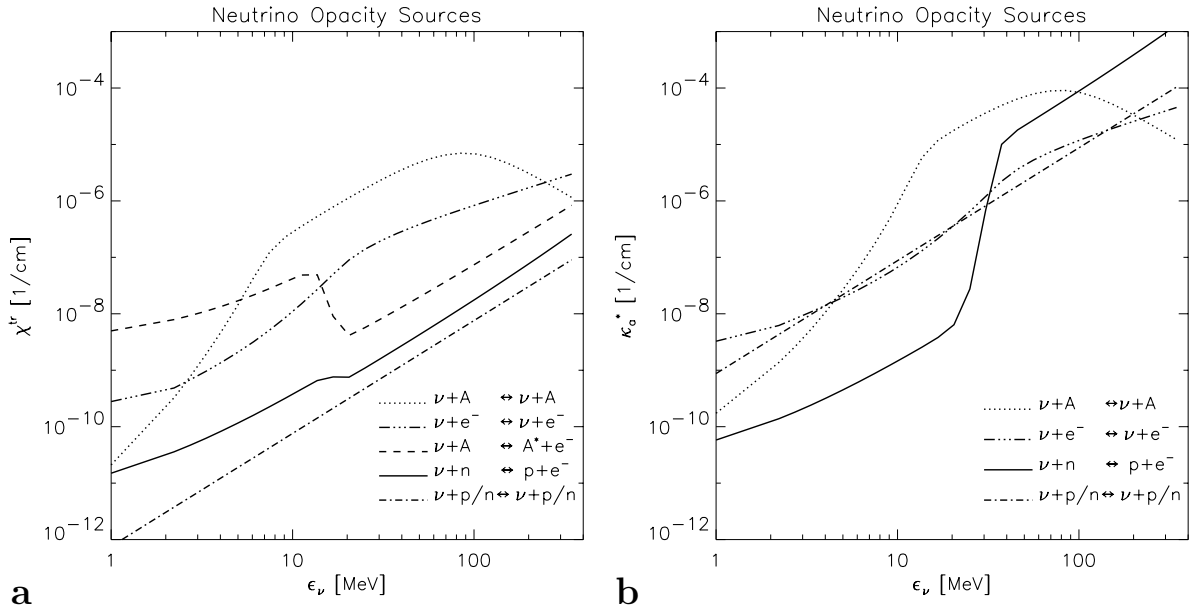


Figure 5.2: Transport opacities (cf. equ. 2.30) for electron neutrinos due to various interaction processes as a function of neutrino energy. The individual interaction rates have been calculated according to the prescriptions detailed in Appendix A. The thermodynamic conditions are defined by $\rho = 10^{11} \text{ g cm}^{-3}$, $T = 10^{10} \text{ K}$ ($s = 0.62 k_B$), $Y_e = 0.45$ (panel **a**), and $\rho = 10^{12} \text{ g cm}^{-3}$, $T = 2 \times 10^{10} \text{ K}$ ($s = 1.03 k_B$), $Y_e = 0.35$ (panel **b**), respectively. Particle abundances have been computed with the equation of state of Lattimer & Swesty (1991). The opacities may be compared with those depicted in Bruenn & Haxton (1991, Figs. 1d,g). The opacity provided by coherent scattering of neutrinos off heavy nuclei (dotted lines) notably deviates from the simple ϵ^2 -scaling at low and high energies. The dip visible for $\epsilon \lesssim 10 \text{ MeV}$ is due to ion screening corrections, whereas the decrease for $\epsilon \gtrsim 100 \text{ MeV}$ is caused by the nuclear form factor (cf. Appendix A.2.4). In panel **a** the opacities due to absorption of neutrinos by free neutrons and heavy nuclei are enhanced at low energies because of stimulated absorption: $\kappa_a^* = j + 1/\lambda$, where j is the emissivity and $1/\lambda$ the (transport) opacity, both uncorrected for blocking effects (cf. equ. A.8). In panel **b** Pauli blocking of final state electrons (the chemical potential of the electron gas is $\mu_e \approx 36 \text{ MeV}$) reduces the interaction rate of the process $\nu_e + n \rightarrow e^- + p$ for low neutrino energies.

which is the maximum mass of a star that can be stabilized against gravity (in Newtonian approximation) by the (zero temperature) degeneracy pressure of relativistic electrons, i. e., $\gamma = 4/3$ (Chandrasekhar 1939). Taking into account the net effect of the finite temperatures, the small pressure contribution of nonrelativistic baryons and the (negative) contribution of Coulomb lattice correlations one finds that the adiabatic exponent in the iron core prior to collapse is only slightly larger than the critical value $\gamma_{\text{crit}} = 4/3$. Electron captures onto free protons and heavy nuclei and the endothermic photo-disintegration of heavy nuclei eventually render the core unstable by reducing the adiabatic exponent below $\gamma_{\text{crit}} = 4/3$ and trigger a collapse on the free-fall time scale of the core (for details see e. g. Mönchmeyer 1993; Müller 1998). The relative importance of the two processes depends on the details of the stellar evolution: While in cores of stars with a main-sequence mass larger than $M \gtrsim 20 M_\odot$ endothermic photo-disintegration of heavy nuclei weakens the vital pressure support, the instability in less massive stars is mainly triggered by electron captures onto free protons and heavy nuclei which diminish the lepton pressure (at the onset on collapse the core is transparent to the produced neutrinos).

With the entropy staying low during collapse (core-collapse calculations and analytical estimates

Reaction	WS18 (NES)	WS18 (NONES)	WS15_nue	WS15
$\nu_e + e^\pm \rightleftharpoons \nu_e + e^\pm$	×	○	×	×
$\nu_e + A \rightleftharpoons e^- + A^*$	×	×	○	×
$\nu_e + A \rightleftharpoons \nu_e + A$	×	×	×	×
$\nu_e + n/p \rightleftharpoons \nu_e + n/p$	×	×	×	×
$\nu_e + n \rightleftharpoons e^- + p$	×	×	×	×
$\bar{\nu}_e + e^\pm \rightleftharpoons \bar{\nu}_e + e^\pm$	○	○	○	×
$\bar{\nu}_e + A \rightleftharpoons \bar{\nu}_e + A$	○	○	○	×
$\bar{\nu}_e + n/p \rightleftharpoons \bar{\nu}_e + n/p$	○	○	○	×
$\bar{\nu}_e + p \rightleftharpoons e^+ + n$	○	○	○	×

Table 5.1: Overview of computed models. Neutrino-matter interaction processes that were included in a particular model are marked by the “×”-symbol in the corresponding column, while a “○”-symbol is drawn if the process was neglected in this model. The stellar models for the progenitor star are identical in both “WS18”-models and in both “WS15”-models. For all computed models the stellar structure in the central regions of the progenitor star was very similar ($M_{\text{Fe}} \approx 1.28 M_\odot$ in all cases; the differences between “WS18” and “WS15” are mostly confined to the outer Helium and Hydrogen layers.).

have shown that prior to the onset of neutrino-trapping, the total increase in entropy amounts to a modest $\Delta s \approx 0.5 k_B$; cf. Shapiro & Teukolsky 1983), nucleons remain bound in heavy nuclei, which implies that the pressure remains to be dominated by the relativistic electron gas. Therefore the collapse cannot be stopped until nuclear densities are reached. Only then, the equation of state stiffens considerably due to the action of repulsive nuclear forces (the adiabatic exponent rises from $\gamma \approx 4/3$ to $\gamma \approx 2 \dots 3$, with the precise value depending on the physics of the nuclear equation of state) and a new stable hydrostatic equilibrium configuration can be attained.

Taking advantage of the approximate adiabaticity of the collapse, Goldreich & Weber (1980) and Yahil (1983) were able to find analytical similarity solutions for the collapse dynamics: The core splits into a subsonically and homologously ($v(r) = f(t) \cdot r$, with some function $f(t) \leq 0$) collapsing inner core (Goldreich & Weber 1980) and a supersonically (Mach-numbers are about 2 to 3) infalling outer core (Yahil 1983). At the edge of the inner core a local minimum in the radial profile of infall velocity is reached (for an illustration, see e. g. Müller 1998, Fig. 3.6). Since matter in the inner core stays in sonic contact during collapse, the bounce caused by the stiffening of the equation of state occurs coherently, i. e. on the sound propagation time scale of the inner core which is of the order of a millisecond, for the entire inner core. At the edge of the subsonic core, pressure waves communicating the bounce throughout the inner core steepen to form the so-called bounce shock that is driven into the supersonically infalling outer core.

5.1.2 Investigated models

Based on the results of our calculations we now discuss a number of physical and numerical aspects of stellar core-collapse and compare our findings with published work. An overview of models and the neutrino-matter interactions considered is given by Table 5.1

Neutrino-electron scattering

It has become a well established fact that inelastic scattering of electron neutrinos off free electrons plays a very important role for the dynamics of the gravitational collapse of a stellar iron core. In

particular, neutrino-electron scattering directly influences one of the physical parameters that are most decisive for success or failure of a supernova explosion, namely the mass of the inner core that forms during collapse and thereby the position, where the bounce shock eventually forms. The latter determines the energy loss the shock suffers from during its propagation through the outer iron core. The main effects of neutrino-electron scattering that are responsible for this are — mutually interconnected — an increased entropy generation associated with a substantially enhanced deleptonization of the collapsing core, which can be understood as follows (Bruenn 1985; Mezzacappa & Bruenn 1993b; Bruenn & Mezzacappa 1997):

During collapse, mainly high energy neutrinos are produced by electron captures on free protons resulting in a neutrino distribution characterized by a mean energy that is much larger than the thermal mean corresponding to the local matter temperature. Inelastic neutrino-electron scattering tends to equilibrate both systems thermally, which gives rise to a net energy transfer from the neutrinos to the stellar matter. Compared to a number of other reactions involving energy transfer between neutrinos and matter, neutrino-electron scattering was in fact found to be the most effective one (Bruenn & Haxton 1991).

The transfer of heat from the neutrino to the matter system increases the entropy of the stellar matter which gives rise to a larger abundance of free protons and thus an increased electron capture rate, which in turn drives entropy generation by neutrino-electron downscattering, closing a positive feedback loop. Yet, the total entropy increase as well as lepton loss during collapse remains of relatively modest magnitude, which is due to the fact that the low energy neutrinos become trapped by the infalling matter as soon as densities of several times $10^{12} \text{ g cm}^{-3}$ are reached in the centre of the core and hence Pauli blocking of final low energy neutrino states inhibits further downscattering.

For the reasons given above, it is crucial for core-collapse simulations, to treat neutrino-electron scattering in a sufficiently accurate manner. In order to verify that all important physical effects of this interaction process are correctly accounted for by our implementation, we have performed two core-collapse simulations, one with neutrino-electron scattering included as described in Appendix A, another with neutrino-electron scattering switched off.

In the following, we discuss the outcome of these simulations and compare our results with similar simulations performed e. g. by Bruenn (1985) and Mezzacappa & Bruenn (1993b). Since we could not employ exactly the same input physics as was used in the latter work — the main differences being the stellar model and the equation of state — the comparison to Mezzacappa & Bruenn (1993b) is mainly qualitative in nature. A truly quantitative check of our implementation, including neutrino-electron scattering, will be presented in the next section.

Numerical model (“WS18”): The initial model comprises an iron core of mass $M_{\text{Fe}} = 1.27 M_{\odot}$ (plus the innermost $0.15 M_{\odot}$ of the adjacent silicon shell) taken from a $18 M_{\odot}$ blue supergiant progenitor star (Woosley, Heger, Weaver, & Langer 1997). Like the models of Mezzacappa & Bruenn (1993b), our simulations are performed in Newtonian gravity, and only electron neutrinos are included. In addition to neutrino-electron scattering we consider the coherent scattering of neutrinos off heavy nuclei, elastic scattering off free nucleons and beta processes with free nucleons and heavy nuclei (see Appendix A for details of the implemented interaction rates).

Results: Figure 5.3a shows the temporal evolution of the entropy profiles as a function of the mass coordinate. The latter is a natural choice, since the entropy per baryon at a given Lagrangian

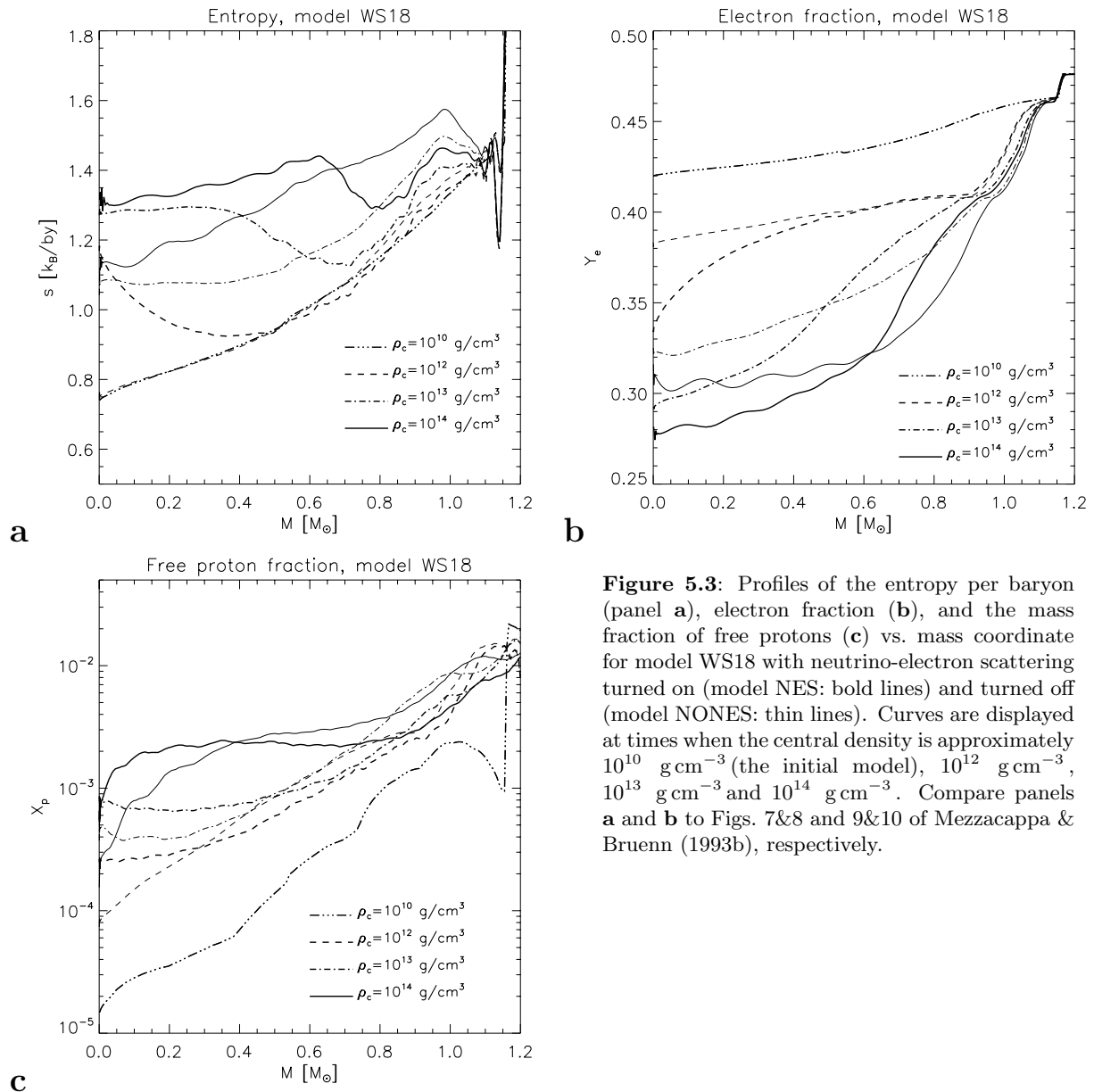


Figure 5.3: Profiles of the entropy per baryon (panel a), electron fraction (b), and the mass fraction of free protons (c) vs. mass coordinate for model WS18 with neutrino-electron scattering turned on (model NES: bold lines) and turned off (model NONES: thin lines). Curves are displayed at times when the central density is approximately 10^{10} g cm⁻³ (the initial model), 10^{12} g cm⁻³, 10^{13} g cm⁻³ and 10^{14} g cm⁻³. Compare panels a and b to Figs. 7&8 and 9&10 of Mezzacappa & Bruenn (1993b), respectively.

coordinate changes in time only due to non-ideal processes such as neutrino transport (or hydrodynamic shocks, which are not present in the collapse phase).

Whereas almost no change in entropy has occurred between $\rho_c = 10^{10}$ g cm⁻³ (the initial model) and $\rho_c = 10^{12}$ g cm⁻³ for the model with neutrino-electron scattering switched off (referred to as model "NONES" in the following), the entropy has considerably increased throughout the inner parts of the core for the model with neutrino-electron scattering enabled (model "NES"). As a result, the increased abundance of free protons (Fig. 5.3c) leads to a higher production rate of neutrinos which are effectively downscattered in energy by ambient electrons. These effects are clearly visible in Fig. 5.4c, which shows that the neutrino distribution function peaks at lower energies and gives a larger integral value ($\int_0^\infty d\epsilon \epsilon^2 M^{(0)}(\epsilon)$ is proportional to the local number

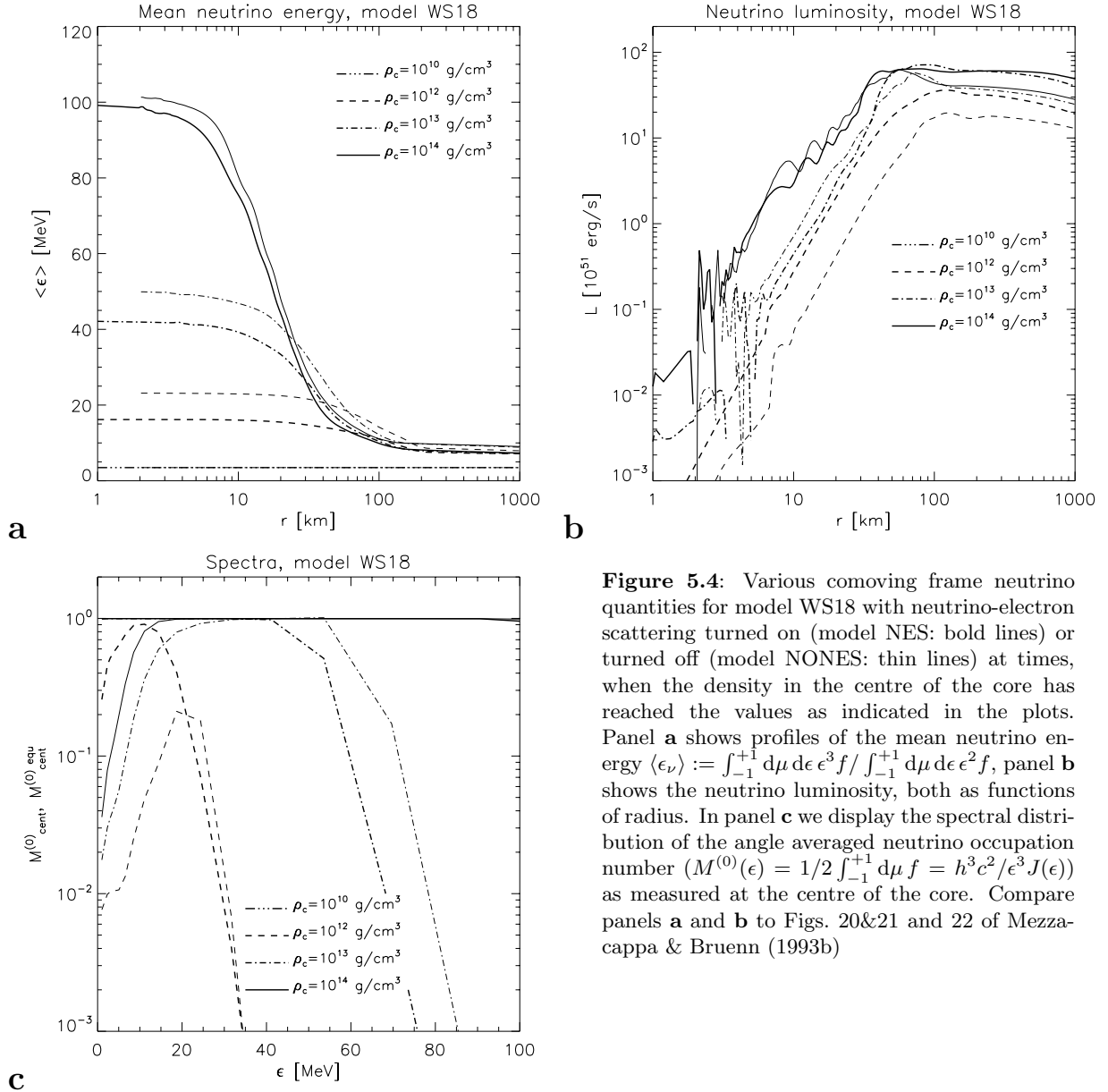


Figure 5.4: Various comoving frame neutrino quantities for model WS18 with neutrino-electron scattering turned on (model NES: bold lines) or turned off (model NONES: thin lines) at times, when the density in the centre of the core has reached the values as indicated in the plots. Panel **a** shows profiles of the mean neutrino energy $\langle \epsilon_\nu \rangle := \int_{-1}^{+1} d\mu d\epsilon \epsilon^3 f / \int_{-1}^{+1} d\mu d\epsilon \epsilon^2 f$, panel **b** shows the neutrino luminosity, both as functions of radius. In panel **c** we display the spectral distribution of the angle averaged neutrino occupation number ($M^{(0)}(\epsilon) = 1/2 \int_{-1}^{+1} d\mu f = h^3 c^2 / \epsilon^3 J(\epsilon)$) as measured at the centre of the core. Compare panels **a** and **b** to Figs. 20&21 and 22 of Mezzacappa & Bruenn (1993b)

density of neutrinos) when neutrino-electron scattering is in effect. Because of the larger mean free paths at lower energies ($\lambda \propto 1/\epsilon^2$), also the depletion of the central parts of the core is facilitated, when the average energy of the neutrinos is lowered due to neutrino-electron scattering. To illustrate this with additional numbers we remark that at $\rho_c = 5 \times 10^{11} \text{ g cm}^{-3}$, the neutrino production rate measured in units of $1/(\text{cm}^3 \cdot \text{MeV} \cdot \text{s})$ peaks at $\epsilon = 22 \text{ MeV}$ (which at that time approximately equals the chemical potential of the electrons) in our model NES. The transport optical depth for neutrinos of this energy is $\tau \approx 280$, corresponding to a time scale of hundreds of milliseconds for diffusing out of the innermost few hundred kilometers of the core. For neutrinos with energies $\epsilon \lesssim 10 \text{ MeV}$, which is roughly the energy, where the peak of the neutrino distribution is shifted to due to neutrino-electron scattering (cf. Fig. 5.4c), this time scale is smaller by roughly

an order of magnitude, enabling the neutrinos to escape from the core carrying away lepton number. Figures (5.3a,b) show that the differences between the electron fraction profiles of model NES and NONES are confined exactly to the same region, where also the entropy profiles differ notably between both models, supporting the argument concerning the interconnection between entropy generation and decrease in electron fraction. By the time the central density has reached $\rho_c = 10^{13} \text{ g cm}^{-3}$, the neutrino distribution at the centre of the core has equilibrated with the matter for model NES, whereas there are still unpopulated low energy states in model NONES (Fig. 5.4c). Therefore, between $\rho_c = 10^{13} \text{ g cm}^{-3}$ and $\rho_c = 10^{14} \text{ g cm}^{-3}$ there is more entropy generation (within a larger part of the inner core) for model NONES.

At $\rho_c = 10^{12} \text{ g cm}^{-3}$, the luminosity of model NES is considerably enhanced throughout the core of model NES as compared to model NONES (Fig. 5.4b). This is a combined effect of the larger neutrino production rates, and hence a larger neutrino fraction in the centre, as well as the increased mean free paths of the neutrinos. Both effects are obviously able to overcompensate the somewhat reduced average neutrino energies (Fig. 5.4a), which, for a given number flux of neutrinos, tend to decrease the total luminosity. As the density increases further, the neutrino fraction (not depicted here) of model NES eventually drops below the values computed in model NONES. Moreover, with the inner core becoming optically thick for low energy neutrinos, no more empty low energy states are available and hence the release of neutrinos from the inner core is no more facilitated markedly by neutrino-electron downscattering. For these reasons the luminosity in the inner core of model NES finally becomes smaller than for model NONES. In the optically thin outer core, the luminosity of model NES remains larger for the same reasons as given for the inner core during earlier epochs.

Figure 5.5 summarizes the consequences of neutrino-electron scattering for the overall collapse dynamics: Due to the reduced number of electrons in the central parts of the core, the mass of the homologously collapsing inner core decreases with increasing deleptonization according to the relation (Goldreich & Weber 1980)

$$M_{\text{HC}} \approx M_{\text{Ch}} = 5.83Y_e^2 \cdot M_{\odot}, \quad (5.2)$$

where M_{Ch} denotes the Chandrasekhar mass (equ. 5.1). As can be seen from Fig. 5.5a, the homologous core (its extent roughly being bounded by the location of the sonic point, where the absolute value of the velocity equals the local sound speed) of model NES is by $\Delta M_{\text{HC}} \approx 0.1 M_{\odot}$ smaller than the more electron-rich core of model NONES. The inner core, its extent being defined by the location of the maximum infall velocity, is smaller in model NES (and the outer core is larger) by $\Delta M_{\text{IC}} \approx 0.15 M_{\odot}$, when $\rho_c = 10^{14} \text{ g cm}^{-3}$. In anticipation of an elaborate discussion of the post-bounce phase we note that this mass difference translates to an additional energy loss of approximately $2.5 \times 10^{51} \text{ erg}$ for the bounce shock that eventually forms on the surface of the inner core. In fact, from extending the simulation of model NONES into the post-bounce phase, it seems that model NONES might indeed produce a prompt supernova explosion, whereas no indications of a successful (prompt) explosion have been found for model NES. The latter results underline the crucial influence of neutrino-electron scattering on the success or failure of the supernova explosion.

Coming back to the collapse dynamics, we note that changes caused by the inclusion of neutrino-electron scattering are visible in the profiles of a number of other quantities too, like e. g. in the density vs. enclosed mass (Fig. 5.5b), which can be employed to explain (see Mezzacappa & Bruenn

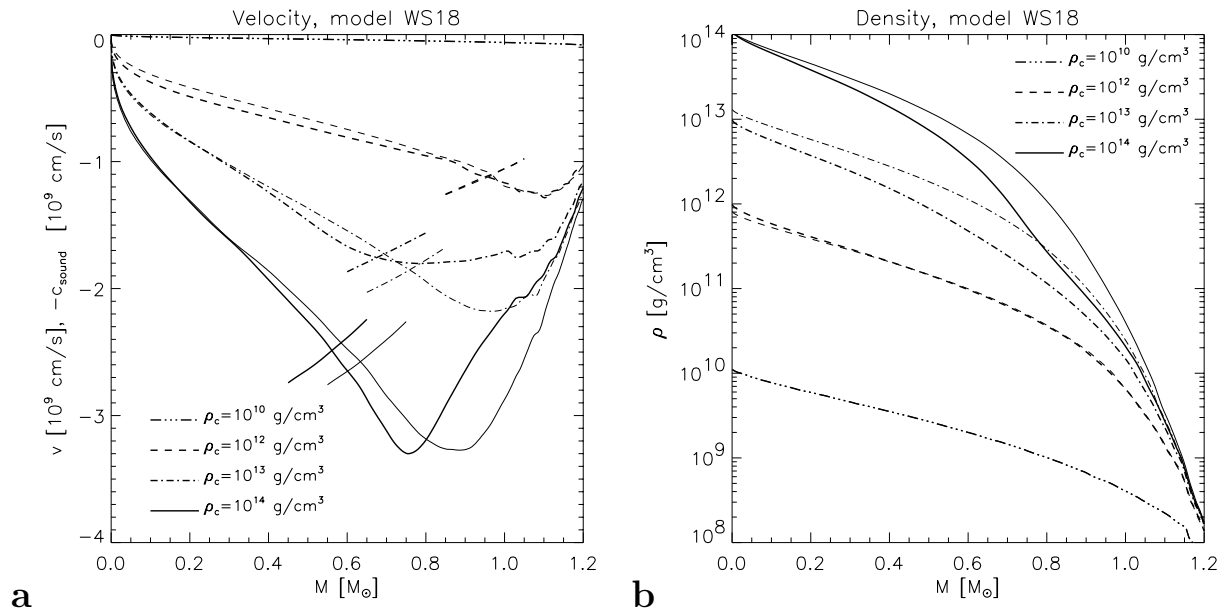


Figure 5.5: Profiles of infall velocity (a) and mass density (b) vs. mass coordinate for model WS18 with neutrino-electron scattering turned on (model NES: bold lines) and turned off (model NONES: thin lines). The short lines in panel a show the (negative of the) local sound speed. Curves are displayed at times when the central density is approximately 10^{10} g cm^{-3} (the initial model), 10^{12} g cm^{-3} , 10^{13} g cm^{-3} and 10^{14} g cm^{-3} . Compare panels a and b to Figs. 3 and 5 of Mezzacappa & Bruenn (1993b), respectively.

1993b, §4.2) related features like e. g. a larger entropy in the outer core of model NONES as compared to model NES (cf. Fig. 5.3a).

Discussion: For all quantities presented above we find good qualitative agreement between our models and the models published by Mezzacappa & Bruenn (1993b). This applies for the radial profiles as well as for their temporal evolution. References to individual figures shown by Mezzacappa & Bruenn (1993b), which our results may be compared with have already been given in the captions of our plots. In particular, we find that the *differential* effects due to the implementation of neutrino-electron scattering — which, in contrast to absolute quantities we consider to be less sensitive to the details of the stellar model employed — are reproduced very well when compared with the results of Mezzacappa & Bruenn (1993b). For example, at $\rho_c = 10^{13}$ g cm^{-3} , the difference in the central entropy amounts to $\Delta s_c := s_c^{\text{NES}} - s_c^{\text{NONES}} = 0.20$ for our model WS18, whereas Mezzacappa & Bruenn (1993b) find $\Delta s_c = 0.22$ (see their Fig. 8 and our Fig. 5.3a). At the same time, the difference in the central electron fraction amounts to $\Delta Y_{e,c} = -0.03$ for our model WS18, whereas Mezzacappa & Bruenn (1993b) compute $\Delta Y_{e,c} = -0.027$ (see their Fig. 10 and our Fig. 5.3b).

Ion screening

During the earlier phases of the gravitational collapse, coherent scattering off heavy nuclei is by far the most important source of neutrino opacity (see Fig. 5.2). For typical neutrino energies, the total scattering rate due to this process is roughly a factor of ten larger than the second

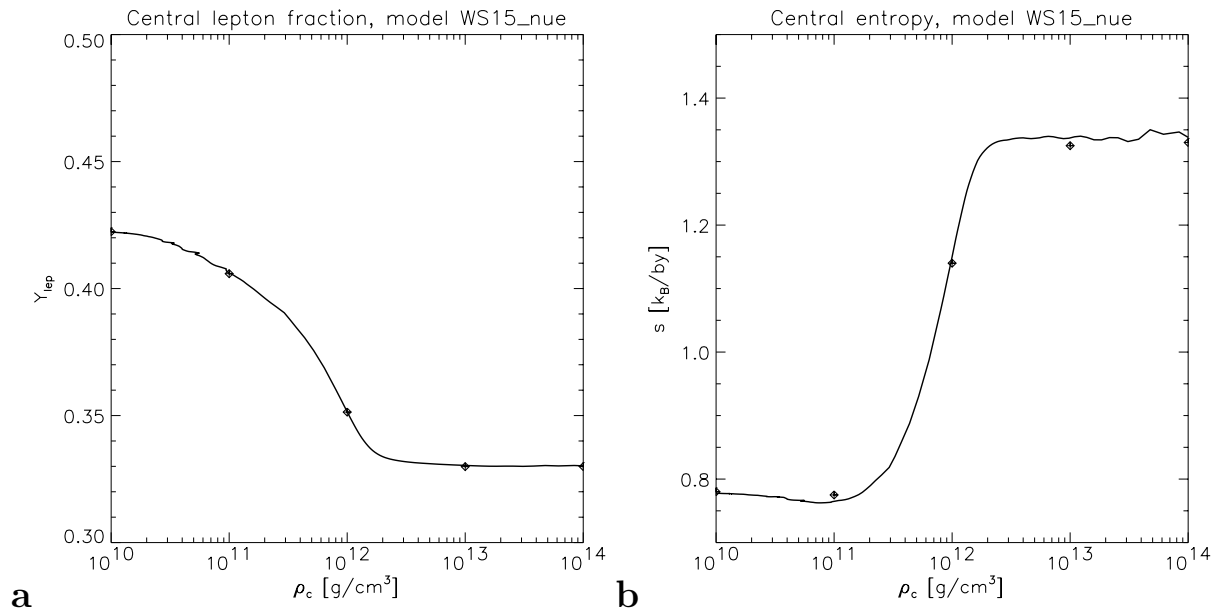


Figure 5.6: Central lepton fraction $Y_{\text{lep}} := Y_e + Y_{\nu_e}$ (panel a) and central entropy per baryon (b) as a function of the central density for our model WS15_nue (solid lines), compared with the results (diamonds) obtained by Bruenn & Mezzacappa (1997, Figs. 4a, 8a).

largest interaction rate, which is inelastic neutrino-electron scattering or elastic neutrino-neutron scattering (cf. Bruenn & Mezzacappa 1997, Table I). The dominant role of the neutrino-nucleus scattering rate for the total opacity suggests that corrections to the “standard” Freedman cross section might have an important influence on the collapse dynamics. Here we will address one of these corrections, namely the reduction of the scattering rate for low energy neutrinos caused by spatial ion-ion correlations (“ion screening”).

Due to the relatively low temperatures and high densities, Coulomb forces are able to keep the heavy nuclei (ions) in a spatially correlated state during core-collapse. For this reason, the scattering *amplitudes* of neutrinos with wavelengths larger than the inter-ion spacing need to be superposed coherently, which — much similar to Bragg reflection on a crystal — leads to a substantially reduced scattering rate for low energy neutrinos (see e. g. Lattimer & Burrows 1990; Horowitz 1997; Bruenn & Mezzacappa 1997). As a consequence of the increased mean free paths, low energy neutrinos more easily leak out of the collapsing core through the “low energy window”, which is opened by the effect of ion screening. Moreover, due to downscattering of high energy electron capture neutrinos by electrons (see previous section), also neutrinos produced with larger energies can contribute to the lepton loss through this “low energy window”. Until the works of Horowitz (1997) and Bruenn & Mezzacappa (1997), the question to what extent the deleptonization and entropy generation in stellar core-collapse simulations are altered by this effect has only briefly been addressed in the literature (Bowers & Wilson 1982; Lattimer & Burrows 1990; Bruenn 1993). Employing the most recent calculations of ion screening corrections (Horowitz 1997), Bruenn & Mezzacappa (1997) have performed detailed numerical simulations in order to investigate claims (Horowitz 1997) that the inclusion of spatial ion correlations might substantially enhance the deleptonization of collapsing iron cores.

These simulations, performed for two different iron cores, one taken from Woosley & Weaver’s

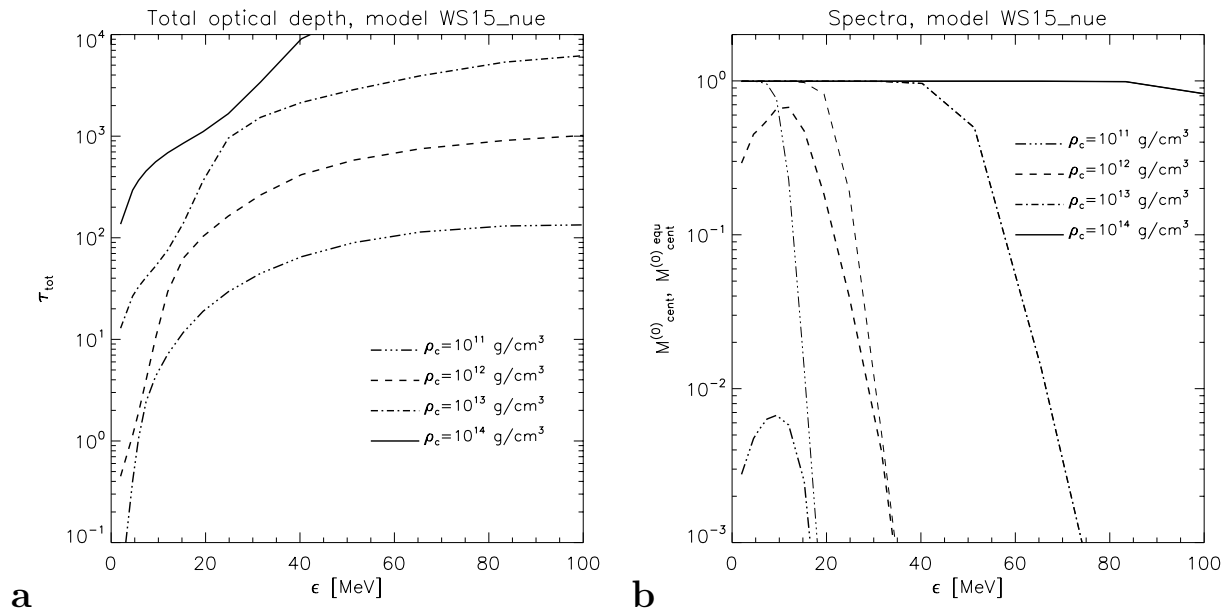


Figure 5.7: Panel **a** shows the energy averaged transport optical depth (for a definition see equ. 5.23) in the centre of the core at times, when the central density has reached the values as indicated by different line styles in the plot. At the same times, the spectral distribution of the angle averaged central neutrino occupation number ($M^{(0)} = 1/2 \int_{-1}^{+1} d\mu f = h^3 c^2 / \epsilon^3 J$, bold lines) is shown together with its equilibrium values (thin lines) in panel **b**. The plots may be compared to Figs. 3 and 7 of Bruenn & Mezzacappa (1997).

15 M_{\odot} model "s15s7b2", the other from their 25 M_{\odot} model "s25s7b8" (cf. Fig. 5.1), show that the "low energy window" opened by introducing ion screening corrections is indeed efficiently filled by neutrinos which have been downscattered in energy space by electrons. However, it was argued that the corresponding neutrino phase space is too small to account for a significant or even catastrophic additional deleptonization of the core as claimed by Horowitz (1997). Bruenn & Mezzacappa (1997) found that the increased deleptonization through the "low energy window" amounts to only a modest $\Delta Y_{\text{lep}} = -0.015$. As a consequence, the mass enclosed by the bounce shock when it forms also turned out to be smaller, but only by a negligible amount ($\Delta M_{\text{shock}} = -0.014 M_{\odot}$ for the 15 M_{\odot} model, and $\Delta M_{\text{shock}} = -0.036 M_{\odot}$ for the 25 M_{\odot} model, respectively) as compared to the models computed without ion screening corrections ($M_{\text{shock}} \approx 0.60 M_{\odot}$ and $M_{\text{shock}} \approx 0.64 M_{\odot}$, respectively).

Numerical model ("WS15_nue"): In order to validate the results of Bruenn & Mezzacappa (1997), we have performed a Newtonian simulation of the collapse phase of an iron core of mass $M_{\text{Fe}} = 1.28 M_{\odot}$ (plus the innermost 0.1 M_{\odot} of the silicon shell) taken from the 15 M_{\odot} progenitor star "s15s7b2" (Woosley 1999; Heger 2000). The input physics, in particular the stellar model and the high-density equation of state, were chosen virtually identical to model "B" computed by Bruenn & Mezzacappa (1997). Besides testing our implementation of the ion screening corrections, this also allowed us to perform a detailed quantitative comparison of the results computed by our new radiation hydrodynamics code with the multi-group flux-limited diffusion method used by Bruenn & Mezzacappa (1997).

For the electron neutrinos, the physical prescriptions for the different interaction processes were

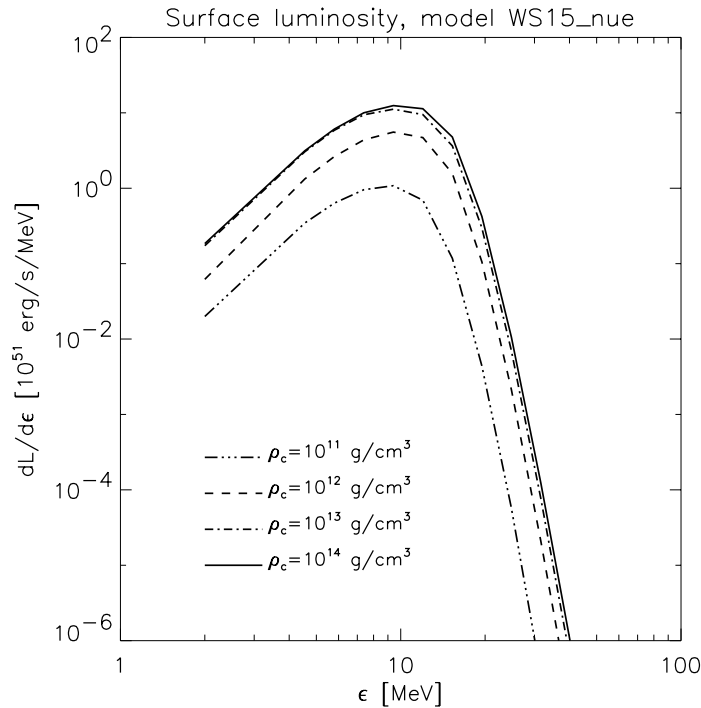


Figure 5.8: Spectrum of the comoving frame luminosity of electron neutrinos at the surface of the iron core at times, when the central density has reached the values as indicated by different line styles in the plot.

the same as Bruenn & Mezzacappa (1997) employed for their model “B”: We include β -processes and elastic scattering of neutrinos off free nucleons (identical to Bruenn 1985; Mezzacappa & Bruenn 1993c), scattering of neutrinos off α -particles and heavy nuclei including the ion screening corrections for the latter process (Horowitz 1997, implemented like Bruenn & Mezzacappa 1997) and neutrino-electron and neutrino-positron scattering (conceptually similar to Bruenn 1985; Bruenn & Mezzacappa 1997). Different from Bruenn & Mezzacappa (1997), we do not calculate the transport of other types of neutrinos, which, however does not make a difference during the collapse phase.

Results: Figure 5.6 displays our results for the deleptonization and entropy generation during collapse. In panel (a) we display the total lepton fraction $Y_{\text{lep}} := Y_e + Y_{\nu_e}$ at the centre of the core as a function of the central density with the latter serving as a suitable time coordinate. The crucial phase for core-deleptonization and entropy generation occurs between central densities of $10^{11} \text{ g cm}^{-3}$ and about $10^{12} \text{ g cm}^{-3}$, when the core is still not highly opaque to the low energy part of the neutrino spectrum (see Fig. 5.7a). For neutrinos of energies $\epsilon \lesssim 20 \text{ MeV}$, ion screening leads to a substantial reduction of the transport optical depth and hence facilitates the transport of neutrino number and energy out of the core (see Fig. A.1 and Bruenn & Mezzacappa 1997, Fig. 3). From Fig. 5.7b it also becomes evident that the neutrino phase space associated with this “low energy window” gets quickly populated during this time. Comparing a calculation including neutrino-electron scattering to one with neutrino-electron scattering switched off (see Fig. 5.4a) it becomes obvious, that it is indeed the “downscattering” of neutrinos off electrons that is responsible for filling the low energy part of the neutrino phase space.

By the time the central density has reached about $2 \times 10^{12} \text{ g cm}^{-3}$, the core has finally become extremely opaque to neutrinos of all energies (Fig. 5.7a). The diffusive transport of neutrino

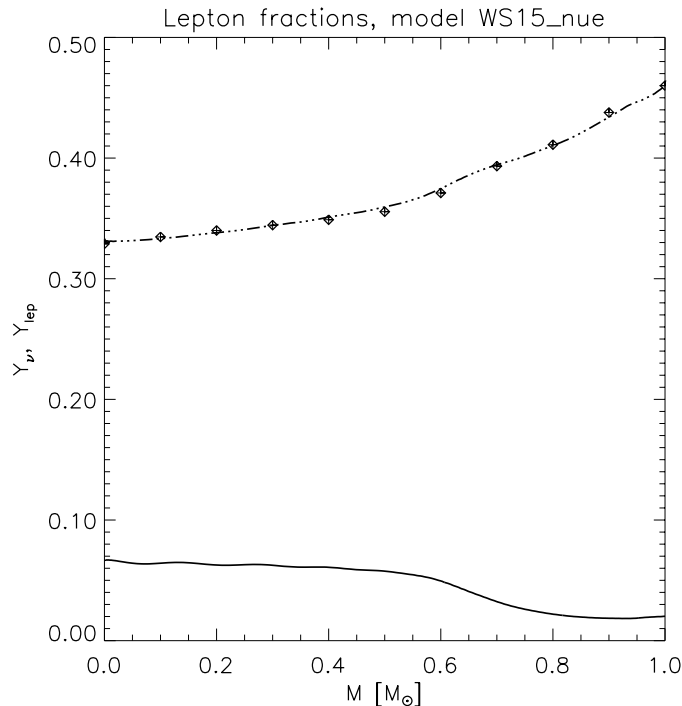


Figure 5.9: Profiles of the total lepton fraction Y_{lep} (dashed-dotted line) and the electron neutrino fraction Y_{ν_e} (solid line) as a function of the enclosed mass at the time when the central density reaches $10^{14} \text{ g cm}^{-3}$. The results of Bruenn & Mezzacappa (1997, Fig. 5a) are plotted as diamonds, for comparison.

number and energy becomes inefficient on collapse time scales and the deleptonization and entropy generation in the inner core effectively ceases (see Fig. 5.6a,b) irrespective of the ion screening corrections, because of the large overall values of the transport optical depth and the fact that the importance of scattering of neutrinos off heavy nuclei decreases relative to other opacity sources (e. g. neutrino-nucleon scattering).

At $\rho_c \approx 10^{13} \text{ g cm}^{-3}$, the neutrinos are in thermal equilibrium with the stellar matter, which is illustrated by Fig. 5.7b, showing that the occupation function is indistinguishable from the Fermi-Dirac spectrum at equilibrium. The angular distribution of the occupation number has also become highly isotropic throughout the innermost $0.5 M_\odot$ of the core, as can be seen from the value of the Eddington factor, which equals $1/3$ in this region (Fig. 5.10).

Discussion: Comparing our results to Bruenn & Mezzacappa (1997), we find excellent agreement of the lepton fraction and the entropy per baryon at the centre of the core as a function of the central density (see Fig. 5.6). Also the total lepton fraction as a function of enclosed mass is reproduced very well (see Fig. 5.9). Using the mass coordinate where the entropy per baryon after core bounce first exceeds a value of $s = 3 k_B$ as the definition for the shock formation point (Bruenn & Mezzacappa 1997), we obtain a value of $M_{\text{shock}} \approx 0.62 M_\odot$ which is about $0.03 M_\odot$ or 5% larger than the value given by Bruenn & Mezzacappa (1997, Table V). For completeness and future comparison, we also show spectra of the surface luminosity as a function of time (Fig. 5.8).

In judging our results, it has, however, to be taken into account that Bruenn & Mezzacappa (1997) employed a multi-group flux-limited diffusion (MGFLD) approximation for treating the neutrino transport, whereas our code attempts to solve the Boltzmann equation. Unfortunately we cannot compare our results directly to other simulations that used an accurate neutrino transport,

but can only rely on somewhat indirect arguments, instead: Mezzacappa & Bruenn (1993b,c) have in great detail compared core-collapse simulations employing the MGFLD approximation with results obtained with their S_N -method for Boltzmann neutrino transport. For the quantities presented above they also find good agreement between the results obtained with the MGFLD code and the more accurate S_N -method throughout the entire inner core. Of course, good overall agreement had to be expected for the inner core for the following reasons: In the very early phases ($\rho_c \lesssim 10^{11} \text{ g cm}^{-3}$) of the collapse, when major parts of the core are still optically thin and a diffusion approximation (cf. equ. 2.32) is not well justified, the evolution is largely dominated by the local emission of neutrinos which escape virtually without further interaction and therefore the precise treatment of the transport of energy and lepton number through the core is not so important. Later ($\rho_c \gtrsim 10^{11} \text{ g cm}^{-3}$) the inner core quickly becomes optically thick and diffusive transport establishes, which, e. g. can be seen from the Eddington factor approaching a value of $1/3$ (Fig. 5.10a). Accordingly, in the inner core the mean flux factor

$$\langle f_H \rangle := \frac{\int_0^\infty d\epsilon H(\epsilon)}{\int_0^\infty d\epsilon J(\epsilon)} \quad (5.3)$$

obtained for our model “WS15_nue” equals the flux factor with $H(\epsilon)$ computed by a MGFLD approximation

$$H^{\text{MGFLD}}(\epsilon) := -3\Lambda\{J(\epsilon)\} \cdot \frac{1}{3\chi^{\text{tr}}(\epsilon)} \frac{\partial J(\epsilon)}{\partial r}, \quad (5.4)$$

where $J(\epsilon)$ is taken from our simulations and χ^{tr} is the transport opacity (cf. equ. 2.30). The “flux limiter” is chosen similar¹ to Bruenn & Mezzacappa (1997) and Bruenn (1985), respectively:

$$\Lambda\{J(\epsilon)\} = \frac{1}{3 + \chi^{\text{tr}}(\epsilon)^{-1} |\partial J(\epsilon)/\partial r| / J(\epsilon)}. \quad (5.5)$$

In the outer core, the situation is different: Mezzacappa & Bruenn (1993b,c) convincingly demonstrate that for a number of quantities there are real and significant deviations of the MGFLD solutions from those obtained with an S_N -method. In particular, they find an electron neutrino fraction which is by up to 20% larger for the Boltzmann run as compared to the MGFLD simulations. For the total lepton fraction, however, this translates to a difference of only 1%, which our results are obviously consistent with (cf. Fig. 5.9). Of course, a more direct and conclusive comparison of our variable Eddington factor method with the latest implementation of an S_N -method (Mezzacappa & Messer 1999) is desirable and is intended to be performed soon.

The seemingly good agreement between the MGFLD flux factor computed by eqns. (5.3–5.5) and our transport results, which, for $\rho_c \gtrsim 10^{12} \text{ g cm}^{-3}$, is visible in Fig. 5.10b also in the outer core is likely to be a coincidence of choosing the particular form (5.5) — which is by no means motivated physically — for the flux limiter. We have also tried other commonly employed flux limiters and found them to provide much poorer approximations in the outer core. In addition, one should keep in mind that the quantity $J(\epsilon)$ that is used to estimate the MGFLD flux factor is taken from an accurate transport calculation and thus evolutionary effects of the MGFLD approximation are not accounted for. This coincidence is also not thought to be responsible for the overall similarity of the

¹For the present purpose it is not necessary to take into account the corrections employed by Bruenn, Buchler, & Yueh (1978) to the more simple form of the flux limiter (5.5).

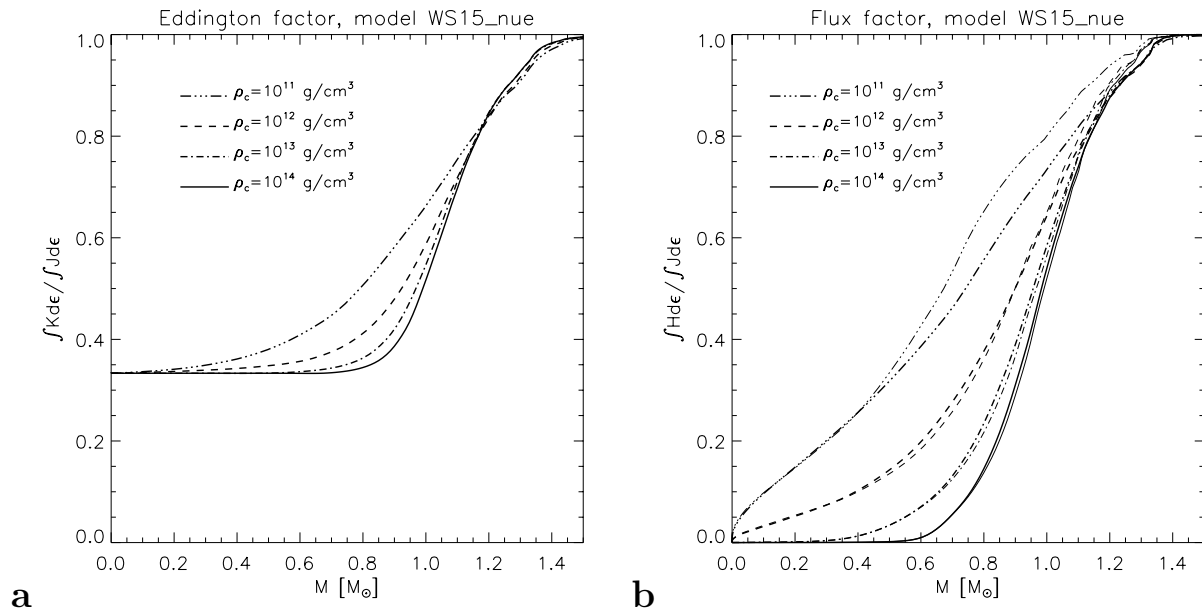


Figure 5.10: Panel **a** shows the Eddington factor (second normalized moment of the specific intensity) as a function of enclosed mass at times, when the central density has reached the values as indicated by different line styles in the plot. At the same times, the flux factor (first normalized moment of the specific intensity) is shown (with bold lines) in panel **b**, together with the flux factor as predicted for a MGFLD calculation (thin lines; see the text for details).

hydrodynamics of Boltzmann and MGFLD core-collapse calculations, where Mezzacappa & Bruenn (1993c,b) found rather good agreement for quantities like profiles of the electron fraction, entropy, density and velocity also in the outer core. It is rather due to the very short time a particular fluid element spends at intermediate optical depths ($0.1 \lesssim \tau \lesssim 1$), which is a consequence of the specifics of the collapse dynamics, that the effect of the MGFLD approximation on the hydrodynamics and thermodynamics of the stellar matter remains of relatively moderate magnitude also in the outer core.

Spectral resolution

For a few quantities discussed so far we observe some spurious oscillations as a function of radial (mass-) coordinate and time, respectively. Figure 5.3, for example, shows these features for the entropy per baryon and the electron fraction as a function of mass for $\rho_c \gtrsim 10^{13}$ g cm⁻³ and $0 \leq M \lesssim 0.6 M_{\odot}$. Similar structures are visible in the neutrino luminosity (Fig. 5.4b) as a function of radius and the central entropy as a function of central density (or time) (Fig. 5.6b).

Mezzacappa & Bruenn (1993c) have found almost identical features in their core-collapse calculations and have identified an insufficient spectral resolution of the degenerate Fermi distribution of the electron neutrinos to be the origin of these oscillations. The argument is detailed in Mezzacappa & Bruenn (1993c, §3.3), here we will only briefly outline the main points.

For the temperatures and densities where the oscillations occur, the neutrino distribution function f is very close to the equilibrium distribution f^{eq} . The latter is well approximated by a

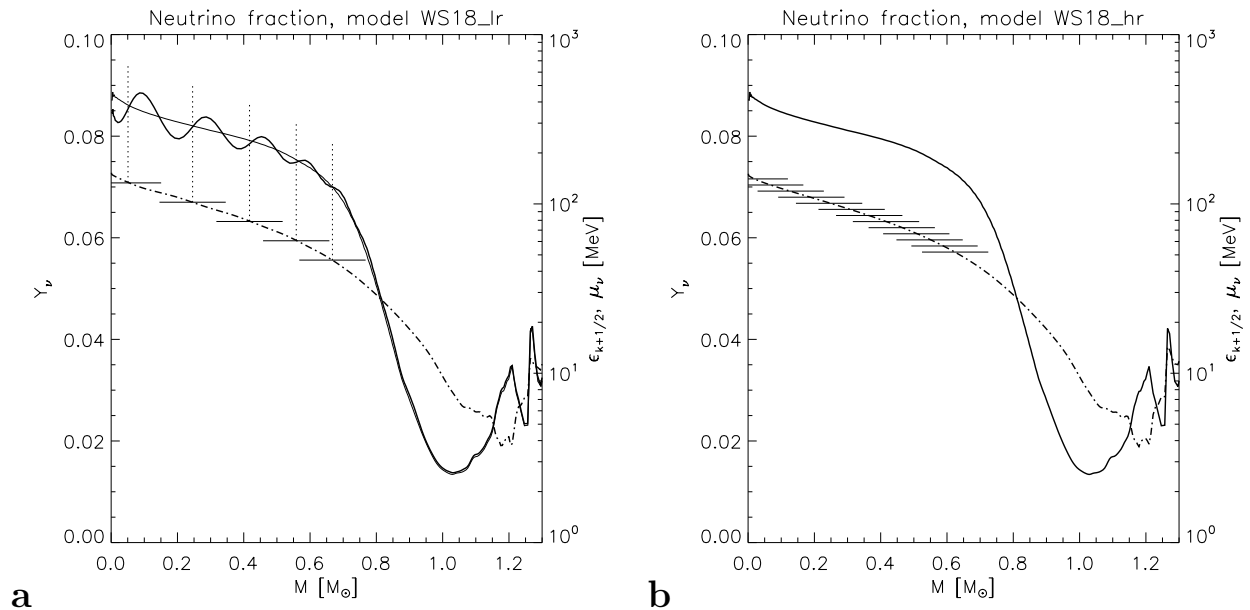


Figure 5.11: Electron neutrino fraction Y_{ν_e} (bold solid line, scale given by the axis on the left hand side of the plot) and electron neutrino equilibrium chemical potential $\mu_{\nu_e}^{\text{eq}}$ (“Fermi surface”, dashed-dotted line, scale given by the axis on the right hand side) for model “WS18” as functions of enclosed mass at the time, when the central density has reached $10^{14} \text{ g cm}^{-3}$. The spectral resolution of the energy grid is indicated by the spacing of the short horizontal lines (right ordinate), which are drawn at boundaries of the energy grid. Panel **a** displays results obtained with “low” spectral resolution (21 energy bins distributed geometrically between 0 and 380 MeV), panel **b** shows the run with “high” spectral resolution (81 energy bins covering the same spectral range). For better comparison Y_{ν_e} from the high-resolution run is drawn as a thin line also in panel **a**.

Fermi-Dirac distribution with zero temperature ($\mu_{\nu_e}^{\text{eq}}/T \simeq 100$) and hence

$$f = f^{\text{eq}}(\epsilon) = \Theta(\mu_{\nu_e}^{\text{eq}} - \epsilon) \quad , \quad \Theta(x) := \begin{cases} 1 & \text{for } x \geq 0, \\ 0 & \text{for } x < 0, \end{cases} \quad (5.6)$$

where the neutrino Fermi energy is given by the equilibrium chemical potential $\mu_{\nu_e}^{\text{eq}} = \mu_e + \mu_p - \mu_n$ (μ_e, μ_p and μ_n denote the chemical potentials including the rest energies of electrons, protons and neutrons, respectively). Since in our as well as in the code of Mezzacappa & Bruenn (1993c) average values of the emissivity (and hence the equilibrium distribution function) within individual energy bins are calculated by a zeroth order quadrature² (cf. eqns. A.36, A.37), the neutrino number density

$$n_{\nu_e} = \frac{4\pi}{(hc)^3} \int_0^\infty d\epsilon \epsilon^2 f(\epsilon) \stackrel{(5.6)}{=} \frac{4\pi}{(hc)^3} \frac{(\mu_{\nu_e}^{\text{eq}})^3}{3} \quad (5.7)$$

²As discussed in Appendix A.2.5 a zeroth order quadrature guarantees that detailed balance holds for our implementation of inelastic scattering reactions. It appears to be difficult to verify this fundamental property numerically when higher-order quadrature formulae are used.

computed by the code is (cf. Mezzacappa & Bruenn 1993c, equ. 67)

$$n_{\nu_e} = \frac{4\pi}{(hc)^3} \sum_{j=0}^{j_F-1} \Delta\epsilon_{j+1/2} \epsilon_{j+1/2}^2 + \begin{cases} \frac{4\pi}{(hc)^3} \Delta\epsilon_{j_F+1/2} \epsilon_{j_F+1/2}^2 & , \text{ if } \mu_{\nu_e}^{\text{eq}} \geq \epsilon_{j_F+1/2} , \\ 0 & , \text{ if } \mu_{\nu_e}^{\text{eq}} < \epsilon_{j_F+1/2} , \end{cases} \quad (5.8)$$

where $\Delta\epsilon_{j+1/2}$ is the width of the energy bin with boundaries ϵ_j and ϵ_{j+1} . The index j_F labels the energy bin, where the Fermi energy of the neutrino distribution is located ($\epsilon_{j_F} < \mu_{\nu_e}^{\text{eq}} \leq \epsilon_{j_F+1}$).

Equation (5.8) implies that in the completely degenerate case there is a sudden rise in the number density (and related quantities), each time the neutrino Fermi energy crosses the zone centre of a particular energy bin. In Fig. 5.11a this can be seen to occur for example at a mass coordinate of $M = 0.5 M_\odot$. Moving further inward, the baryon number density $n_B = m_u^{-1} \rho$ increases with the mass density, while the neutrino number density n_{ν_e} stays constant according to equ. (5.8), and therefore the neutrino fraction $Y_{\nu_e} := n_{\nu_e}/n_B$ decreases again after its initial rise. When the neutrino Fermi energy approaches the zone boundary of the same bin (e. g. at $M = 0.42 M_\odot$), the error introduced by equ. (5.8) vanishes. Almost exactly at this position (see the dotted vertical lines in Fig. 5.11a), the curve for Y_{ν_e} (bold line in Fig. 5.11a) intersects with the reference data (thin line in Fig. 5.11a) drawn from a highly resolved simulation (see below). Moving further towards smaller mass coordinates and higher densities, the neutrino Fermi energy $\mu_{\nu_e}^{\text{eq}}$ increases, but it is now below the zone centre energy of the next higher energy bin. The second case in equ. (5.8) applies, and n_{ν_e} is underestimated, until $\mu_{\nu_e}^{\text{eq}}$ approaches the zone centre and the pattern repeats itself. Due to the finite temperatures the whole pattern is smooth and Y_{ν_e} varies continuously which implies that a second intersection with the reference curve must be present between the mass coordinates of a local minimum of Y_{ν_e} and of a local maximum.

For comparison, we have computed the same model with a significantly enhanced spectral resolution: We spend 81 instead of 21 bins to resolve the energy range between 0 and 380 MeV. The error introduced by equ. (5.8) is considerably smaller, since much less phase-space is associated with an individual energy bin. The results of this simulation are displayed in Fig. 5.11b. We find the neutrino fraction (and related quantities) to be perfectly smooth functions of the mass coordinate. As a reasonable compromise between accuracy and computational load, we find that using approximately 30 (geometrically spaced) energy bins is sufficient to adequately resolve the Fermi surface of the degenerate distribution of electron neutrinos that builds up during collapse.

5.2 Core collapse and post-bounce evolution of a $15 M_\odot$ progenitor star

After having demonstrated that our newly developed radiation hydrodynamics method is able to compute accurate core-collapse models, we are ready to apply the numerical tool also to the interesting post-collapse phase, where a precise treatment of the neutrino transport is indispensable. A few reconsiderations of the physical approximations made for the collapse phase (cf. Sect. 5.1) concerning their validity also during the post-bounce evolution of the core are necessary at first. We will then describe the temporal evolution of one particular model that has been chosen to be able to compare with the MGFLD models of Bruenn (1993) and Bruenn et al. (1995, see also Bruenn & Mezzacappa 1994). Using our results, some of the basic physics characterizing the post-bounce phase which has already been briefly described in the introduction, will be highlighted in the course of describing the model.

5.2.1 Preliminaries

In the hydrodynamic shock wave that is launched by the bouncing inner core, kinetic energy of the infalling outer core material is dissipated into thermal energy. In the beginning typical post-shock temperatures and entropies per baryon are of the order of $T \simeq 10$ MeV and $s \simeq 10 k_B$, respectively. Thus, the large electron degeneracy present during collapse is lowered. Since the electron chemical potential decreases towards lower densities, positrons appear in appreciable number behind the shock at larger radii and electron antineutrinos can be created in the reaction $e^+ + n \rightarrow p + \bar{\nu}_e$. In addition, neutrino pairs of all flavours are produced by electron-positron annihilation.

5.2.2 Numerical model

Our initial model at the onset of collapse is taken from the $15 M_{\odot}$ stellar model “s15s7b2” (Woosley 1999), representative of a star with a relatively small iron core. The numerical grid extends out to a radius of 20 000 km, enclosing a total mass of $2.36 M_{\odot}$, which includes the central iron core ($0 \leq M \leq 1.28 M_{\odot}$), the silicon shell ($1.28 M_{\odot} \leq M \leq 1.77 M_{\odot}$) and a major part of the neon-magnesium-oxygen shell (cf. Fig. 5.1a). In total 400 radial grid zones are used for the hydrodynamics. The zones are initially distributed according to a prescription suggested for core-collapse simulations by Zwerger (1995) that ensures good resolution in the vicinity of the anticipated shock formation point. The hydrodynamic grid is advanced along with the fluid flow in the earlier phases of collapse, and is later kept fixed in time. The neutrino transport is calculated on a Eulerian radial grid consisting of 213 logarithmically spaced zones. The spectrum of neutrino energies is resolved by 27 geometrically spaced energy bins ($\epsilon_0 = 0$ and $\epsilon_{i+1} = \alpha \epsilon_i$ for $i \geq 1$, with $\epsilon_1 = 2$ MeV and $\epsilon_{27} = 380$ MeV). The collapse started without special triggering. In order to compare with the MGFLD simulations of Bruenn et al. (1995) and to the studies of Messer et al. (1998) and Mezzacappa & Messer (1999), hydrodynamics and neutrino transport are calculated in the Newtonian approximation. As in the latter models, the equation of state of Lattimer & Swesty (1991) is invoked for the high density regime ($\rho \gtrsim 10^8$ g cm $^{-3}$), using the value $K = 180$ MeV for the nuclear incompressibility modulus. For the other parameters entering the equation of state, e. g. nuclear saturation density, symmetry energy, etc., we use the “standard” values (see Sect. 3.1.2) as given by Lattimer & Swesty (1991). At lower densities, an equation of state for an ideal gas of a given mixture of baryonic species supplemented by Coulomb-lattice corrections, and ideal gases of electrons, positrons and photons (Janka 1999) is employed. More information about both equations of state and their joint implementation can be found in Sect. 3.1.2 For simplicity, and because we are not primarily interested in nucleosynthesis aspects, nuclear reactions are not taken into account in the low-density regime, where the stellar matter is out of nuclear statistical equilibrium (NSE).

In order to save computer time³, neutrino transport is calculated for electron neutrinos and antineutrinos only. The considered neutrino-matter interactions comprise inelastic scattering of neutrinos off electrons and positrons ($\nu \in \{\nu_e, \bar{\nu}_e\}$)

$$\nu + e^{\pm} \rightleftharpoons \nu + e^{\pm}, \quad (5.9)$$

³The entire simulation of model “WS15”, which was running with a speed of 3 GFlop/s on a single NEC SX-5/3C vector processor (with a theoretical peak performance of 8 GFlop/s) of the “Himiko” machine at the Rechenzentrum Garching took several hundred hours of CPU time.

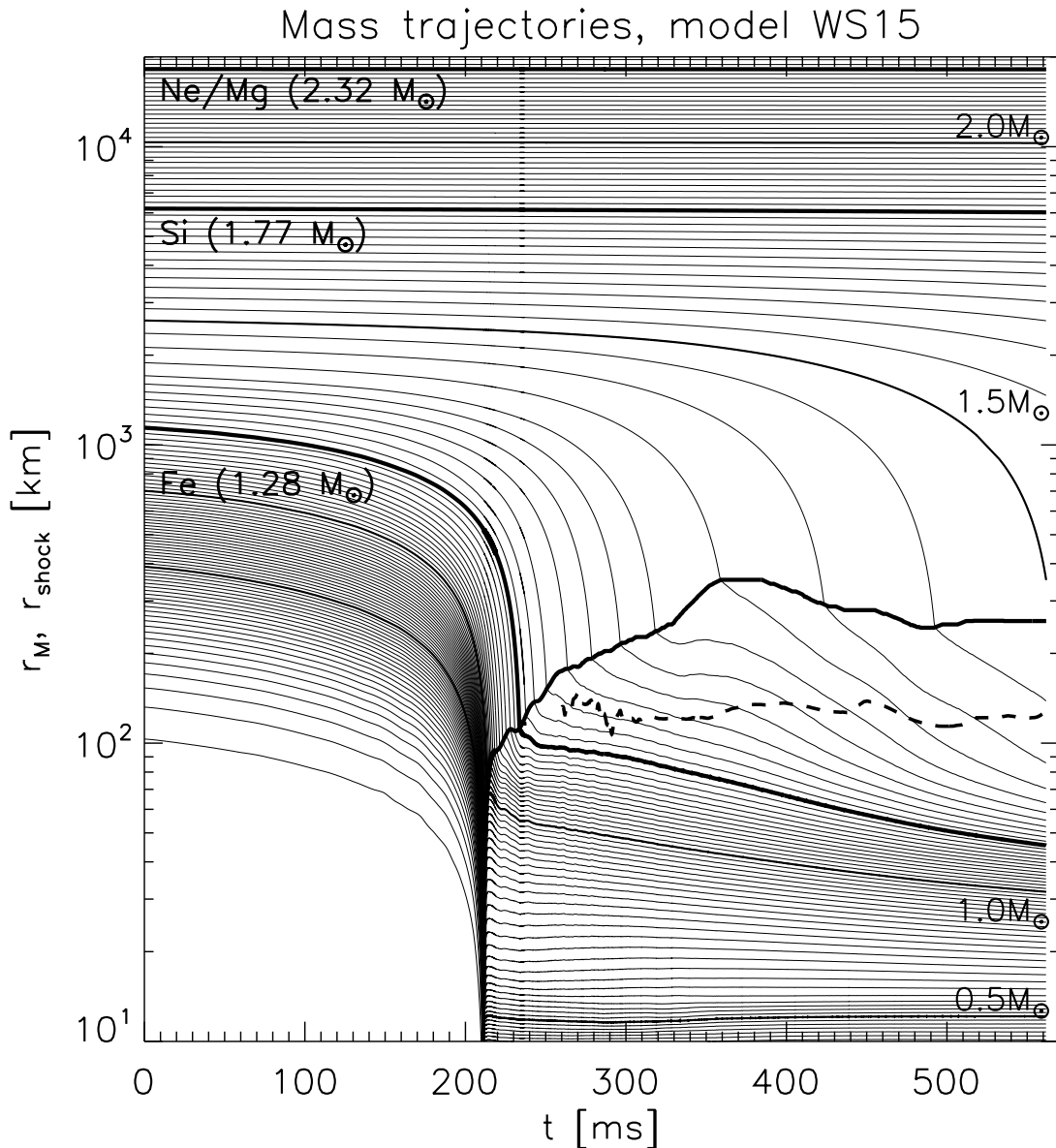


Figure 5.12: Trajectories of selected mass shells vs. time for model “WS15”. The plotted trajectories correspond to mass shells that are equidistantly spaced in intervals of $0.02 M_{\odot}$. Bold lines indicate the trajectories of the initial composition interfaces. The bold line originating at $t_b = 211.60$ ms traces the position of the hydrodynamic shock wave. The dashed curve shows the position of the gain radius (cf. equ. 5.28).

elastic scattering of neutrinos off free nucleons ($\nu \in \{\nu_e, \bar{\nu}_e\}$)

$$\nu + \begin{pmatrix} n \\ p \end{pmatrix} \rightleftharpoons \nu + \begin{pmatrix} n \\ p \end{pmatrix}, \quad (5.10)$$

coherent scattering of neutrinos off heavy nuclei including corrections due to ion-ion correlations

($\nu \in \{\nu_e, \bar{\nu}_e\}$)



electron captures onto free protons



and heavy nuclei



and positron captures by free neutrons



and the inverses of the latter processes. The interaction rates are calculated as detailed in Appendix A. Both the disregard of muon and tau neutrinos and antineutrinos and the omission of pair processes for ν_e and $\bar{\nu}_e$ are justifiable when the specific role of the neutrino transport for the delayed explosion mechanism is to be explored: Neutrino heating and cooling below the stalled shock wave is mediated almost exclusively by the charged-current absorption reactions $\nu_e + n \rightleftharpoons e^- + p$ and $\bar{\nu}_e + p \rightleftharpoons e^+ + n$ with only minor contributions due to pair annihilation, e. g. $e^- + e^+ \rightleftharpoons \nu_e + \bar{\nu}_e$ (Janka 1991a) or inelastic scattering reactions (see also Bruenn 1993, Fig. 6). However, the neglect of muon and tau neutrinos is known to affect the early shock propagation phase (cf. Bruenn 1989a) as well as the thermal evolution of the protoneutron star. Implications for our model will be discussed at the end of this chapter. There it will be argued that the major approximations made for our model (viz. Newtonian gravity, absence of muon and tau flavour neutrinos) most probably *facilitate* the supernova explosion.

5.2.3 Results

We first give an overview of the global evolution of our model that has been followed through core-collapse and bounce and for roughly 450 ms into the post-bounce phase. According to the position and the velocity (note the logarithmic radius scale of Fig. 5.12!) of the shock front, a number of distinct temporal phases can be identified after core collapse. They will be discussed in the subsequent sections.

Overview of the global evolution

Mass trajectories: Figure 5.12 provides a general overview of the complete dynamical evolution of our model “WS15”. We display the trajectories $r_M(t)$ of a number of selected Lagrangian mass shells M , as obtained by inverting the relation

$$M(t, r) = 4\pi \int_0^r dr' r'^2 \rho(t, r') \quad (5.15)$$

with respect to the radial coordinate r . Between $t = 0$ and $t \approx 210$ ms, one recognizes the collapse phase, as characterized by a progressive contraction of the iron core. Mass shells with $M \gtrsim 1.5 M_{\odot}$ remain nearly unaffected by the collapse of the iron core. After roughly 210 ms, core bounce occurs

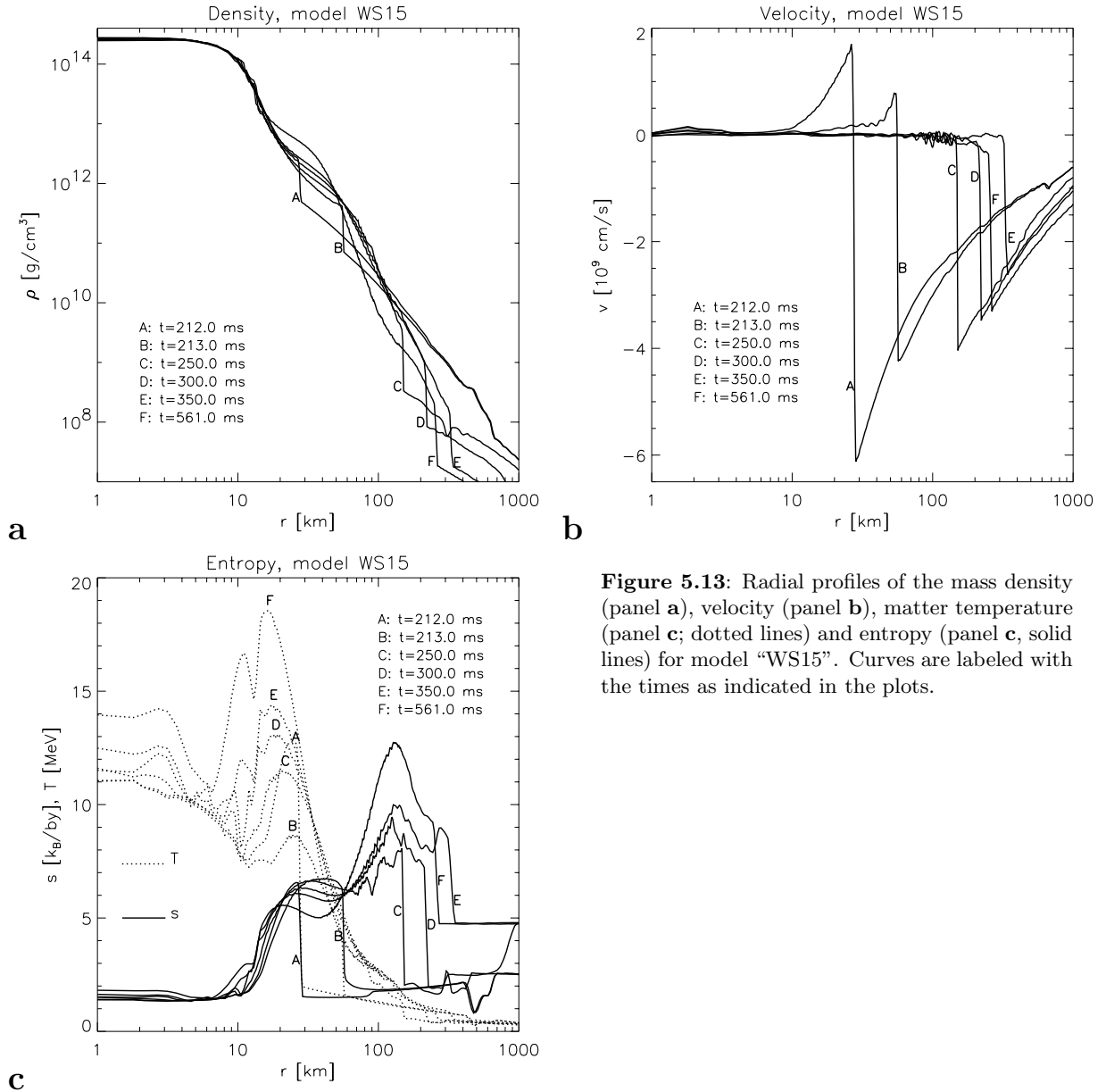


Figure 5.13: Radial profiles of the mass density (panel a), velocity (panel b), matter temperature (panel c; dotted lines) and entropy (panel c, solid lines) for model “WS15”. Curves are labeled with the times as indicated in the plots.

coherently for the inner core ($M_{\text{IC}} \approx 0.6 M_{\odot}$). The rebounding inner core drives a shock wave into the infalling outer core. When passing the hydrodynamic shock, material of the outer core is decelerated and subsequently settles onto the newly formed neutron star. At 160 ms after its formation, the hydrodynamic shock reaches a maximum radius of $r \approx 350$ km, then it recedes again and ends as an accretion shock at $r \approx 250$ km.

Profiles: Figure 5.13 shows the post-bounce evolution of the radial profiles of different hydrodynamic quantities. For the mass density, one recognizes a rapid steepening of the density profile behind the shock with time (see e. g. curves “E” and “F” for $\rho \gtrsim 10^9 \dots 10^{10} \text{ g cm}^{-3}$ in Fig. 5.13a),

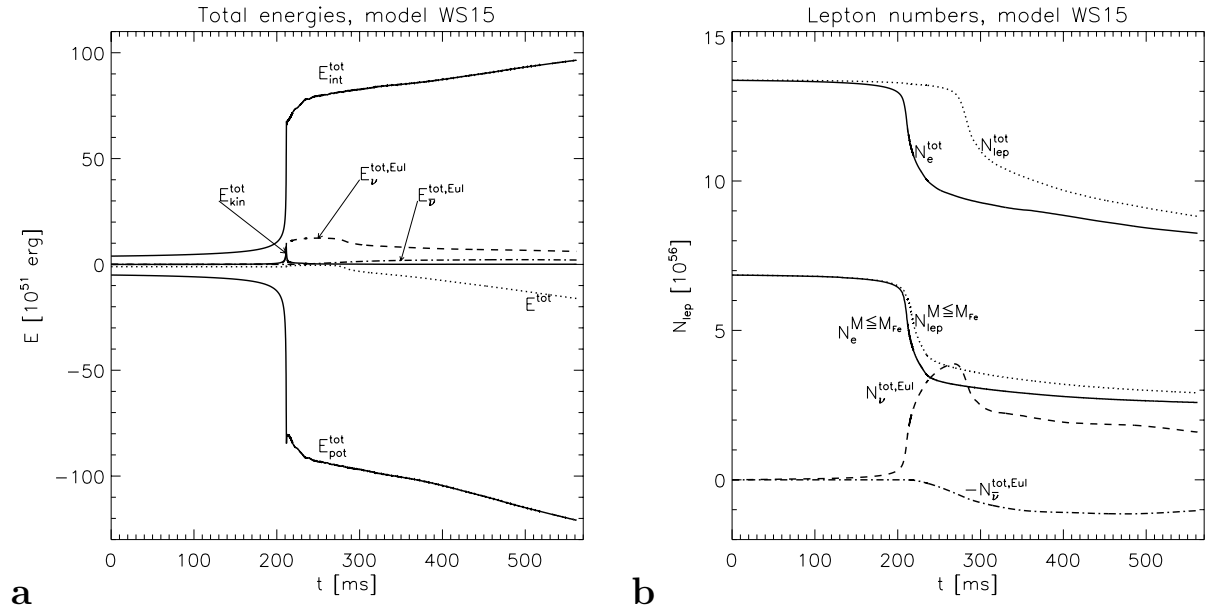


Figure 5.14: Panel **a** shows integral values of some energy quantities as functions of time for model “WS15”: Fluid energies (solid lines), viz. kinetic energy ($E_{\text{kin}}^{\text{tot}}$), gravitational potential energy ($E_{\text{pot}}^{\text{tot}}$), internal energy ($E_{\text{int}}^{\text{tot}}$), and neutrino energies ($E_{\nu_e}^{\text{tot,Eul}}$ and $E_{\bar{\nu}_e}^{\text{tot,Eul}}$, dashed and dashed-dotted lines, respectively). E^{tot} (dotted line) denotes the sum of all individual energies present on the numerical grid. Panel **b** shows integral values on the grid of some lepton numbers: the net number of charged leptons ($N_e^{\text{tot}} := N_{e^-}^{\text{tot}} - N_{e^+}^{\text{tot}}$; upper solid line), the number of electron neutrinos (dashed) and electron antineutrinos (dashed-dotted). The upper thin dotted line shows the total net lepton number ($N_{\text{lep}}^{\text{tot}} := N_{e^-}^{\text{tot}} + N_{\nu_e}^{\text{tot,Eul}} - N_{e^+}^{\text{tot}} - N_{\bar{\nu}_e}^{\text{tot,Eul}}$) residing on the numerical grid. For comparison, panel **b** also shows the net number of charged leptons $N_e^{M \leq M_{\text{Fe}}}$ (lower solid line) and of all leptons (lower thin dotted line) of the “iron core”, i. e. only particles within $0 \leq r \leq r_{M_{\text{Fe}}}$ with $M_{\text{Fe}} = 1.28 M_{\odot}$ are considered.

resulting in the formation of the so-called “cliff” (Bethe & Wilson 1985; Bethe 1990), which bounds the newly formed protoneutron star from the outside “vacuum” (see also Bruenn 1993, Fig. 8).

As the shock propagates outwards the postshock velocities decrease rapidly. With the exception of a short period between 320 ms and 350 ms (see curves “E” and “F” in Fig. 5.13b), where small positive values are found, the velocities immediately behind the shock front have steadily decreased dropping to values of $v \approx -5 \times 10^8 \text{ cm s}^{-1}$ by the time our calculation was terminated (Fig. 5.13b). No indications for a successful shock revival were seen. However, the maximum values of the entropy $s \approx 13 k_{\text{B}}$ (Fig. 5.13c, curve “F”) come close to the value $s \approx 15 k_{\text{B}}$, which is regarded as an estimate for the minimum entropy in the heating region that is required to obtain a successful explosion in this star (e. g. Janka & Keil 1998).

Integral quantities: To conclude the overview, we briefly discuss the temporal evolution of some integral quantities: Figure 5.14a shows the total values on the computational grid of the potential, kinetic, internal energy as well as the energy in electron neutrinos and antineutrinos and the sum of all energies. When equ. (2.62, see also equ. 2.67) is integrated over the computational domain ($0 \leq r \leq R$) one obtains

$$\frac{\partial}{\partial t} (E_{\text{int}}^{\text{tot}} + E_{\text{kin}}^{\text{tot}} + E_{\text{pot}}^{\text{tot}} + E_{\nu_e}^{\text{tot,Eul}} + E_{\bar{\nu}_e}^{\text{tot,Eul}}) = -4\pi R^2 \left[(\rho e + p + \frac{1}{2} \rho v^2) v \right]_{r=R} - L^{\text{Eul}}(R), \quad (5.16)$$

with

$$E_{\text{int}}^{\text{tot}} := \int dV \rho e, \quad E_{\text{kin}}^{\text{tot}} := \frac{1}{2} \int dV \rho v^2, \quad E_{\text{pot}}^{\text{tot}} := \frac{1}{2} \int dV \rho \phi, \quad (5.17)$$

and

$$E_{\nu}^{\text{tot,Eul}} = \int dV E_{\nu}^{\text{Eul}} \quad , \quad \nu \in \{\nu_e, \bar{\nu}_e\}, \quad (5.18)$$

where $E_{\nu}^{\text{tot,Eul}}$ denotes the total energy in neutrinos and antineutrinos, respectively and $L^{\text{Eul}} = 4\pi R^2 (F_{\nu_e}^{\text{Eul}} + F_{\bar{\nu}_e}^{\text{Eul}})$ is the sum of the luminosities of neutrinos and antineutrinos, all measured in the Eulerian frame of reference. When the sum of all energies inside the computational volume ($E_{\text{int}}^{\text{tot}} + E_{\text{kin}}^{\text{tot}} + E_{\text{pot}}^{\text{tot}} + E_{\nu_e}^{\text{tot,Eul}} + E_{\bar{\nu}_e}^{\text{tot,Eul}}$) is corrected for the neutrino energy that is radiated away from the grid and — less important — for the fluid energy that is advected through the outer grid boundary (given by the first term on the rhs. of equ. 5.16), energy is conserved to better than 1% of the maximum potential energy. Figure 5.14b shows the net number of charged (electron flavour) leptons, as defined by

$$N_e^{\text{tot}} := N_{e^-}^{\text{tot}} - N_{e^+}^{\text{tot}} = m_{\text{u}}^{-1} \int dV \rho Y_e, \quad (5.19)$$

together with the total number of electron neutrinos and antineutrinos

$$\mathcal{N}_{\nu}^{\text{tot,Eul}} := \int dV \mathcal{N}_{\nu}^{\text{Eul}} \quad , \quad \nu \in \{\nu_e, \bar{\nu}_e\}. \quad (5.20)$$

A conservation equation for the total lepton number is obtained by integrating equ. (2.64) over the computational domain ($0 \leq r \leq R$) which gives

$$\frac{\partial}{\partial t} (N_e^{\text{tot}} + \mathcal{N}_{\nu_e}^{\text{tot,Eul}} - \mathcal{N}_{\bar{\nu}_e}^{\text{tot,Eul}}) = -4\pi R^2 [n_e v]_{r=R} - \mathcal{L}^{\text{Eul}}, \quad (5.21)$$

where $\mathcal{L}^{\text{Eul}} = 4\pi R^2 (\mathcal{F}_{\nu_e}^{\text{Eul}} - \mathcal{F}_{\bar{\nu}_e}^{\text{Eul}})$ is the number of electron neutrinos minus the number of electron antineutrinos that is radiated away at $r = R$ per unit time. When the lepton number carried away by neutrinos leaving the computational volume and the number of charged leptons that are advected through the outer grid boundary (given by the first term on the rhs. of equ. 5.21) is also taken into account, the total lepton number $N_{\text{lep}}^{\text{tot}} := N_{e^-}^{\text{tot}} + \mathcal{N}_{\nu_e}^{\text{tot}} - N_{e^+}^{\text{tot}} - \mathcal{N}_{\bar{\nu}_e}^{\text{tot}}$ is conserved to within an accuracy of better than 0.1% of the initial number of charged leptons on the grid.

Figure 5.14b reveals that starting with the time of bounce, a large number of electron neutrinos, and somewhat later also electron antineutrinos are created at the expense of the corresponding charged leptons. Figure 5.14b also shows that most of the neutrinos are created within the former iron core (i. e. inside a mass coordinate of $M_{\text{Fe}} = 1.28 M_{\odot}$).

As can be seen from Fig. 5.14a, neutrino energies amount to about 10% of the typical internal energies of the fluid. Starting at about $t \approx 70$ ms after bounce, which is approximately the light-crossing time between the shock wave and the outer grid boundary, one recognizes a steady decrease of the total energy and lepton number present on our computational grid. This is caused by the fact that the intense burst of neutrinos leaves the computational grid at the outer boundary. This burst of electron neutrinos is visible in the neutrino luminosities depicted in Fig. 5.15, where we plot the ν_e and $\bar{\nu}_e$ luminosities and the mean energies as measured at a radius of $r = 1000$ km as

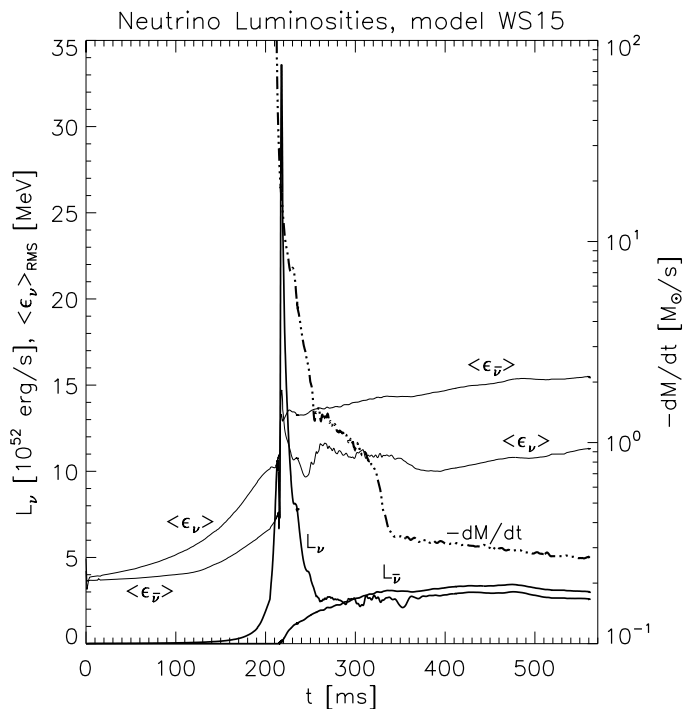


Figure 5.15: Electron neutrino and antineutrino luminosities (bold solid lines) and mean energies (thin solid lines), measured by a comoving observer located at $r = 1000$ km as functions of time. Also shown is the mass accretion rate $dM/dt = 4\pi r_s(t)^2 \rho(t, r_s(t)) v(t, r_s(t))$, through the shock (dashed-dotted line, scale on the right ordinate) its position $r_s(t)$ being defined by the minimum of the infall velocity. The figure can be compared with Bruenn et al. (1995, Figs. 3, 4; see also Bruenn 1993, Fig. 11).

a function of time. The burst arrives at the chosen radial position, only 6 ms after core bounce, reaching a peak value of $L_{\nu_e} = 3.36 \times 10^{53} \text{ erg s}^{-1}$. Within 40 ms the electron neutrino luminosity decreases by more than an order of magnitude until it approximately equals the luminosity of electron antineutrinos. For roughly 200 ms, both luminosities remain almost constant at a value of $L_{\nu_e/\bar{\nu}_e} \approx 3 \times 10^{52} \text{ erg s}^{-1}$, until they begin to decay slowly. Together with the initial rise of the luminosities one notices in Fig. 5.15 a sharp increase of the mean energy of the neutrinos, expressed in terms of the RMS-energy

$$\langle \epsilon_{\nu} \rangle_{\text{RMS}} := \left(\frac{\int_0^{\infty} d\epsilon \epsilon^2 J_{\nu}(\epsilon)}{\int_0^{\infty} d\epsilon J_{\nu}(\epsilon)} \right)^{1/2}, \quad \nu \in \{\nu_e, \bar{\nu}_e\}. \quad (5.22)$$

The RMS-energy of electron neutrinos rises from $\langle \epsilon_{\nu} \rangle_{\text{RMS}} = 10.9$ MeV to $\langle \epsilon_{\nu_e} \rangle_{\text{RMS}} = 14.7$ MeV, drops to $\langle \epsilon_{\nu_e} \rangle_{\text{RMS}} = 10.5$ MeV during the luminosity decline and, after showing some transient variability, increases modestly to reach $\langle \epsilon_{\nu_e} \rangle_{\text{RMS}} = 11.2$ MeV at the time our simulation was terminated. The sudden rise from $\langle \epsilon_{\bar{\nu}_e} \rangle_{\text{RMS}} = 7.6$ MeV to $\langle \epsilon_{\bar{\nu}_e} \rangle_{\text{RMS}} = 13.3$ MeV of the RMS-energy of the electron antineutrinos is followed by a modest increase similar to the case of electron neutrinos. At the end of the calculation a value of $\langle \epsilon_{\bar{\nu}_e} \rangle_{\text{RMS}} = 15.5$ MeV is reached.

Collapse and shock formation

The collapse phase of model “WS15” proceeds virtually identical to model “WS15_nue”, which was already analyzed in detail previously. Concerning the implemented physics, models “WS15_nue” and “WS15” differ only in the facts that in the latter model also electron antineutrinos are taken into account and electron captures onto heavy nuclei are included. As it was argued previously,

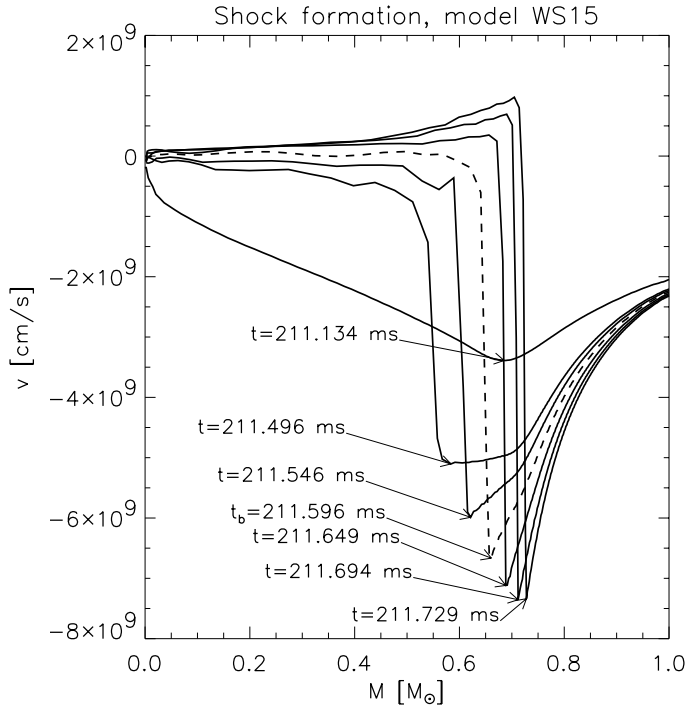


Figure 5.16: Profiles of the velocity vs. enclosed mass for model “WS15”. The corresponding times are given in the plot. The dashed line corresponds to the time of bounce $t_b := 211.60$ ms (see the text).

electron antineutrinos cannot be produced abundantly during collapse due to the high degeneracy of electrons and therefore do not carry appreciable amounts of energy and lepton number. In fact, at core bounce we find the total number of electron antineutrinos on the computational grid to be about six orders of magnitude smaller than the number of electron neutrinos in model “WS15”, and therefore we confirm that the electron antineutrinos can well be neglected for the collapse dynamics (cf. Fig. 5.14b). Due to nuclear shell effects electron captures onto heavy nuclei, a reaction which was also neglected in model “WS15_nue”, already cease when densities of the order of 5×10^{10} g cm $^{-3}$ are exceeded. Before this epoch, the capture rates of heavy nuclei are too small to contribute notably to the deleptonization of the core. The maximum difference between the central lepton fractions and entropies of models “WS15” and “WS15_nue” amounts to $\Delta Y_{\text{lep},c} := Y_{\text{lep}}^{\text{WS15}}(r=0) - Y_{\text{lep}}^{\text{WS15_nue}}(r=0) \approx -0.005$ and $\Delta s_c := s^{\text{WS15}}(r=0) - s^{\text{WS15_nue}}(r=0) \approx 0.01$, which for both quantities is only a few percent of the total change occurring during the entire collapse phase. The maximum differences are found at the time, when the central density is $\rho_c \approx 2 \times 10^{10}$ g cm $^{-3}$. For $\rho_c > 3 \times 10^{11}$ g cm $^{-3}$, the curves of the central lepton fraction as a function of time are practically indistinguishable in both models. The same is true for the central entropy.

Core bounce and shock formation are visible in Fig. 5.16. At $t \approx 211.3$ ms, the equation of state first stiffens at the centre of the homogeneously collapsing inner core (the adiabatic exponent at the centre rises from $\gamma \approx 1.2$ to $\gamma \approx 2.1$; subsequently at $t \approx 211.5$ ms a maximum value of $\gamma \approx 2.4$ is reached). This marks the point of “last good homology”. Only 0.05 ms later, the innermost $0.5 M_{\odot}$ have stopped their infall. At the edge of the subsonic inner core, the pressure waves emanating from the centre steepen to form the bounce shock which detaches and starts propagating outwards.

Adopting the convention to define the location of shock formation employed by Bruenn &

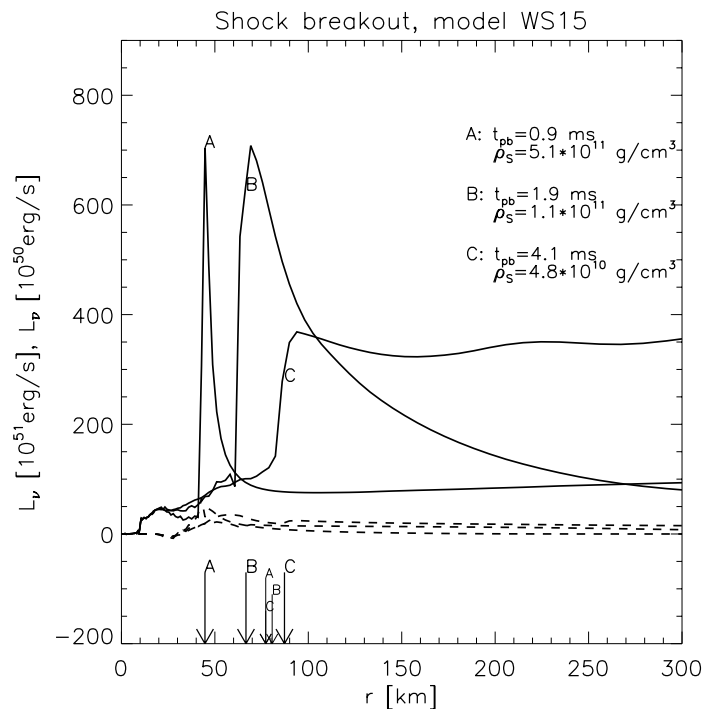


Figure 5.17: Shock breakout for model “WS15”: Radial profiles of the comoving frame neutrino luminosities (solid lines) are displayed for three different post-bounce times (t_{pb}). The corresponding radial positions of the shock are indicated by bold arrows, ρ_{S} denotes the mean of pre and postshock densities. The thin arrows indicate the positions of the (electron) neutrino spheres (for a definition see equ. 5.23). For comparison we also show the antineutrino luminosities (dashed lines, note the different scalings in the plot). The figure may be compared to Bruenn & Haxton (1991, Fig. 9).

Mezzacappa (1997), who consider the radial position inside the inner core, where the entropy per baryon first exceeds a value of $3 k_{\text{B}}$, we find that the shock in model “WS15” forms at a radius of $R_{\text{shock}} = 12.5$ km corresponding to an enclosed mass of $M_{\text{shock}} \approx 0.62 M_{\odot}$. This happens $t_{\text{b}} = 211.60$ ms after the simulation was started, which will be referred to as the time of the bounce in the following. The central density at this time is $\rho_{\text{c}}(t = t_{\text{b}}) = 3.3 \times 10^{14} \text{ g cm}^{-3}$.

Prompt shock propagation

Shock breakout: At early times after core bounce, the hydrodynamic shock is still located well inside the neutrinospheres — defined as the radial position where the average transport optical depth (for a definition of the transport opacity χ^{tr} see equ. 2.30)

$$\langle \tau^{\text{tr}} \rangle(r) := \int_r^{\infty} dr' \frac{\int_0^{\infty} d\epsilon H(r', \epsilon) \chi^{\text{tr}}(r', \epsilon)}{\int_0^{\infty} d\epsilon H(r', \epsilon)} \quad (5.23)$$

equals unity (cf. Janka 1991b, Eqns. 3.55, 3.56) — and thus the neutrino drift velocities in the vicinity of the shock are small compared to the velocity of the material falling through the shock. Therefore only a minor fraction of the neutrinos that are abundantly produced by electron captures onto free protons in the shock heated matter are able to diffuse ahead of the shock front. For this reason, the resulting precursor of the luminosity that is moving with the shock is confined to a narrow region around the shock front (Fig. 5.17, curve A). The large positive gradient of the luminosity that is present behind the shock reflects strong net cooling (and deleptonization) of the post-shock material (cf. equ. 2.59). Ahead of the shock, some of the emitted neutrinos get reabsorbed by the ambient heavy nuclei and free nucleons, yet the net heating rates are much smaller. In particular, the neutrino heating rate above the shock front is not large enough to account for significant

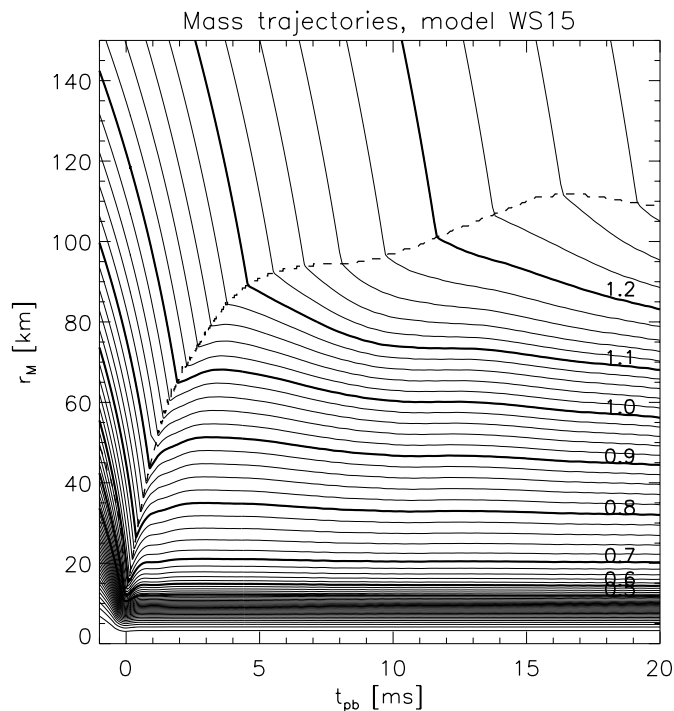


Figure 5.18: Prompt shock propagation of model “WS15”: The radii of selected mass shells is plotted as a function of time after core bounce (see Fig. 5.12 for a global overview). The plotted trajectories correspond to mass shells that are equidistantly spaced in intervals of $0.02 M_{\odot}$. Bold lines are labeled with the corresponding value in units of M_{\odot} . The dashed line traces the radial position of the shock front.

dissociation of the preshock material. If present, a “pre-dissociation” of heavy nuclei into alpha particles or free nucleons would obviously decrease the amount of disintegration energy that is lost by the shock, when heavy nuclei pass the shock front and are broken up into free nucleons and alpha particles (cf. Bruenn & Haxton 1991, for an elaborate study focussing on this subject). When the shock propagates towards lower densities and approaches the neutrinospheres, the neutrinos produced in the shock-heated matter encounter preshock material of decreasing opacity and thus the precursor gets more extended, until finally, when the shock has passed the neutrinospheres (“shock breakout”), the neutrinos escape freely (Fig. 5.17, curve C).

At this time an intense outburst (often called “neutronization burst”) of neutrinos is released and starts to travel outward through the star with the speed of light. For example, at $t_{\text{pb}} := t - t_{\text{b}} = 4.37$ ms, which is roughly 1.4 ms after shock breakout has occurred at $r \approx 80$ km, the burst, which can be recognized by a prominent peak in the neutrino luminosity as a function of time at a given radial position, reaches a radius of $r = 500$ km. Integrating the neutrino luminosity over time, the total energy contained by the burst is calculated as 1.5×10^{51} erg in our model “WS15”.

At $t \approx 280$ ms, the peak has reached the outer boundary of our computational grid which is located at $r = 2 \times 10^4$ km. Accordingly, the integral energy and lepton number on the computational grid start to decrease notably with the rate of the energy (and lepton number) losses, which can be calculated from the sum (and the difference) of the surface luminosities of neutrinos and antineutrinos (and their mean energies) (cf. Fig. 5.14). As can be seen from Fig. 5.17, electron antineutrinos play no substantial role during the first few milliseconds of the prompt shock propagation phase.

As a result of the neutronization burst, a deep trough in the radial profiles of the electron fraction and the total lepton fraction is left behind the shock (see Fig. 5.19), which, by virtue of the diminished lepton pressure, weakens the shock wave. The minimum value of the electron fraction

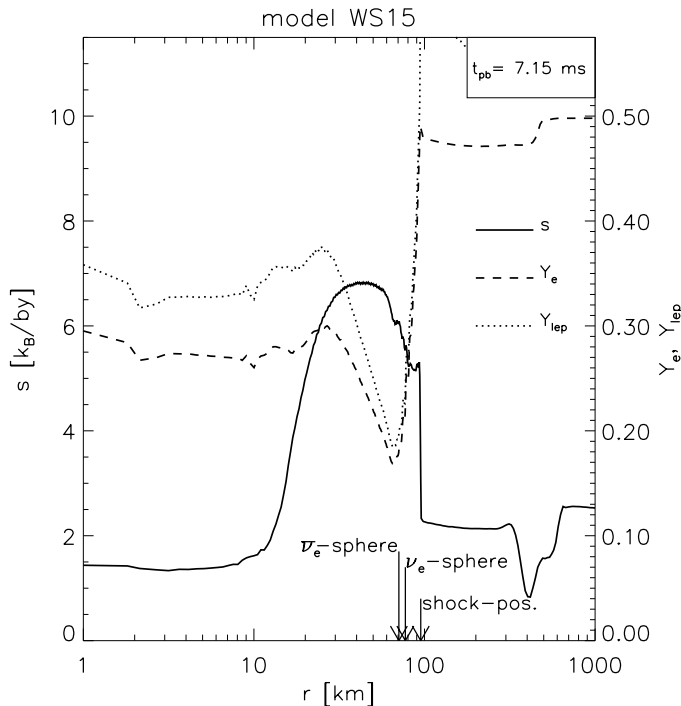


Figure 5.19: Profiles of the entropy per baryon (solid line, scale given by the axis on the left hand side), electron fraction (dashed, scale on the rhs.) and total lepton fraction (dotted, scale on the rhs.) at $t_{\text{pb}} = 7.15$ ms. Arrows point to the radial positions of the neutrinospheres (for a definition see equ. 5.23) and the shock front, respectively. The figure may be directly compared to Bruenn et al. (1995, Fig. 2). See also Bruenn (1993, Fig. 13).

reached just inside the neutrinospheres is somewhat higher in our model ($Y_e(r \approx 70\text{km}) = 0.17$) compared to model “WPE15 ls(180) Newt20” ($Y_e(r \approx 65\text{km}) = 0.13$) of Bruenn et al. (1995). This is consistent with the observation that the number of released electron antineutrinos is slightly larger in our case. The latter can be explained by the different treatment of the neutrino transport (Bruenn et al. 1995 use a MGFLD approximation) and the fact that μ - and τ -neutrinos are absent in our model as compared to Bruenn et al. (1995): When included μ - and τ -neutrinos are able to share the energy liberated by the shocked stellar material with $\bar{\nu}_e$ -neutrinos and hence the luminosity of $\bar{\nu}_e$ -neutrinos will be reduced.

Dissociation losses: Another obstacle to the prompt shock propagation is the loss of thermal energy in (photo-) dissociating heavy nuclei in the hot postshock region. For a complete dissociation of heavy nuclei passing the shock into free nucleons, roughly 8 MeV per single nucleon or more than 10^{51} erg per $0.1 M_{\odot}$ ($\cong 10^{56}$ nucleons) of material are required. In order to compare this with the energy lost due to the neutronization burst in our model, we note that at $t_{\text{pb}} \approx 4$ ms, matter consisting of 75% ^{60}Co , 15% ^4He and 10% free nucleons (mass fractions) passes the shock at a rate of $dM/dt \approx -23 M_{\odot}\text{s}^{-1}$ (see Fig. 5.15). All heavy nuclei get dissolved resulting in a composition that varies between 50% ^4He and 50% free nucleons immediately behind the shock and more than 95% free nucleons 20 km further inside. The corresponding rate of thermal energy consumption amounts to a few times 10^{53} ergs $^{-1}$, which is comparable to the luminosity of the neutronization burst. During the prompt shock propagation phase ($t_{\text{pb}} \lesssim 20$ ms) the shock dissociates roughly $0.6 M_{\odot}$ of iron like material (cf. Fig. 5.18) and thereby loses almost 10^{52} erg of energy.

By the combined action of the neutronization burst and the dissociation losses, only 3.5 ms after core bounce, when the shock has reached a radius of 85 km corresponding to a mass coordinate

of $1.08 M_{\odot}$, the fluid velocity immediately behind the shock front gets negative (Fig. 5.18)⁴. One also recognizes from Fig. 5.18 that the velocity of the shock as measured relative to the centre of the star has decreased substantially by the time $t_{\text{pb}} \approx 5$ ms. The expanding shock turns into a stagnant accretion shock (i. e. the Eulerian radius coordinate of the shock front does not change, yet the shock moves outwards in the Lagrangian mass coordinate) at a radius between 90 km and 110 km at $t_{\text{pb}} \approx 5$ ms. By the rapid accretion of mass (see Fig. 5.15) the shock gets subsequently pushed out to a radius of roughly 220 km within the next 100 ms (see Fig. 5.12).

Neutrino heating

Gain radius: Figure 5.20 shows the net neutrino heating rate as a function of stellar radius at three different times during our simulation “WS15”. Recall that positive values of the *net*-heating rate mean that energy is transferred to the stellar matter, whereas negative values indicate net cooling. All displayed profiles show an extended region beneath the shock, where neutrino heating dominates. Inside the so-called “gain radius” the situation is reversed, and net cooling occurs in a region between the neutrinospheres and the gain radius. The existence of such a pattern has turned out to be a generic feature that almost necessarily arises as a consequence of the thermodynamic conditions in the atmosphere surrounding the newly formed neutron star. It can be understood as follows (for a more thorough analysis, see e. g. Bruenn 1993): The dominating neutrino interactions with the stellar matter between the neutrinospheres and the hydrodynamic shock are the charged current reactions (cf. Fig. 5.21)

$$\begin{aligned}\nu_e + n &\rightleftharpoons e^- + p, \\ \bar{\nu}_e + p &\rightleftharpoons e^+ + n.\end{aligned}\tag{5.24}$$

With the opacities given by equations (A.38, A.39), the heating rate (per baryon; $q_E := n_{\text{B}}^{-1} Q_E$) for the neutrino absorption processes of (5.24) can be rewritten as⁵

$$\begin{aligned}q_E^+(r) &:= 4\pi \frac{m_{\text{u}}}{\rho} \int_0^{\infty} d\epsilon (\kappa_{\text{a},\nu_e}^*(\epsilon) J_{\nu_e}(\epsilon) + \kappa_{\text{a},\bar{\nu}_e}^*(\epsilon) J_{\bar{\nu}_e}(\epsilon)) \\ &\approx \int_0^{\infty} d\epsilon \epsilon^2 (X_n \sigma_{\text{a}} J_{\nu_e}(\epsilon) + X_p \sigma_{\text{a}} J_{\bar{\nu}_e}(\epsilon)) \\ &= X_n \sigma_{\text{a}} \langle \epsilon_{\nu_e} \rangle_{\text{RMS}}^2 \frac{L_{\nu_e}}{4\pi r^2} \frac{1}{\langle f_{H\nu_e} \rangle} + X_p \sigma_{\text{a}} \langle \epsilon_{\bar{\nu}_e} \rangle_{\text{RMS}}^2 \frac{L_{\bar{\nu}_e}}{4\pi r^2} \frac{1}{\langle f_{H\bar{\nu}_e} \rangle},\end{aligned}\tag{5.25}$$

with $\sigma_{\text{a}} := \sigma_0(g_V^2 + 3g_A^2)/(4m_e^2 c^4)$ (cf. eqns. A.38, A.39). X_n and X_p are the mass fractions of free neutrons and protons, respectively. The RMS-energy $\langle \epsilon_{\nu} \rangle_{\text{RMS}}$ and the energy averaged flux factor $\langle f_{H\nu} \rangle$ are defined according to equ. (5.22) and equ. (5.3), respectively ($\nu \in \{\nu_e, \bar{\nu}_e\}$).

Equation (5.25) reveals the basic factors that determine the positive contribution to the net neutrino heating rate. In addition to the abundances of absorbing nucleons, the heating rate depends on the total luminosity, the spectral distribution of the neutrinos via the mean squared energies and

⁴By virtue of $Dr_M(t)/Dt = v$, the fluid velocity is given by the local time derivative of a mass trajectory $r_M(t)$.

⁵Equation (5.25) is derived with the approximation $\kappa_{\text{a}}^*(\epsilon) \propto \epsilon^2$, i. e. blocking of electron and neutrino final states is neglected and the electron rest mass and the rest mass difference between neutron and proton are assumed to be small compared to the neutrino energy (cf. Appendix A.2.1). In the examples presented here, the combined effect of these assumptions amounts to less than one percent difference compared to the results obtained with the exact formulae.

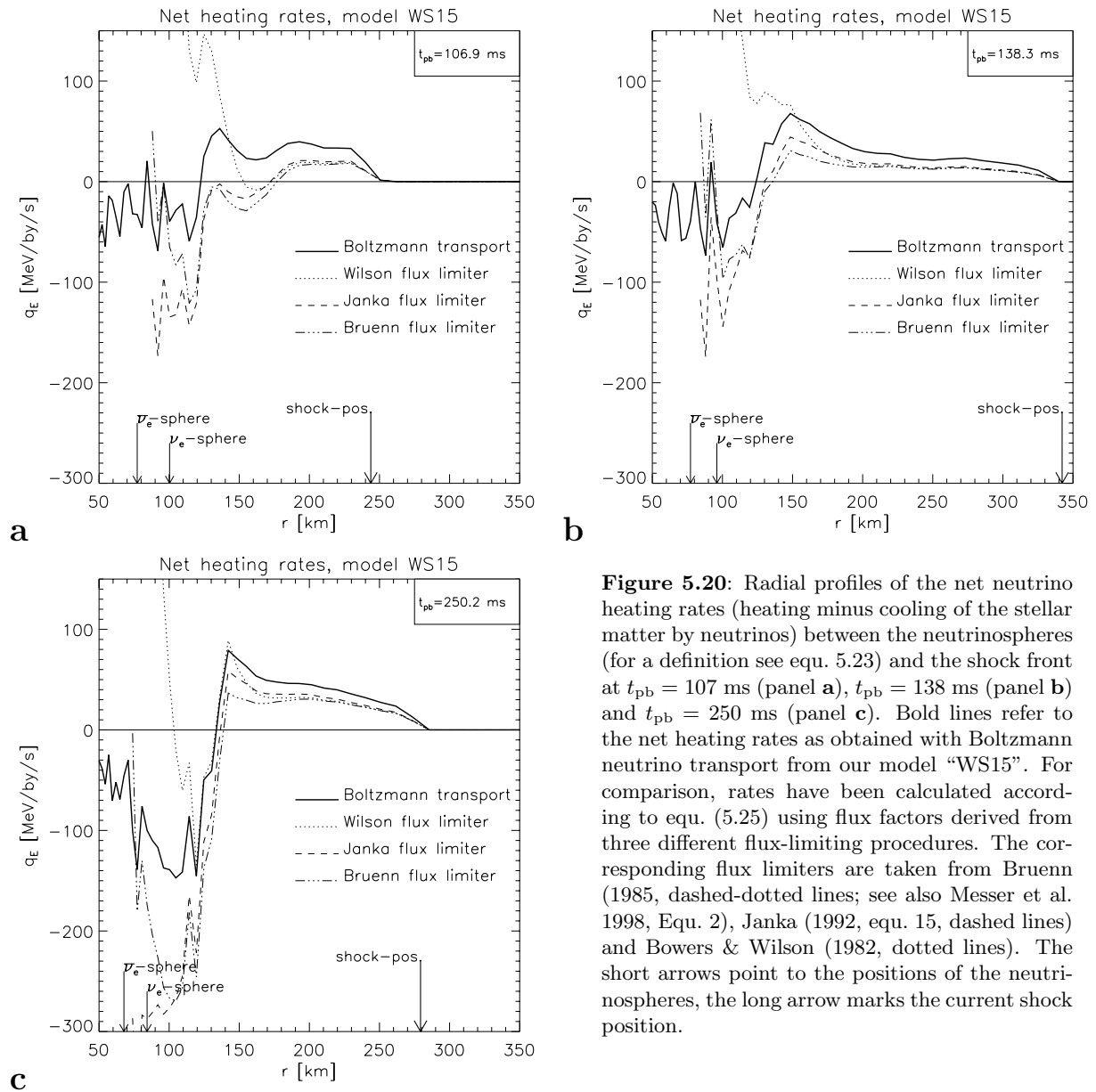


Figure 5.20: Radial profiles of the net neutrino heating rates (heating minus cooling of the stellar matter by neutrinos) between the neutrinospheres (for a definition see equ. 5.23) and the shock front at $t_{\text{pb}} = 107$ ms (panel **a**), $t_{\text{pb}} = 138$ ms (panel **b**) and $t_{\text{pb}} = 250$ ms (panel **c**). Bold lines refer to the net heating rates as obtained with Boltzmann neutrino transport from our model “WS15”. For comparison, rates have been calculated according to equ. (5.25) using flux factors derived from three different flux-limiting procedures. The corresponding flux limiters are taken from Bruenn (1985, dashed-dotted lines; see also Messer et al. 1998, Equ. 2), Janka (1992, equ. 15, dashed lines) and Bowers & Wilson (1982, dotted lines). The short arrows point to the positions of the neutrinospheres, the long arrow marks the current shock position.

the inverse flux factor. The emitted spectra are formed in the vicinity of the neutrinospheres and also the luminosity is determined inside the neutron star. The inverse flux factor can be assumed to be of order unity for the present purposes (cf. Fig. 5.23). Thus, to a first approximation, all three factors are roughly constant as a function of radius and therefore the heating rate (equ. 5.25) scales as

$$q_{\text{E}}^+ \propto r^{-2}. \quad (5.26)$$

The cooling rates due to the electron and positron capture reactions (5.24) on the other hand can

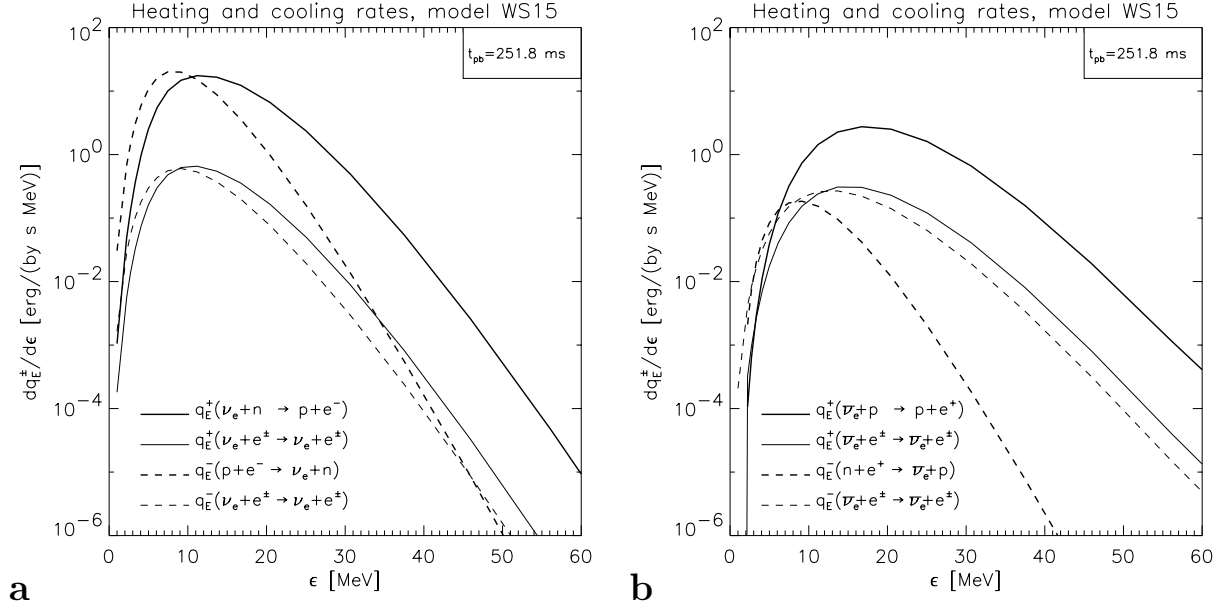


Figure 5.21: Spectral distribution of the heating ($dq_{\text{E}}^+/\text{d}\epsilon$, solid lines) and cooling ($dq_{\text{E}}^-/\text{d}\epsilon$, dashed lines) rates, taken at $r = 150$ km, which is slightly outside the gain radius, where the *net* heating ($q_{\text{E}} := q_{\text{E}}^+ - q_{\text{E}}^-$) peaks. Panel **a** shows the rates for electron neutrinos, panel **b** is for electron antineutrinos. Post bounce time is $t_{\text{pb}} = 138$ ms. Heating is mainly provided by β -processes with free nucleons (bold lines) with only minor contributions due to scattering of neutrinos off charged leptons (thin lines).

be shown to scale with the sixth power of the temperature (see e. g. Janka 1991b, Chap. 3.4.2)

$$q_{\text{E}}^- \propto T^6 \propto r^{-6}, \quad (5.27)$$

where the second proportionality uses $T \propto r^{-1}$ which derives from an analysis of the typical conditions in the atmosphere around the protoneutron star (Bethe 1993). Figure 5.22 illustrates that $T \propto r^{-1}$ is indeed well fulfilled in our model. The much steeper decline of the neutrino and antineutrino cooling rates with radius compared with the heating rates implies the existence of a “gain” radius r_{g} defined by

$$q_{\text{E}}(r_{\text{g}}) := q_{\text{E}}^+(r_{\text{g}}) - q_{\text{E}}^-(r_{\text{g}}) = 0, \quad (5.28)$$

where heating wins farther out ($q_{\text{E}} > 0$ for $r > r_{\text{g}}$) and net cooling dominates below ($q_{\text{E}} < 0$ for $r < r_{\text{g}}$).

The exact value of the gain radius as determined by the definition (equ. 5.28) can be used to perform a consistency check for the computed neutrino luminosity $L_{\nu}(r) := 4\pi r^2 \int_0^{\infty} \text{d}\epsilon 4\pi H_{\nu}(r, \epsilon)$ by invoking the neutrino energy equation (equ. 2.59). Neglecting velocity-dependent terms and assuming stationary state neutrino transport, equ. (2.59) reads

$$\frac{1}{r^2} \frac{\partial}{\partial r} (L_{\nu_e} + L_{\bar{\nu}_e}) = -4\pi Q_{\text{E}}, \quad (5.29)$$

which obviously implies that the gain radius coincides with the position, where the radial gradient of the total neutrino luminosity $L_{\nu_e} + L_{\bar{\nu}_e}$ changes sign. Comparing Fig. 5.20c and Fig. 5.23c one

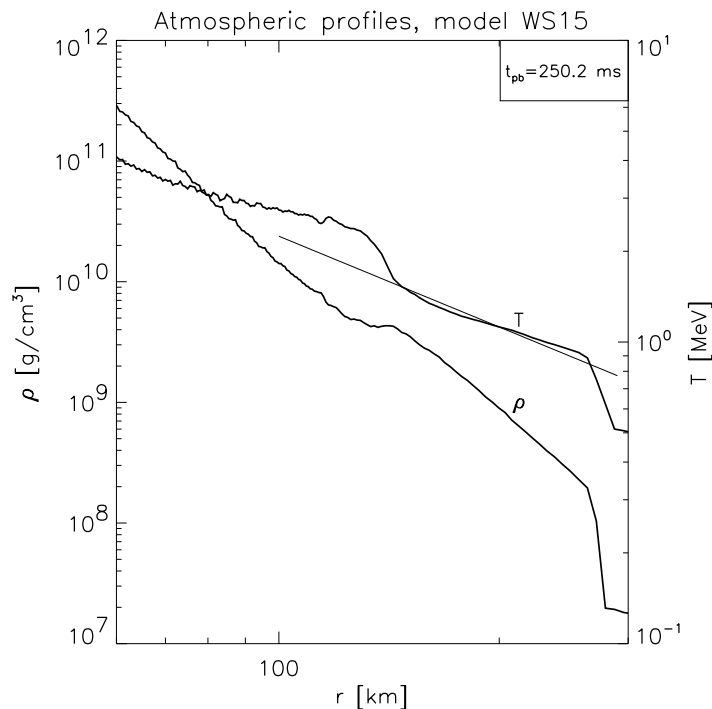


Figure 5.22: Radial profiles of the density (scale given by the axis on the left hand side) and the temperature (scale given by the axis on the right hand side) in the atmosphere surrounding the proton-neutron star for model “WS15”, 250 ms after core bounce. The thin straight line has a slope of r^{-1} .

finds that the gain radius is indeed located at the position of the luminosity maxima at $r_g = 130$ km in our model. For the temporal evolution of the gain radius see Fig. 5.12.

One recognizes an additional sharp rise in the total luminosity at $r \approx 260$ km, which is associated with the shock and reflects the blueshifts of the comoving frame luminosity for observers falling towards the shock with the accretion flow. This increase, however, does not lead to a noticeable rise of the rate of energy exchange with the stellar fluid, which is of no surprise, since the abundances of free nucleons and hence the corresponding absorption and emission rates are extremely small in the preshock matter and therefore the source term almost vanishes.

Flux limiting: Above the neutrinospheres, the density decreases rapidly with radius (cf. Figs. 5.22, 5.13a). Due to the corresponding steep rise of the neutrino transport mean free paths, common flux limiters assume an almost immediate transition to the free streaming regime where the flux factor f_H approaches unity. Thus for a given luminosity, the number and energy density of the neutrinos and hence the interaction rate with the stellar medium is usually underestimated (note that f_H appears in the denominator of equ. 5.25.). In Fig. 5.23a we compare the inverse flux factors displayed at time $t_{pb} = 250$ ms after bounce for our model “WS15” with “effective” flux factors computed by three different flux-limiting procedures. The “effective” MGFLD flux factor is estimated by using the (monochromatic) neutrino energy densities as obtained from our Boltzmann neutrino transport results and employing the MGFLD formula (equ. 5.4) to compute the corresponding flux-limited radiation flux density (cf. the discussion following equ. 5.3).

One notices significant deviations from our transport calculation (model “WS15”) as well as major differences between different flux limiters. As can be seen from Fig. 5.20, this translates into deviations of up to a factor of two for the *net* heating rate, when, e. g. the flux limiters of Bruenn

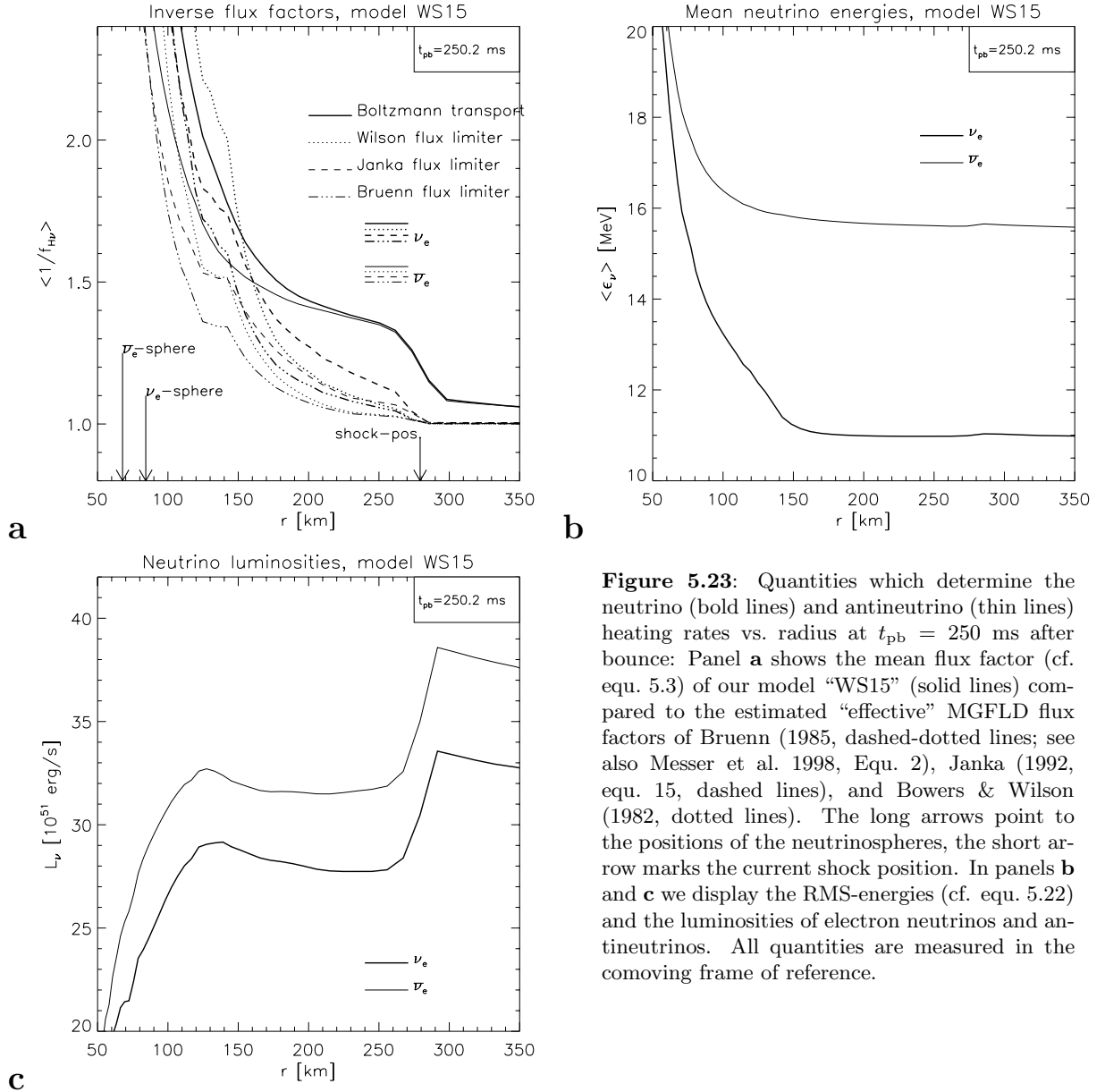


Figure 5.23: Quantities which determine the neutrino (bold lines) and antineutrino (thin lines) heating rates vs. radius at $t_{\text{pb}} = 250$ ms after bounce: Panel **a** shows the mean flux factor (cf. equ. 5.3) of our model “WS15” (solid lines) compared to the estimated “effective” MGFLD flux factors of Bruenn (1985, dashed-dotted lines; see also Messer et al. 1998, Equ. 2), Janka (1992, equ. 15, dashed lines), and Bowers & Wilson (1982, dotted lines). The long arrows point to the positions of the neutrinospheres, the short arrow marks the current shock position. In panels **b** and **c** we display the RMS-energies (cf. equ. 5.22) and the luminosities of electron neutrinos and antineutrinos. All quantities are measured in the comoving frame of reference.

(1985) or Janka (1992) are employed. The flux limiter of Bowers & Wilson (1982) performs even worse by dramatically overestimating the net heating in the vicinity of the gain radius and below. In order to understand the large deviations of the net heating rates one has to recall that below the gain radius one typically finds $|q_{\text{E}}^+/q_{\text{E}}| \approx |q_{\text{E}}^-/q_{\text{E}}| \gtrsim 10$, which implies that small differences in the flux factor (cf. Fig. 5.23a) and hence the heating rate q_{E}^+ can give rise to dramatically different values for the *net* heating rate $q_{\text{E}} := q_{\text{E}}^+ - q_{\text{E}}^-$. Note that for this reason the inconsistencies arising due to our *a posteriori*-estimation of the MGFLD flux with using Boltzmann transport results are much more pronounced in the opaque interior, where the ratios $|q_{\text{E}}^+/q_{\text{E}}|$ and $|q_{\text{E}}^-/q_{\text{E}}|$ are extremely large. We have therefore truncated the displayed profiles of the MGFLD heating rates inside the neutrino spheres, since equilibrium ($q_{\text{E}} \approx 0$) is not reproduced correctly.

t_{pb} [ms]	$\langle \epsilon_{\nu_e} \rangle_L$ [MeV]	$\langle \epsilon_{\nu_e}^2 \rangle_L^{1/2}$ [MeV]	$\eta_{\nu_e}^{\text{eff}}$	$T_{\nu_e}^{\text{eff}}$ [MeV]	$\langle \epsilon_{\bar{\nu}_e} \rangle_L$ [MeV]	$\langle \epsilon_{\bar{\nu}_e}^2 \rangle_L^{1/2}$ [MeV]	$\eta_{\bar{\nu}_e}^{\text{eff}}$	$T_{\bar{\nu}_e}^{\text{eff}}$ [MeV]
138.3	6.7	7.1	(7.1)	(1.1)	11.7	12.6	4.0	2.6
250.2	8.4	9.2	2.9	2.1	12.3	13.3	3.7	2.8
349.4	8.8	9.7	2.6	2.3	12.5	13.6	3.5	3.0

Table 5.2: Spectral properties of the luminosity of electron neutrinos and antineutrinos measured at $r = 1000$ km at the three given times after bounce in model “WS15”. The mean energy $\langle \epsilon_{\nu} \rangle_L := (\int_0^{\infty} d\epsilon dL_{\nu}/d\epsilon)/(\int_0^{\infty} d\epsilon \epsilon^{-1} dL_{\nu}/d\epsilon)$ and the mean squared energy $\langle \epsilon_{\nu}^2 \rangle_L := (\int_0^{\infty} d\epsilon \epsilon dL_{\nu}/d\epsilon)/(\int_0^{\infty} d\epsilon \epsilon^{-1} dL_{\nu}/d\epsilon)$ are used to determine the parameters η_{ν}^{eff} and T_{ν}^{eff} ($\nu \in \{\nu_e, \bar{\nu}_e\}$) of a Fermi-Dirac distribution (equ. 5.30) which is used to fit the actual spectra. Numbers in brackets indicate that no reasonable quality of the fit was obtained (see Fig. 5.24).

Our results might offer a clue to the question, why the early successful explosions obtained by Wilson (1985), who employed the flux limiter of Bowers & Wilson (1982), could not be confirmed by other MGFLD simulations (e. g. Bruenn 1993; Bruenn et al. 1995) using different prescriptions for the flux limiter (Bruenn 1985): The Bowers & Wilson (1982) flux limiter overestimates the neutrino energy deposition below the shock, in contrast to the flux limiter of Bruenn (1985). This also demonstrates that flux limiting does not necessarily lead to an underestimation of the net neutrino heating rates. All these findings illustrate once again that a flux-limiting procedure does not provide a suitable approximation of the neutrino transport which allows to calculate accurate heating rates in the semitransparent regime between the neutrinospheres and the hydrodynamic shock.

Spectral properties of the emitted neutrinos

Following Janka & Hillebrandt (1989) we parameterize the spectral distribution of the emitted neutrinos by a Fermi-Dirac-like distribution function

$$f^{\text{FD}}(\epsilon) = \frac{1}{A} \frac{1}{1 + \exp(\epsilon/T_{\nu}^{\text{eff}} - \eta_{\nu}^{\text{eff}})}, \quad (5.30)$$

where the fit-parameters η_{ν}^{eff} and T_{ν}^{eff} can be determined by the requirements that the mean energy and the mean squared energy of the actual neutrino spectra are reproduced by the corresponding averages of the fit-function (equ. 5.30). The third free parameter A acts as a normalization constant and can be computed from the given values of the number density or energy density of neutrinos. For details of the procedure see Janka & Hillebrandt (1989); Körner (1992).

In Fig. 5.24 we show the (normalized) spectral distribution of the luminosity for our model “WS15” at three different times after bounce as measured at a radius of $r = 1000$ km together with the fitted Fermi-Dirac spectra. With the exception of the electron neutrino spectrum at the earliest time shown (Fig. 5.24a), when still some transient variability of the luminosity and the RMS-energy of electron neutrinos is present (cf. Fig. 5.15), a rather good quality of the fits to the function equ. (5.30) was obtained for both electron neutrinos and antineutrinos. The numerical values of the fit-parameters and the mean energies are summarized in Table 5.2. Values of $\eta_{\nu_e}^{\text{eff}} \approx 3$ and $T_{\nu_e}^{\text{eff}} \approx 2$ for electron neutrinos, and $\eta_{\bar{\nu}_e}^{\text{eff}} \approx 3 \dots 4$ and $T_{\bar{\nu}_e}^{\text{eff}} \approx 3$ for electron antineutrinos, which characterize the spectra of the emitted neutrinos in our model “WS15” were also found in the Monte Carlo transport simulations of Janka & Hillebrandt (1989) and appear to be typical for the later post-bounce evolution ($t_{\text{pb}} \gtrsim 200$ ms).

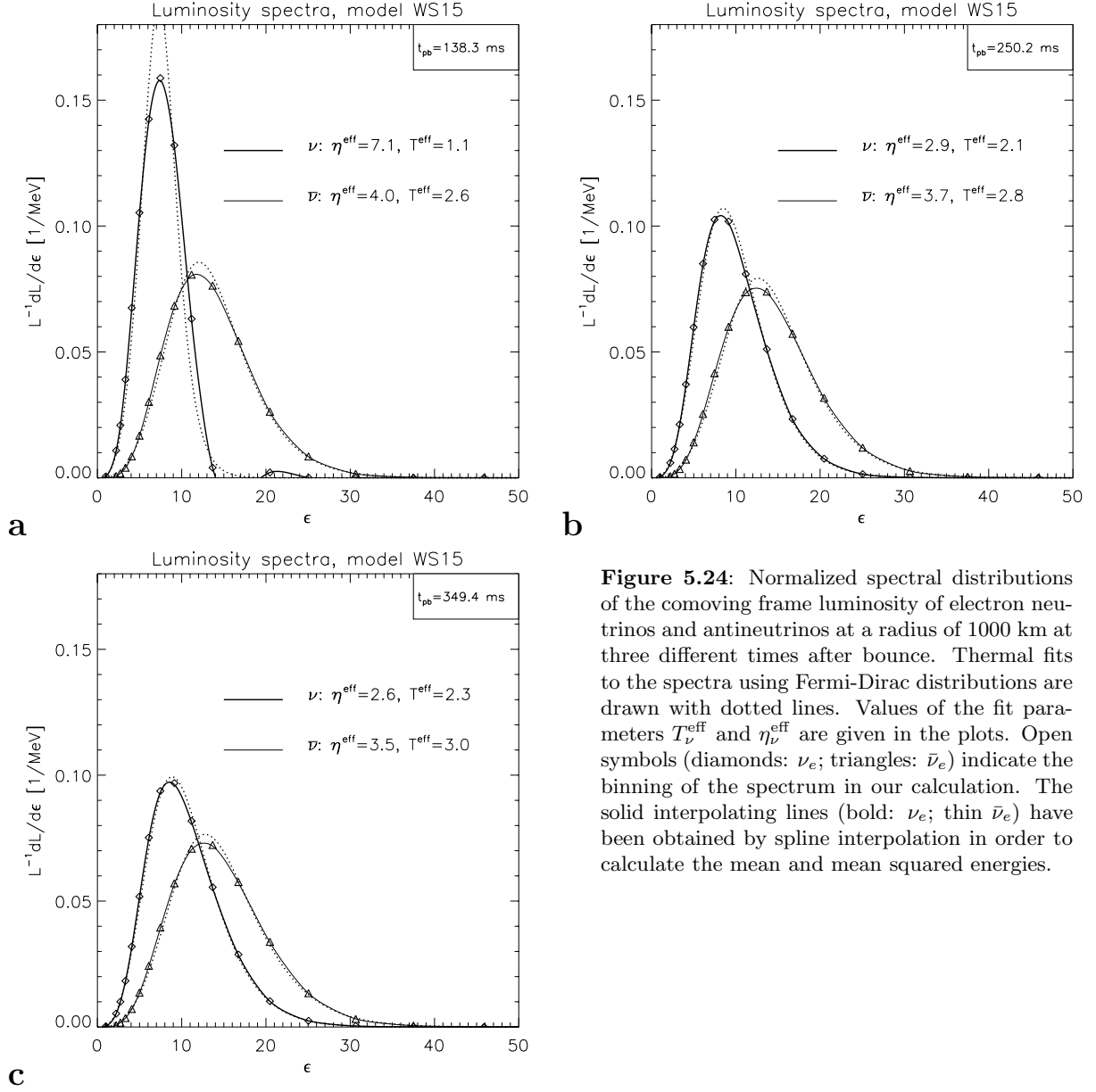


Figure 5.24: Normalized spectral distributions of the comoving frame luminosity of electron neutrinos and antineutrinos at a radius of 1000 km at three different times after bounce. Thermal fits to the spectra using Fermi-Dirac distributions are drawn with dotted lines. Values of the fit parameters T_ν^{eff} and η_ν^{eff} are given in the plots. Open symbols (diamonds: ν_e ; triangles: $\bar{\nu}_e$) indicate the binning of the spectrum in our calculation. The solid interpolating lines (bold: ν_e ; thin $\bar{\nu}_e$) have been obtained by spline interpolation in order to calculate the mean and mean squared energies.

It is important to note that except from the innermost regions of the protoneutron star the neutrinos are not in thermodynamical and chemical equilibrium with the stellar medium and hence T_ν^{eff} and η_ν^{eff} are merely fit-parameters whose values are in general different from the local values of the matter temperature T and the equilibrium chemical potential of neutrinos μ_ν^{eq} . Outside of the protoneutron star T_ν^{eff} and η_ν^{eff} rather contain a superposition of the non-equilibrium effects that shape the spectra in the regions where the neutrinos decouple from local conditions. The values of the fit-parameters T_ν^{eff} and η_ν^{eff} can be used to concisely characterize the basic spectral features of the emitted neutrinos and link computed spectra to observations (for an analysis of the neutrino signal measured from supernova SN 1987A see Janka & Hillebrandt 1989), in particular when the observational data are sparse.

5.2.4 Discussion

Comparison to published models

Comparing our simulation “WS15” to the MGFLD calculation of Bruenn et al. (1995, model “WPE15 ls(180) Newt20”), we find that both models evolve in a similar manner during the first 100 ms after bounce. By this time, the shock has reached a radius of $r_{\text{shock}} \approx 220$ km in both simulations, subsequently gets pushed out somewhat farther until it reaches a maximum radius at $t_{\text{pb}} \approx 150$ ms. This maximum radius reached by the shock, however, is different in the two simulations: In model “WPE15 ls(180) Newt20” the shock finally stalls at $r_{\text{shock}} \approx 250$ km (cf. Bruenn et al. 1995, Fig. 5), which has to be compared with the value $r_{\text{shock}} \approx 350$ km obtained for our model “WS15” (cf. Fig. 5.12).

The luminosities of electron neutrinos released from the innermost 1000 km of the star are very similar in both models. However, the luminosity of electron antineutrinos is larger by a few percent compared to the luminosity of electron antineutrinos found in model “WPE15 ls(180) Newt20” (compare our Fig. 5.15 with Fig. 3 of Bruenn et al. 1995), and starting with $t_{\text{pb}} \approx 90$ ms it exceeds the luminosity of electron neutrinos in our model “WS15” slightly. Between the times $t_{\text{pb}} \approx 50$ ms and $t_{\text{pb}} \approx 150$ ms the mean (RMS) energy of electron neutrinos is considerably larger in our model ($\langle \epsilon_{\nu_e} \rangle_{\text{RMS}} \approx 10\text{--}12$ MeV; see Fig. 5.15) compared to the MGFLD simulation ($\langle \epsilon_{\nu_e} \rangle_{\text{RMS}} \approx 8\text{--}10$ MeV; see Fig. 4 of Bruenn et al. 1995).

Unfortunately, Bruenn et al. (1995) do not show radial profiles of the heating rate for their models. However, we can compare the net heating rates of our model “WS15” with those estimated by using the flux limiter of Bruenn (1985) which has been employed in the MGFLD calculation “WPE15 ls(180) Newt20”. As an effect of the accurate treatment of the angular variation of the radiation field, we obtain neutrino energy deposition rates that are consistently larger due to the more isotropic neutrino distribution, particularly in the region between the neutrinospheres and the gain radius, where net cooling occurs. These findings are in accordance with Messer et al. (1998, see also Burrows et al. 2000) who have reported a tendency of Bruenn’s MGFLD approximation to compute less energetic neutrino spectra and a less isotropic angular distribution than accurate neutrino transport.

Both the harder spectra and the slightly enhanced luminosity of electron antineutrinos together with the more isotropic angular distributions of electron neutrinos and antineutrinos lead to larger heating rates (cf. equ. 5.25) and thus can provide a natural explanation for the larger maximum radius the shock managed to reach in our model “WS15” at $t_{\text{pb}} \approx 150$ ms. However, since in our simulation the mass density is below the lower boundary of the Lattimer & Swesty (1991) equation of state when the shock reaches a radius of $r_{\text{shock}} \approx 250$ km, it is possible, although not likely, that part of the difference of the maximum shock radius found in our model “WS15” compared to the MGFLD simulation of Bruenn et al. (1995) could be associated with a different treatment of the EoS below $\rho \simeq 10^8$ g cm $^{-3}$.

Implications for the delayed explosion mechanism

It has been proposed (Messer et al. 1998; Mezzacappa & Messer 1999) that an improved treatment of the neutrino transport *alone* might already be sufficient to obtain healthy supernova explosions for models that (marginally) failed to explode, when computed with a MGFLD approximation. Comparing our model “WS15” with MGFLD simulations of Bruenn et al. (1995) using Newtonian gravity, it can be concluded that this is not the case, at least not for the specific stellar model

considered. This conclusion is supported by a closer look at the approximations of the physics that entered our model:

Different from the models of Bruenn (1993) and Bruenn et al. (1995), we have not taken into account neutrinos of μ - and τ -flavour. When included, μ - and τ -neutrinos have been demonstrated to be *harmful* to the prompt propagation of the shock (Bruenn 1989a), which backs our argumentation. Also, when μ - and τ -neutrinos are included, a smaller fraction of the energy liberated from the protoneutron star is carried by $\bar{\nu}_e$ -neutrinos, which diminishes the heating rates (recall that neutrino energy deposition behind the shock proceeds almost exclusively via the charged-current reactions $\nu_e + n \rightarrow e^- + p$ and $\bar{\nu}_e + p \rightarrow e^+ + n$) and thus disfavours an explosion. In addition, we have neglected general relativistic effects for the hydrodynamics as well as for the neutrino transport. Comparing the results of Bruenn (1993, model “WPE15 ls(180)”) with those of Bruenn et al. (1995, model “WPE15 ls(180) Newt20”), the Newtonian approximation of the *hydrodynamics* facilitates the prompt shock propagation but it does not seem to alter the overall outcome of the simulations significantly (the shock reached a maximum radius of $r_{\text{shock}} \approx 250$ km in the Newtonian model compared to $r_{\text{shock}} \approx 200$ km in the simulation employing general relativistic hydrodynamics until it receded again in both simulations). Although no conclusive comparisons have been performed for dynamical situations yet, there are strong indications that general relativistic *neutrino transport* diminishes the neutrino heating rates and is thus also obstructive to the explosion (e. g. Janka 1991b; de Nisco, Bruenn, & Mezzacappa 1998). Concerning the initial conditions, we have not varied the progenitor star yet. Progenitors with masses larger than our $15 M_{\odot}$ -model typically have more extended iron cores (cf. Fig. 5.1) and are thus regarded to be even more difficult to explode. However, the possibility to obtain explosions in stars with progenitor masses lower than $M \approx 15 M_{\odot}$ and/or models having even smaller iron cores than our employed model “s15s7b2”, cannot be excluded without performing detailed simulations (cf. Mezzacappa, Liebendörfer, Messer, Hix, Thielemann, & Bruenn 2000).

In summary it seems necessary in order to get supernova explosions by the delayed mechanism to go beyond the general framework of approximations so far employed in self-consistent neutrino-radiation hydrodynamical simulations (i. e. spherical symmetry and “standard microphysics”).

Chapter 6

Summary and Conclusions

Neutrinos are considered to play a crucial role for the explosion mechanism of supernovae of Type II and Type Ib/c (“core-collapse supernovae”). The stalled hydrodynamic shock wave, which was launched by the bounce of the inner parts of the collapsed iron core of a massive star, is thought to be revived by the absorption of a small fraction of the neutrinos liberated from the hot and dense nascent neutron star. Although the fundamental physical effects that govern the evolution of a supernova are supposed to be known, numerical models have so far not been able to show the viability of the neutrino-mediated delayed explosion mechanism convincingly. Although considerable progress has been achieved in our understanding of convective processes during the explosion, the treatment of the neutrino transport is a major weakness of the simulations.

The aim of this thesis was to overcome this fundamental deficiency inherent to current supernova models. In the course of this work a new numerical scheme was developed and tested which allows one to calculate the neutrino transport coupled to the hydrodynamical evolution of a core-collapse supernova in a self-consistent, accurate and computationally efficient way, without invoking *ad-hoc* assumptions about the dependence of the neutrino distribution function on the momentum-space coordinates (i. e. energy and direction of propagation of the neutrinos).

Summary of results

In a variety of simulations concerned with the collapse phase of a supernova, the applicability of the new method to “realistic” supernova calculations was demonstrated. A number of physical effects such as neutrino-electron scattering that is known to sensitively determine the position where the bounce-shock forms and thus can be decisive for the success or failure of the explosion were investigated in detail. By comparisons with published work the overall accuracy of our calculations was verified.

Using the newly developed tool we have simulated the evolution of a $15 M_{\odot}$ -progenitor star (with an iron core mass of $1.28 M_{\odot}$), covering collapse, bounce and the first few hundred milliseconds of the post-bounce evolution, when neutrino heating below the stalled hydrodynamic shock front becomes effective. Especially for the latter phase, a precise calculation of the neutrino transport is of crucial importance, yet the most elaborate studies that have been performed so far relied on the so-called “flux-limited diffusion” approximation, which uses purely *ad-hoc* approximations in the regions of interest. In our simulation, it was for the first time possible to treat the neutrino transport in the post-bounce phase of a core-collapse supernova in a numerically satisfactory way.

Our model did not show a successful supernova explosion. However, compared to published

simulations employing flux limiters for the neutrino transport but otherwise being similar to ours, the neutrino-heated shock wave in our model managed to propagate somewhat farther out before it finally stalled and receded again. The larger shock radius can be explained by an increased neutrino energy deposition between the neutrinospheres and the shock, caused by the harder spectra and a more isotropic angular distribution of the neutrinos in our simulation. Both effects are a consequence of the more accurate treatment of the neutrino transport.

Analyzing the heating rates in terms of a flux-limited diffusion approximation confirms this interpretation, showing that the deposition of neutrino energy behind the stalled shock can be enhanced, if the full momentum-space dependence of the neutrino distribution function is taken into account properly. However, we found this result to be sensitively dependent on the specific functional form (which is not motivated physically) adopted for the flux limiter. One of our tested flux limiters would have largely *overestimated* the energy deposition behind the shock wave in our model, which might be the reason, why in some of the very early simulations (where this form of the flux limiter was used) successful explosions were obtained.

Considering the outcome of our simulation one can conclude that supernova explosions in spherically symmetric models for progenitor masses exceeding $M \approx 15 M_{\odot}$ seem unlikely. This argument is strengthened by the fact that muon and tau flavour neutrinos have been neglected and Newtonian gravity has been invoked for calculating hydrodynamics and neutrino transport. Both approximations, which have been made in order to keep the computational effort within reasonable limits and to facilitate comparisons, most probably favour the occurrence of a supernova explosion. Therefore we do not expect a different outcome when general relativistic effects and multi-flavour neutrino transport are included in future spherically symmetric simulations.

Outlook

It has been demonstrated by multi-dimensional simulations that convective effects play an important role for the explosion mechanism of core-collapse supernovae. Convection inside the newly formed neutron star can boost the neutrino luminosities and thus enhance the neutrino heating, while convective overturn between gain radius and supernova shock transports energy from the region of strongest heating to the shock front, and thus supports the shock expansion.

In the light of our negative result for a spherically symmetric model our next step will be a multi-dimensional simulation of the same $15 M_{\odot}$ -star. In this simulation we will apply our neutrino transport code, which is particularly well suited for a generalization to a multi-dimensional treatment, when certain simplifying assumptions are made. For the specific problem to be considered, lateral and azimuthal neutrino transport in the star, which is described by spherical coordinates, is unimportant, because in the highly opaque neutron star convective inhomogeneities occur only on small angular scales and are rapidly fluctuating, whereas in the convective region behind the shock neutrinos are essentially decoupled from the stellar background. Therefore we will take into account only radial transport by solving the neutrino energy and momentum equations independently in each angular zone of the star, and close these sets of moment equations with a single, universal variable Eddington factor which is obtained by computing the full one-dimensional transport (Boltzmann equation and moment equations) on an angularly averaged stellar background. Due to the stated properties of the convection in the nascent neutron star, this is a good approximation because the variable Eddington factor as a normalized angular moment of the neutrino distribution should not show significant variation with the lateral and azimuthal coordinates of the star. This approach will ensure equilibration in the opaque central region of the star as well as overall energy

conservation. Moreover, it is connected with an acceptable increase of the required computation time, in contrast to a fully multi-dimensional solution of the time-dependent neutrino transport, which is currently definitely out of reach.

In addition to multi-dimensional effects the microphysics of the neutrino-matter interactions in the dense interior of the nascent neutron star is a matter of vivid discussions. In particular nucleon correlations and nucleon recoil in neutral-current neutrino-nucleon scatterings and charged-current neutrino absorption and emission reactions are not included satisfactorily in the current standard description of the neutrino opacities. These effects have been found to decrease the neutrino opacity compared to the treatment employed in our simulations as well as in other supernova models. A future generation of core-collapse simulations will have to take into account an improved description of the microphysics.

Appendix A

Neutrino Opacities

In this chapter we describe the implementation of the neutrino-matter interaction processes considered in our core-collapse and supernova simulations and try to give an outlook on the treatment of some additional reactions to be considered in future applications.

It is a long way from the quantum mechanical transition rate for a particular interaction process to the final expression for the source term entering the Boltzmann equation. Moreover, it unfortunately does not appear to be possible to adopt a notation that is consistent with all the different sources our expressions are taken from. Thus, in order to facilitate comparison and to develop a self-consistent notation to be used in the course of this work we try to give a general overview of the main lines of derivation for the different interaction rates. In Section A.1, we summarize the major intermediate steps in the derivation of the source terms entering the Boltzmann equation and its moment equations without referring to a specific neutrino-matter interaction process. Section A.2 deals with the neutrino reactions we have specifically taken into account in our models. Accordingly, we focus on the electron flavour neutrinos, supplemented by some remarks about a generalization (which is straightforward in most cases) also to the muon and tau flavour to be included in future models. The expressions are mainly drawn from the works of Tubbs & Schramm (1975); Schinder & Shapiro (1982); Bruenn (1985); Mezzacappa & Bruenn (1993b,c) and adopt the same type of physical approximations (referred to as “standard” prescriptions in the course of this work) that were also used by these authors.

A.1 Basic considerations

In the following we discuss the individual contributions of a number of neutrino matter interaction processes to the source term (often called “collision integral”) of the one-dimensional Boltzmann equation

$$\frac{1}{c} \frac{\partial}{\partial t} f + \mu \frac{\partial}{\partial r} f + \frac{1 - \mu^2}{r} \frac{\partial}{\partial \mu} f = \sum_{\{I\}} B_I, \quad (\text{A.1})$$

where the summation runs over the individual interaction processes¹. All quantities are evaluated in the local rest frame of the stellar fluid (if the fluid actually moves, the left hand side of equ. (A.1) changes according to the considerations detailed in Chapter 2). For the moment equations, also the angular moments of the collision integral

$$B_I^{(k)}(\epsilon) := \frac{1}{2} \int_{-1}^{+1} d\mu \mu^k B_I(\epsilon, \mu) \quad (\text{A.2})$$

are required. From these, the source terms appearing on the rhs. of the Boltzmann equation for the specific intensity equ. (2.23) and in the corresponding moment equations for neutrino number and neutrino energy or momentum are easily computed as

$$\begin{aligned} S(\epsilon, \mu) &:= \frac{c}{(2\pi\hbar c)^3} \epsilon^3 \cdot \sum_I B_I(\epsilon, \mu), \\ S_E^{(k)}(\epsilon) &:= \frac{c}{(2\pi\hbar c)^3} \epsilon^3 \cdot \sum_I B_I^{(k)}(\epsilon), \\ S_N^{(k)}(\epsilon) &:= \frac{c}{(2\pi\hbar c)^3} \epsilon^2 \cdot \sum_I B_I^{(k)}(\epsilon). \end{aligned} \quad (\text{A.3})$$

Here and in the following, the dependence of quantities on the spacetime coordinates (t, r) is suppressed in the notation.

A.1.1 Detailed balance

Quite generally, the collision integral can be written as

$$B(\epsilon, \mu) = \tilde{\eta}(\epsilon, \mu) - \chi(\epsilon, \mu) f(\epsilon, \mu), \quad (\text{A.4})$$

where the “emissivity” (cf. equ. 2.5) $\tilde{\eta}$ and the opacity χ in addition to the momentum space coordinates (ϵ, μ) and the (suppressed) spacetime coordinates (t, r) can also depend on the distribution function f (and the distribution function of other neutrino types). All effects due to stimulated emission (relevant for photons) or stimulated absorption (relevant for neutrinos) are already contained in expression (A.4).

If the radiation and the ambient medium are in strict thermodynamical equilibrium, the amount of energy emitted by the material must be exactly balanced by the amount of energy absorbed. This property must hold separately for each frequency $h^{-1}\epsilon$ and angle cosine μ . It is called “detailed balance” for this reason. As a consequence, the “emissivity” $\tilde{\eta}$ and the opacity χ are related by the Kirchhoff-Planck relation

$$\chi f^{\text{eq}} = \tilde{\eta}, \quad (\text{A.5})$$

where f^{eq} denotes the equilibrium distribution function. For neutrinos we have

$$f^{\text{eq}} := \frac{1}{1 + \exp\{(\epsilon - \mu_\nu^{\text{eq}})/T\}}, \quad (\text{A.6})$$

¹Note that an equation like (A.1) holds for each kind of neutrino or antineutrino. Given a Boltzmann equation for a particular type of neutrino, obviously only those interactions contribute to the sum on the rhs. of equ. (A.1), in which neutrinos of that species are actually produced or destroyed. By adopting this as a convention we avoid introducing an additional index for the neutrino type in this section.

where T denotes the temperature (measured in energy units) at local thermodynamic equilibrium (LTE) and μ_ν^{eq} is the neutrino chemical potential at equilibrium (e. g. $\mu_{\nu_e} = \mu_{e^-} + \mu_p - \mu_n$, where μ_{e^-} , μ_p and μ_n are the chemical potentials of electrons, protons and neutrons, respectively).

The detailed balance property and the Kirchhoff-Planck relation, respectively, are exploited in the following ways: First, by employing equ. (A.5) it is not necessary to compute opacities and emissivities separately. We will frequently make use of this simplification in the following. Second, the detailed balance requirement imposes a fundamental constraint on the collision integral, which can be used to judge about the quality of approximations that enter the derivation of a rate for a particular interaction process or its numerical implementation. Recently, Arras & Lai (1999) gave an example which illustrates how a misconstrued expression for the collision integral that was responsible for incorrect physical results could be unmasked by detailed balance arguments.

A.1.2 Neutrino absorption and emission

The expression for the rate of change of the neutrino distribution function due to absorption and emission processes reads (see Bruenn 1985)

$$B_{\text{AE}}(\epsilon, \mu) = j(\epsilon)[1 - f(\epsilon, \mu)] - f(\epsilon, \mu)/\lambda(\epsilon), \quad (\text{A.7})$$

where j denotes the emissivity (uncorrected for blocking effects) and λ is the neutrino absorption mean free path. Using the Kirchhoff-Planck relation (A.5), and introducing the absorption opacity corrected for stimulated absorption².

$$\kappa_{\text{a}}^* := \frac{1}{1 - f^{\text{eq}}} \cdot \frac{1}{\lambda} = j + \frac{1}{\lambda}, \quad (\text{A.8})$$

equation (A.7) can be rewritten as

$$B_{\text{AE}}(\epsilon, \mu) = \kappa_{\text{a}}^*(\epsilon)[f^{\text{eq}}(\epsilon) - f(\epsilon, \mu)]. \quad (\text{A.9})$$

In the latter expression it becomes evident that the source term drives the neutrino distribution function $f(\epsilon, \mu)$ towards its equilibrium value $f^{\text{eq}}(\epsilon) = (1 + \exp[(\epsilon - \mu_\nu^{\text{eq}})/T])^{-1}$. In equilibrium, the source term vanishes in accordance with the detailed balance requirement.

A.1.3 Scattering

Reduction of the scattering kernel

The rate of change of the neutrino distribution function due to scattering of neutrinos off some target particles is given by the collision integral (cf. Cernohorsky 1994, eqns. 2.1, 2.3)

$$B_{\text{S}}(\mathbf{q}) = \int \frac{d^3\mathbf{q}'}{(2\pi)^3} \cdot [f'_\nu(1 - f_\nu)R^{\text{in}}(\mathbf{q}, \mathbf{q}') - f_\nu(1 - f'_\nu)R^{\text{out}}(\mathbf{q}, \mathbf{q}')], \quad (\text{A.10})$$

where the scattering kernels are defined as the following phase space integrals over the distribution function F_{T} of the target particles, which are assumed to obey Fermi statistics:

$$\begin{aligned} R^{\text{in}}(\mathbf{q}, \mathbf{q}') &= \frac{2}{c \cdot (2\pi\hbar c)^3} \int \frac{d^3\mathbf{p}'}{(2\pi)^3} \frac{d^3\mathbf{p}}{(2\pi)^3} (1 - F_{\text{T}})F'_{\text{T}} \mathcal{R}(\mathbf{p}', \mathbf{q}'; \mathbf{p}, \mathbf{q}), \\ R^{\text{out}}(\mathbf{q}, \mathbf{q}') &= \frac{2}{c \cdot (2\pi\hbar c)^3} \int \frac{d^3\mathbf{p}'}{(2\pi)^3} \frac{d^3\mathbf{p}}{(2\pi)^3} (1 - F'_{\text{T}})F_{\text{T}} \mathcal{R}(\mathbf{p}, \mathbf{q}; \mathbf{p}', \mathbf{q}'). \end{aligned} \quad (\text{A.11})$$

²In practice, the identity $\kappa_{\text{a}}^* = j/f^{\text{eq}}$ is used

Time-reversal symmetry implies that the transition rate obeys $\mathcal{R}(\mathbf{p}', \mathbf{q}'; \mathbf{p}, \mathbf{q}) = \mathcal{R}(\mathbf{p}, \mathbf{q}; \mathbf{p}', \mathbf{q}')$, which relates the kernels as follows:

$$R^{\text{in}}(\mathbf{q}, \mathbf{q}') = R^{\text{out}}(\mathbf{q}', \mathbf{q}). \quad (\text{A.12})$$

In addition, the relation

$$R^{\text{in}}(\mathbf{q}, \mathbf{q}') = e^{-(\epsilon - \epsilon')/T} R^{\text{out}}(\mathbf{q}, \mathbf{q}') \quad (\text{A.13})$$

($\epsilon := c|\mathbf{q}|$ is the neutrino energy) can be deduced from the detailed balance requirement (see previous section), stating that the source term (A.10) must vanish if $f \equiv f^{\text{eq}}$, independent of the details of the interaction process (i. e. the functional form of the scattering rate r). Together with equ. (A.12) we obtain

$$\begin{aligned} R^{\text{out}}(\mathbf{q}, \mathbf{q}') &= e^{-(\epsilon' - \epsilon)/T} R^{\text{out}}(\mathbf{q}', \mathbf{q}), \\ R^{\text{in}}(\mathbf{q}, \mathbf{q}') &= e^{-(\epsilon - \epsilon')/T} R^{\text{in}}(\mathbf{q}', \mathbf{q}). \end{aligned} \quad (\text{A.14})$$

The scattering kernels are usually given as a function of the energies ϵ and ϵ' of the ingoing and outgoing neutrino and the cosine ω of the scattering angle. We define

$$\tilde{R}^{\text{in/out}}(\epsilon, \epsilon', \omega) := \frac{1}{(2\pi c)^3} R^{\text{in/out}}(\mathbf{q}, \mathbf{q}'), \quad (\text{A.15})$$

where the scattering angle ω is related to the angular part of the momentum space coordinates (μ, ϕ) and (μ', ϕ') of the in- and outgoing neutrinos by

$$\omega = \mu\mu' + \sqrt{(1 - \mu^2)(1 - \mu'^2)} \cos(\phi - \phi'). \quad (\text{A.16})$$

In order to simplify the expression (A.10) for the collision integral, the scattering kernels (equ. A.15) are expanded into a Legendre series

$$\tilde{R}^{\text{in/out}}(\epsilon, \epsilon', \omega) = \sum_{l=0}^{\infty} \frac{2l+1}{2} \Phi_l^{\text{in/out}}(\epsilon, \epsilon') P_l(\omega), \quad (\text{A.17})$$

with the Legendre coefficients

$$\Phi_l^{\text{in/out}}(\epsilon, \epsilon') = \int_{-1}^{+1} d\omega P_l(\omega) \tilde{R}^{\text{in/out}}(\epsilon, \epsilon', \omega). \quad (\text{A.18})$$

Note that as a consequence of the orthogonality relation (e. g. Bronstein & Semendjajew 1991)

$$\int_{-1}^{+1} d\omega P_l(\omega) P_{l'}(\omega) = \frac{2}{2l+1} \delta_{ll'} \quad (\text{A.19})$$

(and therefore $\int_{-1}^{+1} d\omega P_l(\omega) = 2\delta_{l0}$) an approximation of $\tilde{R}^{\text{in/out}}(\epsilon, \epsilon', \omega)$ by a truncated Legendre series still gives the exact integral value $\int_{-1}^{+1} d\omega \tilde{R}^{\text{in/out}}(\epsilon, \epsilon', \omega)$, independent of the level of truncation $l_{\text{max}} > 0$.

Using the addition theorem

$$P_l(\omega) = P_l(\mu)P_l(\mu') + 2 \sum_{m=1}^l \frac{(l-m)!}{(l+m)!} P_l^m(\mu)P_l^m(\mu') \cos(m(\phi - \phi')) \quad (\text{A.20})$$

to rewrite $P_l(\omega)$ in equ. (A.17), the collision integral gets³

$$\begin{aligned} B_S(\epsilon, \mu) &= (1 - f_\nu) \cdot \int_0^\infty d\epsilon' \epsilon'^2 \int_{-1}^{+1} d\mu' f'_\nu \tilde{R}^{\text{in}}(\epsilon, \mu, \epsilon', \mu') \\ &\quad - f_\nu \cdot \int_0^\infty d\epsilon' \epsilon'^2 \int_{-1}^{+1} d\mu' (1 - f'_\nu) \tilde{R}^{\text{out}}(\epsilon, \mu, \epsilon', \mu'), \end{aligned} \quad (\text{A.21})$$

with

$$\tilde{R}^{\text{in/out}}(\epsilon, \mu, \epsilon', \mu') := \int d\phi' \tilde{R}^{\text{in/out}}(\epsilon, \epsilon', \omega) = 2\pi \sum_{l=0}^\infty \frac{2l+1}{2} \Phi_l^{\text{in/out}}(\epsilon, \epsilon') P_l(\mu) P_l(\mu'). \quad (\text{A.22})$$

When working with the moment equations of the Boltzmann equation it turns out to be useful to rewrite equ. (A.21) as

$$\begin{aligned} B_S(\epsilon, \mu) &= (1 - f_\nu) \cdot 2\pi \sum_{l=0}^\infty (2l+1) P_l(\mu) \int_0^\infty d\epsilon' \epsilon'^2 \Phi_l^{\text{in}}(\epsilon, \epsilon') L'_l(\epsilon') \\ &\quad - f_\nu \cdot 2\pi \sum_{l=0}^\infty (2l+1) P_l(\mu) \int_0^\infty d\epsilon' \epsilon'^2 \Phi_l^{\text{out}}(\epsilon, \epsilon') (\delta_{l0} - L'_l(\epsilon')), \end{aligned} \quad (\text{A.23})$$

where the ‘‘Legendre moment’’ of order l

$$L_l := \frac{1}{2} \int_{-1}^{+1} d\mu P_l(\mu) f(\mu) \quad (\text{A.24})$$

of the distribution function has been introduced. The ‘‘Legendre moments’’ can obviously be written as linear combinations

$$L_l = \sum_{m=0}^l \alpha_m M_m \quad , \alpha_m \in \mathbb{R} \quad (\text{A.25})$$

of the ordinary angular moments $M_m := \frac{1}{2} \int_{-1}^{+1} d\mu \mu^m f(\mu)$. In particular we have:

$$\begin{aligned} L_0 &= M_0, \\ L_1 &= M_1, \\ L_2 &= \frac{1}{2}(3M_2 - M_0), \\ &\vdots \end{aligned} \quad (\text{A.26})$$

³We assume to background medium to be spherically symmetric, which implies that the neutrino distribution functions entering equ. (A.10) are independent of the angle ϕ' .

From equ. (A.23) the source term of the k^{th} moment equation we obtain is obtained. For $k = 0, 1$ we get:

$$\begin{aligned} B_S^{(0)}(\epsilon) &= 2\pi \sum_{l=0}^{\infty} (2l+1)(\delta_{l0} - L_l(\epsilon)) \int_0^{\infty} d\epsilon' \epsilon'^2 \Phi_l^{\text{in}}(\epsilon, \epsilon') L_l'(\epsilon') \\ &\quad - 2\pi \sum_{l=0}^{\infty} (2l+1)L_l(\epsilon) \int_0^{\infty} d\epsilon' \epsilon'^2 \Phi_l^{\text{out}}(\epsilon, \epsilon') (\delta_{l0} - L_l'(\epsilon')), \end{aligned} \quad (\text{A.27})$$

$$\begin{aligned} B_S^{(1)}(\epsilon) &= 2\pi \sum_{l=0}^{\infty} [\delta_{l1} - (l+1)L_{l+1}(\epsilon) - lL_{l-1}(\epsilon)] \int_0^{\infty} d\epsilon' \epsilon'^2 \Phi_l^{\text{in}}(\epsilon, \epsilon') L_l'(\epsilon') \\ &\quad - 2\pi \sum_{l=0}^{\infty} [(l+1)L_{l+1}(\epsilon) + lL_{l-1}(\epsilon)] \int_0^{\infty} d\epsilon' \epsilon'^2 \Phi_l^{\text{out}}(\epsilon, \epsilon') (\delta_{l0} - L_l'(\epsilon')), \end{aligned} \quad (\text{A.28})$$

where in writing equ. (A.28) we have made use of the recursion relation for the Legendre polynomials (see Bronstein & Semendjajew 1991)

$$(l+1)P_{l+1}(\mu) = (2l+1)\mu P_l(\mu) - lP_{l-1}(\mu). \quad (\text{A.29})$$

Note that

$$\int_0^{\infty} d\epsilon \epsilon^2 B_S^{(0)}(\epsilon) = 0 \quad \text{but} \quad \int_0^{\infty} d\epsilon \epsilon^3 B_S^{(0)}(\epsilon) \neq 0, \quad (\text{A.30})$$

i. e. the neutrino number is conserved in the scattering process, but there is a nonvanishing energy exchange between neutrinos and matter during scatterings.

Isoenergetic scattering

When the scattering process involves no energy transfer between neutrinos and target particles (often referred to as “isoenergetic scattering”), we have

$$\tilde{R}^{\text{in/out}}(\epsilon, \epsilon', \omega) \propto \delta(\epsilon - \epsilon'). \quad (\text{A.31})$$

Thus, by virtue of equ. (A.13), the distinction between R^{in} and R^{out} becomes unnecessary. With the definition

$$\Phi_l(\epsilon) := \delta(\epsilon - \epsilon') \Phi_l^{\text{out}}(\epsilon, \epsilon') \equiv \delta(\epsilon - \epsilon') \Phi_l^{\text{in}}(\epsilon, \epsilon'), \quad (\text{A.32})$$

the source terms (A.23, A.27, and A.28) simplify to

$$B_{\text{IS}}(\epsilon, \mu) = 2\pi \sum_{l=0}^{\infty} (2l+1)P_l(\mu) \epsilon^2 \Phi_l(\epsilon) L_l(\epsilon) - 2\pi \epsilon^2 \Phi_0(\epsilon) f_\nu, \quad (\text{A.33})$$

$$B_{\text{IS}}^{(0)}(\epsilon) = 0, \quad (\text{A.34})$$

$$B_{\text{IS}}^{(1)}(\epsilon) = 2\pi \epsilon^2 L_1(\epsilon) (\Phi_1(\epsilon) - \Phi_0(\epsilon)). \quad (\text{A.35})$$

A.1.4 Numerical implementation

For implementation into our multi-group formulation of the moment equations of neutrino transport, the average values of the source terms within individual energy bins have been calculated according to

$$B_{n+1/2}^{(k)} := \frac{1}{(\epsilon_{n+1} - \epsilon_n)} \cdot \int_{\epsilon_n}^{\epsilon_{n+1}} d\epsilon B^{(k)}(\epsilon). \quad (\text{A.36})$$

By assuming the integrand $B^{(k)}(\epsilon)$ to be a piecewise constant function of ϵ we approximate the integral (equ. A.36) to zeroth order (cf. equ. 3.20):

$$B_{n+1/2}^{(k)} \approx B^{(k)}(\epsilon_{n+1/2}). \quad (\text{A.37})$$

A.2 Explicit expressions for various interaction processes

We now turn to the actual computation of the various neutrino-matter interactions and their implementation into our transport scheme. The first two subsections are concerned with β -processes, involving free nucleons and heavy nuclei, respectively. Then scattering of neutrinos off free nucleons as well as coherent scattering off nuclei are presented in the isoenergetic approximation. Inelastic neutrino-electron scattering is then treated in the truncated Legendre series approximation. We do not discuss pair processes such as neutrino-antineutrino annihilation, since they have not yet been taken into account in our models. The implementation of the corresponding kernels can in principle proceed along the lines of our treatment of neutrino-electron scattering (cf. Bruenn 1985, appendix C.VII), with special care for the level of truncation of the Legendre expansion (Pons, Miralles, & Ibanez 1998). Also nucleon-recoil effects in neutral-current neutrino-nucleon scatterings and charged-current neutrino-nucleon absorptions can be included in this way.

A.2.1 Neutrino absorption and emission by free nucleons

With the uncorrected emissivity $j(\epsilon)$ and opacity $\chi(\epsilon)$ as given in Bruenn (1985, eqns. C13–C16), the opacity for absorption of electron neutrinos by free neutrons ($\nu_e + n \rightleftharpoons e^- + p$) reads

$$\kappa_a^*(\epsilon) = \frac{1}{4} \sigma_0 (g_V^2 + 3g_A^2) \frac{F_{e^-}(\epsilon + Q)}{f_{\nu_e}^{\text{eq}}(\epsilon)} \eta_{pn} \frac{\epsilon + Q}{m_e^2 c^4} \sqrt{(\epsilon + Q)^2 - m_e^2 c^4}, \quad (\text{A.38})$$

and the opacity for absorption of electron antineutrinos by free protons ($\bar{\nu}_e + p \rightleftharpoons e^+ + n$) is

$$\kappa_a^*(\epsilon) = \begin{cases} \frac{1}{4} \sigma_0 (g_V^2 + 3g_A^2) \frac{F_{e^+}(\epsilon - Q)}{f_{\bar{\nu}_e}^{\text{eq}}(\epsilon)} \eta_{mp} \frac{\epsilon - Q}{m_e^2 c^4} \sqrt{(\epsilon - Q)^2 - m_e^2 c^4} & \text{for } \epsilon \geq m_e c^2 + Q \\ 0 & \text{else,} \end{cases} \quad (\text{A.39})$$

where $Q := m_n c^2 - m_p c^2$ is the difference of the rest energies of the neutron and the proton and F_{e^\mp} are the Fermi distribution functions of electrons and positrons, respectively. The constants $g_V = 1$ and $g_A = 1.254$ are form factors resulting from virtual strong-interaction processes. With the Fermi constant G_F and the rest energy of the electron $m_e c^2 = 0.511$ MeV, $\sigma_0 := (4(m_e c^2 G_F)^2)/(\pi(\hbar c)^4) = 1.761 \cdot 10^{-44} \text{cm}^2$ denotes the characteristic cross section of weak interactions.

The quantity η_{pn} approximately takes into account the nucleon final-state blocking. Ignoring the recoil of the nucleon it can be approximated as (Bruenn 1985, equ. C14):

$$\eta_{pn} := 2 \int \frac{d^3\mathbf{p}}{(2\pi\hbar c)^3} F_p(\epsilon)[1 - F_n(\epsilon)] = \frac{n_n - n_p}{\exp[(\mu_n - \mu_p - Q)/T] - 1}. \quad (\text{A.40})$$

μ_n and μ_p denote the chemical potentials (including rest mass energy) of neutrons and protons, respectively. η_{np} is defined by the replacement of quantities for neutrons and protons, which is accomplished formally by exchanging the subscripts $n \leftrightarrow p$ in equ. (A.40). In the nondegenerate regime, where blocking is unimportant, one verifies the familiar limits $\eta_{pn} = n_p$ and $\eta_{np} = n_n$.

Implementation

The implementation of equations (A.38) and (A.39) is straightforward. For the blocking correction factors⁴ some care has to be applied: For reasons of computational efficiency, the calculation of the blocking factors via the second equality of equ. (A.40) is clearly preferable to the definition of η_{pn} in terms of the phase space integral (first equality in equ. A.40). However, in deriving the second equality of equ. (A.40), the nucleons are tacitly assumed to be ideal, noninteracting Fermi gases (cf. Bruenn 1985, equ. C14). If, on the other hand, the chemical potentials and number densities are related by an elaborate nuclear equation of state, e. g. by the EoS of Lattimer & Swesty (1991), this assumption does not necessarily hold and using the second equality of equ. (A.40) may lead to unphysical values for the blocking factors. In particular, we have observed that for example the fundamental inequalities $0 < \eta_{pn} < n_p$ (required by the definition of η_{pn} in equ. A.40) is violated within a certain range of temperatures and densities.

Of course, we prefer to use the number densities of neutrons n_n and protons n_p as given by the (realistic) equation of state for computing η_{pn} and η_{np} . In order to avoid the problem of unphysical blocking factors⁵, and in particular to recover the correct nondegenerate limits we recalculate the chemical potentials μ_n and μ_p that enter equ. (A.40) from the given number densities n_n and n_p assuming ideal, noninteracting and nonrelativistic Fermi gases. The inversion of the integral

$$n_{p/n}(\mu_{p/n}) = \frac{(2m_{p/n}c^2)^{3/2}}{2\pi^2\hbar^3} \int_0^\infty dE_e E_e^{1/2} \left(1 + \exp \frac{E_e - \mu_{p/n}}{T} \right)^{-1} \quad (\text{A.41})$$

is done in an approximate way (Hecht 1989, Chap. 2.2)⁶.

A.2.2 Neutrino absorption and emission by heavy nuclei

The description of the absorption of electron neutrinos on nucleons bound in heavy nuclei is very similar to absorption on free nucleons discussed previously. However, since only little is known from experiments about the internal shell structure of the heavy nuclei involved — under the conditions met in core-collapse and supernova explosions the typical heavy nucleus is extremely

⁴Strictly speaking, the quantity $\eta'_{pn} := \eta_{pn}/n_p$ with $0 < \eta'_{pn} \leq 1$ should be addressed as the “blocking *correction* factor”.

⁵Though in principle the phase-space integral in equ. (A.40) could be calculated numerically assuming interacting nucleons, the complete interaction potential of the nucleons as described in the equation of state would have to be employed. This problem is an illustration of the kind of inconsistencies between the equation of state and the employed neutrino opacities that are inherent to all supernova models published thus far.

⁶Equ. (2.22) of Hecht (1989) should read $\eta = n_0^{2/3} \dots$ instead of $\eta = n_0^{3/2} \dots$.

neutron rich — the effects of nuclear structure on the neutrino interaction cross sections must be considered as highly uncertain (cf. Bruenn & Haxton 1991). On the other hand, it has been demonstrated numerically by Bruenn (1985) and Bruenn & Haxton (1991) that for core-collapse supernova calculations, the effects of the uncertainties in these interaction processes are very small compared to other processes and thus do not require an extremely careful treatment (see also our models "WS15_nue" and "WS15" introduced in Chap. 5). We therefore adopt the conventional prescriptions which were used e. g. by Bruenn (1985); Mezzacappa & Bruenn (1993c) for the ν_e absorption opacity on nuclei ($\nu_e + A \rightleftharpoons A^* + e^-$):

$$\kappa_a^*(\epsilon) = \begin{cases} \frac{1}{4}\sigma_0 g_A^2 \frac{2}{7} N_p(Z) N_h(N) \frac{F_{e^-}(\epsilon + Q')}{f_{\nu_e}^{\text{eq}}(\epsilon)} n_A \frac{\epsilon + Q'}{m_e^2 c^4} \sqrt{(\epsilon + Q')^2 - m_e^2 c^4} & \text{for } \epsilon \geq m_e c^2 - Q' \\ 0 & \text{else,} \end{cases} \quad (\text{A.42})$$

where $Q' := m_{A^*} c^2 - m_A c^2 \approx \mu_n c^2 - \mu_p c^2 + \Delta$ denotes the mass difference between the final excited state ($A^*, Z + 1$) and the initial ground state (A, Z). Following Bruenn (1985), we set $\Delta = 3$ MeV for all nuclei. The internal structure of the absorbing nucleus with charge Z and neutron number $N = A - Z$ is represented by the term $2/7 N_p(Z) N_h(N)$ with

$$N_p(Z) = \begin{cases} 0 & Z < 20, \\ Z - 20 & 20 \leq Z < 28, \\ 8 & Z \geq 28, \end{cases} \quad (\text{A.43})$$

$$N_h(N) = \begin{cases} 6 & N < 34, \\ 40 - N & 34 \leq N < 40, \\ 0 & N \geq 40. \end{cases} \quad (\text{A.44})$$

Final state blocking of nuclei can be safely ignored since the gas of nuclei is nondegenerate.

A.2.3 Neutrino-nucleon scattering

Scattering of neutrinos off free nucleons is mediated by neutral currents only, which makes the distinction between neutrinos and antineutrinos unnecessary. Under the assumptions of negligible nucleon recoil and the nucleons being nonrelativistic, the isoenergetic kernel obeys $\tilde{R}_{\text{IS}}(\epsilon, \omega) \propto (1 + \omega)$ (e. g. Bruenn 1985; Mezzacappa & Bruenn 1993c), which implies $\Phi_{l>1}(\epsilon) \equiv 0$ (cf. eqns A.18, A.19). The source terms (eqns. A.33, A.35) simplify to

$$\begin{aligned} B_{\text{IS,nucleons}}(\epsilon, \mu) &= 2\pi(\epsilon^2 \Phi_0(\epsilon) M_0(\epsilon) + 3\epsilon^2 \Phi_1(\epsilon) \mu M_1(\epsilon)) - 2\pi\epsilon^2 \Phi_0(\epsilon) f_\nu(\epsilon) \\ &= \kappa_s^{(0)}(\epsilon) \cdot (M_0(\epsilon) - f_\nu(\epsilon)) + \kappa_s^{(1)}(\epsilon) \mu M_1(\epsilon) \end{aligned} \quad (\text{A.45})$$

$$B_{\text{IS,nucleons}}^{(1)}(\epsilon) = -M_1(\epsilon) \cdot (\kappa_s^{(0)}(\epsilon) - \frac{1}{3}\kappa_s^{(1)}(\epsilon)), \quad (\text{A.46})$$

with

$$\kappa_s^{(0)}(\epsilon) := 2\pi\epsilon^2 \cdot \Phi_0(\epsilon) = \frac{1}{16}\sigma_0 \frac{\epsilon^2}{m_e^2 c^4} \cdot \begin{cases} \eta_{nn}[1 + 3g_A^2] & \text{(neutrons),} \\ 4\eta_{pp}[(C_V - 1)^2 + \frac{3}{4}g_A^2] & \text{(protons),} \end{cases} \quad (\text{A.47})$$

$$\kappa_s^{(1)}(\epsilon) := 2\pi\epsilon^2 \cdot 3\Phi_1(\epsilon) = \frac{1}{16}\sigma_0 \frac{\epsilon^2}{m_e^2 c^4} \cdot \begin{cases} \eta_{nn}[1 - g_A^2] & \text{(neutrons),} \\ 4\eta_{pp}[(C_V - 1)^2 - \frac{1}{4}g_A^2] & \text{(protons),} \end{cases} \quad (\text{A.48})$$

The factors

$$\eta_{nn/pp} := T \frac{\partial n_{n/p}}{\partial \mu_{n/p}} \quad (\text{A.49})$$

approximately account for nucleon final state blocking. $C_V = 1/2 + 2 \sin^2 \theta_W$ and $C_A = 1/2$ (used later on) denote the weak coupling constants. We adopt a value of $\sin^2 \theta_W = 0.23$ for the Weinberg angle.

Implementation

The implementation of eqns. (A.47, A.48) is straightforward. In order to accurately attain the limits $\eta_{nn/pp} = n_{n/p}$ for nondegenerate (and nonrelativistic) and $\eta_{nn/pp} = n_{n/p} \cdot 3T/(2E_{n/p}^F)$, for degenerate (and nonrelativistic) nucleons we prefer the analytic interpolation formula proposed by Mezzacappa & Bruenn (1993c)

$$\eta_{nn/pp} := n_{n/p} \frac{\xi_{n/p}}{\sqrt{1 + \xi_{n/p}^2}}, \quad \text{with} \quad \xi_{n/p} := \frac{3T}{2E_{n/p}^F} \quad (\text{A.50})$$

to a direct numerical evaluation of equ. (A.49).

$$E_{n/p}^F = \frac{0.5(\hbar c)^2}{m_{n/p} c^2} \cdot (3\pi^2 n_{n/p})^{2/3} \quad (\text{A.51})$$

is the Fermi energy.

A.2.4 Coherent scattering of neutrinos off heavy nuclei

The rate of isoenergetic scattering of neutrinos off nuclei (ions) has to be calculated from the coherent superposition of the individual scattering amplitudes of the constituents of the nucleus. As a consequence the rate scales with the *square* of the number of nucleons A constituting the scattering target. In addition, two corrections are currently applied to the scattering rate, one is in effect at low neutrino energies, the other becomes important only at high neutrino energies:

If the neutrino wavelength becomes smaller than the radius of the nucleus (corresponding to neutrino energies of larger than approx. 100 MeV), the phase relationships of the scattering amplitudes are modified by the exact spatial distribution of the individual scattering targets. Coherent superposition of the scattering amplitudes leads to a reduction of the scattering rate for high energy neutrinos. This effect is accounted for by the so-called “nuclear form factor”, which is basically given by the Fourier transform of the nucleon density.

During stellar core-collapse, temperatures are sufficiently small, and densities are sufficiently large, so that the nuclei become spatially correlated due to Coulomb forces. If the neutrino wavelength becomes larger than the inter-ion spacing — for densities of the order of $10^{12} \text{ g cm}^{-3}$ this corresponds to neutrino energies of less than approx. 10 MeV (cf. Fig. A.1) — neutrinos scatter *coherently* off this “ion-lattice”, which leads to significantly reduced reaction rates due to the destructive interference of the individual scattered waves (in the limit $T \rightarrow 0$ one may think of Bragg-reflection of X-rays by a crystal as an electromagnetic analogue).

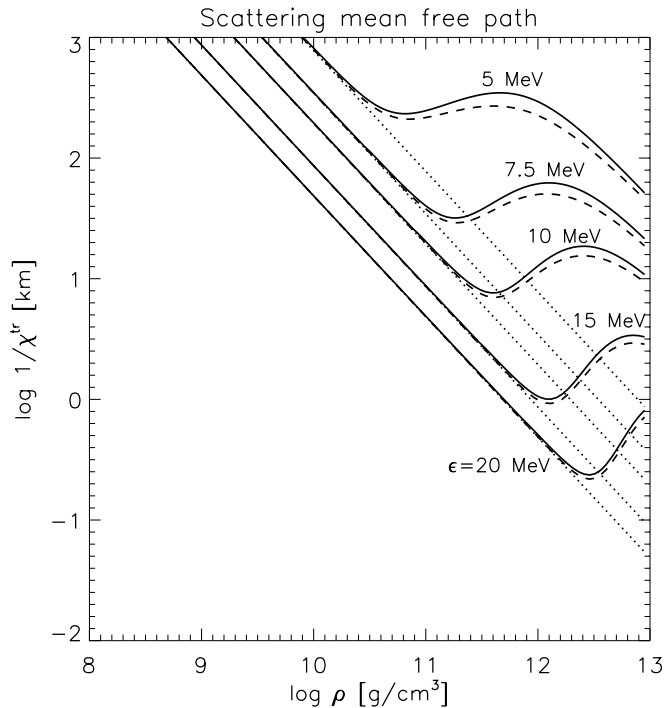


Figure A.1: Transport mean free path due to scattering of electron neutrinos off heavy nuclei as approximated by Horowitz (1997, equ. 18) as a function of the density. The solid curves include the corrections due to ion correlations and electron screening. Dashed curves are with ion correlations only, while for drawing the dotted lines both corrections have been neglected. Top to bottom, the curves are for neutrino energies of $\epsilon = 5, 7.5, 10, 15, 20$ MeV, respectively. Compare this figure to Horowitz (1997, Fig. 1).

The expression for the scattering kernel including both of the corrections introduced above is given by (for an elaborate derivation see the appendix in Bruenn & Mezzacappa 1997)

$$\tilde{R}_{\text{IS,ions}}(\epsilon, \omega) \propto (1 + \omega) e^{-4b\epsilon^2/c^2} \cdot (1 - \omega) \cdot \mathcal{S}_{\text{ion}}(\omega), \quad (\text{A.52})$$

where the exponential is due to the nuclear form factor, and \mathcal{S}_{ion} is the (static) structure factor that arises from ion correlations. In the so-called “static approximation”, this structure factor depends on the local thermodynamical conditions, neutrino energy and the momentum change of the neutrinos (i. e. on the scattering angle). Based on the results of Monte-Carlo simulations, Horowitz (1997) provides convenient analytical fit-formulae for the angularly averaged structure factor

$$\langle \mathcal{S}(\epsilon) \rangle_{\text{ion}} := \frac{3}{4} \int_{-1}^{+1} d\omega (1 + \omega)(1 - \omega) \mathcal{S}_{\text{ion}}(\omega), \quad (\text{A.53})$$

that can readily be used to calculate the transport opacity $\kappa_s^{(0)} - 1/3 \kappa_s^{(1)}$ (cf. equ. 2.30) entering the source term $B_{\text{IS,ions}}^{(1)}$ of the first moment equation. If the nuclear form factor is neglected at first, we have by definition of the corresponding Legendre coefficients (eqns. A.18, A.32)

$$\begin{aligned} \Phi_0^{\text{low}}(\epsilon) - \Phi_1^{\text{low}}(\epsilon) &\equiv \int_{-1}^{+1} d\omega (1 - \omega) \tilde{R}_{\text{IS,ions}}(\epsilon, \omega) \\ &= \frac{1}{64\pi} \sigma_0 \frac{1}{m_e^2 c^4} A^2 n_A C(A, Z) \cdot \int_{-1}^{+1} d\omega (1 + \omega)(1 - \omega) \cdot \mathcal{S}_{\text{ion}}(\omega) \\ &= \frac{1}{64\pi} \sigma_0 \frac{1}{m_e^2 c^4} A^2 n_A C(A, Z) \cdot \frac{4}{3} \langle \mathcal{S}(\epsilon) \rangle_{\text{ion}}, \end{aligned} \quad (\text{A.54})$$

where the “low”-superscript indicates that the expressions are valid only at low neutrino energies due to the omission of the nuclear form factor.

For high neutrino energies, on the other hand, where the ion correlations can safely be ignored, the first two Legendre coefficients read (Bruenn 1985, eqns. C44, C45, with N and Z interchanged!)

$$\Phi_0^{\text{high}}(\epsilon) = \frac{1}{64\pi} \sigma_0 \frac{1}{m_e^2 c^4} A^2 n_A C(A, Z) \cdot \frac{2y - 1 + e^{-2y}}{y^2}, \quad (\text{A.55})$$

$$\Phi_1^{\text{high}}(\epsilon) = \frac{1}{64\pi} \sigma_0 \frac{1}{m_e^2 c^4} A^2 n_A C(A, Z) \cdot \frac{2 - 3y + 2y^2 - (2 + y)e^{-2y}}{y^3}, \quad (\text{A.56})$$

with the abbreviations

$$y := \frac{2(1.07A)^{2/3} \epsilon^2 (10^{-13} \text{cm})^2}{5(\hbar c)^2} \quad (\text{A.57})$$

and

$$C(A, Z) := \left[(C_A - C_V) + (2 - C_A - C_V) \frac{2Z - A}{A} \right]^2. \quad (\text{A.58})$$

Both limits can be combined to obtain an approximate expression for the transport opacity (cf. equ. A.46) that is valid for any neutrino energy (Bruenn & Mezzacappa 1997):

$$\begin{aligned} \kappa_s^{(0)}(\epsilon) - \frac{1}{3} \kappa_s^{(1)}(\epsilon) &= 2\pi \epsilon^2 (\Phi_0(\epsilon) - \Phi_1(\epsilon)) \\ &= \frac{1}{32} \sigma_0 \frac{\epsilon^2}{m_e^2 c^4} A^2 n_A C(A, Z) \cdot 2 \frac{y - 1 + (1 + y)e^{-2y}}{y^3} \cdot \langle \mathcal{S}(\epsilon) \rangle_{\text{ion}}. \end{aligned} \quad (\text{A.59})$$

Using the limits $\lim_{\epsilon \rightarrow \infty} \langle \mathcal{S}(\epsilon) \rangle_{\text{ion}} = 1$ and $\lim_{\epsilon \rightarrow 0} 2 \frac{y - 1 + (1 + y)e^{-2y}}{y^3} = 4/3$, one easily verifies that equ. (A.59) attains the correct limits as given by equations (A.54–A.56). The overall accuracy of the approximation was estimated by Bruenn & Mezzacappa (1997) to be of the order of a few percent, given the typical thermodynamical conditions met in supernova simulations.

Implementation

The implementation of the transport opacity entering the source term $B_{\text{IS,ions}}^{(1)}(\epsilon)$ is straightforward. We calculate the ion-correlation correction $\langle \mathcal{S}(\epsilon) \rangle_{\text{ion}}$ and also the additional correction factor due to electron screening as detailed in Horowitz (1997). The latter correction applies for electron neutrinos and antineutrinos only. For the Boltzmann equation, we have to make a minor additional approximation: The correction factor $\langle \mathcal{S}(\epsilon) \rangle_{\text{ion}}$ as provided by Horowitz (1997) applies only for the combination $\Phi_0 - \Phi_1$ (cf. eqns. A.54, A.59) and not for the Legendre coefficients Φ_0 and Φ_1 individually, which are needed for calculating the collision integral for the Boltzmann equation (equ. A.33). Therefore we simply assume $\Phi_0(\epsilon) \propto \langle \mathcal{S}(\epsilon) \rangle_{\text{ion}}$ and $\Phi_1(\epsilon) \propto \langle \mathcal{S}(\epsilon) \rangle_{\text{ion}}$, which implies

$$\Phi_0(\epsilon) \approx \frac{1}{64\pi} \sigma_0 \frac{1}{m_e^2 c^4} A^2 n_A C(A, Z) \cdot \frac{2y - 1 + e^{-2y}}{y^2} \langle \mathcal{S}(\epsilon) \rangle_{\text{ion}}, \quad (\text{A.60})$$

$$\Phi_1(\epsilon) \approx \frac{1}{64\pi} \sigma_0 \frac{1}{m_e^2 c^4} A^2 n_A C(A, Z) \cdot \frac{2 - 3y + 2y^2 - (2 + y)e^{-2y}}{y^3} \langle \mathcal{S}(\epsilon) \rangle_{\text{ion}}. \quad (\text{A.61})$$

In effect, the angular dependence of the ion-correlation correction is not exactly accounted for in the Boltzmann equation. The approximation, however, only influences the *closure relation* for the moment equations. It neither affects the Legendre coefficients at larger neutrino energies (where $\langle \mathcal{S}(\epsilon) \rangle_{\text{ion}}$ is close to unity and eqns. A.55, A.56 apply) nor does it destroy the consistency of the Boltzmann equation and its moment equations. Also the expression for the transport opacity (equ. A.59) which enters the first moment equation is not altered. Moreover, it has been shown that the overall effect of the ion-correlation correction in stellar core-collapse is of only moderate importance (Bruenn & Mezzacappa 1997; this work, Sect. 5.1.2).

A.2.5 Inelastic scattering of neutrinos off charged leptons

For the scattering of neutrinos off charged leptons (“neutrino-electron scattering”: NES), we approximate the dependence of the scattering kernel on the scattering angle by truncating the Legendre expansion (A.22) at $l_{\text{max}} = 1$. For our purposes, this has been shown to provide a sufficiently accurate approximation (see Smit & Cernohorsky 1996; Mezzacappa & Bruenn 1993b). The collision integral (A.23) and its first two moments (A.27, A.28) then read (see Cernohorsky 1994)

$$B_{\text{NES}}(\epsilon, \mu) = \kappa_{\text{NES}}^{(0)}(\epsilon) - f_{\nu}(\epsilon) \kappa_{\text{NES}}^{(1)}(\epsilon) - \mu f_{\nu}(\epsilon) \kappa_{\text{NES}}^{(2)}(\epsilon) + \mu \kappa_{\text{NES}}^{(3)}(\epsilon), \quad (\text{A.62})$$

$$B_{\text{NES}}^{(0)}(\epsilon) = \kappa_{\text{NES}}^{(0)}(\epsilon) - M_0(\epsilon) \kappa_{\text{NES}}^{(1)}(\epsilon) - M_1(\epsilon) \kappa_{\text{NES}}^{(2)}(\epsilon), \quad (\text{A.63})$$

$$B_{\text{NES}}^{(1)}(\epsilon) = -M_1(\epsilon) \kappa_{\text{NES}}^{(1)}(\epsilon) - M_2(\epsilon) \kappa_{\text{NES}}^{(2)}(\epsilon) + \frac{1}{3} \kappa_{\text{NES}}^{(3)}(\epsilon), \quad (\text{A.64})$$

with

$$\begin{aligned} \kappa_{\text{NES}}^{(0)}(\epsilon) &:= \frac{1}{2} \int_0^{\infty} d\epsilon' \epsilon'^2 \Phi_0^{\text{in}}(\epsilon, \epsilon') M_0(\epsilon'), \\ \kappa_{\text{NES}}^{(1)}(\epsilon) &:= \frac{1}{2} \int_0^{\infty} d\epsilon' \epsilon'^2 [\Phi_0^{\text{out}}(\epsilon, \epsilon') + (\Phi_0^{\text{in}}(\epsilon, \epsilon') - \Phi_0^{\text{out}}(\epsilon, \epsilon')) M_0(\epsilon')], \\ \kappa_{\text{NES}}^{(2)}(\epsilon) &:= \frac{3}{2} \int_0^{\infty} d\epsilon' \epsilon'^2 [\Phi_1^{\text{in}}(\epsilon, \epsilon') - \Phi_1^{\text{out}}(\epsilon, \epsilon')] M_1(\epsilon'), \\ \kappa_{\text{NES}}^{(3)}(\epsilon) &:= \frac{3}{2} \int_0^{\infty} d\epsilon' \epsilon'^2 \Phi_1^{\text{in}}(\epsilon, \epsilon') M_1(\epsilon'). \end{aligned} \quad (\text{A.65})$$

Expressions for the Legendre coefficients

The Legendre coefficients can be written as (Yueh & Buchler 1977)

$$\Phi_l^{\text{out}}(\epsilon, \epsilon') = \alpha_{\text{I}} A_l^{\text{I}}(\epsilon, \epsilon') + \alpha_{\text{II}} A_l^{\text{II}}(\epsilon, \epsilon') \quad (l = 0, 1), \quad (\text{A.66})$$

where the constants $\alpha_{\text{I/II}}$ are combinations of the coupling constants (see e. g. Cernohorsky 1994). The coefficients ($k \in \{\text{I, II}\}$)

$$A_l^k(\epsilon, \epsilon') = \frac{\sigma_0}{8m_e^2 c^4 \pi^2 (\hbar c)^3} \int_{\max(0, \epsilon' - \epsilon)}^{\infty} dE_e F_e(E_e) (1 - F_e(E_e + \epsilon - \epsilon')) H_l^k(\epsilon, \epsilon', E_e) \quad (\text{A.67})$$

obey

$$A_l^k(\epsilon', \epsilon) = e^{-(\epsilon - \epsilon')/T} A_l^k(\epsilon, \epsilon'), \quad (\text{A.68})$$

which is in accordance with eqns. (A.12–A.14). In the integrals, $F_e(E_e)$ denotes the Fermi distribution function of the charged leptons (with parameters μ_e and T), evaluated at the lepton energy E_e . For $l = 0, 1$ the functions $H_l^{I/\text{II}}(\epsilon, \epsilon', E_e)$ are given by Yueh & Buchler (1977, eqns. A3–A8)⁷. Expressions for $l = 2$ can be found in Smit & Cernohorsky (1996).

Implementation

The integral over the energy of the charged leptons in equ. (A.67) is calculated numerically by a (N_{Leg})-point Gauss-Legendre quadrature followed by a trailing (N_{Lag})-point Gauss-Laguerre quadrature. Usually we set $N_{\text{Leg}} = 30$ and $N_{\text{Lag}} = 10$

In calculating the matrix A_l^k — which is a computationally expensive task, since for each matrix element $A_l^k(\epsilon_j, \epsilon_{j'})$, the numerical quadrature in equ. (A.67) has to be performed for all radial gridpoints — it suffices to explicitly compute $A_l^k(\epsilon_j, \epsilon_{j'})$ by equ. (A.67) only for $\epsilon_j \leq \epsilon_{j'}$. In order to obtain the missing matrix elements, the symmetry properties given by equ. (A.12) and equ. (A.13) can be exploited (Cernohorsky 1994). In doing so, not only the computational work is reduced by almost a factor of two, but even more importantly, we are also able to verify the requirement of detailed balance to within the roundoff error of the machine (see also below). On the other hand, by calculating the entire matrix $A_l^k(\epsilon_j, \epsilon_{j'})$ via a numerical integration of (equ. A.67), the accuracy of the latter can be tested (Cernohorsky 1994) by checking that the matrix fulfils the symmetry properties (eqns. A.12, A.13). Note that for each type of charged lepton (i. e. electrons and positrons in our models), a separate set of matrices $A_{l=1\dots N_l}^{I,\text{II}}$ has to be calculated. Once they have been computed, the Legendre coefficients for all types of neutrinos under consideration are efficiently calculated using equ. (A.66).

In order to evaluate the collision integral (A.62) and its moments (A.63, A.64), the integrals over neutrino energy appearing in equ. (A.65) are approximated by a simple zeroth-order quadrature. For example, the numerical approximation for $\kappa_{\text{NES}}^{(0)}$ reads

$$\kappa_{\text{NES}}^{(0)}(\epsilon_{j+1/2}) \approx \frac{1}{2} \sum_{j=0}^{N_\epsilon-1} (\epsilon'_{j+1} - \epsilon'_j) \epsilon'^2_{j+1/2} \Phi_0^{\text{in}}(\epsilon_{j+1/2}, \epsilon'_{j+1/2}) M_0(\epsilon'_{j+1/2}), \quad (\text{A.69})$$

where N_ϵ denotes the number of energy bins. By a tedious but straightforward calculation one verifies that the detailed balance requirement ($B_{\text{NES}} \equiv 0$, if $f \equiv f^{\text{eq}}$) is also fulfilled for our *numerical approximation* of the collision integral and its angular moments, provided that

- the integrals over neutrino energy appearing in equ. (A.65) are approximated by a 0th-order quadrature formula,
- the integrals over the individual energy bins which have to be performed for the source terms that enter the multi-group moment equations are approximated as given by equ. (A.37), which in particular implies that the equilibrium distribution function is approximated as $f_{n+1/2}^{\text{eq}} \approx f^{\text{eq}}(\epsilon_{n+1/2})$, and
- the symmetry relations for the numerical approximations of the Legendre coefficients are explicitly enforced by employing eqns. (A.12–A.13) as outlined above.

⁷With the following corrections (Bruenn 1985) to equ. (A5'): $\frac{4}{3}E^4w \rightarrow \frac{4}{3}E^4w'$, $\frac{8}{3}E^3w^2 \rightarrow \frac{8}{3}E^3w'^2$ and also to equ.(A8): $-\frac{8}{3}ww'^4 \rightarrow -\frac{8}{3}ww'^3$.

By the same arguments and using the same prerequisites we are able to verify also the conservation of particle number (equ. A.30) in the corresponding finite difference representation.

Finally a minor difference in the numerical implementation of the neutrino-electron scattering kernels into the transport scheme (eqns. 3.23, 3.24, 3.28, 3.29) compared to the other neutrino-matter interaction processes discussed so far has to be mentioned: The source terms (eqns. A.62–A.64) for neutrino-electron scattering obviously depend on the neutrino distribution and its angular moments as well as on the thermodynamic state of the stellar medium (the electron distribution function F_e which appears in equ. A.67 depends on the chemical potential μ_e and on the temperature T) which changes⁸ during a transport timestep according to eqns. (3.9, 3.10). Whereas the dependence of the source terms (eqns. A.62–A.64) on the neutrino distribution and its angular moments are treated fully implicitly in the discretized equations (3.23, 3.24, 3.28, 3.29), the matrices (equ. A.67) are computed only once at the beginning of each transport timestep in order to save computer time. Employing this approximation we have found no differences in the solutions when compared to a fully implicit implementation of the scattering kernels.

⁸Of course, neutrino-electron scattering cannot change the electron fraction of the medium (cf. equ. A.30), but in general also other interaction processes which do contribute to the source term $S_N^{(0)}$ are in effect.

Bibliography

- Arras P. & Lai D. (1999). Can Parity Violation in Neutrino Transport Lead to Pulsar Kicks? *ApJ* **519**, 745–749.
- Baade W. & Zwicky F. (1934). Supernovae and Cosmic Rays. *Phys. Rev.* **45**, 138.
- Baschek B., Efimov G.V., Von Waldenfels W., & Wehrse R. (1997). Radiative Transfer in Moving Spherical Atmospheres. II. Analytical Solution for Fully Relativistic Radial Motions. *A&A* **317**, 630–635.
- Bethe H.A. (1990). Supernova Mechanisms. *Reviews of Modern Physics* **62**, 801–866.
- Bethe H.A. (1993). SN 1987A - An Empirical and Analytic Approach. *ApJ* **412**, 192–202.
- Bethe H.A. & Wilson J.R. (1985). Revival of a Stalled Supernova Shock by Neutrino Heating. *ApJ* **295**, 14–23.
- Blinnikov S.I., Eastman R., Bartunov O.S., Popolitov V.A., & Woosley S.E. (1998). A Comparative Modeling of Supernova 1993J. *ApJ* **496**, 454–472.
- Bowers R.L. & Wilson J.R. (1982). A Numerical Model for Stellar Core Collapse Calculations. *ApJS* **50**, 115–159.
- Bronstein I. & Semendjajew K. (1991). *Taschenbuch der Mathematik*. Verlag Harri Deutsch, Thun und Frankfurt/Main.
- Bruenn S.W. (1985). Stellar Core Collapse - Numerical Model and Infall Epoch. *ApJS* **58**, 771–841.
- Bruenn S.W. (1989a). The Prompt-Shock Supernova Mechanism. I - The Effect of the Free-Proton Mass Fraction and the Neutrino Transport Algorithm. *ApJ* **340**, 955–965.
- Bruenn S.W. (1989b). The Prompt-Shock Supernova Mechanism. II - Supranuclear EOS Behavior and the Precollapse Model. *ApJ* **341**, 385–400.
- Bruenn S.W. (1993). Numerical Simulations of Core Collapse Supernovae. In Guidry M. & Strayer M. (eds.), *Nuclear Physics in the Universe*, First Symposium on Nuclear Physics in the Universe, 31–50, Oak Ridge, Tennessee, USA. Institute of Physics Publishing, Bristol and Philadelphia.
- Bruenn S.W., Buchler J.R., & Yueh W.R. (1978). Neutrino Transport in Supernova Models - A Multi-group, Flux-limited Diffusion Scheme. *Ap&SS* **59**, 261–284.
- Bruenn S.W. & Haxton W.C. (1991). Neutrino-nucleus Interactions in Core-collapse Supernovae. *ApJ* **376**, 678–700.

- Bruenn S.W. & Mezzacappa A. (1994). Prompt Convection in Core Collapse Supernovae. *ApJ* **433**, L45–L48.
- Bruenn S.W. & Mezzacappa A. (1997). Ion Screening Effects and Stellar Collapse. *Phys. Rev. D* **56**(12), 7529–7547.
- Bruenn S.W., Mezzacappa A., & Dineva T. (1995). Dynamic and Diffusive Instabilities in Core Collapse Supernovae. *Phys. Rep.* **256**, 69–94.
- Burrows A., Hayes J., & Fryxell B.A. (1995). On the Nature of Core-Collapse Supernova Explosions. *ApJ* **450**, 830–850.
- Burrows A. & Sawyer R.F. (1998). Effects of Correlations on Neutrino Opacities in Nuclear Matter. *Phys. Rev. C* **58**, 554–571.
- Burrows A. & Sawyer R.F. (1999). Many-body Corrections to Charged-current Neutrino Absorption Rates in Nuclear Matter. *Phys. Rev. C* **59**, 510–514.
- Burrows A., Young T., Pinto P., Eastman R., & Thompson T. (2000). A new Algorithm for Supernova Neutrino Transport and some Applications. *ApJ submitted, preprint astro-ph/9905132 (v2)*.
- Carlson B. (1967). *Computational Methods in Physics*.
- Carpenter R., Droegemeier K., Woodward P., & Hane C. (1989). Application of the Piecewise Parabolic Method (PPM) to Meteorological Modeling. *Monthly Weather Review* **118**, 586–612.
- Castor J. (1972). Radiative Transfer in Spherically Symmetric Flows. *ApJ* **178**, 779–792.
- Cernohorsky J. (1994). Symmetries in Neutrino-electron Scattering. *ApJ* **433**, 247–249.
- Chandrasekhar S. (1939). *A Introduction to the Study of Stellar Structure*. Dover books on advanced mathematics, New York, Dover.
- Clayton D.D. (1983). *Principles of Stellar Evolution and Nucleosynthesis*. Univ. Chicago Press, Chicago, 2nd edn.
- Colella P. & Woodward P. (1984). The Piecewise Parabolic Method (PPM) for Gas-Dynamical Simulations. *J. Comp. Phys.* **54**, 174.
- Dai W.W. & Woodward P.R. (1996). Iterative Implementation of an Implicit-Explicit Hybrid Scheme for Hydrodynamics. *J. Comp. Phys.* **124**, 217–229.
- Dai W.W. & Woodward P.R. (1998). Numerical Simulations for Radiation Hydrodynamics I. Diffusion Limit. *J. Comp. Phys.* **142**, 182–207.
- Dai W.W. & Woodward P.R. (2000). Numerical Simulations for Radiation Hydrodynamics II. Transport Limit. *J. Comp. Phys.* **157**, 199–233.
- de Nisco K.R., Bruenn S.W., & Mezzacappa A. (1998). The Effects of General Relativity on Core-collapse Supernovae. In Mezzacappa A. (ed.), *Stellar Evolution, Stellar Explosions and Galactic Chemical Evolution*, 571, Bristol. IOP.

- Dorfi E. (1998). *Radiation Hydrodynamics: Numerical Aspects and Applications*, chap. 3. In Steiner & Gautschy (1998).
- Dorfi E. (1999). Implicit Radiation Hydrodynamics for 1D-problems. *Journal of Computational and Applied Mathematics* **109**, 153–171.
- Fischer R. (1998). private communication.
- Flowers E. & Itoh N. (1976). Transport Properties of Dense Matter. *ApJ* **206**, 218–242.
- Freeman B. et al. (1968). DASA report 2135, Systems, Science, and Software, Inc., La Jolla.
- Fryxell B., Müller E., & Arnett W. (1989). Hydrodynamics and Nuclear Burning. preprint MPA-449, Max Planck Institut für Astrophysik, Garching.
- Godunov S.K. (1999). Reminiscences about Difference Schemes. *J. Comp. Phys.* **153**, 6–25.
- Goldreich P. & Weber S.V. (1980). Homologously Collapsing Stellar Cores. *ApJ* **238**, 991–997.
- Hannestad S., Janka H.T., Sigl G., & Raffelt G. (2000). Electron-, Mu-, and Tau-Number Conservation in a Supernova Core. *Phys. Rev. D* *submitted, preprint astro-ph/9912242* .
- Hecht T. (1989). *Deleptonisierung und Kühlung junger Neutronensterne*. Diplomarbeit, Technische Universität München.
- Heger A. (2000). private communication.
- Herant M., Benz W., & Colgate S. (1992). Postcollapse Hydrodynamics of SN 1987A - Two-dimensional Simulations of the Early Evolution. *ApJ* **395**, 642–653.
- Herant M., Benz W., Hix W.R., Fryer C.L., & Colgate S.A. (1994). Inside the Supernova: A Powerful Convective Engine. *ApJ* **435**, 339–361.
- Hillebrandt W. (1987). Stellar Collapse and Supernova Explosions. In Pacini F. (ed.), *High Energy Phenomena Around Collapsed Stars*, vol. C 195 of *NATO-ASI*, 73–104, Dordrecht. Reidel.
- Horowitz C. (1997). Neutrino Trapping in a Supernova and the Screening of Weak Neutral Currents. *Phys. Rev. D* **55**(8), 4577–4581.
- Hummer D. & Rybicki G. (1971). Radiative Transfer in Spherically Symmetric Systems. The Conservative Grey Case. *MNRAS* **152**, 1–19.
- Janka H.T. (1991a). Implications of Detailed Neutrino Transport for the Heating By Neutrino-antineutrino Annihilation in Supernova Explosions. *A&A* **244**, 378–382.
- Janka H.T. (1991b). *Neutrino Transport in Type II Supernovae and Protoneutron Stars By Monte Carlo Methods*. Ph.D. thesis, Technische Universität München. preprint MPA-587.
- Janka H.T. (1992). Flux-limited Neutrino Diffusion versus Monte Carlo Neutrino Transport. *A&A* **256**, 452–458.
- Janka H.T. (1999). private communication.

- Janka H.T. (2000). Core-collapse Supernovae — Successes, Problems and Perspectives. *Nuclear Physics A* **663&664**, 119c–131c.
- Janka H.T. & Hillebrandt W. (1989). Neutrino Emission from Type II Supernovae - an Analysis of the Spectra. *A&A* **224**, 49–56.
- Janka H.T. & Keil W. (1998). Perspectives of Core-Collapse Supernovae beyond SN 1987A. In Labhardt L., Binggeli B., & Buse R. (eds.), *Supernovae and Cosmology*, 7. Astronomisches Institut, Universität Basel.
- Janka H.T., Keil W., Raffelt G.G., & Seckel D. (1996). Nucleon Spin Fluctuations and the Supernova Emission of Neutrinos and Axions. *Phys. Rev. Lett.* **76**, 2621–2624.
- Janka H.T. & Müller E. (1996). Neutrino Heating, Convection, and the Mechanism of Type II Supernova Explosions. *A&A* **306**, 167–198.
- Keil W. (1997). *Konvektive Instabilitäten in entstehenden Neutronensternen*. Ph.D. thesis, Technische Universität München.
- Keil W., Janka H.T., & Müller E. (1996). Ledoux Convection in Protoneutron Stars — A Clue to Supernova Nucleosynthesis? *ApJ* **473**, L111–L114.
- Kifonidis K., Plewa T., Janka H.T., & Müller E. (2000). Nucleosynthesis and Clump Formation in a Core-Collapse Supernova. *ApJ* **531**, L123–L126.
- Kippenhahn R. & Weigert A. (1990). *Stellar Structure and Evolution*. Astronomy and Astrophysics Library. Springer, Berlin.
- Körner A. (1992). *Numerische Behandlung des Neutrinotransportes in Typ-II-Supernovae durch Lösung der Boltzmann-Gleichung und ihrer Momentengleichungen*. Diplomarbeit, Technische Universität München.
- Körner A. & Janka H.T. (1992). Approximate Radiative Transfer by Two-moment Closure - When is it Possible? *A&A* **266**, 613–618.
- Landau L. & Lifschitz E. (1991). *Lehrbuch Der Theoretischen Physik Bd. 6. Hydrodynamik*. Verlag Harri Deutsch.
- Lattimer J. & Burrows A. (1990). Effects of the Equation of State in Neutron Stars and in Stellar Collapse. In Danziger I. & Kjar K. (eds.), *SN 1987A and Other Supernovae*, no. 37 in ESO/EPIC Workshop, 69–81, Marciana Marina, Isola d' Elba, Italy.
- Lattimer J., Pethick C., Ravenhall D., & Lamb D. (1985). Physical Properties of Hot, Dense Matter - the General Case. *Nucl. Phys. A* **432**(3), 646–742.
- Lattimer J. & Swesty F. (1991). A Generalized Equation of State for Hot, Dense Matter. *Nucl. Phys. A* **535**, 331–376.
- LeVeque R. (1998). *Nonlinear Conservation Laws and Finite Volume Methods*, chap. 1. In Steiner & Gautschy (1998).

- LeVeque R.J. (1992). *Numerical Methods for Conservation Laws*. Lectures in Mathematics. Birkhäuser, ETH Zürich.
- Lindquist R. (1966). Relativistic Transport Theory. *Annals of Physics* **37**, 487–518.
- Lowrie R.B., Morel J.E., & Hittinger J.A. (1999). The Coupling of Radiation and Hydrodynamics. *ApJ* **521**, 432–450.
- Mayle R., Wilson J.R., & Schramm D.N. (1987). Neutrinos from Gravitational Collapse. *ApJ* **318**, 288–306.
- Mayle R.W. (1985). *Physical Processes in Collapse Driven Supernova*. Ph.D. thesis, California Univ., Berkeley.
- Mazurek T.J. (1976). Pauli Constriction of the Low-energy Window in Neutrino Supernova Models. *ApJ* **207**, L87–L90.
- Messer O.E.B., Mezzacappa A., Bruenn S.W., & Guidry M.W. (1998). A Comparison of Boltzmann and Multi-group Flux-limited Diffusion Neutrino Transport During the Post Bounce Shock Reheating Phase in Core-Collapse Supernovae. *ApJ* **507**, 353–360.
- Mezzacappa A. & Bruenn S.W. (1993a). A Numerical Method for Solving the Neutrino Boltzmann Equation Coupled to Spherically Symmetric Stellar Core Collapse. *ApJ* **405**, 669–684.
- Mezzacappa A. & Bruenn S.W. (1993b). Stellar Core Collapse - A Boltzmann Treatment of Neutrino-electron Scattering. *ApJ* **410**, 740–760.
- Mezzacappa A. & Bruenn S.W. (1993c). Type II Supernovae and Boltzmann Neutrino Transport - The Infall Phase. *ApJ* **405**, 637–668.
- Mezzacappa A., Calder A.C., Bruenn S.W., Blondin J.M., Guidry M.W., Strayer M.R., & Umar A.S. (1998a). The Interplay between Protoneutron Star Convection and Neutrino Transport in Core-Collapse Supernovae. *ApJ* **493**, 848+.
- Mezzacappa A., Calder A.C., Bruenn S.W., Blondin J.M., Guidry M.W., Strayer M.R., & Umar A.S. (1998b). An Investigation of Neutrino-driven Convection and the Core Collapse Supernova Mechanism using Multi-group Neutrino Transport. *ApJ* **495**, 911+.
- Mezzacappa A., Liebendörfer M., Messer O., Hix W., Thielemann F., & Bruenn S. (2000). The Simulation of a Spherically Symmetric Supernova of a $13 M_{\odot}$ Star with Boltzmann Neutrino Transport, and its Implications for the Supernova Mechanism. preprint astro-ph/0005366.
- Mezzacappa A. & Messer O. (1999). Neutrino Transport in Core Collapse Supernovae. *Journal of Computational and Applied Mathematics* **109**, 281–319.
- Mihalas D. (1980). Solution of the Comoving-Frame Equation of Transfer in Spherically Symmetric Flows. VI. Relativistic Flows. *ApJ* **237**, 574–589.
- Mihalas D. (1998). *Radiation Hydrodynamics*, chap. 2. In Steiner & Gautschy (1998).
- Mihalas D. & Klein R. (1982). On the Solution of the Time-Dependent Inertial-Frame Equation of Radiative Transfer in Moving Media to $\mathcal{O}(v/c)$. *J. Comp. Phys.* **46**, 97–137.

- Mihalas D. & Mihalas B. (1984). *Foundations of Radiation Hydrodynamics*. Oxford University Press.
- Mihalas D. & Weaver R. (1982). Time-dependent Radiative Transfer with Automatic Flux Limiting. *J. Quant. Spec. Radiat. Transf.* **28**(3), 213–222.
- Mohapatra R. & Pal P. (1991). *Massive Neutrinos in Physics and Astrophysics*, vol. 41 of *World Scientific Lecture Notes in Physics*. World Scientific.
- Mönchmeyer R. (1993). *Modellrechnungen zum Kollaps massereicher, rotierender Sterne*. Ph.D. thesis, Technische Universität München.
- Müller E. (1990). Supernova Theory and the Nuclear Equation of State. *J. Phys. G.* **16**, 1571–1598.
- Müller E. (1991). Multidimensional Hydrodynamical Simulations of Supernova Explosions. In Audouze J., Bludman R., Mochkovitch R., & Zinn-Justin J. (eds.), *Supernovae*, Les Houches Summer School. Elsevier Science Publishers B.V.
- Müller E. (1998). *Simulation of Astrophysical Fluid Flow*, chap. 4. In Steiner & Gautschy (1998).
- Müller E. & Janka H.T. (1997). Gravitational Radiation from Convective Instabilities in Type II Supernova Explosions. *A&A* **317**, 140–163.
- Myra E.S. & Bludman S.A. (1989). Neutrino Transport and the Prompt Mechanism for Type II Supernovae. *ApJ* **340**, 384–395.
- Plewa T. & Müller E. (1999). The Consistent Multi-fluid Advection Method. *A&A* **342**, 179–191.
- Pons J.A., Miralles J.A., & Ibanez J.M.A. (1998). Legendre Expansion of the $\nu\bar{\nu} \rightleftharpoons e^+e^-$ Kernel: Influence of High Order Terms. *A&AS* **129**, 343–351.
- Press W., Teukolsky S., Vetterling W., & Flannery B. (1992). *Numerical Recipes in Fortran*. Cambridge University Press, 2nd edn.
- Raffelt G. (1996). *Stars as Laboratories for Fundamental Physics — The Astrophysics of Neutrinos, Axions, and other Weakly Interacting Particles*. Univ. of Chicago Press.
- Raffelt G.G. & Seckel D. (1995). Self-consistent Approach to Neutral-current Processes in Supernova Cores. *Phys. Rev. D* **52**, 1780–1799.
- Raffelt G.G., Seckel D., & Sigl G. (1996). Supernova Neutrino Scattering Rates reduced by Nucleon Spin Fluctuations: Perturbative Limit. *Phys. Rev. D* **54**, 2784–2792.
- Rampp M. & Janka H.T. (2000). Spherically Symmetric Simulation with Boltzmann Neutrino Transport of Core Collapse and Post-Bounce Evolution of a $15 M_{\odot}$ Star. *ApJ* **539**, L33–L36.
- Reddy S., Prakash M., & Lattimer J.M. (1998). Neutrino Interactions in Hot and Dense Matter. *Phys. Rev. D* **58**, 3009.
- Riffert H. (1986). A General Eulerian Formulation of the Comoving-Frame Equation of Radiative Transfer. *ApJ* **310**, 729–732.

- Ruffert M. (1992). Collisions between a White Dwarf and a Main-sequence Star. II. Simulations using Multiple-nested Grids. *A&A* **265**, 82–105.
- Sato K. (1975). Supernova Explosion and Neutral Currents of Weak Interaction. *Progress in Theoretical Physics* **54**, 1325–1338.
- Schinder P.J. (1990). Exact Expressions and Improved Approximations for Interaction Rates of Neutrinos with Free Nucleons in a High-temperature, High-density Gas. *ApJS* **74**, 249–273.
- Schinder P.J. & Bludman S.A. (1989). Radiative Transport in Spherical Static Spacetime — General Relativistic Tangent-ray Method for the Variable Eddington Factors. *ApJ* **346**, 350–365.
- Schinder P.J. & Shapiro S.L. (1982). Neutrino Emission from a Hot, Dense, Plane-parallel Atmosphere in Hydrostatic Equilibrium. II - Numerical Methods and Interaction Functions. *ApJS* **50**, 23–37.
- Schinder P.J. & Shapiro S.L. (1986). Neutrino Transport in a Type II Supernova Environment. In Mihalas D. & Winkler K.H. (eds.), *Radiation Hydrodynamics in Stars and Compact Objects*, vol. 255 of *Lecture notes in physics*, 121–140. Springer-Verlag.
- Shapiro S. & Teukolsky S. (1983). *Black Holes, White Dwarfs, and Neutron Stars — the Physics of Compact Objects*. John Wiley and Sons, New York.
- Smit J.M. & Cernohorsky J. (1996). Legendre Expansion of the Neutrino-electron Scattering Kernel. *A&A* **311**, 347–351.
- Smit J.M., Cernohorsky J., & Dullemond C.P. (1997). Hyperbolicity and Critical Points in Two-moment Approximate Radiative Transfer. *A&A* **325**, 203–211.
- Smit J.M., van den Horn L.J., & Bludman S.A. (2000). Closure in Flux-limited Neutrino Diffusion and Two-moment Transport. *A&A* **356**, 559–569.
- Steiner O. & Gautschy A. (eds.) (1998). *Computational Methods for Astrophysical Fluid Flow*. Lecture Notes: Saas Fee Advanced Course 27. Springer, Berlin.
- Stone J., Mihalas D., & Norman M. (1992). ZEUS-2D: A Radiation Magnetohydrodynamics Code for Astrophysical Flows in Two Space Dimensions. III. The Radiation Hydrodynamic Algorithms and Tests. *ApJS* **80**, 819–845.
- Suzuki H. (1994). Supernova Neutrinos. In Fukugita M. & Suzuki H. (eds.), *Physics and Astrophysics of Neutrinos*, 763–847. Springer, Berlin.
- Swesty F. (1996). Thermodynamically Consistent Interpolation for Equation of State Tables. *J. Comp. Phys.* **1(127)**, 118–127.
- Tubbs D. & Schramm D. (1975). Neutrino Opacities at High Temperatures and Densities. *ApJ* **201**, 467–488.
- Wilson J.R. (1985). Supernovae and Post-Collapse Behavior. In Centrella J., LeBlanc J., & Bowers R. (eds.), *Numerical Astrophysics*, 422–434, Boston. Univ. Illinois, Urbana-Champaign US, Jones and Bartlett.

- Woosley S. (1999). private communication.
- Woosley S., Heger A., Weaver T., & Langer N. (1997). SN 1987A — Presupernova Evolution and the Progenitor Star. preprint MPA-1024, MPI f. Astrophysik, Garching.
- Yahil A. (1983). Self-similar Stellar Collapse. *ApJ* **265**, 1047–1055.
- Yamada S. (2000). Reduction of Neutrino-nucleon Scattering Rate By Nucleon-nucleon Collisions. *Nuclear Physics A* **662**, 219–232.
- Yamada S., Janka H.T., & Suzuki H. (1999). Neutrino Transport in Type II Supernovae: Boltzmann Solver vs. Monte Carlo Method. *A&A* **344**, 533–550.
- Yamada S. & Toki H. (2000). Neutrino-nucleon Reaction Rates in the Supernova Core in the Relativistic Random Phase Approximation. *Phys. Rev. C* **61**(1), 5803.
- Yorke H. (1980). Numerical Solution of the Equation of Radiation Transfer in Spherical Geometry. *A&A* **86**, 286–294.
- Yueh W.R. & Buchler J.R. (1977). Neutrino Transport in Supernova Models - S_N Method. *ApJ* **217**, 565–577.
- Zwergner T. (1995). *Der Gravitationskollaps rotierender Polytrope*. Ph.D. thesis, Technische Universität München.

Danksagung

Dank gebührt an erster Stelle meinen Eltern, die mich während meiner langen Ausbildung in vielfältiger Weise großzügig unterstützt haben.

Meinem Betreuer Hans-Thomas Janka gilt ein ganz besonderer Dank für die gleichermaßen interessante wie angenehme Zusammenarbeit während der vergangenen drei Jahre. Er war mit unermüdlichem Einsatz stets um den Fortgang des Projektes bemüht, und seiner Erfahrung auf dem Gebiet des Neutrino-transportes ist es wesentlich zu verdanken, daß auch während schwieriger Phasen immer wieder Auswege und Lösungen gefunden werden konnten. Thomas war darüberhinaus immer für Gespräche und Diskussionen jeglicher Art zugänglich. Nicht zuletzt danke ich ihm für mühevollles Korrekturlesen.

Meinem Doktorvater Wolfgang Hillebrandt danke ich für die freundliche Aufnahme in seine Arbeitsgruppe mit ihren ausgezeichneten Arbeitsbedingungen, sowie für die kritische Durchsicht des Manuskripts dieser Arbeit.

Ich danke allen, die mit der Administration der Computersysteme am MPI für Astrophysik und am Rechenzentrum Garching, wo ein Großteil der Simulationen zu dieser Arbeit durchgeführt wurden, betraut sind. Die hier herrschenden hervorragenden Bedingungen beim täglichen Umgang mit den Rechnern tragen nicht unwesentlich zum Gelingen einer Arbeit bei. Herrn Norbert Grüner danke ich für die angenehme und lehrreiche Zusammenarbeit bei der Betreuung der Internetseiten des Instituts.

Allen Mitarbeitern am Institut sei für die freundschaftliche Atmosphäre gedankt. Viele wertvolle Tips und Hilfen, Computerprogramme, sowie interessante Diskussionen verdanke ich u. a. den Herren Wolfgang Keil, Konstantinos Kifonidis, Ewald Müller und Maximilian Ruffert. Herr Rudolf Fischer von der Firma NEC hat mir wertvolle Hinweise zur Optimierung meines Programmes gegeben.

Stan Woosley und Alexander Heger danke ich für die Überlassung ihrer Sternmodelle.

Nicht zuletzt danke ich Andreas Kercek für die kameradschaftliche Atmosphäre in unserem gemeinsamen Arbeitszimmer.

Curriculum Vitae

Name: Markus Johannes Rampp
Geburtsdatum: 1.7.1971
Geburtsort: Krumbach (Schwaben)

Schulbildung: 09/77–07/81 Grundschule in Krumbach-Niederraunau
09/81–06/90 Simpert-Kraemer-Gymnasium, Krumbach
06/90 Abitur

Wehrdienst: 07/90–06/91 in Germersheim und Leipheim (Bundesluftwaffe)

Hochschulausbildung: 10/91–09/93 Grundstudium der allgemeinen Physik an der Technischen Universität (TU) München. Wahlfach: Numerische Mathematik
10/93 Diplom-Vorprüfung
10/93–03/97 Hauptstudium der allgemeinen Physik an der TU München. Wahlfächer: Astrophysik, Differentialgeometrie
12/95–12/96 Diplomarbeit am Max-Planck-Institut für Astrophysik, Garching unter Betreuung von Dr. habil. E. Müller und Dr. M. Ruffert. Thema: „*Berechnung des Gravitationswellensignals bei Entstehung und Verschmelzung von Neutronensternen*“
03/97 Erlangung des akademischen Grades „Diplom-Physiker (Univ.)“
seit 03/97 Doktorand am MPI für Astrophysik, Garching unter der Betreuung von Prof. Dr. W. Hillebrandt und Dr. H.-Th. Janka.

